The Effect of Grid Operating Conditions on the Harmonic Performance of Grid-Connected PV Inverters

Hong Soo Goh

A thesis submitted for the degree of

Doctor of Philosophy

September 2011

School of Electrical, Electronic & Computer Engineering

Newcastle University

Abstract

Solar energy is a readily available alternative energy source that can be utilised to help reduce carbon emission; typically created by traditional, yet depleting, fossil fuel sources such as coal, gas and oil. For this reason, there has been a rapid increase in the installation and development of grid-connected Photovoltaic (PV) systems.

Typically, grid-connected PV systems require a power electronic inverter to interface with the distribution grid. This thesis is concerned with the power quality interactions which arise between the distribution grid and the connected inverter. In particular, it considers the effect of grid operating conditions on the harmonic performance of the system.

In the first part of the thesis, the mechanism of the interaction between the distribution grid and the grid-connected inverter system is investigated. Specific attention is given to researching the impact this interaction has on the current controller of the grid-connected inverter system. Initially, a simulation model is developed to investigate the effect that variation in the grid operating conditions has on the harmonic performance of the PV inverter current controller. Simulation results demonstrate that the magnitude and relative phase angle of the background grid voltage harmonics (with respect to the fundamental) has a direct impact on the inverter system output current harmonics. The second part of the thesis focuses on the experimental validation of these simulation results. An experimental grid-connected inverter system is described, and the harmonic performance is fully analysed and assessed. Results are shown to compare favourably with theoretical and simulation studies. During the experimental work, the inverter output low pass filter is found to interact with the grid impedance; creating a low impedance resonance whose frequency varies over time with respect to the grid impedance. For this reason, the final part of the thesis concentrates on the suppression of this resonance. A novel adaptive PI control scheme is devised, which is tuned via feedback from a resonance detection bandpass. The proposed control scheme is experimentally compared to a conventional PI control scheme and shown to offer superior harmonic and resonant characteristics.

Acknowledgements

My first and foremost thanks go to my parent, who have been constantly support, help and guide me through everything I do. I would also like to thank Newcastle University, as without their funding this work would not have been carried out.

I would like to take this opportunity to express my sincere gratitude to my first supervisor, Dr. Matthew Armstrong for his guidance, advice and determination in giving valuable information and support throughout this project. Special thanks to my second supervisor, Dr. Bashar Zahawi, who offer his input and supports. Many thanks to the lecturer and technical staff in Power Electronics, Drives and Machines Research Group: Dr. Dave Atkinson, James Richardson, Dr. John Bennett and Dr. Chris Bateman, for their valuable advice and assistant throughout the duration of the work.

The support of the staff from mechanical workshop, electronic workshop, and electrical workshop: Jack, Allan, Stuart, Luke, Jeff, Darren, Stephen Robson and Stephen Mitchell, in helping with the construction of the equipment enclosure, PCB board and electrical wiring etc. are also greatly appreciated.

A special thanks to all of my colleagues in Power Electronics, Drives and Machines Research Group for their valued friendship and help during my time at Newcastle University.

Finally, special acknowledgement must also go to my family for being so supportive and encouraging throughout my whole studies.

Table of Contents

List of Figures

List of Tables

List of Abbreviations and Symbols

Abbreviations

AC	Alternative Current
A/D	Analogue to Digital Conversion
ADC	Analogue to Digital Converter
BP	Bandpass
CFL	Compact Fluorescent Lamps
CM	Common Mode
CPU	Central Processing Unit
CSP	Concentrated Solar Power
D/A	Digital to Analogue Conversion
DAC	Digital to Analogue Converter
DC	Direct Current
DT	Dead-time
DFT	Discrete Fourier Transform
DNO	Distribution Network Operator
DSP	Digital Signal Processor
EMC	Electromagnetic Compatibility
EMI	Electromagnetic Interference
EOC	End of Conversion
EREC	European Renewable Energy Council
ESR	Equivalent Series Resistance
EU	European Union
FACTS	Flexible AC Transmission Systems
GHG	Green House Gas
GUI	Graphical User Interface
HDF	Harmonic Distortion Factor
HF	High Frequency
HP	Highpass
HPS	High Pressure Sodium
HV	High Voltage
HVDC	High Voltage DC
IDC	Insulated-Displacement Connector

IEA	International Energy Agency
IEEE	Institute of Electrical and Electronic Engineers (USA)
IET	Institute of Engineering and Technology (UK)
IGBT	Insulated Gate Bipolar Transistor
ISR	Interrupt Service Routine
LF	Low Frequency
LP	Lowpass
LTI	Linear Time Invariant
LV	Low Voltage
MISO	Multi Input Single Output
MOSFET	Metal Oxide Field Effect Transistor
MPP	Maximum Power Point
MPPT	Maximum Power Point Tracking
MV	Medium Voltage
NPC	Neutral Point Clamped
PCC	Point of Common Coupling
PEDM	Power Electronics, Drives and Machines
PF	Power Factor
PI	Proportional-Integral
PLL	Phase locked loop
PV	Photovoltaic
PVPS	Photovoltaic Power System
PWM	Pulse Width Modulation
RES	Renewable Energy Sources
RMS	Root Mean Square
SISO	Single Input Single Output
SMPS	Switched Mode Power Supply
SNR	Signal to Noise Ratio
SOC	Start of Conversion
THD	Total Harmonic Distortion
TNO	Transmission Network Operator
UPF	Unity Power Factor
UPS	Uninterrupted Power Supply
VSC	Voltage Source Converter
ZCD	Zero Crossing Detector

Symbols

ϕ	Power factor angle
ϕ_X	Ideal inverter bridge power factor angle
ϕ_X'	Resultant inverter bridge power factor angle
δ	Angle of inverter bridge output voltage with respect to PCC voltage
θ	Phase angle
ω	Angular frequency
ΔV_X	Average of voltage deviation over a cycle of bridge output voltage
C	Capacitor/Capacitance
C_{DC}	DC link capacitor
C_f	Lowpass filter capacitor/capacitance
C_{pk}	Peak of carrier signal
d	duty ratio
dt	dead-time
$\varepsilon_r(k)$	Error signal of current feedback control in microcontroller
f	Frequency
f_1	fundamental frequency
$f_{cut\text{-}off}$	Lowpass filter cut-off frequency
F_s	Sampling frequency
f_{sw}	Switching frequency
f_{res}	resonant frequency
I	Current
I_{demand}	Demand current of current controller
I_{DC}	DC link current
I_G	Grid total supply current
I_O	Inverter system output current
I_{par}	Current of parallel resonant circuit
I_{ref}	Reference current of current controller
Irms	RMS current
I_{ser}	Current of series resonant circuit
Ithd	Current total harmonic distortion
I_X	Inverter bridge output current
K_i	Integral gain of PI controller
K_p	Proportional gain of PI controller

L	Inductor/Inductance
L_f	Lowpass filter inductor/inductance
L_g	Grid inductance
m_a	Modulation depth
$m_c(k)$	Modulating single generated by PI controller in microcontroller
$m_c(t)$	Modulating signal generated by PI controller
M_{dt}	Number of dt over a cycle of ideal fundamental bridge output voltage
$m_i(k)$	Modulating signal generated by the integral term of PI controller
$m_p(k)$	Modulating signal generated by the proportional term of PI controller
$m_s(t)$	Single update modulating signal
n^{th}	Harmonic order
P	Real power
Q	Reactive power
R	Resistor/Resistance
R_C	Capacitor series resistance
R_L	Inductor series sesistance
T_1	Period of fundamental component
T_{dt}	Period of dead-time
T_S	Sampling time
V	Voltage
V_{DC}	DC link voltage
V_G	Background grid voltage
V_{Lf}	Voltage drop across lowpass filter inductor
V_{PCC}	Point of common coupling voltage
Vrms	RMS voltage
Vthd	Voltage total harmonic distortion
V_X	Inverter bridge output voltage
X	Reactance
X_C	Capacitive reactance
X_L	Inductive reactance
Z	Impedance
Z_{Cf}	Impedance of lowpass filter capacitor
Z_{har}	Harmonic impedance
Z_{Lf}	Impedance of lowpass filter inductor
Z_g	Grid impedance

Chapter 1. Introduction

1.1 Introduction

Photovoltaic (PV) systems are used to harvest electricity from the most abundant source on the earth, the sun. It employs solar cells, made from semiconductor material such as silicon, to convert solar radiation into direct current (DC) electricity through the photovoltaic effect (Moller [1]). PV systems are environmentally friendly and unlike other renewable technologies, such as wind turbines and hydroelectric systems, are not affected by "NIMBYism" (acronym for "Not in My Backyard"); used to describe opposition by residents to a proposal for a new development close to home (Livezey [2]); hence it is practical to install at any onshore location, such as tall buildings and housing estates. Figure 1.1 shows an example of a 443 kW grid-connected PV plant, Forum I PV Pergola that interfaces with the 25kV medium voltage (MV) distribution grid in Barcelona, Spain.

Figure 1.1 View of 443 kW Forum I PV Pergola in Barcelona, Spain.

Since the initial adoption of the Kyoto Protocol [3], announced in 1997 and entered into force in 2005, there has been significant emphasis on reducing greenhouse gas (GHG) emissions by the 37 industrialized countries signed up to the Kyoto Protocol and the European community to help prevent unwanted potential climate change. Article 2(a) of the Kyoto Protocol enforces the parties to:

"(a) Implement and/or further elaborate policies and measures in accordance with its national circumstances, such as:
(iv) Research on, and promotion, development and increased use of, new and renewable forms of energy, of carbon dioxide sequestration technologies and of advanced and innovative environmentally sound technologies;".

In order to achieve this, many industrialised countries seek the means to decarbonise electricity generation by replacing conventional coal and fossil fuel fired plants with renewable technology alternatives. As part of the solution to this, and also to help meet growing energy requirements, PV systems are generally acknowledged as a major contributing green energy source for low voltage distribution networks (normally 110V to 440V AC). Due to the growing demand for renewable energy sources, the manufacture of solar cells and photovoltaic technologies has advanced dramatically in recent years. At the same time, as PV technology has matured, power conversion efficiency (typically between 12% and 15% as reported in [4]) has improved and considerable cost reductions have been achieved in the production of the solar panel [5]. It has been reported by Clark [6] that the price of PV panels has already dropped from more than $2 per watt in 2009 to about $1.50 per watt in 2011, and it is forecast in the report that the price will fall close to the $1 mark in 2013 if those rates of decline continue. As these improvements continue to be made, they will provide the opportunity for further development of PV systems.

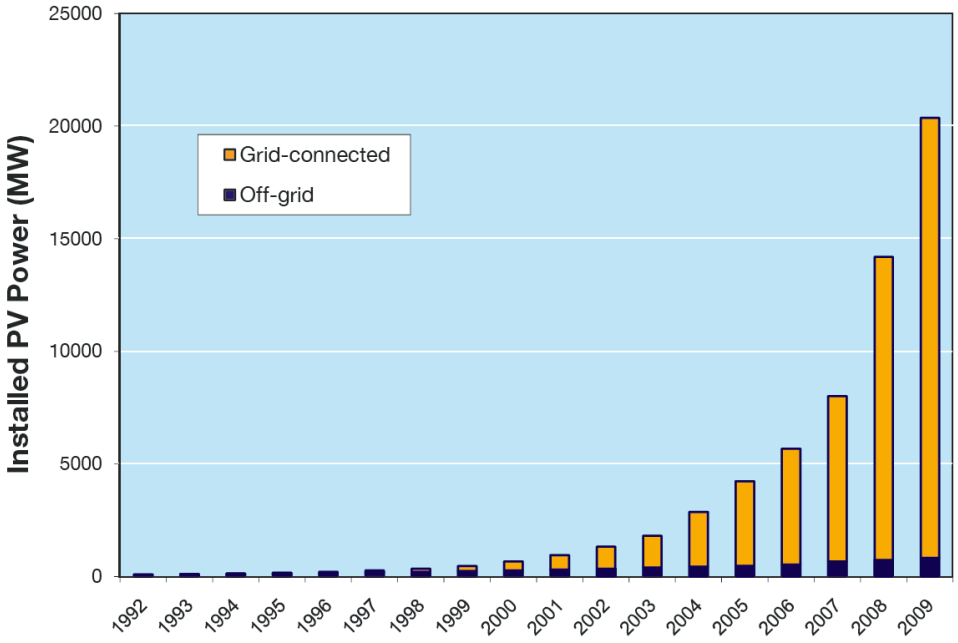

Figure 1.2 Cumulative installed grid-connected and off grid PV power in IEA PVPS member countries [7]. (Figure courtesy of IEA)

Figure 1.2 shows the cumulative installed grid-connected and off-grid PV power in the member countries of the International Energy Agency (IEA) Photovoltaic Power System (PVPS) programme since 1992 (data obtained from IEA Trends Report 2009 [7]). It shows the rapid growth in PV system installation up to 2009 while reflecting a significant increase in grid-connected PV systems as a percentage of the overall worldwide PV market. Amongst the countries that are committed to reducing GHGs via the Kyoto Protocol, the European Union (EU) has adopted a communication (COM(2007) 1 [8]) to achieve the ambitious target of supplying all energy consumption by renewable energy sources (RES) by 2050. Table 1.1 show the estimated contribution from the different RES to overall electricity consumption in 2007, 2020, 2030 and 2050, as reported by the EU energy vision up to 2050 [9]. These figures are plotted in the report [9] and recalled in Figure 1.3 to highlight the proportion of RES to the overall foreseeable electricity consumption.

	2007	**2020**	**2030**	**2050**
Wind	*104*	*477*	*833*	*1552*
Hydro	*325*	*384*	*398*	*448*
PV	*5.4*	*180*	*556*	*1347*
Biomass	*102*	*250*	*292*	*496*
Geothermal	*5.8*	*31*	*169*	*601*
CSP	*0.8*	*43*	*414*	*385*
Ocean	-	*5*	*18*	*158*
Total RES-E (TWh)	*543*	*1370*	*2407*	*4987*

Where CSP is concentrated solar power; RES-E is renewable energy sources electricity.

Table 1.1 Contribution of renewable electricity technologies to electricity consumption (TWh) [9].

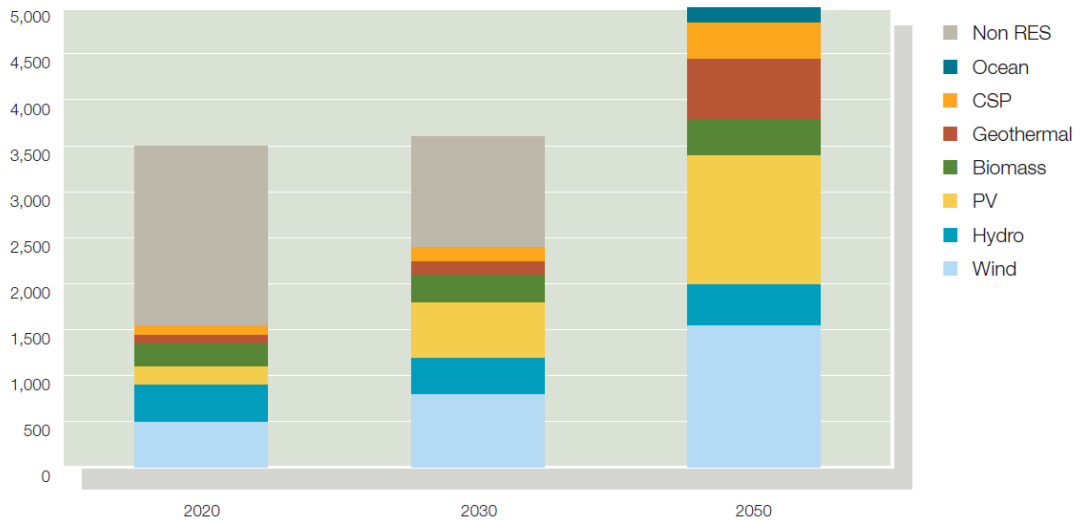

Figure 1.3 Contribution of renewable electricity technologies to electricity consumption (TWh) [9]. (Figure courtesy of EREC)

From Figure 1.2 and Figure 1.3, it can be seen that the penetration of grid-connected PV systems is set to reach unprecedented levels in the near future. This implies that not only the capacity of the PV generation will be increased, but also the level of interaction between PV systems and the electrical network will also rise significantly. The robustness of the PV system and quality of the power produced will have a considerable impact on the reliability and sustainable security of the energy supply.

Typically, a power electronic inverter is used to interface PV modules with the electrical grid. This power electronic inverter is controlled using a pulse width modulation (PWM) technique and operates in a current controlled mode to inject, unity power factor, sinusoidal current into electrical grid with low levels of distortion. Unfortunately, unwanted interactions arise when power electronic inverters are connected to the distribution grid. It has been shown that grid-connected PV inverters affect the operating conditions of the distribution grid under certain circumstances. Verhoeven [10] suggested that harmonic currents injected into the electrical grid by PV inverters will affect the power quality of the electrical grid, and in areas of high PV system penetration, potentially cause unwanted islanding. It is also known that the harmonic currents generated by PV inverters can cause malfunctioning of grid side protection devices [11]. Further problems, such as local voltage rise and network voltage fluctuations, are mentioned by Povlsen [12], Hacker, Thornycroft, et al. [13] and Canova, Spertino, et al. [14].

It has also been shown that the operating conditions of the grid can have an impact on the performance of the grid-connected inverter system. Simmons and Infield [15] demonstrated an increase in current total harmonic distortion (THD) at the output of a grid-connected inverter, and linked this to the distortion present in the grid voltage waveform. It was also suggested that the current waveform is more sinusoidal at increasing power levels, due to the finite resolution and discretisation of the ADC devices used for current measurement. As the number of grid-connected installations continues to increase, the effect of these interactions is likely to be magnified. Furthermore, the current control performance of a grid-connected PV inverter is sensitive to grid operating conditions, such as the power quality of the voltage waveform and the grid impedance. These conditions vary continuously, which makes it difficult to ensure the inverter system is tuned for optimum performance over long periods of time. An additional issue is the occurrence of resonance between the distribution grid and the PV inverter, as suggested by Enslin, Hulshorst, et al. [16].

Resonance occurs over a narrow frequency range when the grid impedance is coupled to the PV system impedance. As a result of this resonance effect, in circumstances where significant harmonics are produced by PV inverters, the power quality standards [17-19] at the point of common coupling (PCC) can be exceeded.

With the anticipated increase in grid-connected renewable systems, these reported issues are likely to become an increasing problem. They all have a significant potential to impact on the operation of the distribution grid. For this reason, there is considerable motivation to improve the harmonic performance of grid-connected PV inverters and enhance their robustness to variations in grid operating condition. Therefore, it is the aim of this research to specifically investigate the interaction between grid operating conditions, which vary over time, and the current controlled grid-connected PV inverter. By understanding these interactions, an adaptive control method is developed to enable the inverter to operate at optimum performance irrespective of grid operating conditions.

1.2 Operation of Grid-Connected PV System

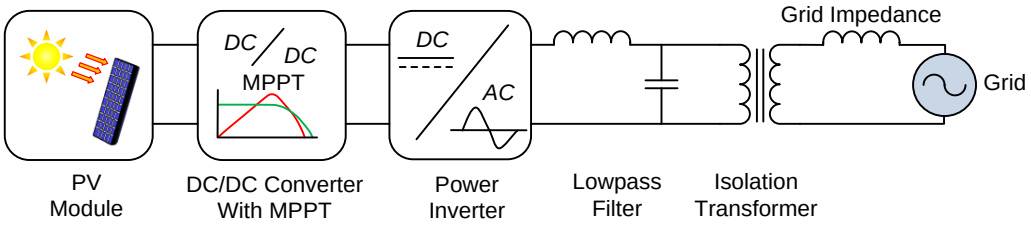

Figure 1.4 Typical arrangement of grid-connected PV system.

Figure 1.4 shows the typical arrangement of a grid-connected PV inverter system with two energy conversion stages. In the first stage, a DC/DC converter is used to transform the voltage output of the PV module to a sufficiently high enough level to be accepted by the power inverter. This DC/DC converter usually incorporates a maximum power point tracking (MPPT) controller to operate the PV module at its highest efficiency point (Messenger and Ventre [20]). The second stage of the energy conversion involves the conversion of DC current to AC sinusoidal current through a power electronic inverter. Typically, an H-Bridge inverter is used in single-phase grid-connected applications (Armstrong, Atkinson, et al. [21]). As the inverter is controlled using pulse width modulation (PWM), a lowpass filter is placed at the output of the inverter bridge to attenuate any high frequency harmonics. Constrained by regulation [17, 22], an isolation transformer is often presented at the output to eliminate the possibility of unwanted DC current being injected into the distribution grid, and also to provide electrical isolation between the grid-connected PV system and the grid.

1.2.1 *PV Module*

A PV module is comprised of individual solar cells that are electrically connected in series and parallel to achieve a desired DC output voltage and current for the PV module. An example is shown in Figure 1.5; this is a Solarex MSX-5 PV module with 36 solar cells connected in series. Each solar cell is made from silicon, which converts the light energy (photons) from the sun into DC current through the photovoltaic effect. Knaupp [23] has evaluated the design of PV module in reducing the "hot-spot" and shading effects.

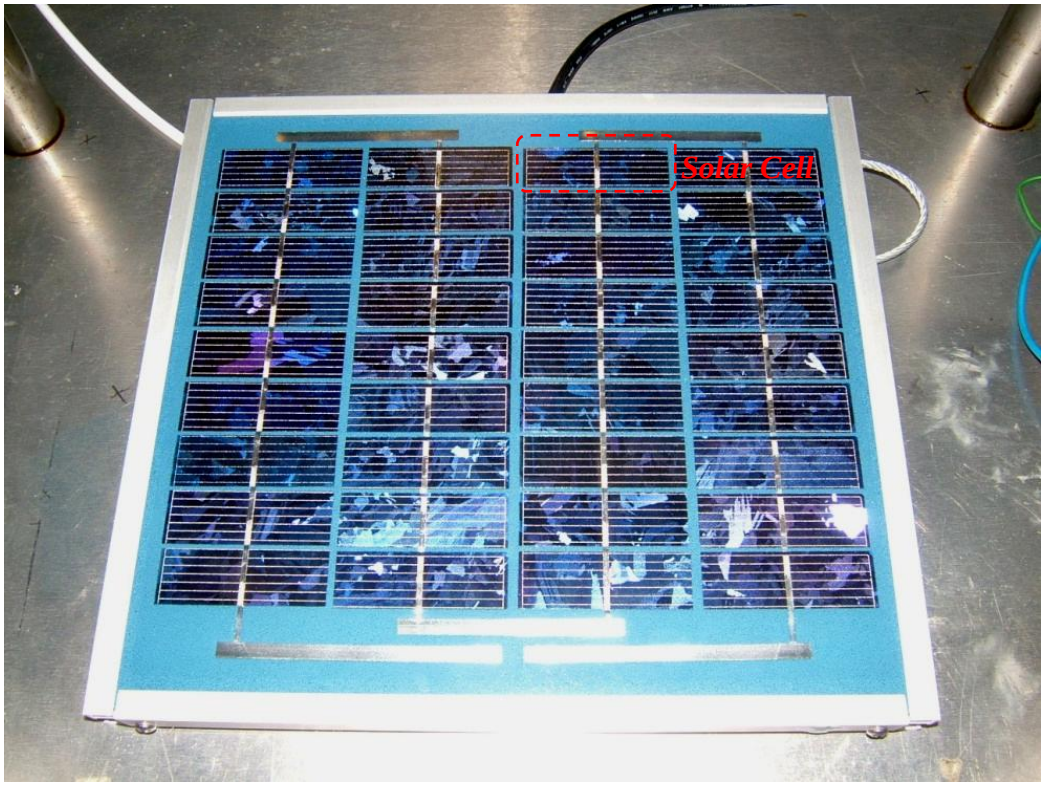

Figure 1.5 An example of Solarex MSX-5 PV module.

The typical current–voltage (I-V) characteristics of a PV module are shown in Figure 1.6. This is specifically the characteristics of the Solarex MSX-5 PV module under standard test condition (STC); illumination of 1kW/m^2, spectral distribution of AM1.5, and cell temperature of 25°C is assumed. In Figure 1.6, short-circuit current (Isc) and open-circuit voltage (Voc) are the maximum current and voltage that the PV module can produce. However, the instantaneous power output of the PV module is the product of the output current and the terminal voltage of the PV module, so neither of these conditions are appropriate operating point for the PV module (short-circuit voltage (Vsc) and open-circuit current (Ioc) are zero, which leads to zero power production).

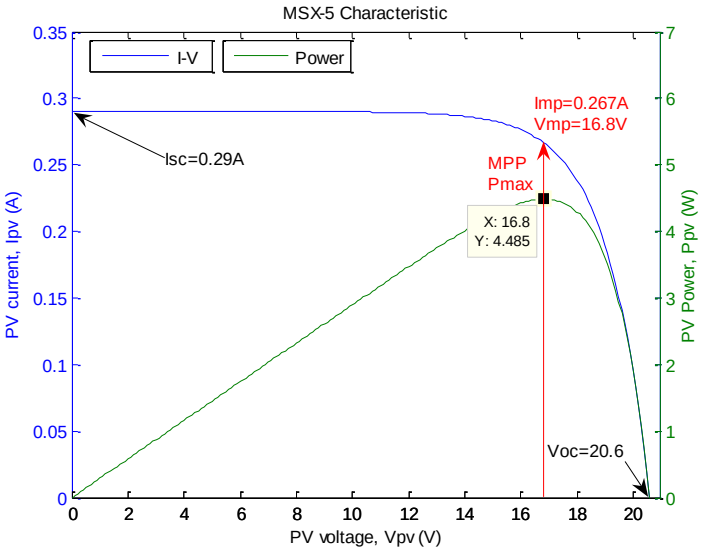

Figure 1.6 I-V curve of Solarex MSX-5 PV module.

The output power (P) characteristics of the PV module are also shown in Figure 1.6. The output power increases with terminal output voltage until maxima is reached (Pmax); it then begins to drop as the terminal voltage continues to increase due to the rapid decline in output current from the module. To achieve maximum efficiency from the PV module, both the output current and terminal voltage of the PV module have to be controlled to ensure the module operates around the maximum power point (MPP), as shown by Imp and Vmp in Figure 1.6. The MPP of the PV module I-V curve is affected by the temperature of the PV cells and the intensity of light. These effects are demonstrated by Messenger and Ventre [20], Koizumi and Kurokawa [24], Li and Wang [25]. Also, it is shown by Bzura [26] that the maximum output power of the grid-connected PV system coincides with the summer peak load period of the distribution network in New England, United States (US); in this case defined as the period from 10am to 4pm Eastern Daylight Saving Time.

1.2.2 *DC/DC Converter and Maximum Power Point Tracking*

PV module connections must adhere to strict wiring regulation for health and safety reasons. The voltage levels must be kept relatively low, typically less than 100V DC (Armstrong [27]). However, it is typical for the DC/AC inverter to have a higher DC link voltage (typically 380-400V DC) to deliver power into the distribution network at fully rated mains voltage. To match the DC link voltage of the DC/AC inverter, a boost converter is normally employed to step-up the output voltage of the PV modules. Figure 1.7 shows the circuit diagram of conventional boost converter used for stepping up the input voltage. The basic operation of this boost converter is well known and explained extensively by Mohan, Undeland, et al. [28].

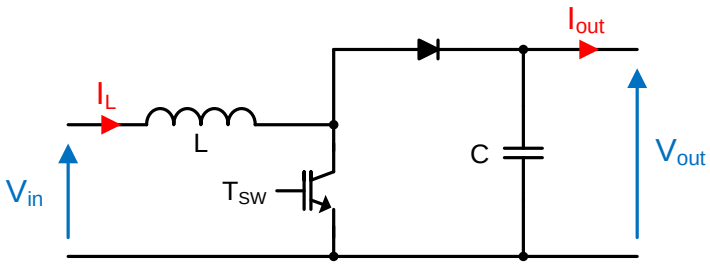

Figure 1.7 Circuit diagram of boost converter.

Whilst the simple boost converter in Figure 1.7 is commonly used to boost the output voltage of the PV module, a similar effect can be achieved by employing a high frequency (HF) transformer and alternative power converter arrangement, as shown in Figure 1.8. This is sometimes preferred as it can reduce the size and weight of the PV system whilst also providing electrical isolation between the PV module and the DC/AC inverter. Schonholzer [29] stepped-up the PV module output voltage by employing an inverter and HF transformer, while Calais, Myrzik, et al. [30] boosted the PV module output voltage by utilising a HF transformer and boost converter. More complicated topologies with HF transformer are also presented by Blaabjerg, Teodorescu, et al. [31] (HF transformer with push-pull converter and boost chopper), and Lindgren [32] (HF transformer with fly-back and forward converter).

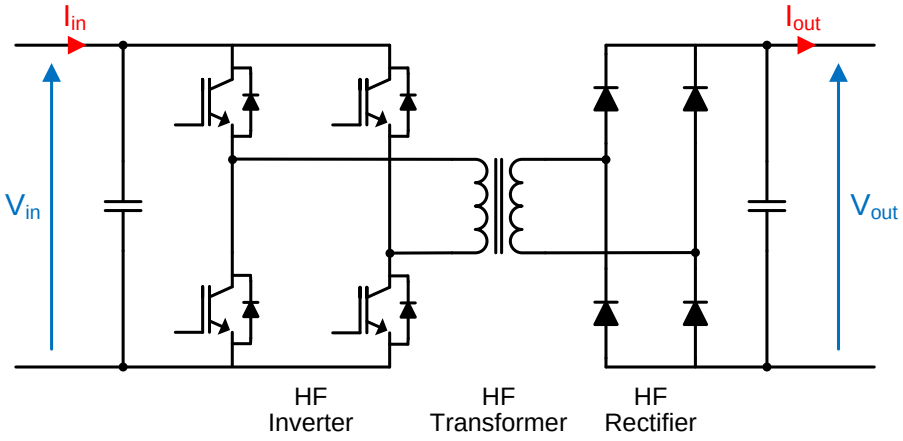

Figure 1.8 Typical circuit diagram of boost converter utilising HF transformer.

An important aspect of the DC/DC converter is the maximum power point tracking (MPPT) system. Most PV systems are now equipped with the function to track the MPP (as shown by Figure 1.6) of the PV module, which varies with light intensity and temperature etc. Here, the DC/DC converter is typically used to operate the PV module at the instantaneous MPP via digital control techniques. Amongst the diverse MPPT algorithms, Perturb and Observe (P&O) is the most commonly used algorithm due to its ease of implementation (Blaabjerg, Teodorescu, et al. [31]). Alternative schemes are

demonstrated by Ho and Chung [33], Djarallah and Zeidane, et al. [34], although it is noted that a vast number of algorithms have been proposed and discussed in literature.

1.2.3 *Power Inverter*

As electric energy is delivered by the distribution network in the form of AC, it is necessary for the grid-connected PV system to inject AC current with low levels of distortion into the distribution network. Typically, this is achieved via a PWM controlled power electronic inverter that operates in a current controlled mode to inject, unity power factor, sinusoidal current into the distribution network. Unipolar and Bipolar voltage switching are the two most common switching strategies amongst a large number of alternative PWM schemes (Mohan, Undeland, et al. [28]). A Proportional-Integral (PI) controller, with grid voltage feed-forward and DC link ripple compensation, is then typically employed to carry out the current control. Figure 1.9 shows the circuit arrangement of an H-bridge inverter which is commonly used in single-phase applications.

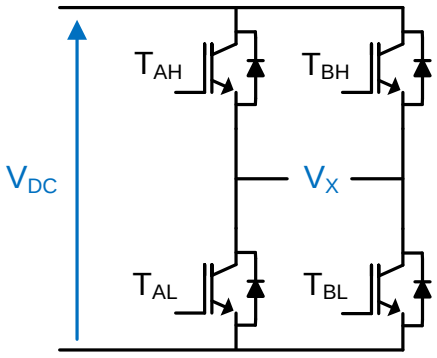

Figure 1.9 Circuit arrangement of H-bridge inverter.

Alternatives to this power converter topology are often seen in literature. For high voltage applications, the individual power electronic switches in Figure 1.9 can be replaced by a number of cascaded power electronic switches to form a multilevel inverter (Abeyasekera [35]). Furthermore, half-bridge inverters [28] and neutral point clamped (NPC) inverters [35-37] can be seen in certain PV applications.

1.2.4 *Lowpass Filter*

Due to the relatively high PWM switching frequency of the DC/AC inverter, the output of the inverter consists of equivalent high frequency pulses that contain a wide range of harmonic components. To prevent these harmonics being injected into the distribution network, a passive lowpass filter is placed at the output of the inverter to attenuate the

high frequency harmonic components. In practice, a 2nd order LC or 3rd order LCL is commonly used. Figure 1.10 shows the circuit arrangement of a 2nd order LC lowpass filter. This particular filter circuit will be used in this research.

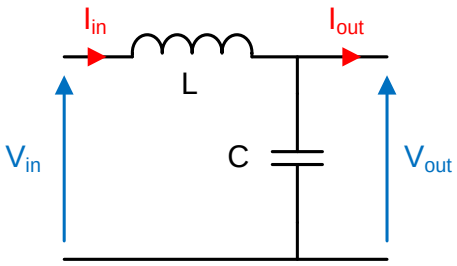

Figure 1.10 Circuit arrangement of a 2nd order lowpass LC filter.

Designing a lowpass LC filter is relatively simple and straightforward. However, it is common in industry to increase the size of the filter capacitor and reduce the size of the inductor whilst retaining the same filter cut-off frequency (Enslin and Hulshorst [16]). In this way, the power losses caused by the equivalent series resistance (ESR) of the filter inductor can be reduced. In addition, the cost, size and weight of the overall filter can normally be reduced with lower inductance values. In contrast, special attention must be paid in designing the lowpass LCL filter in grid-connected application as it introduces an additional low impedance resonance, this has been demonstrated by Ahmed, Finney, et al. [38], Jalili and Bernet [39], Karshenas and Saghafi [40].

1.2.5 *DC Current Injection and Isolation Transformer*

Traditionally, it is very difficult to design a power electronic inverter in such a way that there is no DC current injected into the grid (Kitamura, Yamamoto, et al. [41]). This DC current is caused by deficiencies in the current controller, imbalance in the turn-on and turn-off times of individual devices, pulse width imbalance in the PWM process, and mismatch in the alignment of the gate drive signal (Armstrong, Atkinson, et al. [21]). Excessive amounts of DC current injection into the grid are not usually permitted by the Distribution Network Operators (DNO). Adequate means to suppress, or sometimes fully eliminate, the DC current injection must be present before connection is made to the network. DC current injection into the network has been shown to cause several problems on the network; such as corrosion in underground cables, malfunction of protection devices, source transformer saturation and magnetising current distortion (Bowtell and Ahfock [42]). The guidelines and standards of DC current for low voltage distribution network (typically 110V to 230V AC of phase voltage) in six selected countries are summarised by Salas, Olias, et al. [43] and reflected in Table 1.2.

Country	Standard	Max DC current permitted with transformer	Max DC current permitted without transformer
Australia	*AS 4777.2*	*5mA*	*5mA*
Germany	*DIN VDE 126*	-	*1000mA*
Japan	*Technical Guideline for the Grid Interconnection*	*1% inverter rated current*	*1% inverter rated current*
Spain	*RD 1663/2000*	-	*No Limits*
United Kingdom	*ER G83/1*	-	*5mA*
USA	*IEEE 929-2000*	*0.5% inverter rated current*	*0.5% inverter rated current*

Table 1.2 DC current guidelines and regulations in six selected countries [43].

To eliminate the risk of DC current injection, PV inverter systems connected to the grid typically employ a mains frequency isolation transformer. In addition, this transformer provides the advantage of galvanic isolation between the PV system and the distribution grid. However, this transformer has a significant impact on the cost, volume, weight and power loss within the PV system. To avoid these drawbacks, researches [21, 42] have shown that it is possible to eliminate the DC current injection by compensation methods within the PV inverter current controller. In this way, the requirement for the isolation transformer may be eliminated, subject to local regulations. Transformerless topologies have successfully been demonstrated by Armstrong, Atkinson, et al. [21], Gonzalez, Lopez, et al. [44], Lopez, Teodorescu, et al. [45], Bowtell and Ahfock [42]. Furthermore, a technique for real-time measurement of DC current injection is presented by Wang, Guo, et al. [46].

1.2.6 *Grid Synchronisation*

Grid-connected PV inverter systems are conventionally designed to operate at unity power factor with respect to the grid voltage. To achieve this, it is necessary to synchronise the output current of the PV system with the network voltage. Amongst the many techniques for synchronisation, zero crossing detection (ZCD) is a simple and low cost implementation. It detects the zero crossing point of the voltage waveform through a simple comparator circuit. However, the performance of the ZCD is significantly affected by the quality of the voltage waveform as the harmonics or notches that appear on the voltage waveform could lead to false triggering of the comparator circuit. To avoid this, a lowpass filter is normally used to filter out the harmonics and notches in

the voltage waveform before feeding into the comparator circuit (Armstrong [27]). More advanced and complicated synchronisation techniques use a Phase Locked Loop (PLL) (Abeyasekera [35] and Blaabjerg, Teodorescu, et al. [47]). This method is more precise and robust to waveforms with high levels of distortion.

1.2.7 *Anti-Islanding*

In the event of an abnormality on the electrical supply network (such as loss of mains due to fault on the network), or deliberate switch off for maintenance etc., the grid-connected PV system is required by regulation to disconnect from the electrical network within a statutory duration to prevent islanding (ENA G83/1 [22]). This is primarily to guarantee the safety of persons working on the electrical network following any abnormality, or during periods of maintenance. It also ensures the safety of sensitive equipment being connected to the electrical network which may be damaged by fluctuations on the network voltage caused by an unstable PV inverter still connected to the supply when the utility is absent (Verhoeven [10]). Islanding phenomenon of grid-connected PV systems and their instability during islanding are demonstrated by Kitamura, Matsuda, et al. [48]. To detect an islanding situation, it is possible to employ one of two passive methods; monitoring the grid voltage magnitude or frequency. Any variation in these two parameters, outside of normal conditions, can be viewed as the result of a transition from normal to islanding operation. An enhanced version of passive anti-islanding method is demonstrated by Kim, Seo, et al. [49], and Valentini, Munk-Nielsen, et al. [50]. In contrast to detecting islanding by passive methods, active methods detect the availability of the utility supply by introducing a deliberate disturbance into the electrical network and measuring the response to this disturbance. This approach has been successfully demonstrated by Yu, Matsui, et al. [51], and Sun, Matsui, et al. [52].

1.3 Thesis Overview

This thesis consists of five main parts. The first part of this thesis, comprising of this chapter, presents the background of the PV system and general discussion on the operation of a grid-connected PV system. The second part of this thesis (Chapter 2 and Chapter 3) demonstrates the modelling and implementation of an experimental grid-connected PV inverter system. Chapter 2 highlights the steps in obtaining a system transfer function to create a Linear Time Invariant (LTI) model of the grid-connected PV inverter system. Furthermore, a schematic model of the grid-connected PV inverter

system is presented in this chapter. Both the LTI model and schematic model are used to demonstrate the interaction between the PV inverter and the distribution grid using Matlab/Simulink® software package. Chapter 3 then discusses the development of the grid-connected PV inverter system hardware which is later used for experimental research and validation of the simulation results. Chapter 4 investigates the impact of grid operating conditions on the grid-connected PV inverter system. It investigates in depth, the interactions which arise and the impact on the harmonic performance of the PV inverter current controller. Chapter 5 and Chapter 6 consider the excitation of resonance phenomena between the PV inverter and the distribution grid and methods to suppress this resonance. Chapter 5 deals with resonant excitation due to excessive proportional gain within the PI controller when a change in grid impedance is observed. Chapter 6 then presents a novel adaptive proportional gain PI control scheme to suppress the resonance. Simulation and experimental results are presented to verify the performance of the proposed scheme. Finally, Chapter 7 summaries the research work carried out in this thesis. Conclusions are drawn and areas for future research are clearly identified and discussed.

1.4 Summary

This chapter provides a general discussion on PV inverter systems. In particular, it highlights the rapid increase in the use of grid-connected PV systems for energy generation. Following this, an overview of grid-connected PV system technology is presented. The aim of the research is then defined; to study the details of interaction between the grid-connected PV inverter systems and the distribution grid; and then to develop a novel adaptive control algorithm to suppress the resonance effects which appear in these systems. The following chapters will describe in detail the work has been carried out in the research.

Chapter 2. Modelling of Grid-Connected PV Inverter System

2.1 Introduction

This chapter presents the development of a grid-connected PV inverter system model in Matlab/Simulink®. This model is used throughout the thesis for simulation studies and detailed analysis which is often difficult to carry out experimentally, or without significant resources. A detailed understanding of the model, and an appreciation of the assumptions made in the modelling process, is essential to fully interpret the results shown later in the thesis.

The first section of this chapter presents the steps taken to develop a Linear Time Invariant (LTI) model of a grid-connected PV inverter in Matlab®. The overall LTI model is derived from the transfer function analysis of the core components within the systems, such as inverter, LC filter, PI controller, PWM, and distribution grid. This LTI model shows the frequency response of the PV inverter system with respect to the parameters of the distribution grid. The second section of this chapter presents a schematic model of the grid-connected PV inverter system. This model is developed in Simulink®; using a combination of standard Simulink® signal blocks and SimPower toolbox blocks which allow for electrical engineering components to be readily included. The model is able to simulate the time varying behaviour of the grid-connected PV inverter system and express its interaction with the distribution grid by time varying voltage and current waveforms. Furthermore, the distribution grid model and inverter system are built on parameters derived from practical experimentation. Thus, the validity of the simulation model is verified by comparison with real experimental data.

2.2 LTI Model of Grid-Connected PV Inverter System

If a system is linear and time invariant, then it is amenable to analysis using many techniques, some common techniques such as Laplace transform, Fourier transform, state-space model and Z-transform are mentioned by Lutovac, Tosic, et al. [53], Strum and Kirk [54]. Provided certain assumptions are made, a grid-connected PV inverter systems can be represented by a Linear Time Invariant (LTI) model. In the time domain, the LTI model of PV inverter system can be described by linear differential equations with constant coefficients. In the frequency domain, a Laplace transform can be derived. For systems which include a microcontroller, such as the digital current controller of a

typical PV inverter, a discrete domain model can be determined. This model can account for digitisation effects including sampling, signal delays, and quantisation.

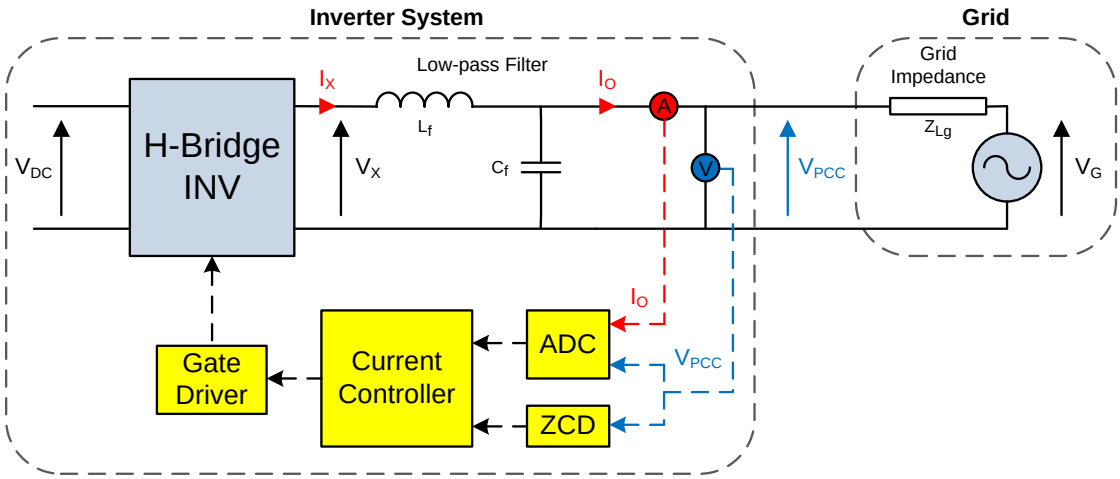

Figure 2.1 Typical arrangement of PV inverter system connected to distribution grid at PCC.

Figure 2.1 shows a typical arrangement of a PV inverter system connected to distribution grid at a point of common coupling (PCC). The system consists of continuous time signals (voltage and current signals) and digital signals in the current control loop. For this reason, an overall LTI model is developed via differential equations, Laplace transforms, and discretized equation. Hence, the behaviour and response of the grid-connected PV inverter system at particular frequency can be analysed via its LTI model. Note the transformations and signal processing of the signals are discussed in [53-55].

2.2.1 *Modelling of System Impedances*

In a typical grid-connected PV inverter system, the lowpass (L_f and C_f) filter connected at the output side of the inverter bridge is used to attenuate the switching harmonics. This lowpass filter interfaces with the lumped distribution grid impedance seen by the PV inverter system at the PCC. According to standard IEC 60725 [56], the maximum grid impedance of distribution grid for a single-phase two-wire 230V 50Hz supply in the United Kingdom is 0.4+j0.25 Ω (equivalent to 0.4Ω and 0.796mH of grid resistance and grid inductance respectively). Further analysis and measurement of grid impedance is presented by Heskes, Rooik, et al. [57]. The PV inverter lowpass filter impedance and grid impedance form a LCL arrangement as shown in Figure 2.1. By neglecting the effect of digital current control loop, the system can be simplified as shown in Figure 2.2. From this, the transfer function model of the PV system can be determined. Similar

analysis on the transfer function of an LCL branch is presented by Abeyasekera, Johnson, et al. [58], Twining and Holmes [59]. Note that here the resistances, R_{Lf}, R_{Cf} and R_g, are added into the figure as the equivalent series resistance (ESR) of filter inductance (L_f), filter capacitance (C_f), and grid inductance (L_g) respectively.

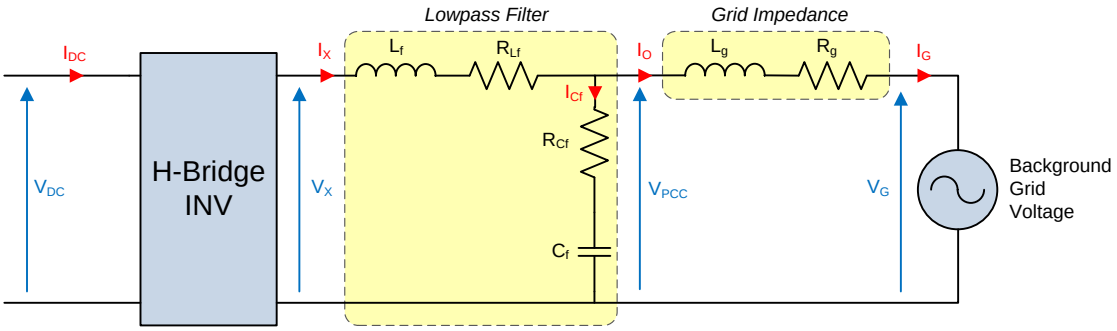

Figure 2.2 Equivalent circuit of LCL branch for inverter filter impedance and grid impedance.

As shown in Figure 2.2, the instantaneous voltage across the lowpass filter inductor (voltage difference between V_X and V_{PCC}) is a function of the rate of change of inverter bridge output current (I_X) and the voltage across its ESR. The relationship can be expressed in the time domain by a simple differential equation shown in Equation (2.1).

$$V_X(t) - V_{PCC}(t) = L_f \frac{dI_X(t)}{dt} + R_{Lf} I_X(t) \tag{2.1}$$

In the frequency domain, the equivalent Laplace representation is given by Equation (2.2).

$$\begin{aligned} V_X(s) - V_{PCC}(s) &= L_f s I_X(s) + R_{Lf} I_X(s) \\ V_X(s) - V_{PCC}(s) &= I_X(s)\left(L_f s + R_{Lf}\right) \end{aligned} \tag{2.2}$$

By rearranging Equation (2.2), the Laplace transfer function of the lowpass filter inductor (L_f) that represents its output/input characteristic can be obtained as shown in Equation (2.3).

$$H_{Lf}(s) = \frac{I_X(s)}{V_X(s) - V_{PCC}(s)} = \frac{1}{L_f s + R_{Lf}} \tag{2.3}$$

For the filter capacitor (C_f) branch in Figure 2.2, the PCC voltage is a function of the integral of the current flowing through the capacitor and the voltage across its ESR, and can be expressed by the differential equation in Equation (2.4).

$$V_{PCC}(t) = I_{Cf}R_{Cf} + \frac{1}{C_f}\int I_{Cf}dt \tag{2.4}$$

Similar to the filter inductor, the Laplace transfer function of the filter capacitor can be obtained (Equation (2.5) and Equation (2.6)). Note that in this derivation, the current flowing through the capacitor branch is substituted by the difference between the inverter bridge output current (I_X) and inverter system output current (I_O).

$$V_{PCC}(s) = R_{Cf}I_{Cf}(s) + \frac{1}{C_f}\frac{1}{s}I_{Cf}(s)$$
$$V_{PCC}(s) = I_{Cf}(s)\left(R_{Cf} + \frac{1}{C_f s}\right) \tag{2.5}$$

Since $I_{Cf}(s) = I_x(s) - I_o(s)$,

$$V_{PCC}(s) = (I_X(s) - I_O(s))\left(\frac{R_{Cf}C_f s + 1}{C_f s}\right)$$
$$H_{Cf}(s) = \frac{V_{PCC}(s)}{I_X(s) - I_O(s)} = \frac{R_{Cf}C_f s + 1}{C_f s} \tag{2.6}$$

Using the same approach, the transfer function of the grid impedance that represents its output/input characteristic can be obtained (Equation (2.7) to Equation (2.9)).

$$V_{PCC}(t) - V_G(t) = L_g\frac{dI_O(t)}{dt} + R_g I_O(t) \tag{2.7}$$

$$V_{PCC}(s) - V_G(s) = L_g s I_O(s) + R_g I_O(s)$$
$$V_{PCC}(s) - V_G(s) = I_O(s)(L_g s + R_g) \tag{2.8}$$

$$H_{Lg}(s) = \frac{I_O(s)}{V_{PCC}(s) - V_G(s)} = \frac{1}{L_g s + R_g} \tag{2.9}$$

From this, the linkage between the filter inductor, filter capacitor, and grid impedance of the LCL branch as shown in Figure 2.2 can be expressed by combining their transfer

functions as given in Equation (2.3), Equation (2.6), and Equation (2.9) respectively. The direct link between these transfer functions is shown in Figure 2.3.

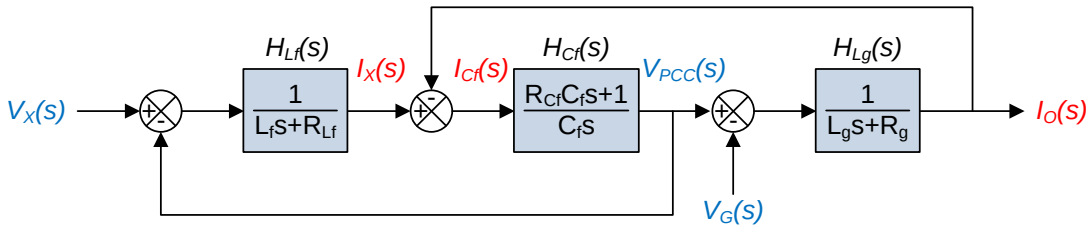

Figure 2.3 Block diagram of transfer functions linkage in LCL branch.

By lumping together the individual component transfer functions, a single Laplace transfer function describing the output/input characteristic of the whole system can be derived:

$$I_O(s) = \left\{\left\{\left[(V_X(s) - V_{PCC}(s))\frac{1}{L_fs + R_{Lf}}\right] - I_O(s)\right\}\frac{R_{Cf}C_fs + 1}{C_fs} - V_G(s)\right\}\frac{1}{L_gs + R_g}$$

$$I_O(s) = \left\{\left\{\frac{V_X(s) - V_{PCC}(s)}{L_fs + R_{Lf}} - I_O(s)\right\}\frac{R_{Cf}C_fs + 1}{C_fs} - V_G(s)\right\}\frac{1}{L_gs + R_g}$$

$$I_O(s) = \left\{\left\{\frac{V_X(s) - V_{PCC}(s) - I_O(s)(L_fs + R_{Lf})}{L_fs + R_{Lf}}\right\}\frac{R_{Cf}C_fs + 1}{C_fs} - V_G(s)\right\}\frac{1}{L_gs + R_g}$$

$$I_O(s) = \left\{\frac{[V_X(s) - V_{PCC}(s) - I_O(s)(L_fs + R_{Lf})](R_{Cf}C_fs + 1)}{C_fs(L_fs + R_{Lf})} - V_G(s)\right\}\frac{1}{L_gs + R_g}$$

$$I_O(s) = \left\{\frac{[V_X(s) - V_{PCC}(s) - I_O(s)(L_fs + R_{Lf})](R_{Cf}C_fs + 1) - V_G(s)C_fs(L_fs + R_{Lf})}{C_fs(L_fs + R_{Lf})}\right\}\frac{1}{L_gs + R_g}$$

$$I_O(s) = \frac{[V_X(s) - V_{PCC}(s) - I_O(s)(L_fs + R_{Lf})](R_{Cf}C_fs + 1) - V_g(s)C_fs(L_fs + R_{Lf})}{C_fs(L_fs + R_{Lf})(L_gs + R_g)}$$

(2.10)

Rearranging $V_{PCC}(s) - V_G(s) = I_o(s)(L_gs + R_g)$ yields:

$$V_{PCC}(s) = I_O(s)(L_gs + R_g) + V_G(s)$$

(2.11)

Substituting Equation (2.11) into Equation (2.10) yields:

$$I_O(s) = \frac{[V_X(s) - I_O(s)(L_gs + R_g) - V_G(s) - I_O(s)(L_fs + R_{Lf})](R_{Cf}C_fs + 1) - V_G(s)C_fs(L_fs + R_{Lf})}{C_fs(L_fs + R_{Lf})(L_gs + R_g)}$$

$$0 = \frac{V_X(s)(R_{Cf}C_fs+1) - I_O(s)(L_gs+R_g)(R_{Cf}C_fs+1) - V_G(s)(R_{Cf}C_fs+1) - I_O(s)(L_fs+R_{Lf})(R_{Cf}C_fs+1)}{C_fs(L_fs+R_{Lf})(L_gs+R_g)}$$
$$+ \frac{-V_G(s)C_fs(L_fs+R_{Lf}) - I_O(s)C_fs(L_fs+R_{Lf})(L_gs+R_g)}{C_fs(L_fs+R_{Lf})(L_gs+R_g)}$$

$$0 = V_X(s)(R_{Cf}C_fs+1) - I_O(s)(L_gs+R_g)(R_{Cf}C_fs+1) - V_G(s)(R_{Cf}C_fs+1) - I_o(s)(L_fs+R_{Lf})(R_{Cf}C_fs+1) - V_G(s)C_fs(L_fs+R_{Lf}) - I_O(s)C_fs(L_fs+R_{Lf})(L_gs+R_g)$$

$$0 = V_X(s)(R_{Cf}C_fs+1) - V_G(s)[(R_{Cf}C_fs+1) + C_fs(L_fs+R_{Lf})] - I_O(s)[(L_gs+R_g)(R_{Cf}C_fs+1) + (L_fs+R_{Lf})(R_{Cf}C_fs+1) + C_fs(L_fs+R_{Lf})(L_gs+R_g)]$$

$$V_X(s)(R_{Cf}C_fs+1) - V_G(s)[(R_{Cf}C_fs+1) + C_fs(L_fs+R_{Lf})] = I_O(s)[(L_gs+R_g)(R_{Cf}C_fs+1) + (L_fs+R_{Lf})(R_{Cf}C_fs+1) + C_fs(L_fs+R_{Lf})(L_gs+R_g)]$$

$$V_X(s)(R_{Cf}C_fs+1) - V_G(s)[R_{Cf}C_fs+1+C_fL_fs^2+C_fR_{Lf}s] = I_O(s)[L_gR_{Cf}C_fs^2+L_gs+R_gR_{Cf}C_fs+R_g+L_fR_{Cf}C_fs^2+L_fs+R_{Lf}R_{Cf}C_fs+R_{Lf}+C_fL_fL_gs^3+C_fL_fR_gs^2+C_fR_{Lf}L_gs^2+C_fR_{Lf}R_gs]$$

$$V_X(s)(R_{Cf}C_fs+1) - V_G(s)[C_fL_fs^2+C_f(R_{Cf}+R_{Lf})s+1] = I_O(s)[C_fL_fL_gs^3+C_f(L_gR_{Cf}+L_fR_{Cf}+L_fR_g+R_{Lf}L_g)s^2+(L_g+R_gR_{Cf}C_f+L_f+R_{Lf}R_{Cf}C_f+C_fR_{Lf}R_g)s+(R_g+R_{Lf})]$$

(2.12)

Equation (2.12) shows the input-output relationship of LCL branch in Laplace form, where inverter bridge output voltage ($V_X(s)$) and background grid voltage ($V_G(s)$) are the inputs of LCL branch, while LCL output current ($I_O(s)$) is the output. The transfer function of LCL branch with respect to the difference between inverter bridge output voltage ($V_X(s)$) and background grid voltage ($V_G(s)$) can be obtained by rearranging Equation (2.12), as shown by Equation (2.13).

$$G_{LCL}(s) = \frac{I_O(s)}{V_X(s)(R_{Cf}C_fs+1) - V_G(s)[C_fL_fs^2+C_f(R_{Cf}+R_{Lf})s+1]}$$
$$= \frac{1}{C_fL_fL_gs^3+C_f[L_g(R_{Cf}+R_{Lf})+L_f(R_{Cf}+R_g)]s^2+[L_g+L_f+C_f(R_gR_{Cf}+R_{Lf}R_{Cf}+R_{Lf}R_g)]s+(R_g+R_{Lf})}$$

(2.13)

The overall block diagram of the LCL branch transfer function is shown in Figure 2.4.

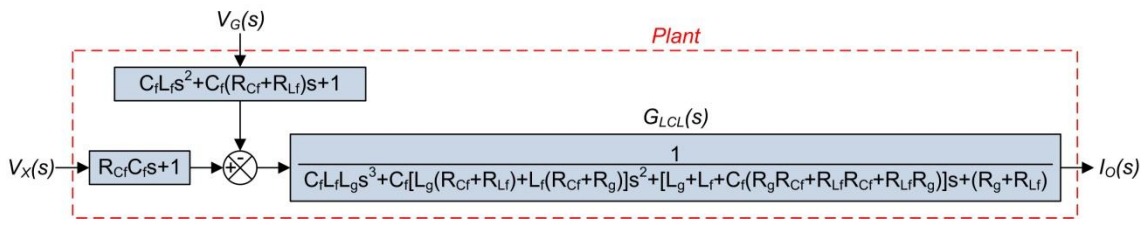

Figure 2.4 Block diagram of LCL branch transfer function.

The transfer function model shown in Figure 2.4 consists of two inputs; inverter bridge output voltage ($V_X(s)$) and background grid voltage ($V_G(s)$). In this form, the model may be considered to be a multiple input single output (MISO) system. This is difficult to analyse. To simplify the analysis, the open loop response of the model can be obtained by assuming the background grid voltage as a disturbance. This can be achieved by rearranging Equation (2.13), to yield the open loop response as shown in Equation (2.14).

$$\frac{I_O(s)}{V_X(s)\left\{(R_{Cf}C_f s+1)-\frac{V_G(s)}{V_X(s)}\left[C_f L_f s^2+C_f(R_{Cf}+R_{Lf})s+1\right]\right\}}$$

$$=\frac{1}{C_f L_f L_g s^3+C_f\left[L_g(R_{Cf}+R_{Lf})+L_f(R_{Cf}+R_g)\right]s^2+\left[L_g+L_f+C_f(R_g R_{Cf}+R_{Lf}R_{Cf}+R_{Lf}R_g)\right]s+(R_g+R_{Lf})}$$

$$G_{OL-LCL}(s)=\frac{I_O(s)}{V_X(s)}$$

$$=\frac{(R_{Cf}C_f s+1)-\frac{V_G(s)}{V_X(s)}\left[C_f L_f s^2+C_f(R_{Cf}+R_{Lf})s+1\right]}{C_f L_f L_g s^3+C_f\left[L_g(R_{Cf}+R_{Lf})+L_f(R_{Cf}+R_g)\right]s^2+\left[L_g+L_f+C_f(R_g R_{Cf}+R_{Lf}R_{Cf}+R_{Lf}R_g)\right]s+(R_g+R_{Lf})} \quad \textbf{(2.14)}$$

The block diagram equivalent of the LCL branch can then be shown in Figure 2.5. Note that the developed LCL branch transfer function model may be verified by equivalent circuit calculation. The full detail of this calculation is presented in Appendix I.

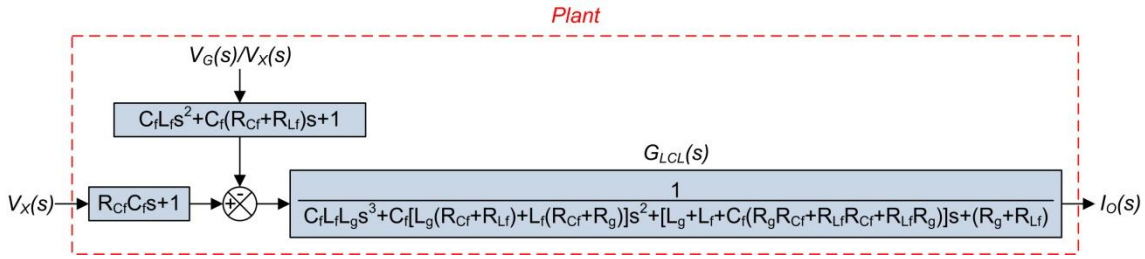

Figure 2.5 Block diagram of LCL branch open loop response.

Using the transfer function in Equation (2.14), Figure 2.6 and Figure 2.7 show the magnitude and phase angle of the LCL output current (I_O). They clearly show the effect of the grid inductance on the current gain of the LCL branch. This characteristic is discussed extensively in Section 4.5.

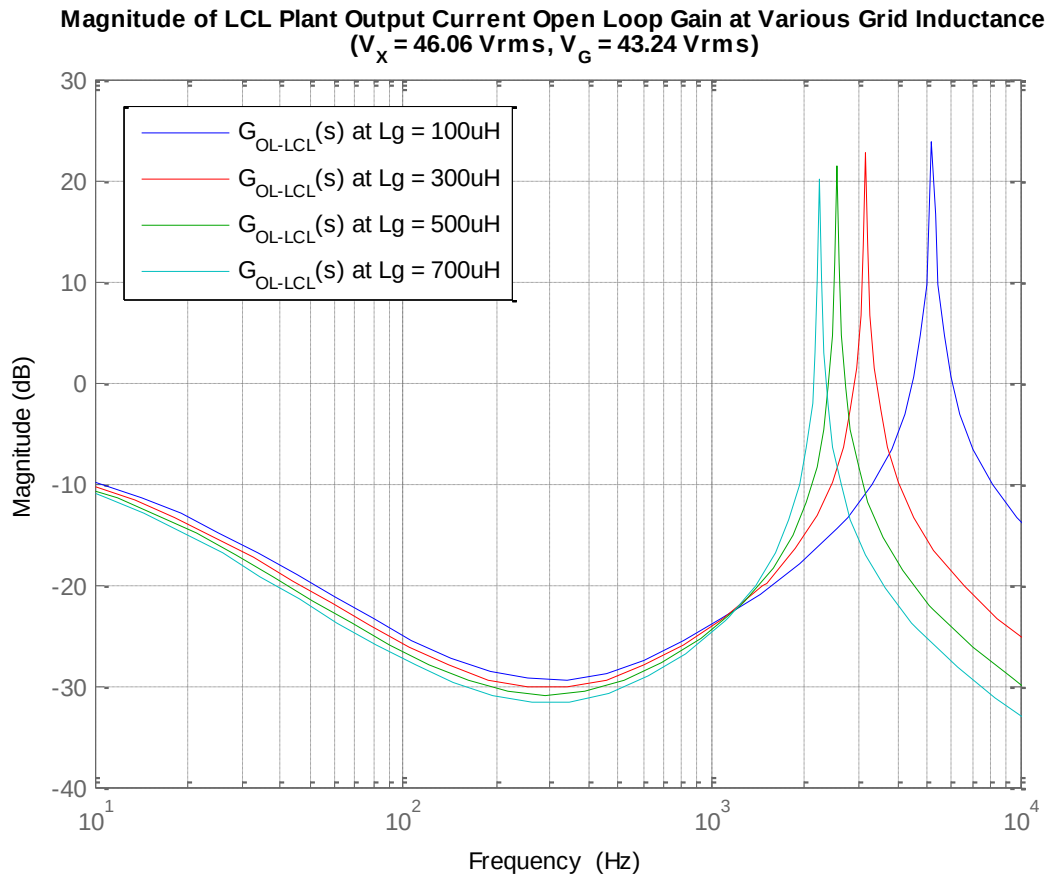

Figure 2.6 Magnitude of LCL branch output current with various grid inductances.

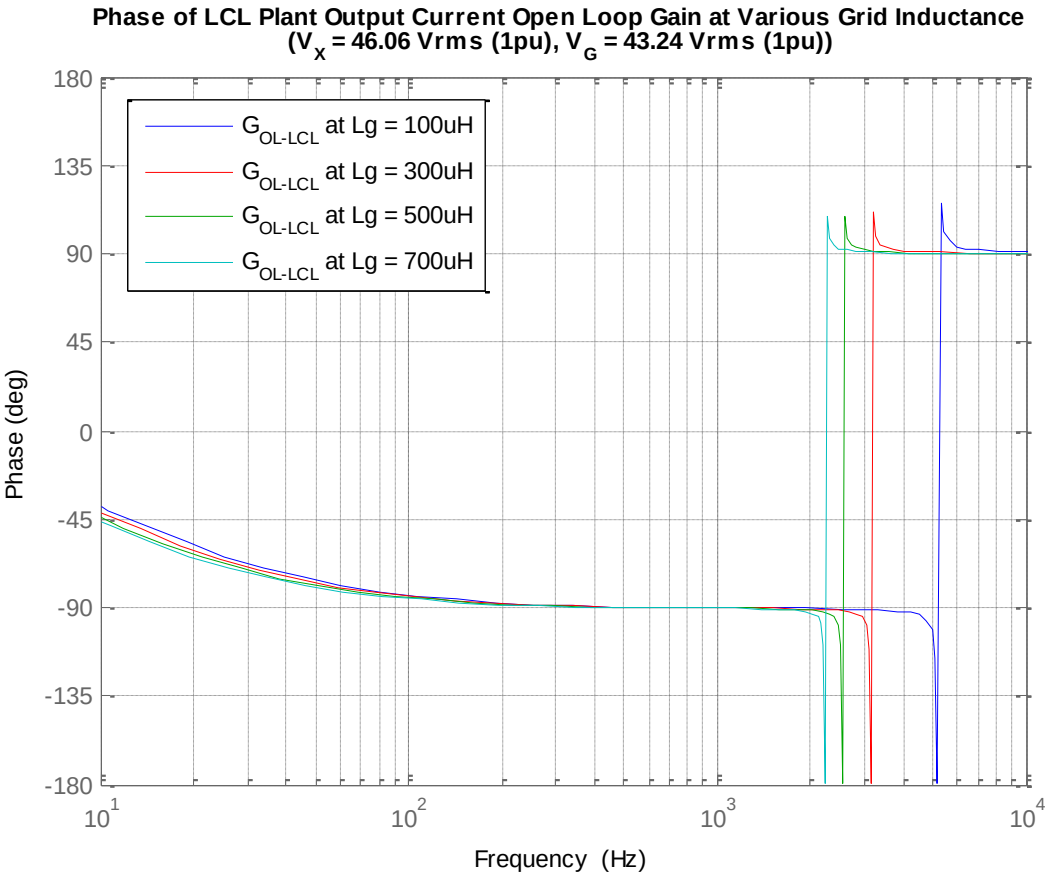

Figure 2.7 Phase angle of LCL branch output current with various grid inductances.

2.2.2 *Modelling of PI Current Controller*

Proportional - integral (PI) controllers are widely used throughout the field of control systems. This type of controller consists of a proportional term (K_P) that responds directly to an error signal, and an integral term (K_i) that responds to the error signal and any system disturbances. Due to the nature of their response, the proportional term and integral term are sometimes referred to as command response and disturbance response respectively. Although both the proportional gain and integral gain are improved by high loop gains, Ellis [60] suggested that a high proportional gain provides a higher bandwidth and better ability to reject disturbances with high frequency content, while a high integral gain helps the control system reject lower frequency disturbances.

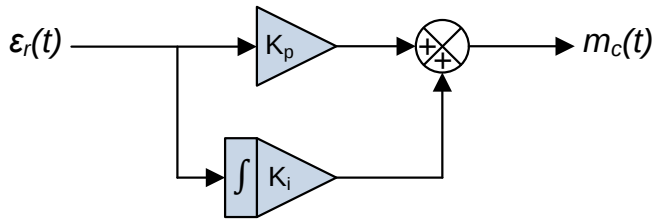

Figure 2.8 Control block of a typical PI controller in time domain.

The block diagram of a typical PI controller in the time domain is shown in Figure 2.8. The relationship between the input (error signal ($\varepsilon_r(t)$)) and output (control signal ($m_c(t)$)) of the PI controller (shown in Figure 2.8) can be given by the well-known expression in Equation (2.15) (Buso and Mattavelli [61]), and its Laplace form can be expressed as shown in Equation (2.16) by applying Laplace transform.

$$m_c(t) = K_p\varepsilon_r(t) + K_i\int \varepsilon_r(t)dt \tag{2.15}$$

$$m_c(s) = K_p\varepsilon_r(s) + K_i\frac{\varepsilon_r(s)}{s}$$
$$m_c(s) = \varepsilon_r(s)\left(K_p + \frac{K_i}{s}\right) \tag{2.16}$$

To obtain the transfer function of PI controller, Equation (2.16) is rearranged to yield the transfer function in Laplace domain as shown in Equation (2.17).

$$G_{PI}(s) = \frac{m_c(s)}{\varepsilon_r(s)} = \frac{K_p s + K_i}{s} \tag{2.17}$$

So far, the PI controller has been presented in the continuous domain. However, a digital controller is used in this research; hence a discrete time model of the PI controller is also developed. Various methods can be used to discretize the continuous time system, such as backward Euler, forward Euler and Trapezoidal (Tustin) etc. The effect of different discretization methods and their distortion limit is explained by Buso and Mattavelli [61]. For simplicity, backward Euler integration ($s = \frac{z-1}{zT_s}$) is implemented to discretize the PI controller. In this process, the Laplace term (s) in the continuous time PI controller transfer function (Equation (2.17)) is substituted by the term $\frac{z-1}{zT_s}$. The transfer function of the discrete PI controller is shown by Equation (2.18) and the normalised expression is shown in Equation (2.19).

$$G_{PI}(s) = \frac{K_p s + K_i}{s}$$

$$G_{PI}(s) = K_p + \frac{K_i}{s}$$

For backward Euler $s = \frac{z-1}{zT_s}$,

$$G_{PI}(z) = K_p + \frac{K_i}{\frac{z-1}{zT_s}}$$

$$G_{PI}(\mathrm{z}) = K_p + K_i T_s \frac{z}{z-1} \qquad \textbf{(2.18)}$$

$$G_{PI}(z) = \frac{K_p(z-1) + K_i T_s z}{z-1}$$

$$G_{PI}(\mathrm{z}) = \frac{K_p \mathrm{z} - K_p + K_i T_s z}{z-1}$$

$$G_{PI}(z) = \frac{(K_p + K_i T_s)z - K_p}{z-1} \qquad \textbf{(2.19)}$$

Before the PI controller equation is applied in the digital controller, it must be converted to difference equation suitable for microcontroller implementation. This is achieved by the well-known parallel realisation of discrete time PI controller by separately manipulating the proportional and integral terms of discrete PI controller as shown by Equation (2.20). The expressions for proportional term and integral term are shown by Equation (2.21) and Equation (2.22) respectively.

$$G_{PI}(z) = \frac{m_c(z)}{\varepsilon_r(z)} = K_p + K_i T_s \frac{z}{z-1}$$

$$m_c(k) = K_p \varepsilon_r(k) + K_i T_s \frac{z}{z-1} \varepsilon_r(k) \quad \textbf{(2.20)}$$

From Equation (2.20), the proportional term can be expressed as:

$$m_p(k) = K_p \varepsilon_r(k) \quad \textbf{(2.21)}$$

Likewise for the integral term, also obtained from Equation (2.20), can be expressed as:

$$\begin{aligned} m_i(k) &= K_i T_s \frac{z}{z-1} \varepsilon_r(k) \\ m_i(k) &= K_i T_s \frac{1}{1-z^{-1}} \varepsilon_r(k) \\ (1-z^{-1}) m_i(k) &= K_i T_s \varepsilon_r(k) \\ m_i(k) - z^{-1} m_i(k) &= K_i T_s \varepsilon_r(k) \\ m_i(k) &= K_i T_s \varepsilon_r(k) + z^{-1} m_i(k) \end{aligned} \quad \textbf{(2.22)}$$

Equation (2.23) shows the difference equations of the PI controller implemented in the microcontroller. The PI control algorithm is clearly depicted by the control block shown in Figure 2.9.

$$\begin{cases} m_p(k) = K_p \varepsilon_r(k) \\ m_i(k) = K_i T_s \varepsilon_r(k) + z^{-1} m_i(k) \\ m_c(k) = m_p(k) + m_i(k) \end{cases} \quad \textbf{(2.23)}$$

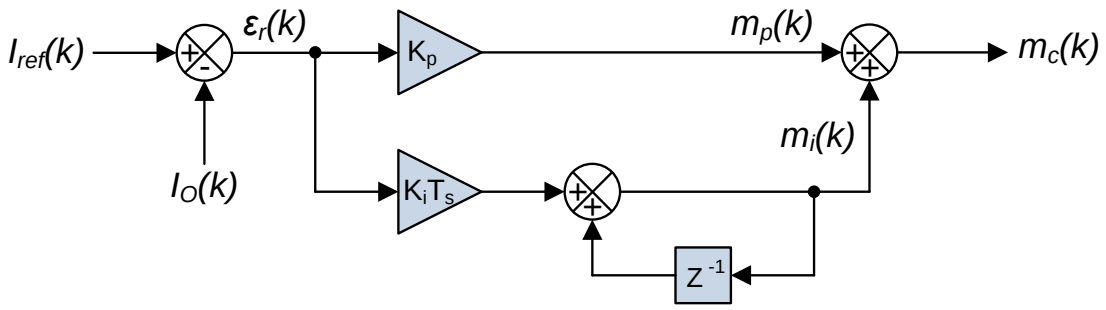

Figure 2.9 Control block of the digital PI controller.

2.2.3 *Modelling of PWM*

Figure 2.10 shows a representation of single update triangle carrier Pulse Width Modulation (PWM) (Buso and Mattavelli [61]). This scheme is applied in this research. The value of the control signal which is generated by the PI controller ($m_c(t)$ in Figure 2.8) is presented to the Compare Unit of the Texas Instrument® TMS320F2812 DSP at a fixed sampling time (T_s) by the Event Manager of the DSP (Texas Instrument [62]), as shown by the modulating signal, $m_s(t)$, in Figure 2.10. In practice, the inverter output voltage ($V_X(t)$) switches between the positive DC link voltage ($+V_{DC}$) and 0V (or negative DC link voltage ($-V_{DC}$) and 0V) during the positive cycle (or negative cycle) of the control signal in Unipolar PWM (Mohan, Undeland, et al. [28]). This is very complicated to model in LTI form. The LTI form typically gives an average signal based on the ratio of the system output signal to the input signal. There is no regard to the detail of the switching behaviour. Therefore, as both Unipolar and Bipolar PWM generate the same fundamental output voltage, Bipolar PWM is applied in the LTI model to simplify the analysis.

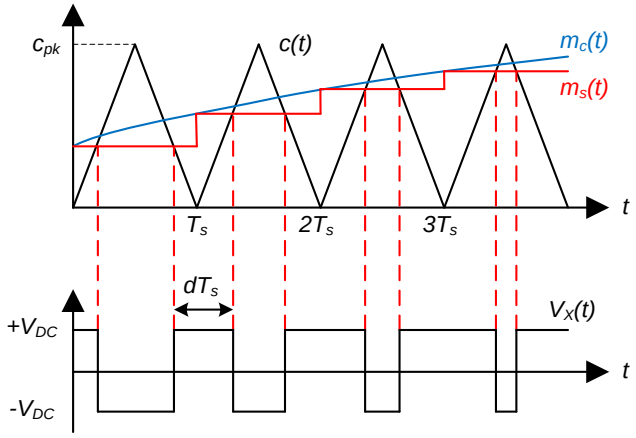

Figure 2.10 Single update PWM with triangle carrier.

The duty cycle (d), which is the fraction of time in a cycle that the single update modulating signal ($m_s(t)$) is higher than the triangle carrier ($c(t)$), can be expressed by the value of a single update modulating signal in a cycle ($m_s(nT_s)$) to the peak of triangle carrier (c_{pk}), as given in Equation (2.24).

$$d = \frac{m_s(nT_s)}{c_{pk}}, n = 1, 2, 3, \ldots \quad \textbf{(2.24)}$$

To model the sample-and-hold effect caused by the single update triangle carrier PWM a Padé approximation, as suggested by Buso and Mattavelli [61], is introduced to act as the delay effect on the modulating signal. This approximation is shown by the Laplace expression in Equation (2.25).

$$d = \frac{m_c(s)}{c_{pk}} \frac{1 - s\frac{T_s}{4}}{1 + s\frac{T_s}{4}} \tag{2.25}$$

The output of the H-bridge inverter ($V_X(t)$ in Figure 2.10) swings between the positive and negative DC link voltage, producing a fundamental output (average) voltage magnitude corresponding to the duty cycle. It can be expressed as the ratio of total voltage range between positive DC and negative DC, as shown by Equation (2.26). It is also noted that the voltage drops across the inverter bridge transistors are neglected to simplify this analysis.

$$V_X(s) = d2V_{DC}$$

$$V_X(s) = \frac{m_c(s)}{c_{pk}} \frac{1 - s\frac{T_s}{4}}{1 + s\frac{T_s}{4}} 2V_{DC} \tag{2.26}$$

By rearranging Equation (2.26), the PWM Laplace transfer function can be obtained, as shown by Equation (2.27).

$$G_{PWM}(s) = \frac{V_X(s)}{m_c(s)} = \frac{1}{c_{pk}} \frac{1 - s\frac{T_s}{4}}{1 + s\frac{T_s}{4}} 2V_{DC} \tag{2.27}$$

Figure 2.11 shows the block diagram of the single update triangle carrier PWM model.

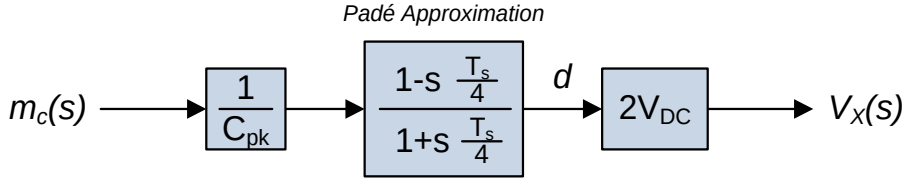

Figure 2.11 Block diagram of single update triangle carrier PWM.

2.2.4 *Model of Grid-Connected PV Inverter System*

The LTI model of the grid-connected PV inverter system is then developed by cascading the transfer functions of the PI controller (Equation (2.17)), PWM model (Equation (2.27)) and LCL branch (Equation (2.13)). The overall closed loop current control model of the grid-connected PV inverter system can then be developed as shown in Figure 2.12. The closed loop response of the model is discussed extensively in Section 4.5. It is noted that a gain of "I_{pk}/c_{pk}", which is the ratio of peak LCL output current ($I_{pk}=\sqrt{2}I_O$) to the peak of triangle carrier (c_{pk}, shown in Figure 2.10), is included to represent the conversion ratio of the current transducer and the ADC that is present in the current feedback loop to interface the analogue domain and the digital microcontroller domain. However, the system model in Figure 2.12 consists of two input variables ($I_{ref\text{-}\mu C}(s)$ and $V_G(s)$) forming a multi input single output (MISO) system. This MISO system produces two transfer function responses; one corresponding to each particular input. Hence, the discretization of the system model must be carried out individually for each of the two continuous transfer functions. Again, the derivation of the transfer function for the MISO system is discussed in Section 4.5.

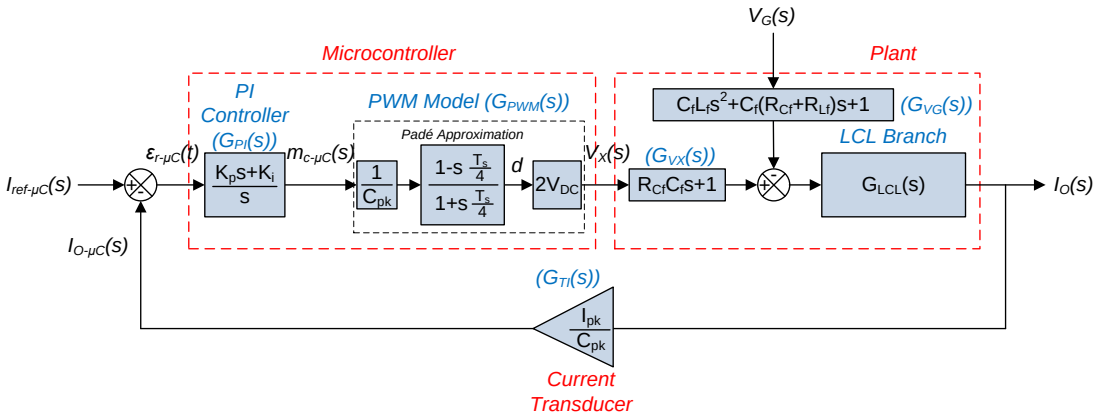

Figure 2.12 Block diagram of grid-connected PV inverter system with current feedback in continuous time Laplace domain.

2.2.5 *Discretization of LTI Grid-Connected PV Inverter System Model*

To analyse the inverter in the discrete domain, a z-transfer function model is required. For this reason, all of the transfer functions in the control loop of Figure 2.12 have to be transformed into the z domain. There are several well recognised methods to transform the system from continuous time to discrete time (Lutovac, Tosic, et al. [53], Strum and Kirk [54]). Five of the most common methods are readily available in Matlab® [63]. These are zero order hold (ZOH), triangle approximation (sometimes referred to as

modified first-order hold), impulse-invariant mapping, bilinear approximation (sometimes referred to as Tustin approximation) and zero-pole matching equivalent. Of the five discretization methods, ZOH is implemented here to discretize the continuous time transfer function of the grid-connected PV inverter system model in Figure 2.12. The 'c2d' function in Matlab® allows for convenient transformation into the equivalent discrete system.

2.2.6 *Closed Loop Frequency Response of Grid-Connected PV Inverter System Model*

The LTI models of the grid-connected PV inverter system in continuous time and discrete time are compared in Matlab® with the parameters shown in Table 2.1. The actual values in Table 2.1 are obtained from the experimental hardware developed (to be described in Chapter 3) to allow for direct comparison between simulation and practical results.

DC link Voltage, V_{DC}	*100 V*
Peak Background Grid voltage, V_G	*$(2*43.2423\sqrt{2})$ V*
Peak Inverter Output Current, I_{pk}	*$(2*12.5\sqrt{2})$ A*
Peak Microcontroller Reference Current Demand, $I_{ref\text{-}\mu C}$	*$[(2*7\sqrt{2})/I_{pk}]*3750$ A*
Controller sampling frequency, F_s	*20 kHz*
Controller sampling time, T_s	*$(1/F_s)$ s*
Peak of triangle carrier, c_{pk}	*3750*
Digital controller proportional gain, K_p	*1.1*
Digital controller integral gain, K_iT_s	*0.6 rad*
Analogue controller proportional gain, K_p	*K_p*
Analogue controller integral gain, K_i	*$(K_iT_s)/T_s$ $rads^{-1}$*
Lowpass filter inductor, L_f	*1.8mH*
Lowpass filter inductor ESR, R_{Lf}	*0.15 Ω*
Lowpass filter capacitor, C_f	*10μF*
Lowpass filter capacitor ESR, R_{Cf}	*0.0566Ω*
Grid inductance, L_g	*300μH*
Gird resistance, R_g	*0Ω*

Table 2.1 Model parameters of grid-connected PV inverter system for closed loop frequency response.

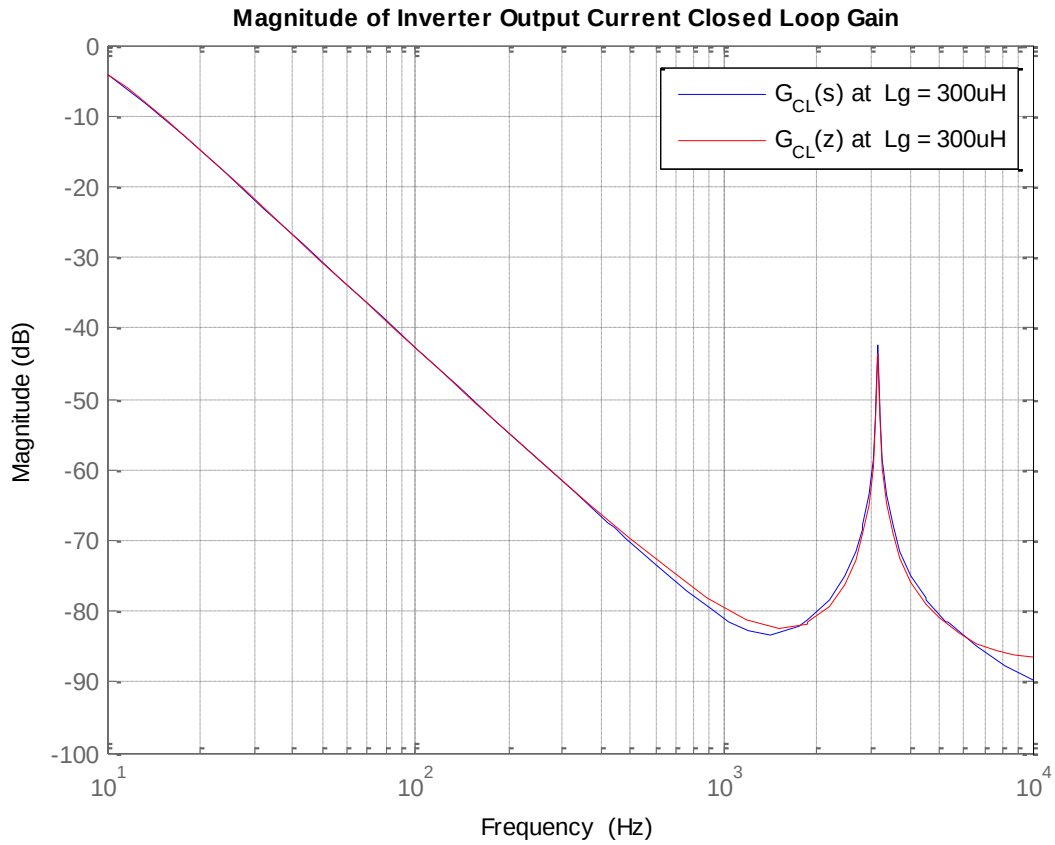

Figure 2.13 Magnitude comparison of inverter system closed loop frequency response with continuous time model ($G_{CL}(s)$) and discrete time model ($G_{CL}(z)$).

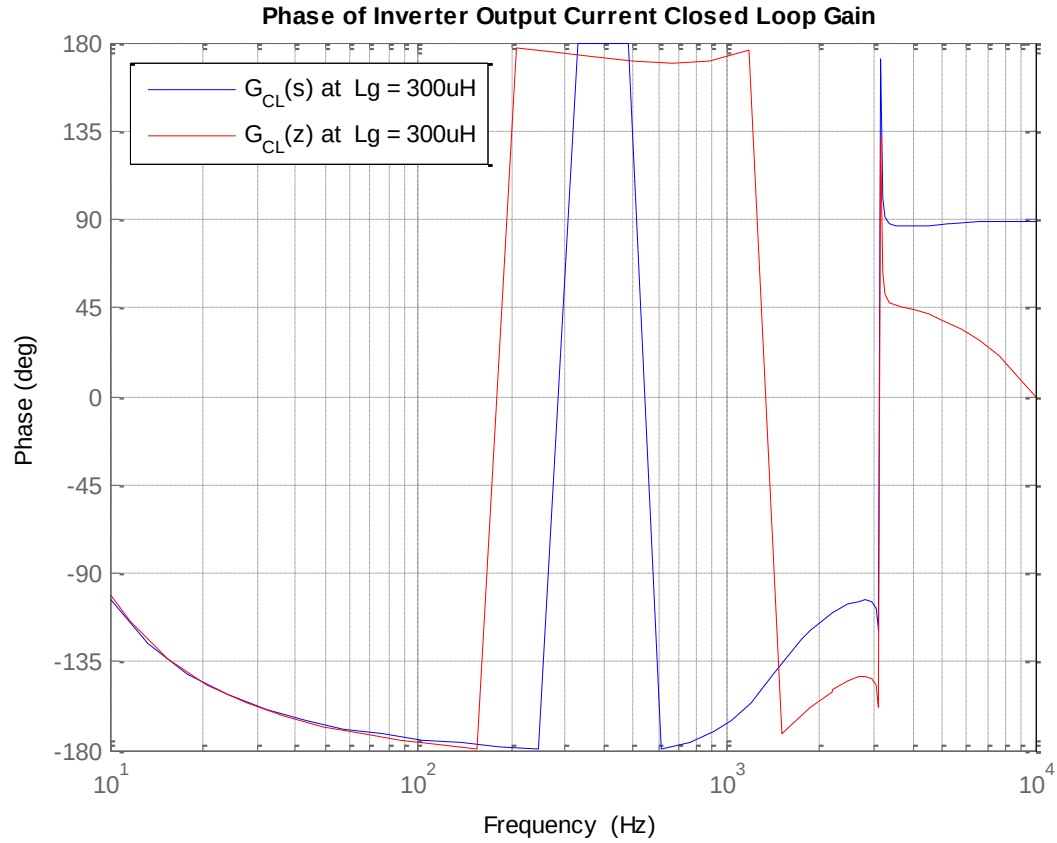

Figure 2.14 Phase comparison of inverter system closed loop frequency response with continuous time model ($G_{CL}(s)$) and discrete time model ($G_{CL}(z)$).

The closed loop frequency responses of the continuous time and discrete time grid-connected PV inverter system models are compared in Figure 2.13 (magnitude) and Figure 2.14 (phase) respectively. Figure 2.13 shows the magnitude of both models give similar gain in the low frequency range (< 400Hz) and slight variation in the higher frequency range. This is due to the sample and hold effect (similar to low pass filter) and quantisation errors that are involved in the discretization of the continuous system; hence variation is observed in the responses of the continuous time model and discrete time model in Figure 2.13 and Figure 2.14. Noted that the impact of delays caused by the sample and hold effect in discrete time system are particularly obvious on the phase response of the grid-connected PV inverter system models as shown in Figure 2.14. More detailed discussion concerning the effect of the control loop gain on the harmonic performance of the PV inverter is presented in Section 4.5.

2.3 Simulink® Model of Grid-Connected PV Inverter System

To assess the performance of the grid-connected PV inverter and its interaction with the distribution network, a complete simulation model is developed in Matlab/Simulink® software package. Figure 2.15 shows the simulation model in Simulink® environment. To simulate a system response which is very close to real-life circumstances, the control section (such as PI controller, ADC, PWM etc.) of the model is developed by the signal based Simulink® block while the power section (passive components, diode, IGBT etc.) is modelled by electrical based SimPower blocks. In this way, the simulation model is able to express the interaction with the distribution grid in the form of electrical signals, such as voltage and current waveforms. Furthermore, the values of passive components are based on the real-life values measured by a Fluke® PM6304 RCL Meter. The background grid voltage model is built based on the voltage harmonic data (magnitude and phase angle of harmonics up to the 50^{th} harmonic) of the distribution grid, as measured by a Yokogawa® PZ4000 Power Analyser and analysed via Matlab/Simulink® post processing.

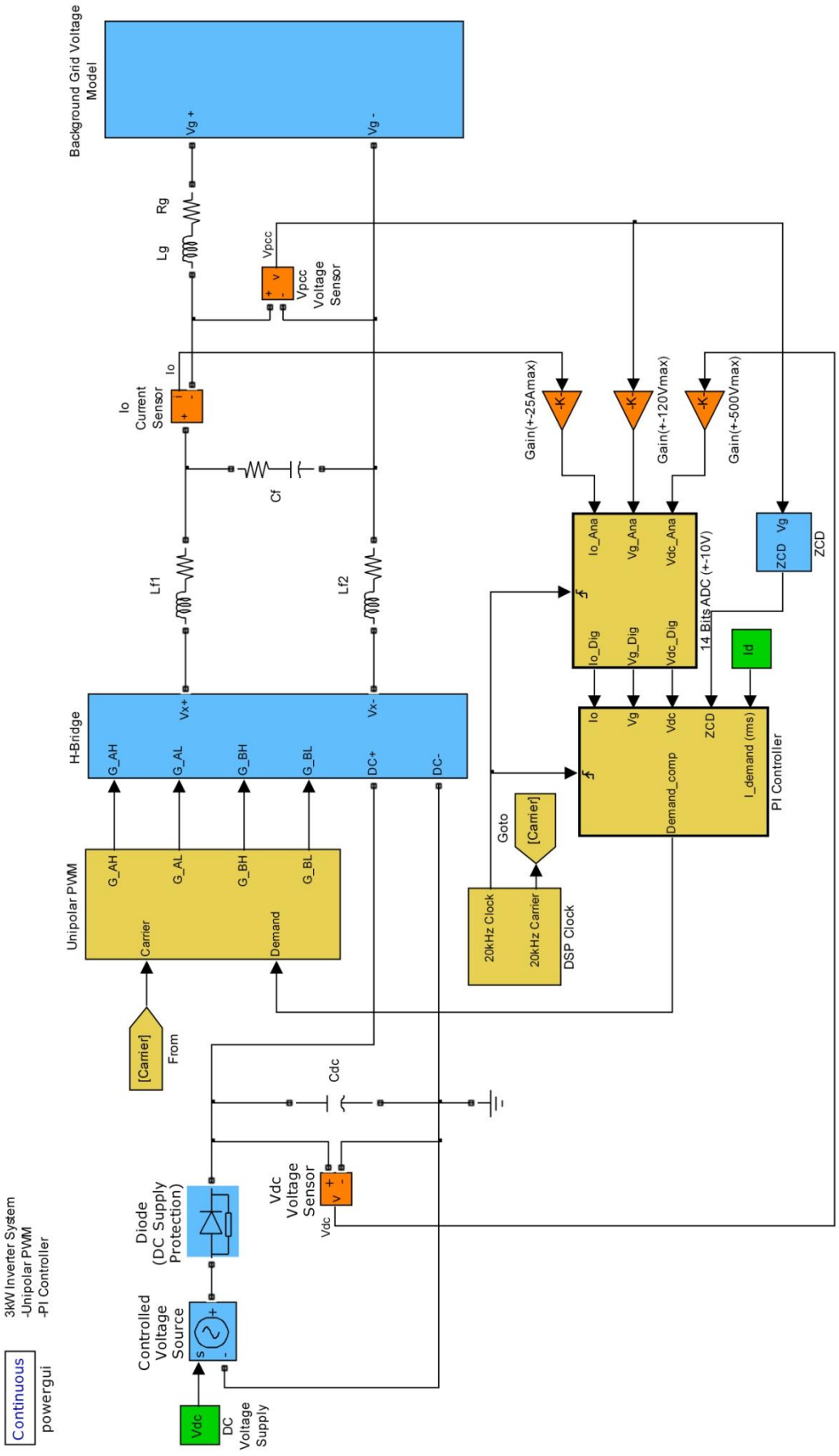

Figure 2.15 Simulink® model of grid-connected PV inverter system.

2.3.1 *Measurement and Controller*

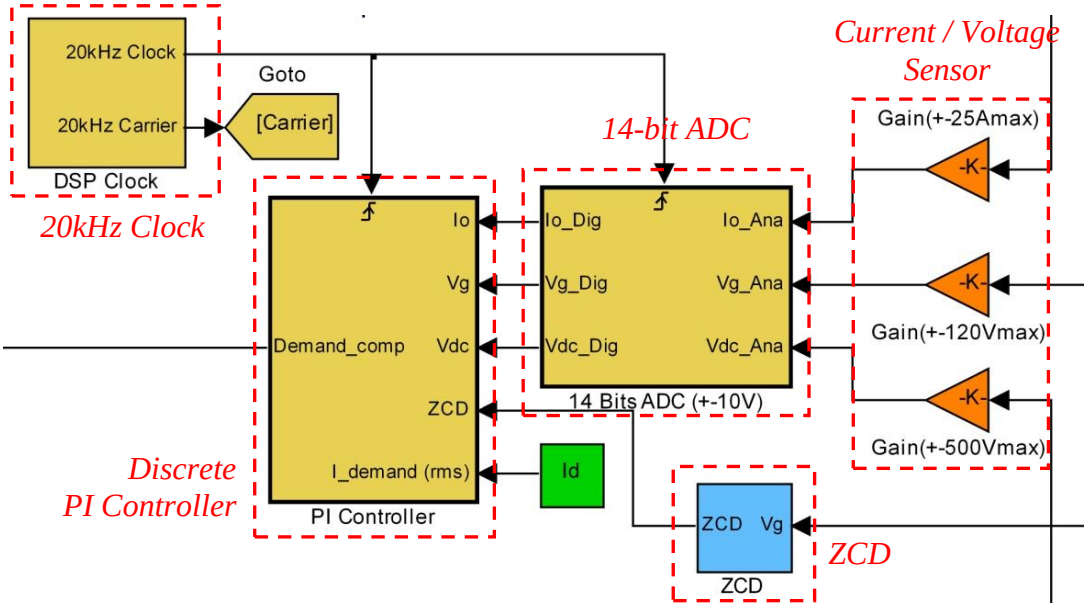

Figure 2.16 Measurement and controller sections of grid-connected PV inverter system model.

The measurement and controller sections of the grid-connected PV inverter system model are shown in Figure 2.16. As shown in the figure, the gains are used to represent the current/voltage sensing circuit to transform the system current and voltage signals to the range of ±10V. Here the gains are defined by the conversion ratio of current/voltage sensor and the amplifier ratio calibrated to the range of ±10V output. The output of the current/voltage sensing blocks are then read by a 14-bit analogue to digital converter (ADC) model that converts the scaled sensor signals to a 16-bit integer through a quantizer. This matches the specification of the ADC of the Link Research LR-F2812DAQ daughtercard used in practice.

The PI control loop is implemented in a 16-bit fixed point Texas Instrument® TMS320F2812 DSP in the practical experiments. This is modelled by the discrete PI controller block as shown in Figure 2.16. The detail of this PI controller is shown in Figure 2.17. In this discrete PI controller, the reference sinusoidal current waveform is generated by the sine table (in Sine Generation block of Figure 2.17) with 60,000 samples. It is synchronised with the distribution grid voltage via the triggering signal provided by the zero crossing detector (ZCD) in the Figure 2.16. As shown by Simulink® block of discrete PI controller (Figure 2.17), the synchronised reference current (I_ref) is compared to the measured output current signal (Io) in order to obtain the instantaneous error value that manipulate by the proportional term and integral term of PI control loop. Moreover, the terminal voltage (Vg) feedforward term and dead-time

compensation block is added to the output of PI control loop. To prevent the integral windup and over modulation of Pulse Width Modulation (PWM), saturation blocks are added to the integral term and control loop output respectively.

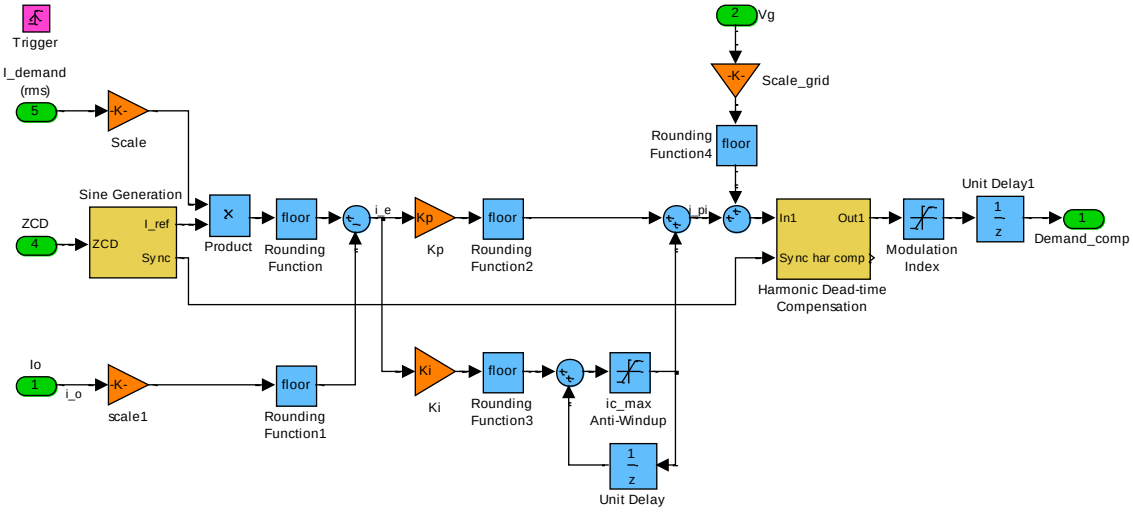

Figure 2.17 Detailed Simulink® block of discrete PI controller.

The Interrupt Service Routine (ISR) of Texas Instrument® DSP based current control loop is set to trigger at 20 kHz in the practical experiments. Therefore, both the ADC and discrete PI controller sections in Figure 2.16 are triggered by the 20 kHz clock in the simulation model.

2.3.2 *PWM Model*

Unipolar PWM is implemented in the grid-connected PV inverter in practical experiment. In simulation model, this is modelled by the Unipolar PWM block in Figure 2.15; this accurately reflects the control demand to the 20 kHz triangle carrier (counter from 0 to highest peak of 3750) given by discrete PI controller and DSP clock respectively, as shown by the detailed Simulink® block of Unipolar PWM in Figure 2.18. Since the same DSP clock is used for both the triangle carrier and the discrete PI controller, the control demand is updated at the lower limit of the triangle carrier (the point that carrier counter equal to 0) in every cycle. In practical experiment, the compare register of DSP is also loaded at the same point as the simulation model. Furthermore, a delay block is introduced to create the dead-time effect of the gate signal to be delivered by the Unipolar PWM block.

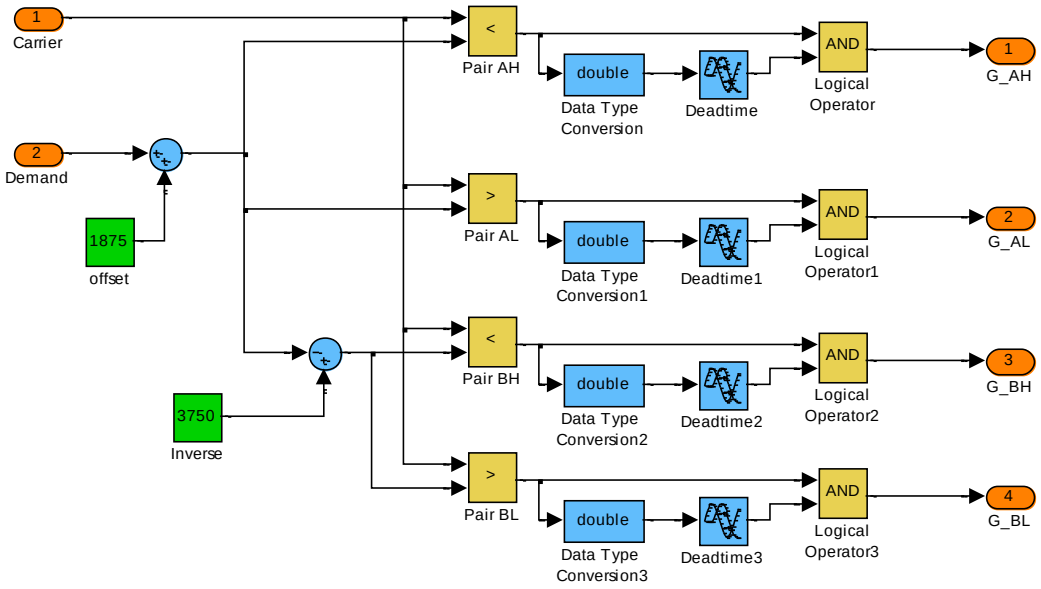

Figure 2.18 Detailed Simulink® block of Unipolar PWM.

2.3.3 *Power Electronic H-bridge Inverter*

The H-bridge inverter in Figure 2.15 is modelled by four Insulated Gate Bipolar Transistor (IGBT) models with freewheeling diode. These blocks are available in SimPower, as shown by Figure 2.19. The switching of the IGBT is controlled by the digital gate signal delivered by Unipolar PWM block in Figure 2.18. Although the simulation time of the Matlab/Simulink® model is significantly increased by introducing the SimPower IGBT model into the simulation, it provide more detailed instantaneous current characteristic at freewheeling loop of inverter system that are too complicated to model using conventional signal based Simulink® blocks.

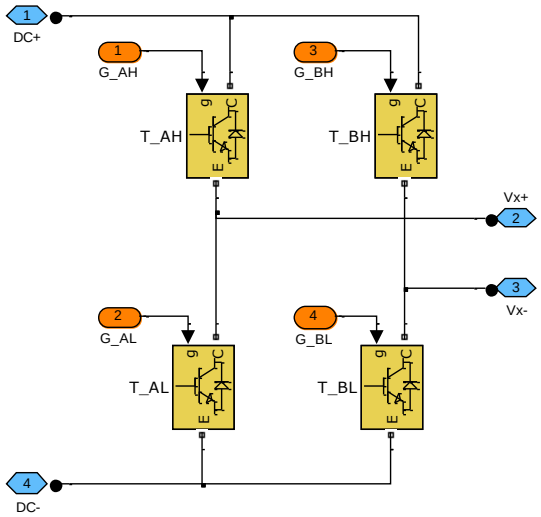

Figure 2.19 SimPower model of IGBT H-bridge inverter.

2.3.4 *Harmonic Model of Background Grid Voltage*

The simulation model of PV inverter system as shown in Figure 2.15 is interfaced with background grid voltage model via grid impedance. To model the background grid voltage, practical experiment is carried out to interface the PV inverter system with the distribution grid in the laboratory. The grid impedance is varied during the experiment and the voltage waveform of background grid voltage at particular grid impedance is recorded by Yokogawa® PZ4000 Power Analyser. The harmonic data is then obtained through FFT function analysis in Matlab/Simulink®. To reconstruct the background grid voltage waveform in simulation, the harmonic data given by the FFT analysis, such as frequency, magnitude and phase angle, are utilised to create a range of sinusoidal signals for particular frequency components in Simulink®. These sinusoidal signals are summed and transformed to SimPower domain to create a background grid voltage waveform that consists of a range of harmonic components, as shown in Figure 2.20.

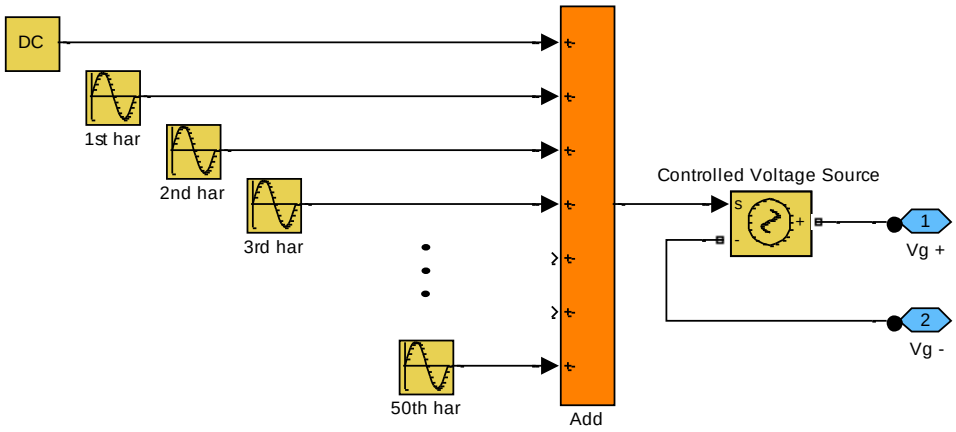

Figure 2.20 Simulink® model of background grid voltage.

2.3.5 *Simulation Result of Grid-Connected PV Inverter System in Simulink®*

The simulation model is verified by comparing the simulation result to the practical measurement. Figure 2.21 and Figure 2.22 show the comparison of PCC voltage and inverter system output current harmonic profile in practical and simulation respectively when 92.2μH of grid inductance is applied. As shown in Figure 2.21 the harmonic profile of PCC voltage in simulation is very close to the PCC voltage harmonic profile in practical. In Figure 2.22, the inverter system output current harmonic profile in simulation has higher harmonic magnitude than in practical. This is due to the damping effect of parasitic impedance in practical experiment which is very difficult to include in simulation, such as the equivalent series resistance (ESR) of the filter inductor and

inductor used to simulate the grid impedance. In real-life, the inductor ESR varies with frequency and has its own self-resonant frequency (Bartoli, Reatti, et al. [64]). However, the harmonic profile of the inverter system output current in simulation still gives a similar trend to the harmonic profile in practical.

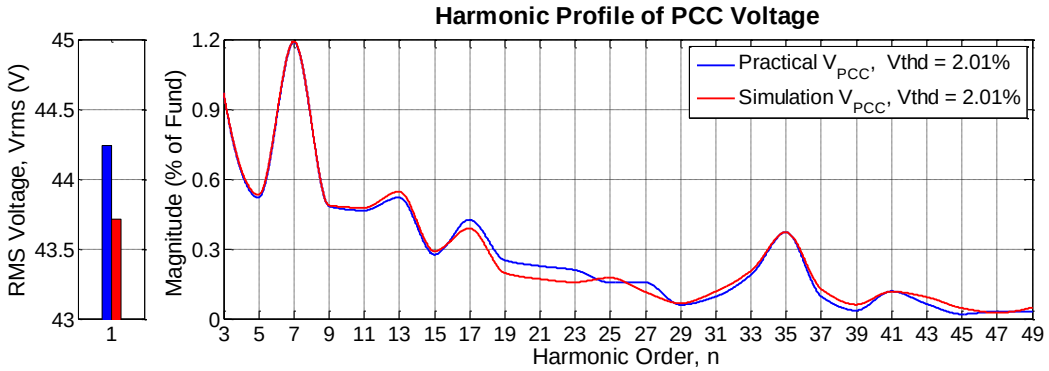

Figure 2.21 Comparisons of PCC voltage (V_{PCC}) harmonic profile in practical and simulation.
(V_{DC} = 100V, V_G = 43V RMS, L_f = 1.8mH, C_f = 10µF, L_g = 92.2µH, K_p =1.1, K_i = 0.6, F_s = 20kHz.)

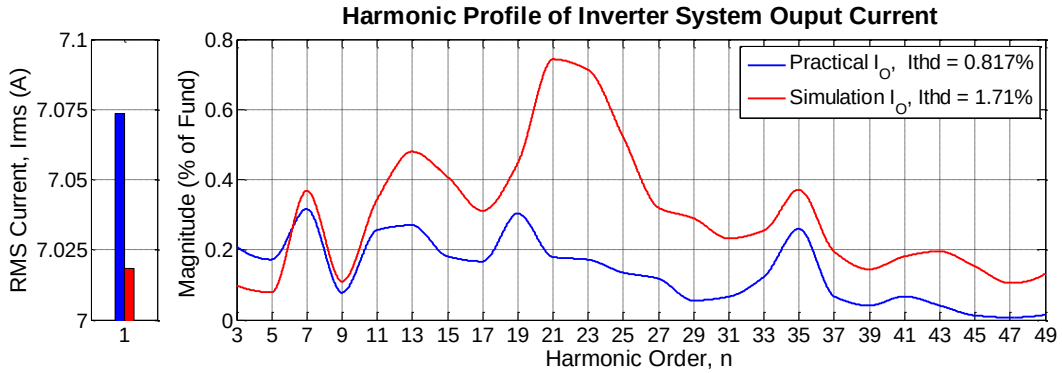

Figure 2.22 Comparisons of inverter system output current (I_O) harmonic profile in practical and simulation.
(V_{DC} = 100V, V_G = 43V RMS, L_f = 1.8mH, C_f = 10µF, L_g = 92.2µH, K_p =1.1, K_i = 0.6, F_s = 20kHz.)

2.4 Summary

This chapter discusses the steps in modelling a grid-connected PV inverter system. In the first part of this chapter, the transfer function for each section of the system, such as LCL branch of the system, continuous/discrete time PI controller and PWM inverter system, is developed. The LTI model of the overall grid-connected PV inverter system is then implemented by cascading the transfer function for each section of the system to form a closed loop model with output current feedback. The closed loop frequency response of the LTI model in continuous time and discrete time are compared and presented. The result show that the magnitude of both responses give similar gain in the

low frequency range and slightly variation in the higher frequency range due to digitisation effects. The developed LTI model is employ in Chapter 4 for the detailed analysis on the interaction between the grid-connected PV inverter system and distribution grid.

The second part of this chapter discusses the modelling of the grid-connected PV inverter system in Matlab/Simulink®. The H-bridge inverter is implemented using IGBT models with freewheeling diode that are readily available in SimPower as it provides more detailed instantaneous current characteristics. The fidelity of the Simulink® model has been assessed by comparing the simulation results with the results obtained in practical experiment. This comparison has shown that the harmonic performance of Simulink® model gives a similar trend to the harmonic data obtained in practical experiment and hence it can be used to represent the proposed experimental grid-connected PV inverter system. This high fidelity model of grid-connected PV inverter system is employed in Chapter 4 to assess the effect of variation in the background grid voltage harmonic on the harmonic performance of PV inverter current controller.

Chapter 3. Implementation of Grid-Connected PV Inverter System

3.1 Introduction

This chapter discusses the implementation of a grid-connected inverter system for the experimental phase of the research work. An overview of the test experimental hardware is provided, and the grid connection sequence is presented. This is followed by a detailed description of the system components and the microcontroller platform. To control the microcontroller in real-time, a host computer running LabVIEW^{TM} is used to communicate with the microcontroller via an RS232 serial interface. Details of this arrangement are also presented in this chapter.

3.2 Overview of Experimental Grid-Connected PV Inverter System

Figure 3.1 Test rig for experimental grid-connected PV inverter system.

To investigate the interaction between the PV inverter and the distribution network, an experimental test facility is first designed, and then installed, in the Power Electronics, Drives and Machines (PEDM) laboratory at Newcastle University. Figure 3.1 shows an overview of the power electronic inverter and auxiliary measurement equipment, host computer, and digital signal processing equipment for real-time control of the system. A more detailed schematic of the test facility is shown in Figure 3.2.

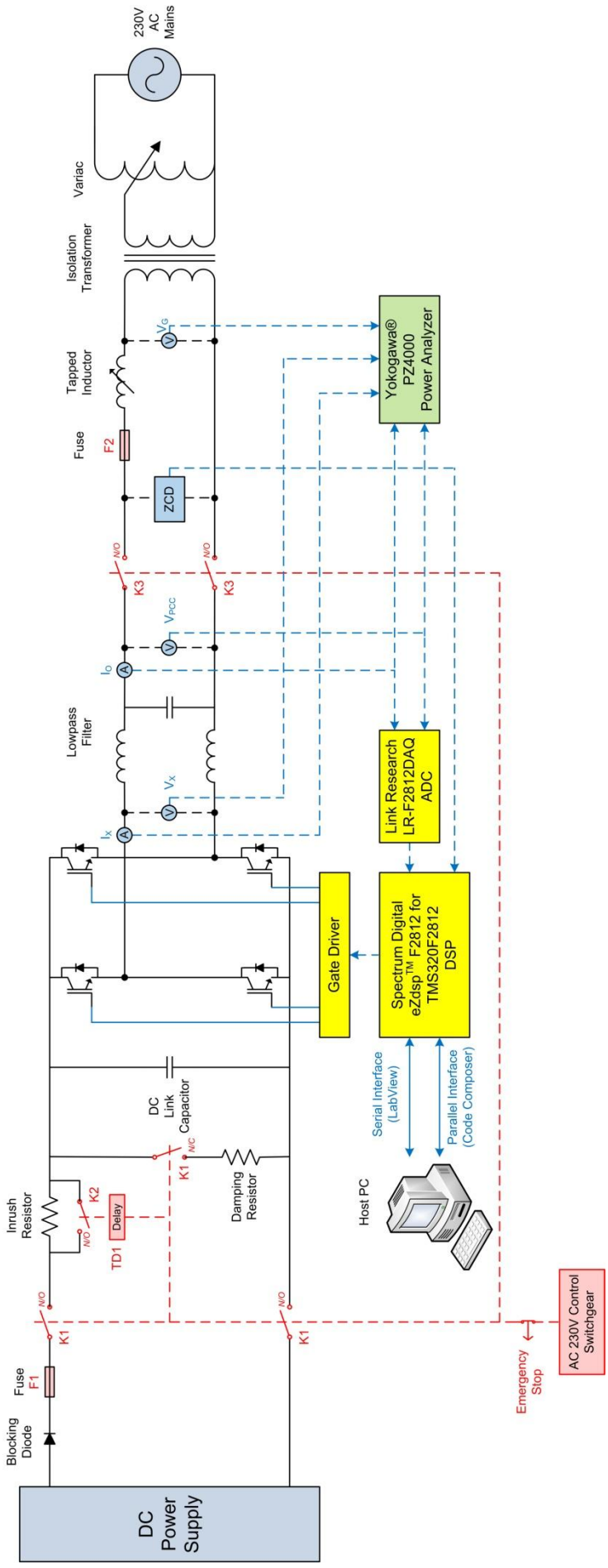

Figure 3.2 Test circuit for experimental grid-connected PV inverter system.

As shown in Figure 3.2, the experimental system consists of an IGBT H-bridge inverter connected to a DC link voltage provided by a DC power supply. The output of the inverter system is connected to a low pass LC filter, and then coupled to the distribution grid via an isolation transformer and variac. Between the lowpass LC filter and the isolation transformer, a tapped inductor is included to simulate the variation in grid impedance. During the experiment, the microcontroller system is employed to control the output current of the inverter system. A Yokogawa® PZ4000 Power Analyser is used to monitor and record the output waveform of the test circuit for post-processing and analysis. Part of the post processing procedure involves Fast Fourier Transform (FFT) analysis of the current and voltage waveforms in Matlab/Simulink®. For protection and safety purposes, the test inverter system has fuses in-line with the DC link input and inverter system output. In addition, the experimental inverter system can be quickly disabled, or isolated in case of emergency, by a switchgear contactor circuit. Finally, a blocking diode is placed between the DC power supply and the inverter DC link to prevent reverse current flowing into the DC power supply as it is not designed for sinking power. A full description of the peripheral experimental components (variac, isolation transformer and earthed cage) and measurement equipment is presented in Appendix III, while the grid connection sequence is presented in Appendix IV.

3.3 Experimental H-bridge Inverter Module

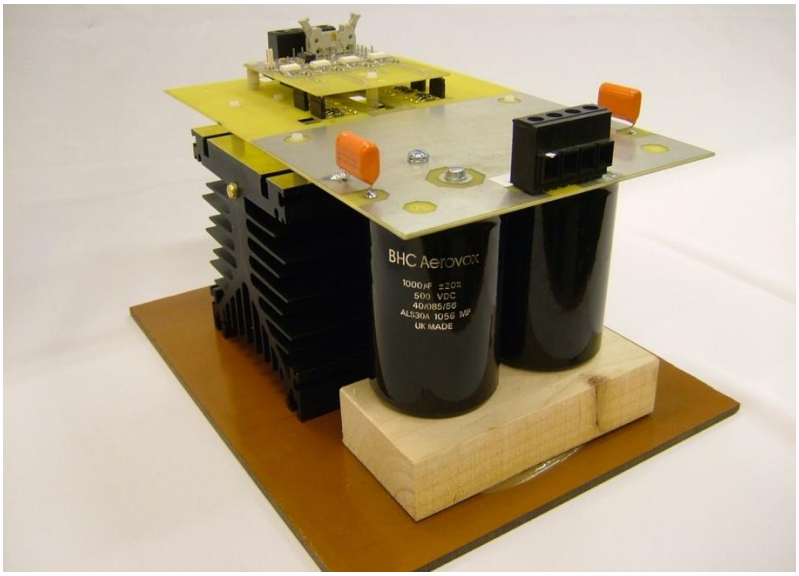

Figure 3.3 Experimental H-bridge inverter module.

An experimental H-bridge inverter module is built for the purpose of investigating the interaction between the PV inverter and the distribution grid. The H-bridge inverter module is shown in Figure 3.3. This photograph shows the inverter module is made up

of two PCB boards; the main power board appears on the bottom, and a smaller gate drive board which sits above and plugs into the power board. The large copper area on the power board (as shown in Figure 3.3) is the DC link connection (positive and negative rails on bottom and top layers respectively) to reduce the circuit resistance and increase the current capacity. It is designed as a laminar structure where the positive rail lies directly below the negative rail to reduce the parasitic inductance of the DC link (SGS-Thomson [65] and Armstrong [27]). 2-off electrolytic capacitors rated for 500V DC (1000μF each) are connected in parallel across the DC link to minimise low frequency voltage ripple on the DC link. Furthermore, 2-off polyester film capacitors (470nF each) are also connected in parallel across the DC link for the purpose of filtering high frequency components. The H-bridge inverter itself is made up by 4-off TO-3P ultrafast IGBTs (Fairchild USD series FGA40N60UFD) with integrated freewheeling diode. The IGBTs are attached on the heatsink as shown in Figure 3.4.

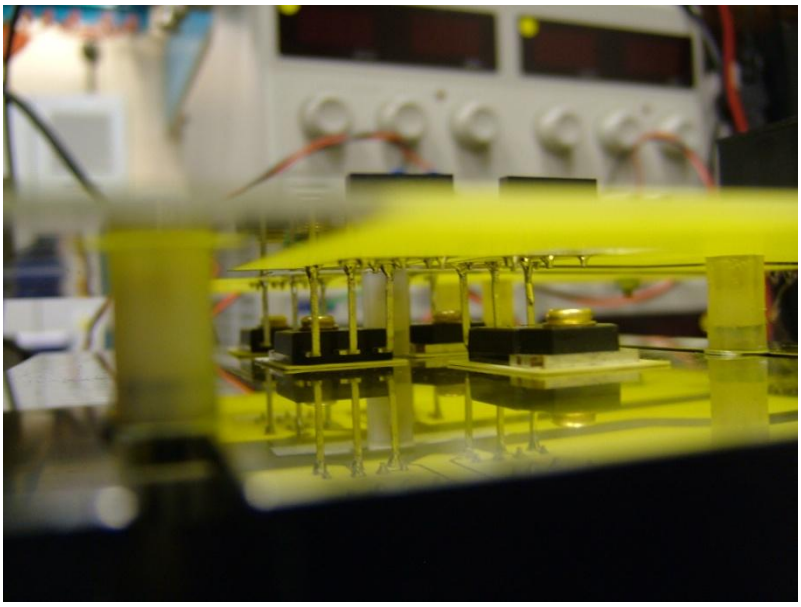

Figure 3.4 Fairchild UFD IGBTs of H-bridge inverter that attached on the heat sink.

The H-bridge inverter IGBTs are driven by the gate drive board as shown in Figure 3.5. The gate drivers take the PWM switching signal provided by the microcontroller module and switch the IGBTs by applying the gate voltage across IGBT gate and emitter (V_{GE}). An Avago Technologies® HCPL-316J gate driver is utilised. This is a galvanically isolated device, whereby the input voltage signal is passed via an opto-coupler to the inverter side of the chip. This helps to isolate the low voltage side of the chip from the high voltage circuitry of the H-Bridge. Furthermore, this gate driver provides V_{CE} desaturation (DESAT) detection function and be able to deliver maximum output current of 2.5A.

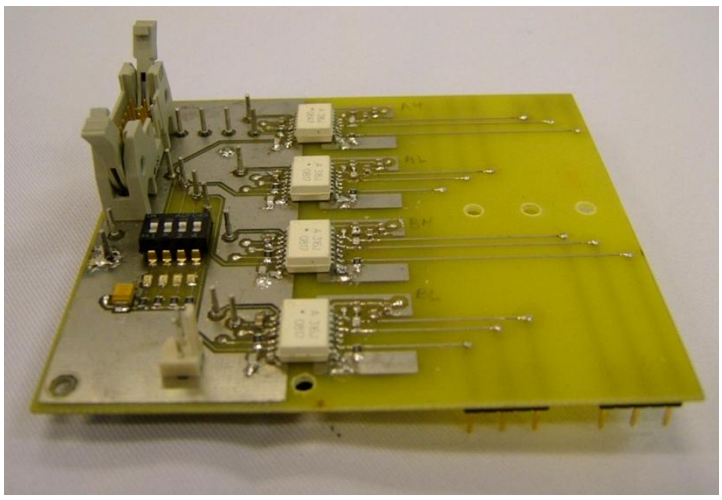

Figure 3.5 Gate drive board for H-bridge inverter.

3.4 Current/Voltage Measurement

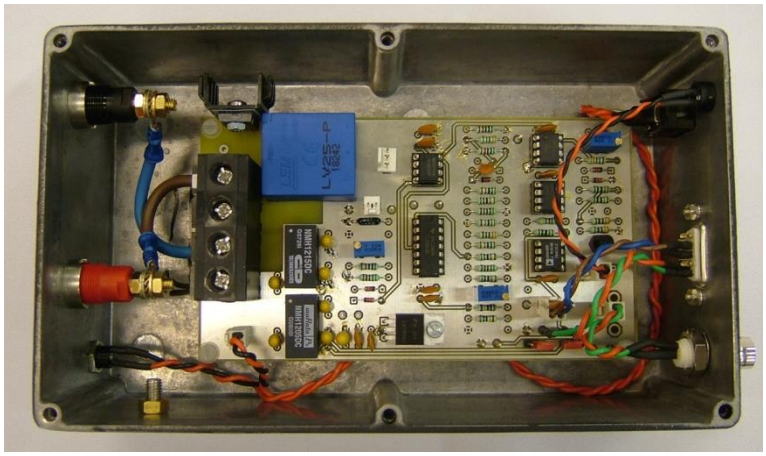

Figure 3.6 Voltage measurement board.

For the purposes of output current control and inverter terminal voltage feedforward compensation; current and voltage measurement boards are included to measure and scale the inverter system output current and inverter terminal voltage. The constructed voltage measurement board is shown in Figure 3.6. The current measurement board design is virtually the same as the voltage measurement board, apart from the input circuitry which has to be designed around the appropriate transducer (as shown by the schematics of current and voltage measurement boards in Appendix II). These measurement boards implement hall-effect transducers (current: LEM LAH 25-NP, voltage: LEM LV 25-P) due to their good overall performance, high immunity to external interference, and ease of use. The measured signal is scaled and calibrated to provide the output measurement signal of ±10V. For fault detection, the measurement boards also provide over voltage/current circuitry. This circuitry generates a fault flag which can readily be fed back to the DSP and protection circuitry.

3.5 Zero Crossing Detection

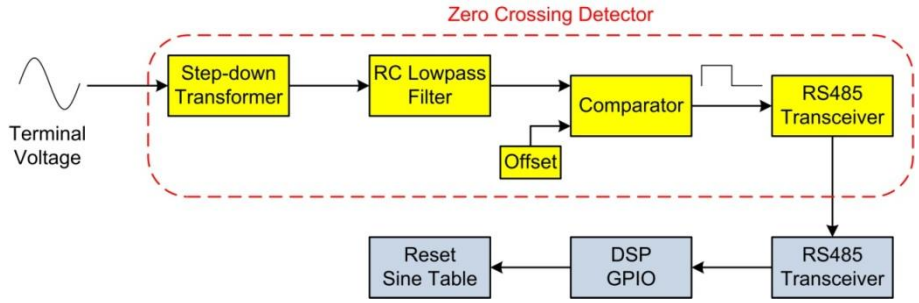

Figure 3.7 Block diagram of zero crossing detection.

The grid-connected PV inverter system must operate in unity power factor with respect to the network voltage. In practice, this can be achieved by a Phase-Locked Loop (PLL) or Zero Crossing Detector (ZCD). For simplicity and low implementation cost, the ZCD is chosen for the synchronisation of the inverter output current in this research. Figure 3.7 shows the block diagram of the zero crossing detection circuit. As the ZCD employs low voltage electronics (±15V DC) for zero crossing detection, the terminal voltage at the output of grid-connected PV system is first stepped-down through a transformer. The RC lowpass filter (10kΩ resistor and 22nF capacitor) is then implemented at the input of the comparator to filter out any noise on the stepped-down terminal voltage signal. Noisy signals can cause false triggering of the ZCD. The filtered voltage signal is then compared to the reference voltage to create the corresponding rectangular pulse that transmitted by RS485 transceiver. As the lowpass filter causes a phase shift in the voltage signal, the reference voltage is offset to compensate the phase shift error. The cut-off frequency and transfer function of the RC lowpass filter can be obtained by the well-known expressions shown in Equation (3.1) and Equation (3.2) respectively (Tomlinson [66]), while Equation (3.3) and Equation (3.4) shown the gain and phase shift of RC lowpass filter at 50Hz respectively. The constructed ZCD for synchronisation is shown in Figure 3.8 and its schematic diagram is shown in Appendix II.

$$f_{cut-off} = \frac{1}{2\pi RC} = \frac{1}{2\pi \times 10k\Omega \times 22\text{n}F} = 723.4Hz \quad \textbf{(3.1)}$$

$$H_{RC}(s) = \frac{1}{1 + RCs} \quad \textbf{(3.2)}$$

$$G_{50Hz} = |H_{RC}(j\omega)| = \frac{1}{\sqrt{1+(\omega RC)^2}} = \frac{1}{\sqrt{1+(2\pi \times 50Hz \times 10k\Omega \times 22\text{nF})^2}} = 0.9976\,V/V \quad \textbf{(3.3)}$$

$$\varphi_{50Hz} = \angle H_{RC}(j\omega) = -tan^{-1}(\omega RC) = -tan^{-1}(2\pi \times 50Hz \times 10k\Omega \times 22nF) = 3.95° \quad \textbf{(3.4)}$$

Figure 3.8 Zero crossing detector for terminal voltage synchronization.

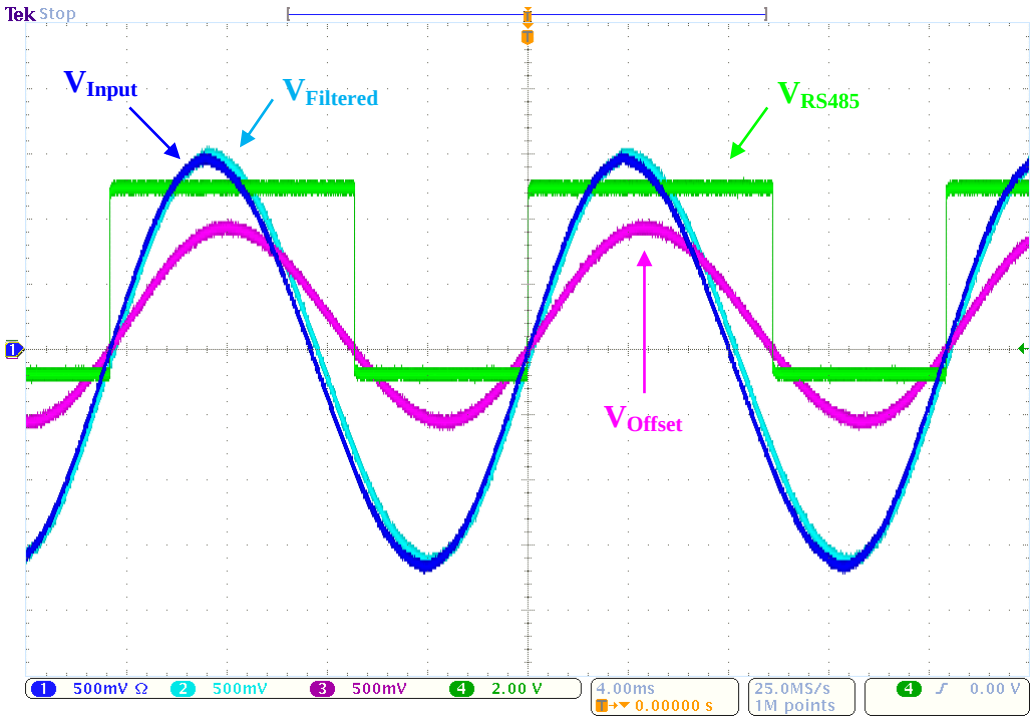

Figure 3.9 Waveforms of ZCD input voltage (V_{Input}), filtered input voltage ($V_{Filtered}$), voltage across comparator input with offset (V_{Offset}), and differential voltage at RS485 output terminal (V_{RS485}).

Figure 3.9 presents the waveform of ZCD, which is typically observed in the practical experimentation. The phase shift caused by the lowpass filter is observed on the filtered input voltage ($V_{Filtered}$ in Figure 3.9). The differential voltage at the output of the RS485 transceiver (V_{RS485}) is a rectangular pulse. This is simply generated using an LM393 comparator. The comparator compares the post-filtered input voltage against the phase compensated DC offset voltage (in an ideal case, with no phase shift from the low pass filter, this DC voltage would be zero). Note that the rectangular pulse is transmitted via RS485 interface and detected by the General Purpose Input/Output (GPIO) of the TMS320F2812 DSP (Texas Instrument [62]).

3.6 Controller Detail

The experimental grid-connected PV inverter system is controlled by a Texas Instrument® TMS320F2812 Digital Signal Processor (DSP). Some additional interface electronics is designed to create a complete controller module. Figure 3.10 shows the controller module built for the purpose of this research project. It is made up of 3 component parts; the main DSP development board, a commercially available ADC/DAC daughtercard, and an in-house designed interface board. Figure 3.11 shows the key functionality of the 3 boards and how they interface with each other and the host PC.

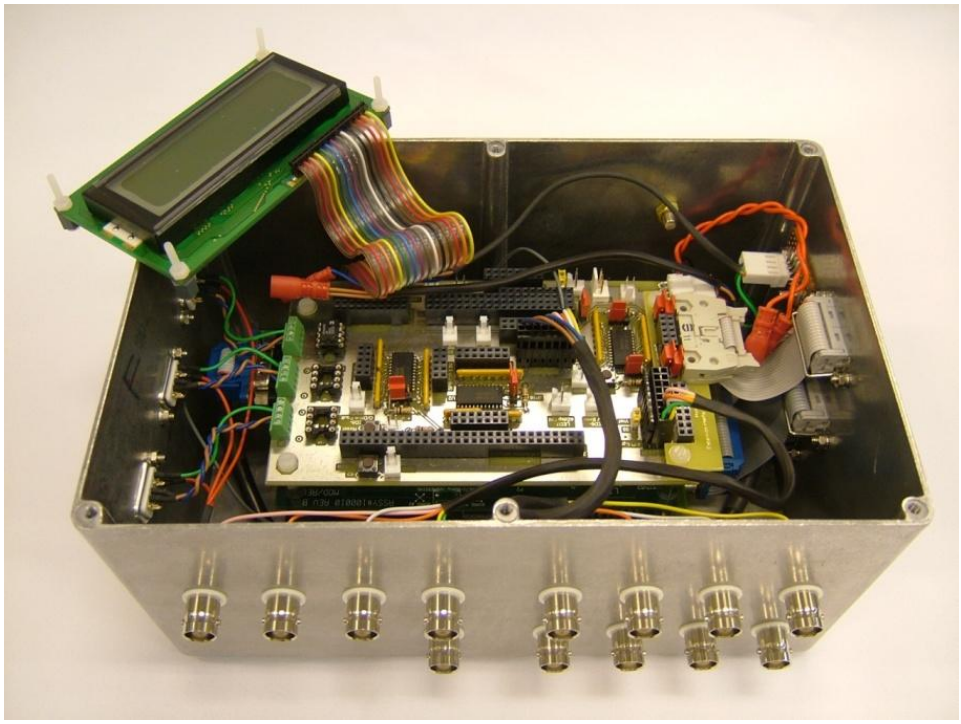

Figure 3.10 Controller module.

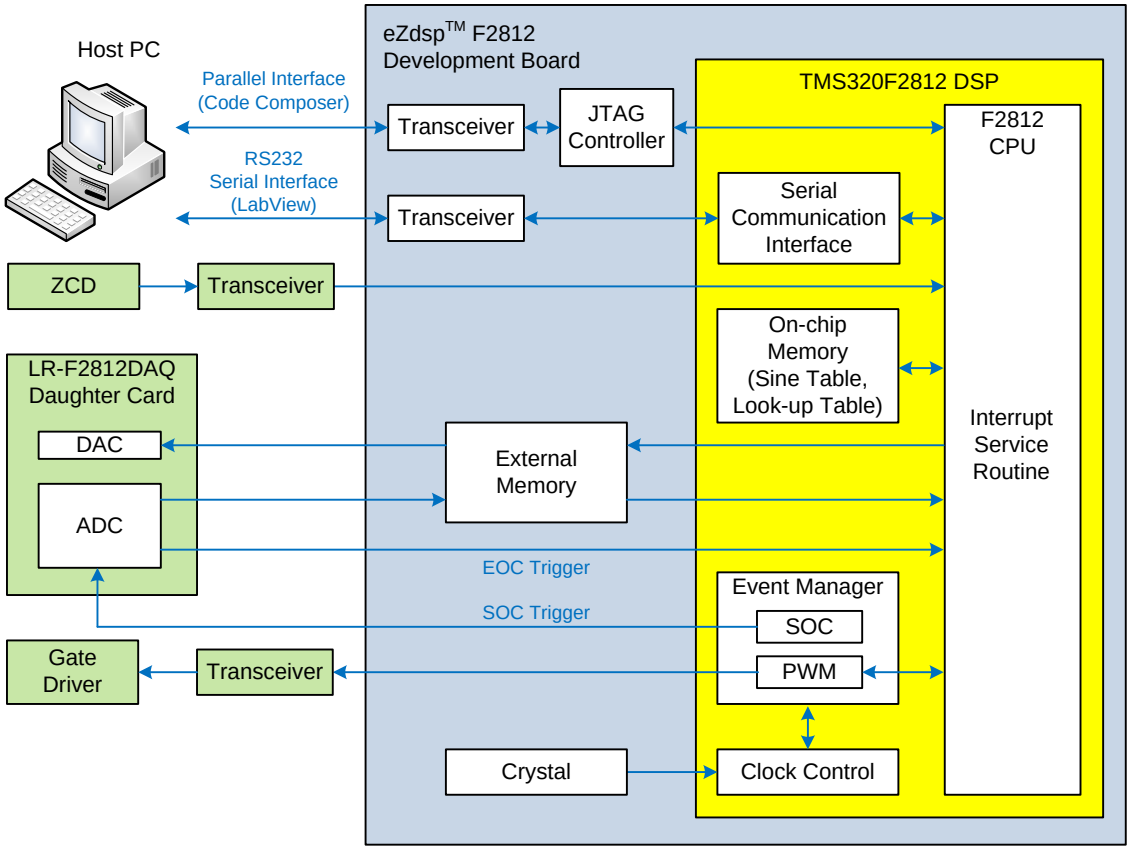

Figure 3.11 Controller overview.

3.6.1 *Spectrum Digital eZdsp™ F2812 DSP Development Board*

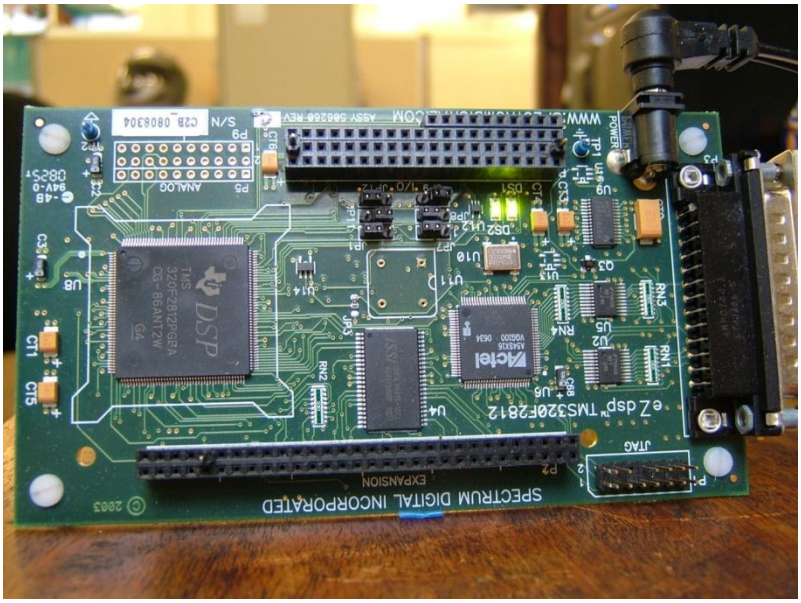

Figure 3.12 Spectrum Digital eZdsp™ F2812 development board.

The main control algorithm for the PV inverter system is implemented on the Spectrum Digital eZdsp™ F2812 DSP development board, as shown in Figure 3.12. Its central processing unit (CPU) is based on the Texas Instrument® 32-bit Fixed Point TMS320F2812 DSP. The CPU is programmed to execute an Interrupt Service Routine

(ISR) containing the main current control loop and other peripheral functions (such as serial port communication etc) whenever an external hardware interrupt signal is observed by the DSP. This hardware interrupt is directly taken from the End of Conversion (EOC) trigger signal of the Analogue to Digital Converter (ADC) on the LR-F2812DAQ daughtercard (to be described in Section 3.6.2). In this way, the ISR is fully synchronised with the sampling system. The interface with the host PCs LabVIEW™ GUI is managed by the eZdsp™ F2812 DSPs integrated Serial Communication Interface (SCI) via RS232 serial port. Note, in this research work, the integrated ADC in the F2812 DSP is not utilised as it does not provides simultaneous conversion of multiple ADC channels.

3.6.2 *Link Research LR-F2812DAQ Daughtercard*

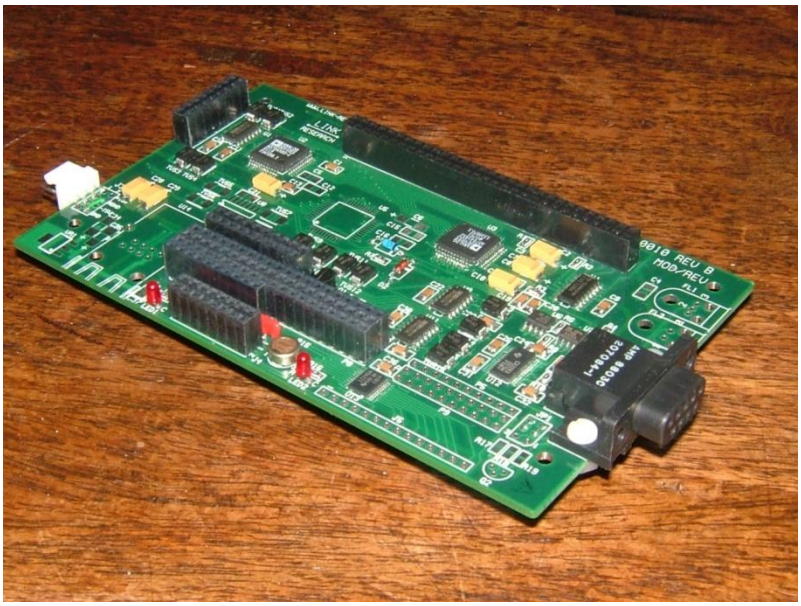

Figure 3.13 Link Research LR-F2812DAQ daughtercard for eZdsp™ F2812.

The analogue to digital conversion (A/D) and digital to analogue conversion (D/A) is carried out on the Link Research LR-F2812DAQ daughtercard, as shown in Figure 3.13. It has a similar footprint to the Spectrum Digital eZdsp™ F2812 DSP development board and directly plugs into this DSP board. It provides 4 ADC channels; 14-bit simultaneous A/D sampling and 8 DAC channels; 14-bit D/A simultaneous updating with ±10V input and output range respectively. The A/D sampling is triggered by the Start of Conversion (SOC) pulse provided by the DSP clock. As mentioned earlier, the ADC EOC pulse is then used to trigger the ISR of the DSP.

3.6.3 *Interface Board*

An in-house interface board is designed and built to interface with the eZdsp™ F2812 development board and LR-F2812DAQ daughtercard. Figure 3.14 shows the constructed interface board. It consists of 3-off transceivers used to interface the various 5V signals (e.g. from the ZCD circuit) to the 3.3V output/input signal level of the DSP and an additional 3-off transceivers for the RS485 interface. Finally, an Insulated-Displacement Connector (IDC) is also provided for a direct connection to the gate drive board shown in Figure 3.5.

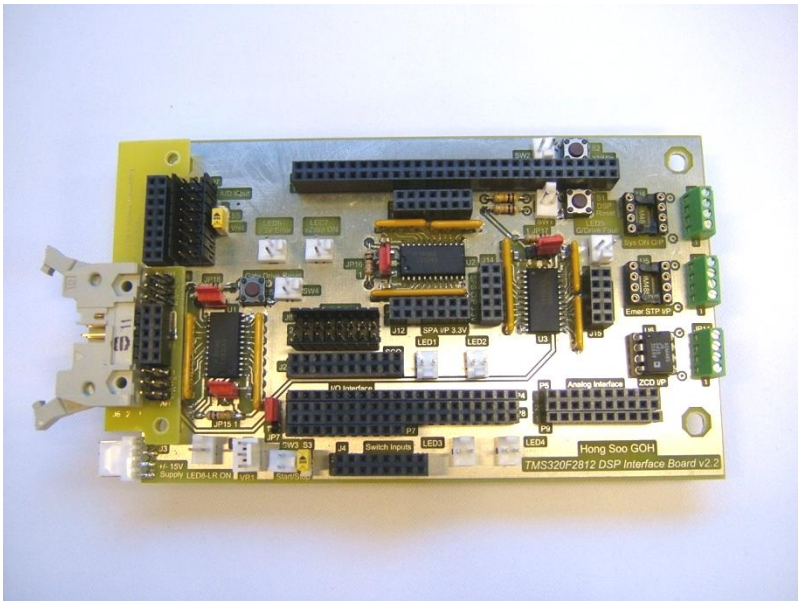

Figure 3.14 Interface board for eZdsp™ F2812 development board.

3.6.4 *LabVIEW™ Interface for Real-time Control and Communication*

National Instrument® LabVIEW™ software package is used to implement a Graphical User Interface (GUI) and for high-level control of the DSP controller operation in real-time. This is achieved through a RS232 serial interface between the TMS320F2812 DSP and the host computer. Figure 3.15 presents a typical screenshot of the GUI. This GUI is programmed to update the current demand of the controller and transfer high-level control commands (e.g. controller gains) to the DSP. Simultaneously, it also reads and presents important variables within the DSP on the screen for the user.

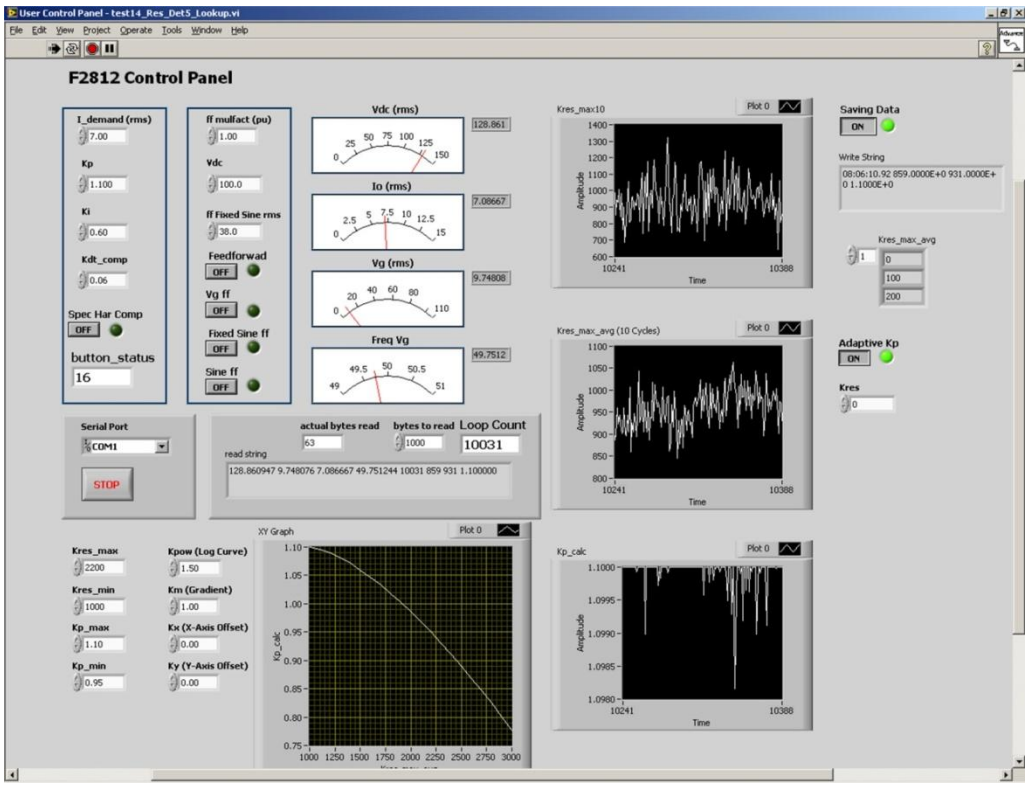

Figure 3.15 LabVIEW™ GUI with controller interface for real-time control.

3.6.5 *Current Control Method*

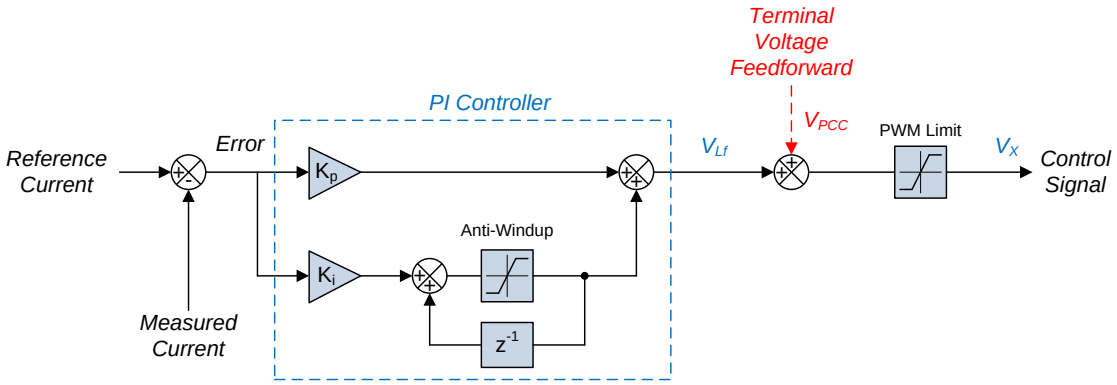

Figure 3.16 Control block of PI controller with terminal voltage feedforward implemented in DSP.

A conventional Proportional-Integral (PI) control algorithm with terminal voltage feedforward is implemented within the ISR of the DSP. It is used for current control of the grid-connected PV inverter system. This control strategy is expressed by the control block in Figure 3.16. To prevent integral windup and PWM over-modulation, the integral term and overall output control signal are clamped by the saturation blocks "Anti-Windup" and "PWM Limit" respectively (as shown in Figure 3.16).

3.6.6 *Unity Power Factor Control of PV Inverter System*

The grid-connected PV inverter system is typically designed to operate in unity power factor (PF). In other words, it is desired to inject current that is in-phase with the network voltage at its output terminal (PCC voltage in this case) into the distribution grid. As the PV inverter system is typically coupled to the distribution grid through a passive lowpass filter (LC or LCL arrangement), the inverter output current that is flowing through the filter inductance and injected into the distribution grid will cause the voltage drop across the filter inductance. To inject rated inverter output current (I_O), with zero phase shift with respect to the PCC voltage, the controller has to generate an inverter bridge output voltage (V_X) that overcomes the PCC voltage (V_{PCC}) and the voltage drop across the filter inductor (V_{Lf}); which is 90° leading the PCC voltage due to the effect of inductive reactance. At this point, the inverter system is operating at unity power factor to inject real power (P) into the distribution grid and hence there is no reactive power (Q) supply from the inverter system. This is shown by the circuit diagram in Figure 3.17(a). Here, the filter capacitor is neglected as it has a very high impedance at low frequency (such as 50Hz fundamental frequency). Figure 3.17(b) shows the phasor diagram of the voltage and current vectors at unity power factor. It shows that the inverter system output current, hence the real power generated by the inverter system, can be increased by raising the magnitude of the inverter output voltage. However, to maintain unity power factor, the relative leading angle of the inverter output voltage with respect to PCC voltage (δ) must be increased to keep the voltage drop across the filter inductor leading the PCC voltage by 90°.

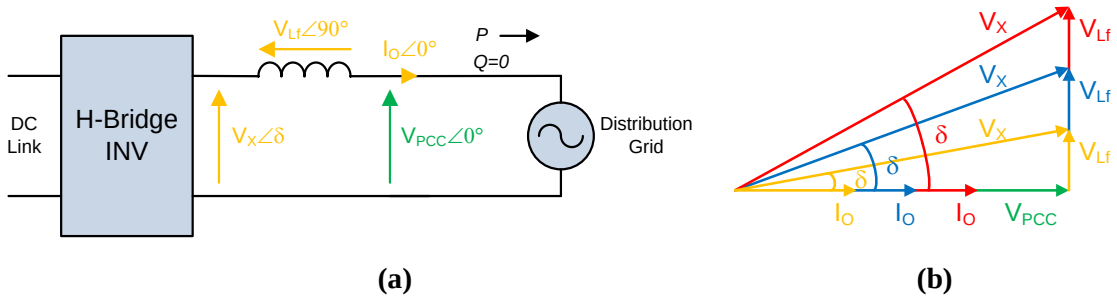

Figure 3.17 Operation of grid-connected PV inverter system at unity power factor. (a) Circuit diagram; (b) Phasor diagram of output power control for various power levels.

From the current controller point of view, the conventional PI controller (as shown in Figure 3.16) has to calculate the control signal that overcomes the voltage drop across the filter inductor and counter-balance the PCC voltage (V_{Lf}+V_{PCC}) if terminal voltage feedforward is not applied. To reduce the burden on the PI controller, it is possible to

implement a voltage feedforward scheme, whereby the terminal voltage (PCC voltage in this case) is fed into the output of the PI controller, as shown by the red arrow in Figure 3.16 (Armstrong, Atkinson, et al. [21, 27, 67] and Ellis [60]). By feeding the PCC voltage forward ("V_{PCC}" in Figure 3.16), the PI controller just needs to calculate the control signal component that compensates for the voltage drop across the filter inductor ("V_{Lf}" in Figure 3.16).

3.6.7 *Flexible Power Control of PV Inverter System*

As the installation and capacity of grid-connected PV systems continues to increase rapidly [7], [68], [47], conventional grid-connected PV systems (originally designed to operate at unity power factor) are likely to be required to offer more flexible control solutions. This may include real power and reactive power control to improve grid reliability, voltage regulation, and reduce power loss. This is particularly important in the latest Smart Grid systems. Here, dynamic power flow and reliability is of prime importance. Recent grid-connected PV inverter system developments with flexible power control and power factor (PF) correction are demonstrated by Dasgupta, Mohan, et al. [69, 70], Dasgupta, Sahoo, et al. [71], Kim, Gwonjong, et al. [72], Turitsyn, Sulc, et al. [73], Cagnano, Tuglie, et al. [74]. More advanced power control can be achieved by flexible control of the magnitude and phase angle of the inverter system output current (I_O) through the current controller, which in turn affects the magnitude and phase angle of the inverter bridge output voltage (V_X). Figure 3.18 and Figure 3.19 show the control of grid-connected PV inverter system for reactive power (Q) and real power (P) respectively.

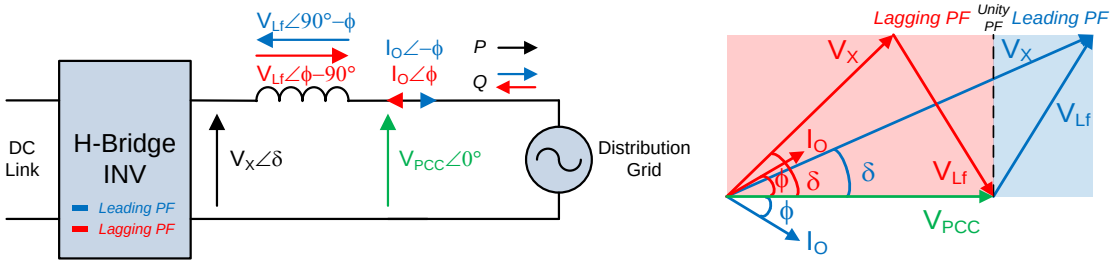

(a) **(b)**

Figure 3.18 Reactive power (Q) control of grid-connected PV inverter system. (a) Circuit diagram; (b) Phasor diagram.

As shown by the phasor diagram in Figure 3.18(b), the reactive power flow can be controlled by the phase difference between the PCC voltage and the inverter system output current, hence the PF angle "ϕ" (sometime referred as load angle). With the

lagging PF angle (as shown by blue "ϕ" in Figure 3.18(b)), the vector of V_X points to the blue shaded region in Figure 3.18(b) and hence the voltage drop across filter inductor (V_{Lf}) is no longer leading the vector of V_{PCC} by 90°; it is leading the V_{PCC} vector by an angle less than 90°. In this region, the vector length of V_X increases with ϕ. At this point, the PV inverter system is operating at leading PF (load convention) to inject reactive power into the distribution grid and the amount of reactive power flow increases with the vector of V_X. In contrast, the vector of V_X points to the red shaded region in Figure 3.18(b) with leading PF angle (as shown by red "ϕ" in Figure 3.18(b)). In this region, the vector length of V_X decreases as ϕ increases and the vector of V_{Lf} is lagging the vector of V_{PCC}. At this point, the PV inverter system is operating at lagging PF (load convention) to draw reactive power from the distribution grid. The amount of reactive power flow increases as the vector of V_X decreases. Therefore, it can be concluded that the reactive power of PV inverter circuit, as shown in Figure 3.18(a), flows from the higher magnitude voltage vector to the lower magnitude voltage vector. The amount of reactive power flow increases with the difference between the magnitude of the two corresponding vectors (the difference between vectors V_X and V_{PCC}).

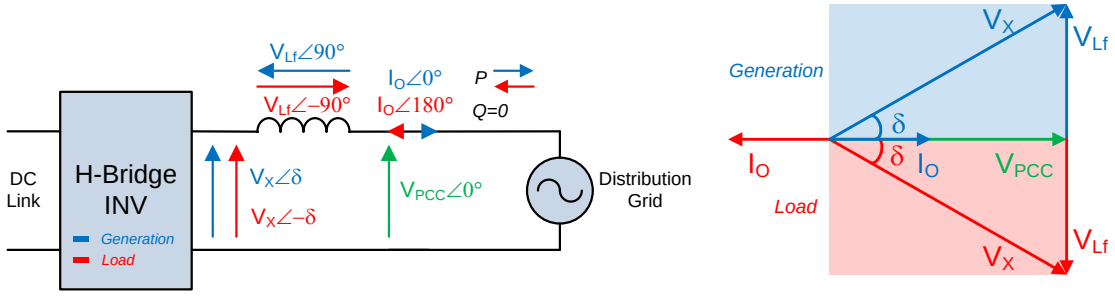

(a) **(b)**

Figure 3.19 Real power (P) control of PV inverter system. (a) Circuit diagram; (b) Phasor diagram.

As shown by the phasor diagram for unity power factor in Figure 3.19(b), real power flow can be controlled by the phase angle of inverter bridge output voltage (δ) to the PCC voltage. With the leading δ (as shown by blue "δ" in Figure 3.19(b)), the vector of V_X is leading the vector of V_{PCC} and hence the voltage drop across filter inductor (V_{Lf}) is leading the vector of V_{PCC} by 90°. This causes the vector of V_X to point towards the blue shaded region in Figure 3.19(b) and its length increases with δ for I_O in-phase with V_{PCC}. At this point, the PV inverter system is operating as a generator to inject real power into the distribution grid and the amount of real power flow increases with δ. Vice-versa, the vector of V_X lags the vector of V_{PCC} with the lagging δ (as shown by red

"δ" in Figure 3.19(b)). The vector of V_X points to the red shaded region in Figure 3.19(b) and its length increases with δ for I_O anti-phase with V_{PCC}. At this point, the PV inverter system is operating as a load to draw real power from the distribution grid and the amount of real power flow increases with δ. Therefore, it can be concluded that the real power of PV inverter circuit diagram as shown in Figure 3.19(a) is flowing from the leading voltage vector to the lagging voltage vector (such as vectors of V_X and V_{PCC}), and the amount of real power flow increases with the angle between two corresponding vectors (such as δ).

3.7 Bandpass Filter for Resonance Detection

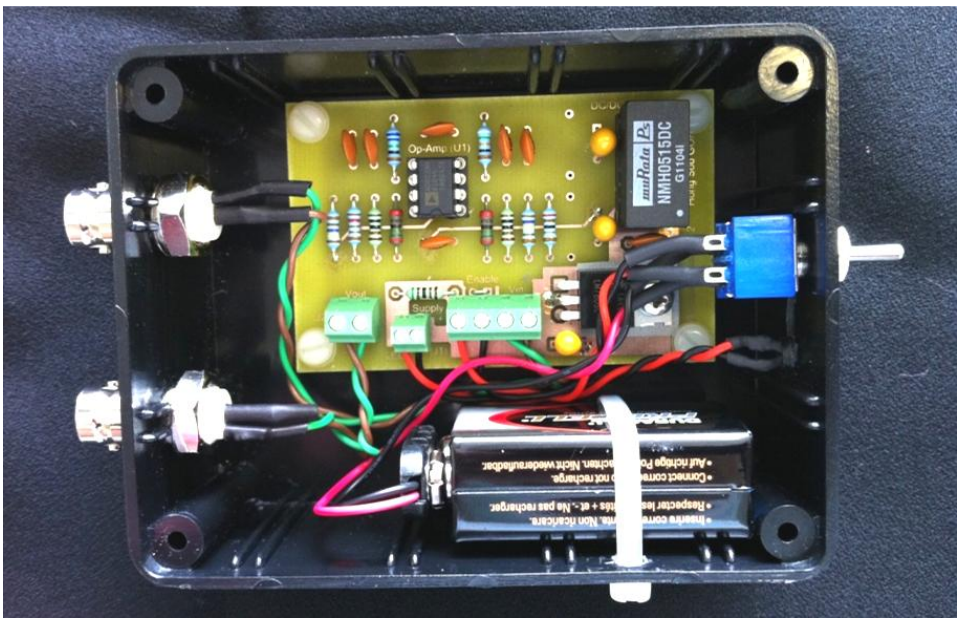

Figure 3.20 Active bandpass filter for resonance detection.

An active bandpass filter (shown in Figure 3.20) is used to capture any resonant harmonic components in the circuit. It is a 4th order Sallen-Key filter with 26.02dB passband gain. Moreover, it has a centre frequency of 2 kHz and passband bandwidth of 1 kHz respectively. More detailed discussion on this bandpass filter is presented in Chapter 6 of this thesis. Noted that schematic diagram of the bandpass filter is presented in Appendix II.

3.8 System Isolation and Circuit Protection

In the event of emergency, an emergency stop button can be pressed to safely isolate the experimental system (visible on front of cage in Figure 3.1). Isolation of the experimental grid-connected PV inverter system is facilitated by means of contactors that are directly controlled by switchgear (as shown in Figure 3.21 and schematic of

protection circuit in Appendix VI). The switchgear controls connection of the inverter to the DC link power supply via the contactor located on the DC link terminal (K1 in Figure 3.2) and to the distribution grid via an additional contactor placed at the output terminal of lowpass filter (K3 in Figure 3.2).

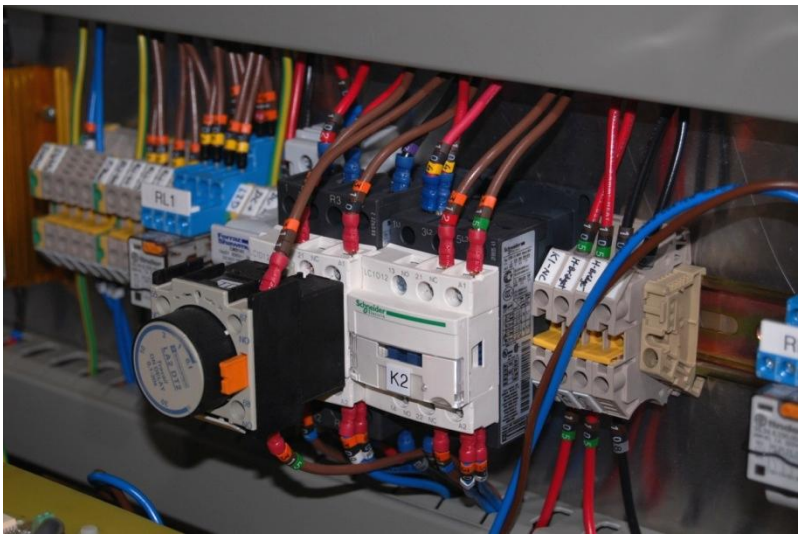

Figure 3.21 Control switchgear for system isolation and protection.

Two large electrolytic capacitors are (2-off 1000μH, 500V, electrolytic capacitors) located in the DC link to stabilise the DC link voltage. At the first instant of DC link power up, a high value of inrush current will flow into DC link circuit. The test circuit is protected from this by an inrush protection circuit (as shown in Figure 3.2). A resistor (330Ω) is placed in parallel with a normally open contactor (N/O of K2 as shown in Figure 3.2). A timer delay block is attached to the contactor, and will hold the contactor open for 3 seconds at turn-on of the system. This is ample time to allow the capacitor to charge up sufficiently under limited current conditions as the capacitors only take 1.52s of charge up time to reach 90% of DC link voltage. This is calculated through Equation (3.6) that derived from the well-known expression in Equation (3.5) (Alexander and Sadiku [75], Hughes [76]).

$$V_{capacitor} = V_{in}\left(1 - e^{-t/RC}\right) \tag{3.5}$$

$$\begin{aligned} 0.9pu &= 1.0pu\left(1 - e^{-t/RC}\right) \\ t &= -RC\ln(0.1) \\ t &= -[330\Omega \times 2000\mu F \times \ln(0.1)] \\ t &= 1.52s \end{aligned} \tag{3.6}$$

In the event of DC link power off, it is desirable to remove the energy in the DC link capacitors. This is achieved by a "power dump circuit" which is connected in parallel with the DC link capacitors. The "power dump circuit" simply comprises of a damping resistor (680Ω) in series with a normally closed contactor (N/C of K1 as shown in Figure 3.2). To protect the system from over current, fast acting fuses are placed before the DC link and at the output terminal of inverter system. These fuses will blow open-circuit in the event of excessive current flow.

3.9 Summary

This chapter has described the experimental grid-connected PV inverter system developed within the PEDM laboratory. A description of the experimental hardware has been presented and the key peripheral components of the experimental facility, such as switchgear and protection circuit have been described. Finally, an overview of the controller and LabVIEW^{TM} interface have been presented, along with the discussion on the current control algorithm and the flexible control of real power and reactive power flow. By understanding the hardware platform, it is possible to put the experimental results in the forthcoming chapters into better context.

Chapter 4. Interaction of Grid-Connected PV Inverter and Distribution Grid

4.1 Introduction

This chapter discusses the interaction between the grid-connected PV inverter and the distribution grid. In particular, it is concerned with the effect of the variations in background grid voltage harmonic profile and grid impedance on the harmonic performance of grid-connected PV inverter. The first part of this chapter presents the analysis in the mechanism of interaction between the lowpass filter of the PV inverter and the grid impedance. The linkage between the voltage at Point of Common Coupling (PCC) and the voltages at the PV inverter bridge output and background grid voltage is explained. To demonstrate the effect of grid impedance on the output current gain of the PV inverter current controller, the closed loop response of the PV inverter current control loop is obtained. The response is then further analysed for a range of grid impedance values. The second part of this chapter presents the simulation results of the high fidelity grid-connected PV inverter system model in Matlab/Simulink®. In the simulation, the individual harmonics of the background grid voltage and grid impedance are varied in a controlled manner. The effect on the output current of the grid-connected PV inverter system is then analysed to identify the corresponding effects.

4.2 PV Inverter Interface to Distribution Network

Typically, conventional small scale grid-connected PV systems are connected at the distribution level (e.g. 230V distribution network in United Kingdom). Here, each PV system is capable of generating power up to the range of several kilowatts only. However, there are many large scale (in megawatts range) three-phase grid-connected PV systems which have been built over the last decade, and many more are currently being construction or proposed. For example, the Nellis Solar Power Plant located at Nevada, United State of America commenced operation in December 2007 and has a power generation capacity of 14.2 MW (Nellis Air Force Base [77]). Moreover, it is reported by Mulliken [78] that a 1 MW plant is the most common and newsworthy solar power plant in 2011.

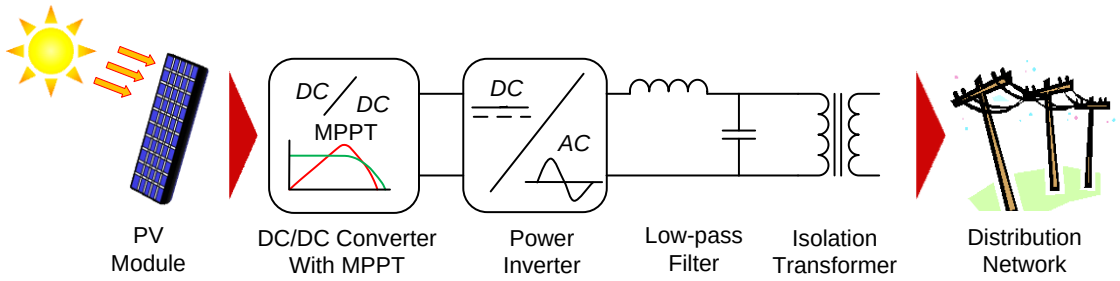

Figure 4.1 Typical arrangement of grid-connected PV system.

Unlike conventional standalone PV systems, grid-connected PV systems interface to the distribution network, as shown by the typical arrangement of grid-connected PV system in Figure 4.1. The inverter then typically injects unity power factor current into the network. However, the grid is a dynamic system and its characteristics are likely to change over time. As discussed and analysed in Appendix VII, this is a consequence of the operating conditions and the nature of the loads and sources connected to the network. This results in complex interactions between the grid and the current controller of the PV system which can affect the power quality performance of the grid-connected inverter.

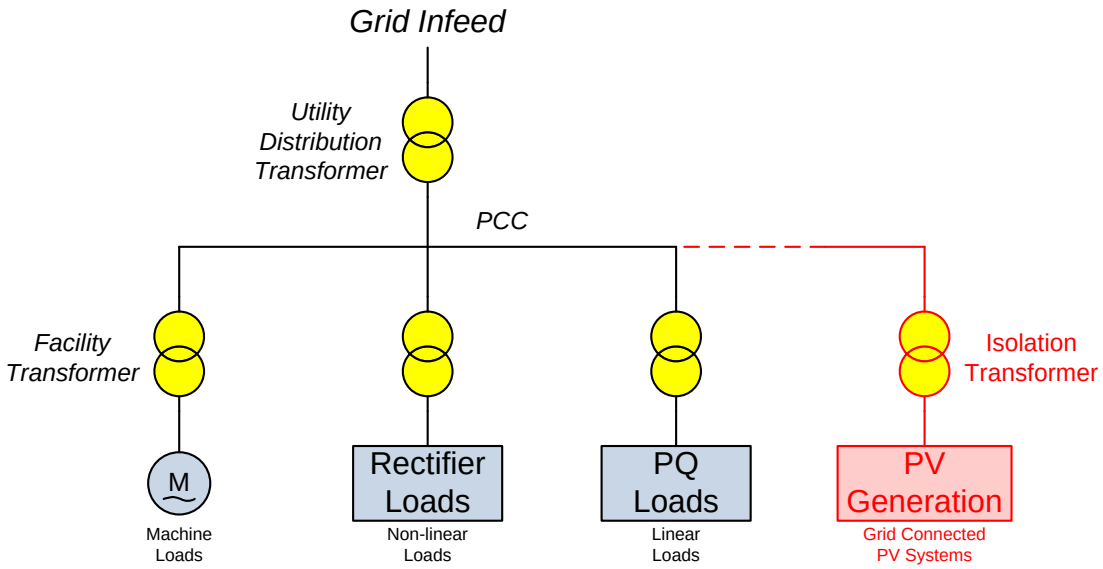

Figure 4.2 Typical distribution grid with PV system connected to PCC.

Figure 4.2 shows the layout of a typical distribution network with a PV system connection. Grid-connected PV systems are normally connected alongside the various loads connections to the PCC. Therefore, variation in the operating conditions of the distribution grid, which in turn cause the grid harmonics to change, will now also affect the performance of the grid-connected PV system current controller.

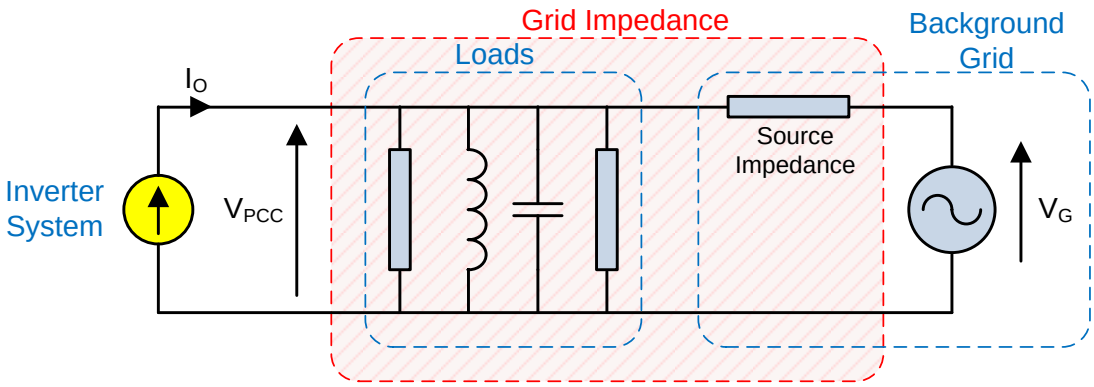

Figure 4.3 Equivalent circuit of a single-phase distribution grid with inverter system and loads connected at PCC.

Figure 4.3 shows the equivalent circuit of a single-phase distribution grid with inverter system and various types of loads connected at PCC. The inverter system can be modelled as a current source which injecting the current into the grid while various type of loads can be modelled by resistance, reactance and capacitance which are connected in parallel with the inverter system. For analysis purpose, the loads impedance connected to the PCC and source impedance can be lumped into single inductive impedance, named as grid impedance (Z_{Lg}), as shown by the red box in Figure 4.3. For a single-phase two-wire 230V 50Hz supplies in United Kingdom, the reference impedance of 0.4+j0.25 Ω (equivalent to 0.4Ω and 0.796mH of grid resistance and grid inductance respectively) are given by IEC standard IEC 60725 [56] as the maximum grid impedance of distribution grid. Furthermore, analysis and calculation of grid impedance are presented by Heskes, Rooij, et al. [57]. It is noted that grid impedance depends upon the operating condition of the grid and thus it is varies over time.

Grid voltage distortion and variation in its operating condition is discussed in Appendix VII, while the interaction between the grid voltage waveform and the current controller of grid-connected PV inverter will be discussed in this chapter.

4.3 Effect of Voltage Distortion at PCC on Output Current of Grid-Connected Inverter

As discussed in Appendix VII that the voltage waveform at PCC is affected by the loading condition of connected loads. This caused the voltage at the PCC to deviate from an ideal sine wave, which in turn causes the voltage harmonic profile at the PCC to change over time.

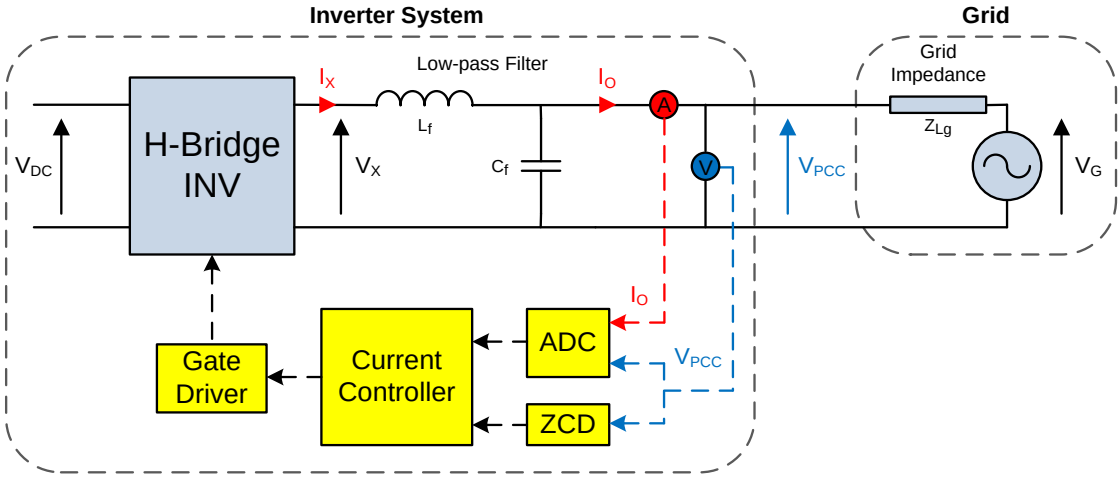

Figure 4.4 Output current control of grid-connected inverter.

In a grid-connected PV system, the current controller is normally employed to interface with the grid and to control the current injected into the grid. Figure 4.4 shows the output current control of grid-connected inverter interfaced with grid impedance (form by lumped loads and supply impedance) and grid supply at PCC. To simplify the analysis, the isolation transformer is neglected as it does not has significant effect on the low order harmonics (harmonics < 50^{th}) of PV inverter output current and voltage. Ideally, the grid-connected PV system is design to inject the ideal sinusoidal current into the grid by controlling the switching of power electronic switches in inverter bridge and attenuation of high frequency harmonics by lowpass filter located at the output of inverter bridge. The switching of power electronic switches is controlled by the current controller in order to generate 40 kHz switching frequency PWM pulses (generated by 20 kHz Unipolar PWM) at the output of inverter bridge which in turn causes the current to flow through the lowpass filter then injected into the grid. The output current (I_O) injected into the grid is affected by the voltage at PCC (V_{PCC}) that interacts with voltage at inverter bridge output (V_X) and background grid voltage (V_G). Moreover, output current injected into the grid and voltage at PCC (if grid voltage feedforward topology is implemented), are measured by current and voltage sensor respectively then feedback into the control loop of current controller at every control cycle. Therefore, change in grid voltage operating conditions that vary the voltage harmonic profile at PCC over time will affect the performance of inverter current controller which in turn affects the output current of inverter system injected into the grid.

Figure 4.5 shows the harmonic components of inverter output current (I_O) versus corresponding voltage at PCC (V_{PCC}) at three different times of a day with an experimental inverter connected to the simulated low voltage background grid in

practical experiment. As shown by the results in Figure 4.5, the output current of the inverter is affected by the harmonic profile of voltage at PCC. The low order harmonics (from 3rd to 19th harmonics) of inverter output current distinctly changes in response to the variation in harmonic profile of voltage at PCC.

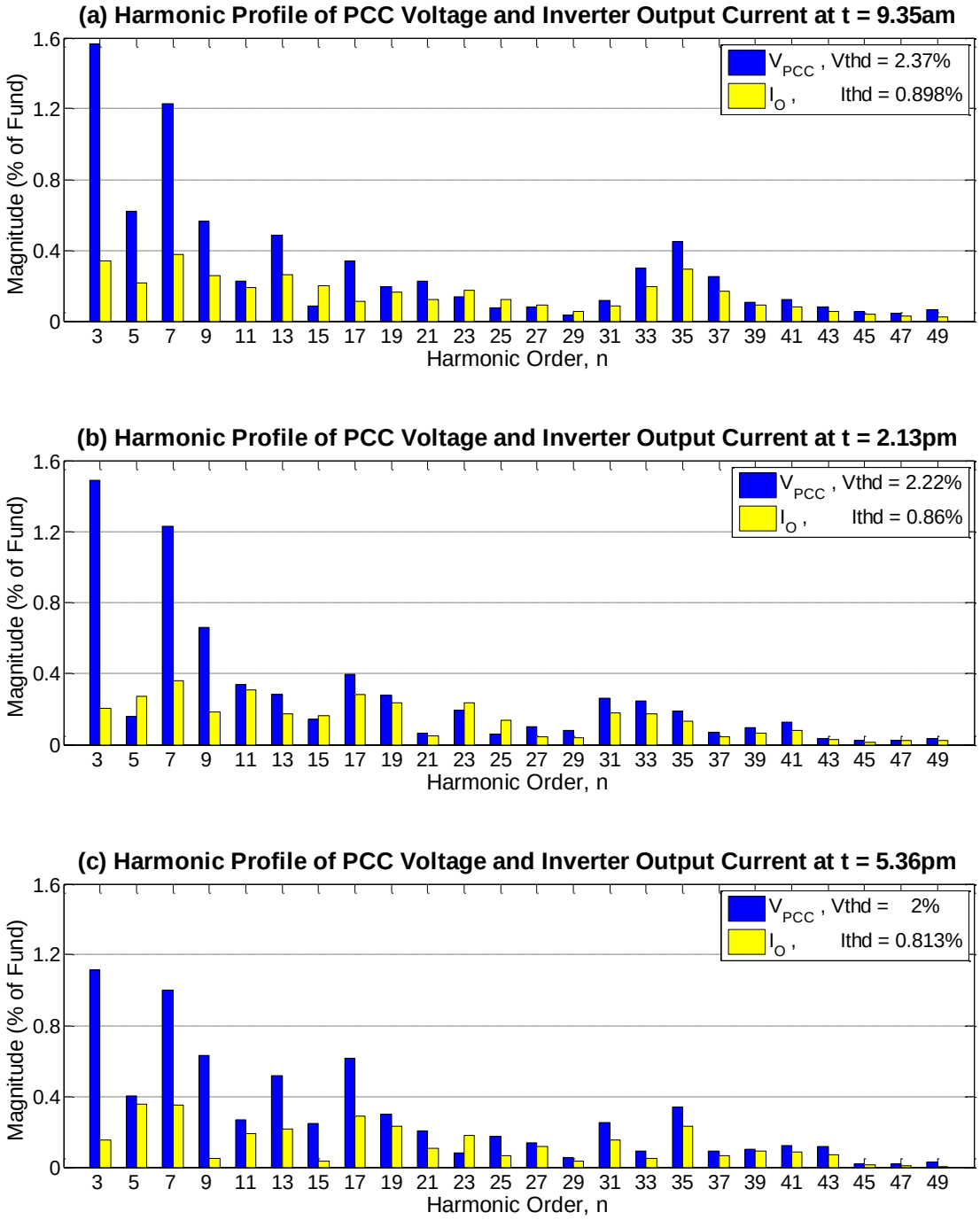

Figure 4.5 Time variant in harmonic profile of PCC voltage (V_{PCC}) and corresponding inverter system output current (I_O), for three different time of the day.
(I_{demand} = 7A RMS, V_{DC} = 100V, V_G = 43.24V RMS, K_p = 1.1, K_i=0.6.)

4.4 Mechanism of Harmonic Interaction in the Network

The electrical current flowing through a branch is corresponding to the applied voltage and limited by the effective impedance, as given by the well-known Ohm's Law (Alexander and Sadiku [75], Hughes [76]). The theory can be applied on the inverter system connected to the distribution grid at PCC as shown in Figure 4.4, the magnitude and direction of inverter bridge output current (I_X) and inverter system output current (I_O) injected into the distribution grid correspond to the magnitude and phase angle difference of the voltages between both ends of its current path. As current control loop of digital controller controls the voltage output at inverter bridge (V_X) for a corresponding current demand, to simplify the analysis the effect of control loop can be neglected and the inverter bridge output voltage is represented by a range of voltage harmonics. As the inductive and capacitive reactances of LCL branch in Figure 4.4 are frequency dependent, the interaction between the inverter bridge output voltage and background grid voltage can be modelled by the impedance of LCL components and the voltage sources at corresponding harmonic order (multiple of fundamental frequency), as shown in Figure 4.6, where the harmonic order and the vector of the harmonic at corresponding harmonic order are denoted by the symbol ***n*** and $\boldsymbol{h_n}$ respectively. In the model, the current harmonic at particular harmonic order is proportional to the corresponding voltage harmonic that is applied across its impedance at corresponding harmonic order. Similar model has been presented by Jalili and Bernet [39], Lee, Park, et al. [79], for the design of LCL filter but the interaction of the voltage and current harmonic within the LCL branch is barely discussed.

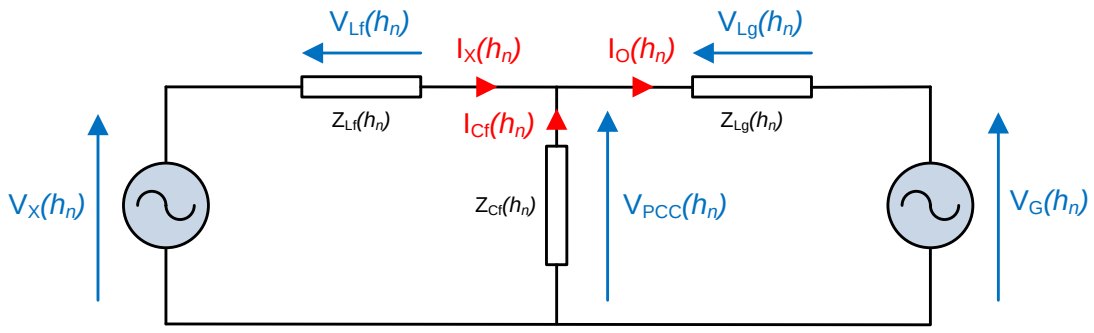

Figure 4.6 Harmonic model of distribution grid with inverter system connected at PCC, neglecting the effect of current controller and H-bridge.

As the reactance of the inductor and capacitor is directly and inversely proportional to the order of fundamental frequency respectively, the effective reactance of filter inductance (X_{Lf}), filter capacitance (X_{Cf}) and grid inductance (X_{Lg}) at particular

harmonic order, can be obtained by expression as shown in Equation (4.1) – Equation (4.3).

$$X_{Lf}(h_n) = \omega_n L_f = 2\pi f_1 L_f n \tag{4.1}$$

$$X_{Cf}(h_n) = \frac{1}{\omega_n C_f} = \frac{1}{2\pi f_1 C_f n} \tag{4.2}$$

$$X_{Lg}(h_n) = \omega_n L_g = 2\pi f_1 L_g n \tag{4.3}$$

In complex analysis, the impedances of the inductor and capacitor are dominated by the real component and imaginary component. Hence, the impedance of filter inductance (Z_{Lf}), filter capacitance (Z_{Cf}) and grid inductance (Z_{Lg}) at particular harmonic order can be expressed by their equivalent series resistance (ESR) and their reactance at particular harmonic order, as shown in Equation (4.4) – Equation (4.6).

$$\vec{Z}_{Lf}(h_n) = R_{Lf} + jX_{Lf}(h_n) \tag{4.4}$$

$$\vec{Z}_{Cf}(h_n) = R_{Cf} - jX_{Cf}(h_n) \tag{4.5}$$

$$\vec{Z}_{Lg}(h_n) = R_g + jX_{Lg}(h_n) \tag{4.6}$$

Different to conventional circuit which supply by only one voltage source, harmonic modelled in Figure 4.6 consists of two voltage sources connected at both end of the circuit which cause PCC voltage (V_{PCC}) to be affected by grid voltage (V_G) and inverter bridge output voltage (V_X) at the same time. For analysis purpose, the well-known Superposition Theorem (Alexander and Sadiku [75], Hughes [76]) can be applied to obtain the particular harmonic order of voltage at PCC (as shown in Appendix VIII), yield Equation (4.7).

$$\vec{V}_{PCC}(h_n) = \frac{\vec{V}_X(h_n)\vec{Z}_{Lg}(h_n) + \vec{V}_G(h_n)\vec{Z}_{Lf}(h_n)}{\vec{Z}_{Lf}(h_n) + \vec{Z}_{Lg}(h_n) + \dfrac{\vec{Z}_{Lf}(h_n)\vec{Z}_{Lg}(h_n)}{\vec{Z}_{Cf}(h_n)}} \tag{4.7}$$

By knowing the vector of PCC voltage at particular harmonic order from Superposition Theorem, the voltage drop across the filter inductor (V_{Lf}) and grid inductance (V_{Lg}) at particular harmonic order can then be obtained by subtracting inverter bridge output voltage, PCC voltage and grid voltage at particular harmonic order, as shown by Equation (4.8) and Equation (4.9) respectively.

$$\vec{V}_{Lf}(h_n) = \vec{V}_X(h_n) - \vec{V}_{PCC}(h_n) \tag{4.8}$$

$$\vec{V}_{Lg}(h_n) = \vec{V}_{PCC}(h_n) - \vec{V}_G(h_n) \tag{4.9}$$

As current flowing through a branch is corresponding to the applied voltage and the effective impedance, output current of inverter bridge (I_X) at particular harmonic order is limited by filter inductance and corresponds to the voltage difference between inverter bridge and PCC, while output current of inverter system (I_O) at particular harmonic order is limited by grid inductance and corresponding to the voltage difference between PCC and the grid source, as shown in Equation (4.10) and Equation (4.11) respectively.

$$\vec{I}_X(h_n) = \frac{\vec{V}_{Lf}(h_n)}{\vec{Z}_{Lf}(h_n)} = \frac{\vec{V}_X(h_n) - \vec{V}_{PCC}(h_n)}{\vec{Z}_{Lf}(h_n)} \tag{4.10}$$

$$\vec{I}_O(h_n) = \frac{\vec{V}_{Lg}(h_n)}{\vec{Z}_{Lg}(h_n)} = \frac{\vec{V}_{PCC}(h_n) - \vec{V}_G(h_n)}{\vec{Z}_{Lg}(h_n)} \tag{4.11}$$

By substituting Equation (4.7) into Equation (4.10) and (4.11), the output current of inverter bridge and inverter system at particular harmonic order can be expressed as Equation (4.12) and Equation (4.13) respectively.

$$\vec{I}_X(h_n) = \frac{\vec{V}_X(h_n) - \vec{V}_G(h_n) + \vec{V}_X(h_n)\dfrac{\vec{Z}_{Lg}(h_n)}{\vec{Z}_{Cf}(h_n)}}{\vec{Z}_{Lf}(h_n) + \vec{Z}_{Lg}(h_n) + \dfrac{\vec{Z}_{Lf}(h_n)\vec{Z}_{Lg}(h_n)}{\vec{Z}_{Cf}(h_n)}} \tag{4.12}$$

$$\vec{I}_O(h_n) = \frac{\vec{V}_X(h_n) - \vec{V}_G(h_n) - \vec{V}_G(h_n)\dfrac{\vec{Z}_{Lf}(h_n)}{\vec{Z}_{Cf}(h_n)}}{\vec{Z}_{Lf}(h_n) + \vec{Z}_{Lg}(h_n) + \dfrac{\vec{Z}_{Lf}(h_n)\vec{Z}_{Lg}(h_n)}{\vec{Z}_{Cf}(h_n)}} \quad \textbf{(4.13)}$$

As shown by Equation (4.12) and (4.13), the inverter bridge output current (I_X) and inverter system output current (I_O) with respect to inverter bridge output voltage (V_X) and grid voltage (V_G) (which are function of PCC voltage (V_{PCC})), are attenuated by the combined effect of grid impedance (Z_{Lg}), filter inductive impedance (Z_{Lf}) and filter capacitive impedance (Z_{Cf}). Therefore, variation in grid voltage harmonic profile and grid impedance will in turn vary the vector of inverter system output current and thus affecting the output current harmonic profile and magnitude. Noted that the harmonic profile and magnitude of PCC voltage are affected by inverter bridge output voltage, grid voltage, as well as any load connected to the PCC.

To verify the model and mechanism of harmonic in the LCL network as discussed above, practical experiment is carried out in the laboratory. In the practical experiment, the experimental PI controlled current feedback inverter system is interfaced to a 43V rms background grid through 300μH of grid inductance, while 7A rms of inverter output current is injected into the grid. The waveforms of current and voltage in the experimental circuit are measured by Yokogawa® PZ4000 Power Analyser and then analysed by the FFT function in Matlab/Simulink®. Amongst the harmonic data of the waveforms obtained in FFT analysis, the harmonic data of background grid voltage and inverter bridge output voltage are substituted into Equation (4.7), Equation (4.12), and Equation (4.13) to calculate the harmonics of PCC voltage (V_{PCC}), inverter bridge output current (I_X), and inverter system output current (I_O) respectively. These harmonic data that obtained via mathematical calculation are then compared to the harmonic data that obtained via practical measurement in order to validate the proposed interaction equations (Equation (4.7), Equation (4.12), and Equation (4.13)), as shown by the harmonic magnitude and phase angle of PCC voltage (V_{PCC}), inverter bridge output current (I_X) and inverter system output current (I_O) in Figure 4.7, Figure 4.8 and Figure 4.9 respectively.

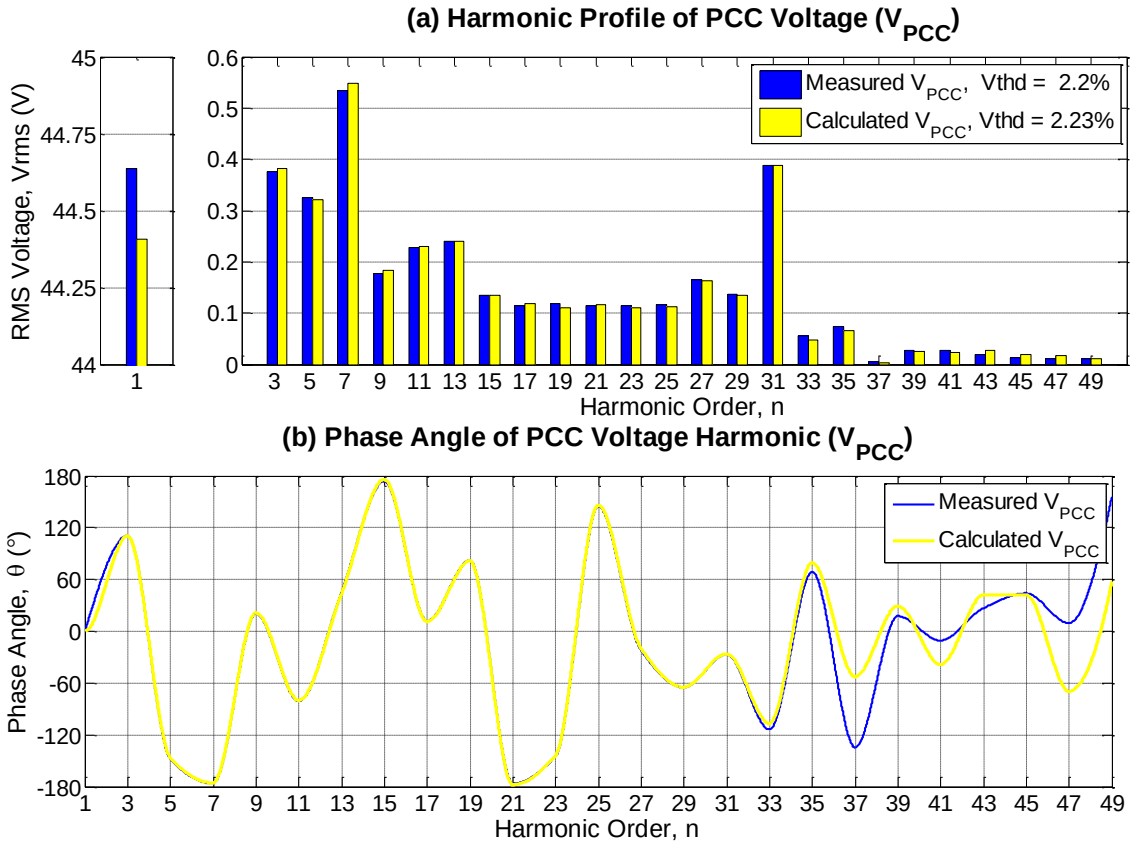

Figure 4.7 Comparison of measured and calculated PCC voltage (V_{PCC}) harmonic profile and harmonic phase angle.

(I_{demand} = 7A RMS, V_{DC} = 100V, V_G = 43.24V RMS, K_p = 1.1, K_i=0.6.)

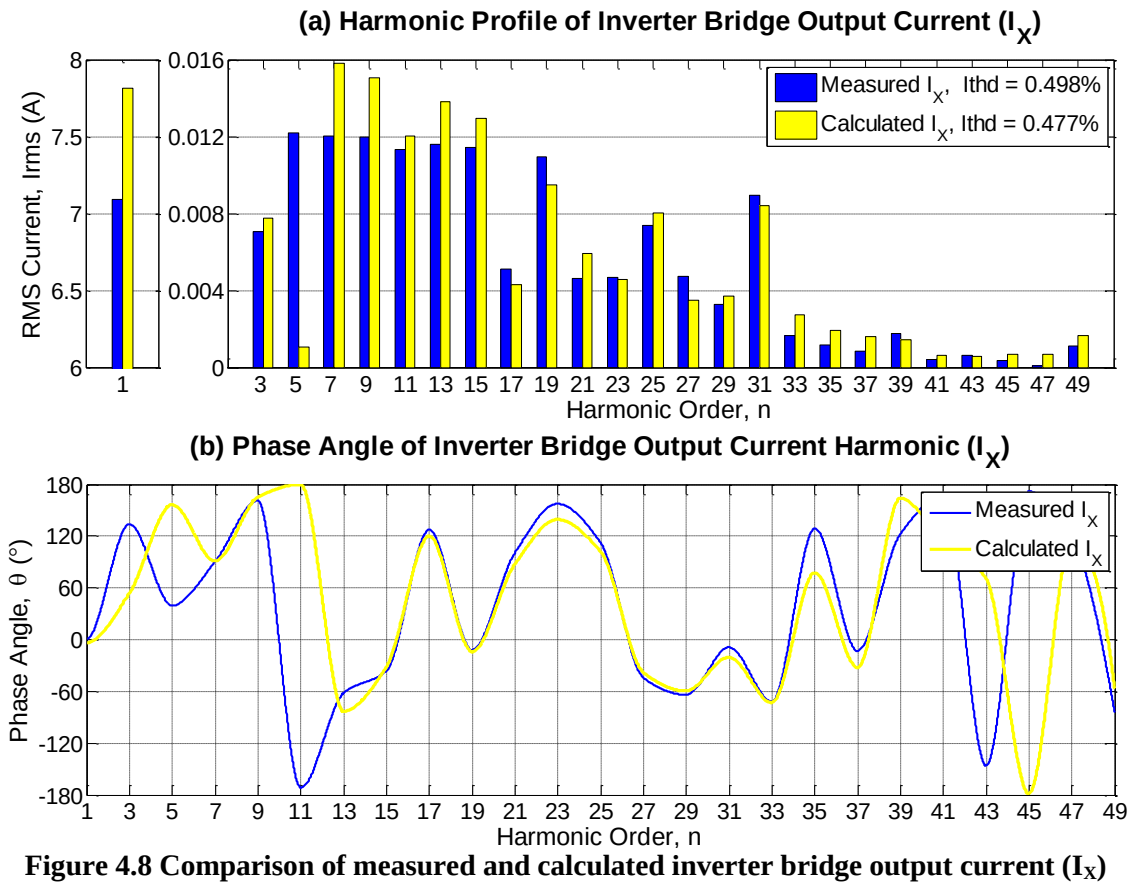

Figure 4.8 Comparison of measured and calculated inverter bridge output current (I_X) harmonic profile and harmonic phase angle.

(I_{demand} = 7A RMS, V_{DC} = 100V, V_G = 43.24V RMS, K_p = 1.1, K_i=0.6.)

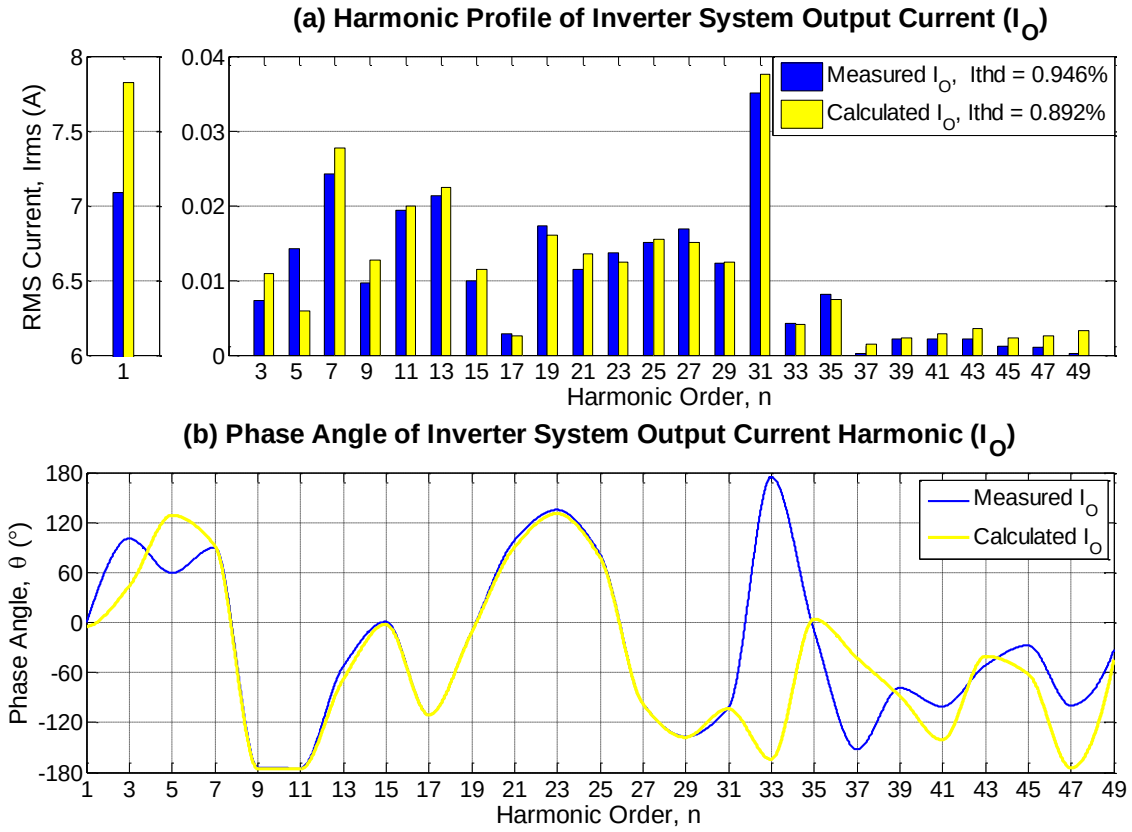

Figure 4.9 Comparison of measured and calculated inverter system output current (I_O) harmonic profile and harmonic phase angle.
(I_{demand} = 7A RMS, V_{DC} = 100V, V_G = 43.24V RMS, K_p = 1.1, K_i=0.6.)

As shown in the harmonic profile of PCC voltage (Figure 4.7(a)), inverter bridge output current (Figure 4.8(a)) and inverter system output current (Figure 4.9(a)), the magnitude of harmonic components in practical experiment is very close to the magnitude obtained from the calculation. Small variation between the magnitude of measured and calculated harmonic components may be due to the ESR of the inductor that, in practice, varies with frequency and has its own self-resonant frequency [64], which are neglected in the calculation. Likewise, the harmonic phase angle plot of PCC voltage (Figure 4.7(b)), inverter bridge output current (Figure 4.8(b)) and inverter system output current (Figure 4.9(b)) show that the calculated phase angle of harmonics are closed to the phase angle of harmonic obtained in practical measurement. It is noted that the deviation between measured and calculated phase angle is increased from 33rd harmonic due to the limitation in sampling frequency of the measurement equipment that loss the accuracy at high harmonic order. Besides that, the big different in measured and calculated phase angle of inverter bridge output current (11th and 45th in Figure 4.8(b)) and inverter system output current (33rd in Figure 4.9(b)) are due to wrapping effect of phase angle when the angle is beyond 180° and in fact the both angles are very close.

4.5 Interaction between Inverter System and Distribution Grid

4.5.1 *Relationship between Grid Impedance, PCC Voltage and Inverter System Output Current*

As the reactive component is frequency dependent, the capacitive impedance (Z_{Cf}) and inductive impedance (Z_{Lf}) of inverter filter, as well as grid impedance (Z_{Lg}) (shown in Figure 4.4) are varied over the range of frequencies, as shown in Figure 4.10. It shows that the magnitude of inverter filter capacitor (10μF) impedance is significant at low frequency range and decay exponentially at higher frequency, while the magnitude of inverter filter inductor (1.8μH) impedance and grid impedance (303μH) are tiny at low frequency and significantly increased at high frequency range.

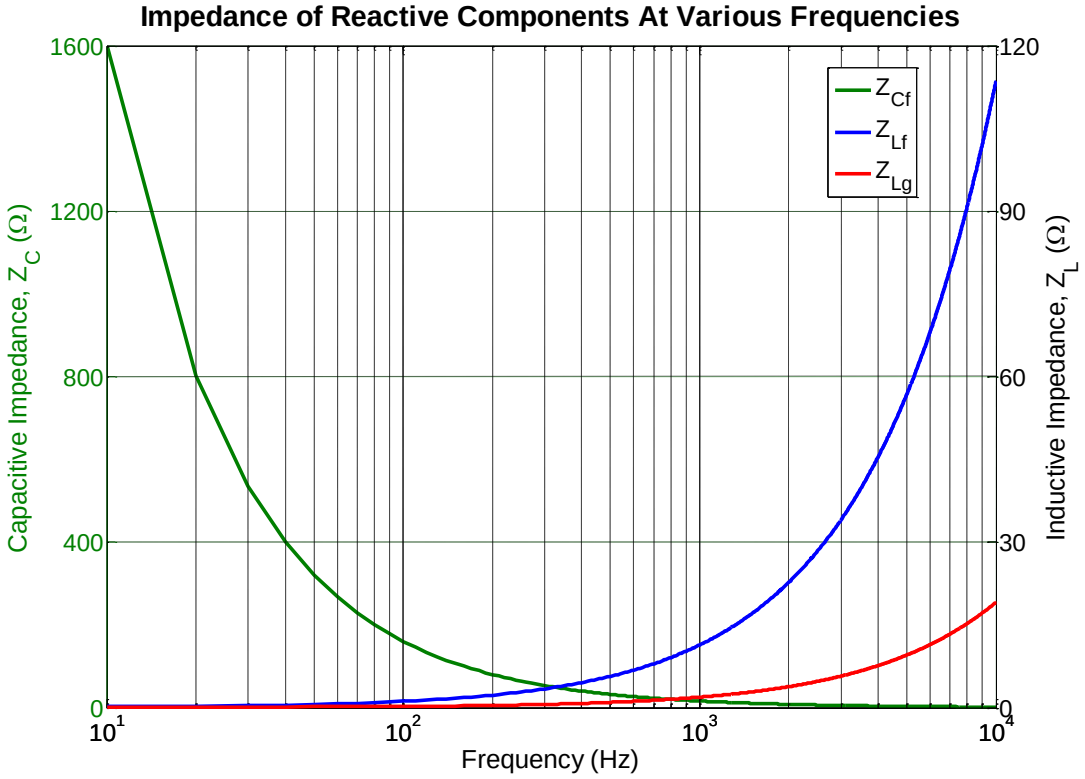

Figure 4.10 Variation of filter capacitive impedance (Z_{Cf}), filter inductive impedance (Z_{Lf}) and grid impedance (Z_{Lg}) over the range of frequencies.
(L_f = 1.8mH, C_f = 10μF, L_g = 303μH.)

In Equation (4.7), voltage at PCC is determined by the combined effect of inverter filter impedances (Z_{Lf} and Z_{Cf}) and grid impedance (Z_{Lg}). At low frequency range, high value of filter capacitor impedance will cause the term $\frac{\vec{Z}_{Lf}\vec{Z}_{Lg}}{\vec{Z}_{Cf}}$ in Equation (4.7) very much less than the term $\vec{Z}_{Lf} + \vec{Z}_{Lg}$, which in turn cause the voltage at PCC only determined by filter inductor impedance and grid impedance, yield Expression (4.14). At high

frequency range, low value of filter capacitor impedance will cause the term $\frac{\vec{Z}_{Lf}\vec{Z}_{Lg}}{\vec{Z}_{Cf}}$ in Equation (4.7) very much greater than the term $\vec{Z}_{Lf} + \vec{Z}_{Lg}$, which in turn cause the voltage at PCC to be determined by significant value of the term $\frac{\vec{Z}_{Lf}\vec{Z}_{Lg}}{\vec{Z}_{Cf}}$ and lead to low magnitude of PCC voltage as the capacitive impedance is tiny at high frequency, while the inductive impedance is significant, yield Expression (4.15).

At low frequency, $\frac{\vec{Z}_{Lf}\vec{Z}_{Lg}}{\vec{Z}_{Cf}} \ll \vec{Z}_{Lf} + \vec{Z}_{Lg}$, yield

$$\vec{V}_{PCC} = \frac{\vec{V}_X\vec{Z}_{Lg} + \vec{V}_G\vec{Z}_{Lf}}{\vec{Z}_{Lf} + \vec{Z}_{Lg}} \tag{4.14}$$

At high frequency, $\frac{\vec{Z}_{Lf}\vec{Z}_{Lg}}{\vec{Z}_{Cf}} \gg \vec{Z}_{Lf} + \vec{Z}_{Lg}$ and $\vec{Z}_{Lf}\vec{Z}_{Lg} \gg \vec{Z}_{Cf}$ yield

$$\vec{V}_{PCC} = \frac{\vec{V}_X\vec{Z}_{Lg} + \vec{V}_G\vec{Z}_{Lf}}{\frac{\vec{Z}_{Lf}\vec{Z}_{Lg}}{\vec{Z}_{Cf}}} = \frac{\vec{Z}_{Cf}\left(\vec{V}_X\vec{Z}_{Lg} + \vec{V}_G\vec{Z}_{Lf}\right)}{\vec{Z}_{Lf}\vec{Z}_{Lg}} \cong 0 \tag{4.15}$$

Likewise for the output current expression in Equation (4.13), high value of filter capacitive impedance at low frequency range will cause the term $\frac{\vec{Z}_{Lf}\vec{Z}_{Lg}}{\vec{Z}_{Cf}}$ in Equation (4.13) very much less than the term $\vec{Z}_{Lf} + \vec{Z}_{Lg}$, which in turn cause the output current of inverter system only attenuated by filter inductive impedance and grid impedance, yield Expression (4.16). At high frequency range, low value of filter capacitor impedance will cause the term $\frac{\vec{Z}_{Lf}\vec{Z}_{Lg}}{\vec{Z}_{Cf}}$ in Equation (4.13) very much greater than the term $\vec{Z}_{Lf} + \vec{Z}_{Lg}$, which in turn cause the output current of inverter system to be attenuated by significant value of the term $\frac{\vec{Z}_{Lf}\vec{Z}_{Lg}}{\vec{Z}_{Cf}}$ and lead to low magnitude of inverter system output current as the capacitive impedance is small at high frequency, while inductive impedance is significant, yield Expression (4.17).

At low frequency, $\frac{\vec{Z}_{Lf}\vec{Z}_{Lg}}{\vec{Z}_{Cf}} \ll \vec{Z}_{Lf} + \vec{Z}_{Lg}$ and $\frac{\vec{Z}_{Lf}}{\vec{Z}_{Cf}} \cong 0$ yield

$$\vec{I}_O = \frac{\vec{V}_X - \vec{V}_G}{\vec{Z}_{Lf} + \vec{Z}_{Lg}} \tag{4.16}$$

At high frequency, $\frac{\vec{Z}_{Lf}\vec{Z}_{Lg}}{\vec{Z}_{Cf}} \gg \vec{Z}_{Lf} + \vec{Z}_{Lg}$ and $\vec{Z}_{Lf}\vec{Z}_{Lg} \gg \vec{Z}_{Cf}$ yield

$$\vec{I}_O = \frac{\vec{V}_X - \vec{V}_G - \vec{V}_G \frac{\vec{Z}_{Lf}}{\vec{Z}_{Cf}}}{\frac{\vec{Z}_{Lf}\vec{Z}_{Lg}}{\vec{Z}_{Cf}}} = \frac{\vec{Z}_{Cf}(\vec{V}_X - \vec{V}_G) - \vec{V}_G\vec{Z}_{Lf}}{\vec{Z}_{Lf}\vec{Z}_{Lg}} \cong 0 \quad \textbf{(4.17)}$$

4.5.2 *Effect of Grid Impedance on Fundamental PCC Voltage and Inverter System Output Current*

The voltage level at PCC depends upon the stiffness of the distribution grid that affected by the upstream conditions (e.g. supply transformer impedance at source substation and cabling circuit impedances) and the loading conditions at PCC (e.g. type, capacity and impedance of electrical devices connected at PCC). Although the stiffness of the grid is affected by so many factors, the stiff grid is reflected by lower value of grid inductance (L_g) and vice-versa for the weak grid [80].

The voltage at PCC (V_{PCC}) can be approximated as shown by Equation (4.7). However, at low frequency ranges, the voltage at PCC is approximated by Equation (4.14). For a stiff grid, the low value of L_g causes the effect of the terms $\vec{Z}_{Lg}$ and $\vec{V}_X\vec{Z}_{Lg}$ in Equation (4.14) to be negligible hence $\vec{V}_{PCC}$ is dependent on the term $\vec{V}_G\vec{Z}_{Lf}$ and determined by $\vec{Z}_{Lf}$ only. For a weak grid, L_g is competitive with the filter inductance (L_f) of inverter system. The effect of the term $\vec{V}_X\vec{Z}_{Lg}$ on $\vec{V}_{PCC}$ in Equation (4.14) must be included with the effect of the term $\vec{V}_G\vec{Z}_{Lf}$, and $\vec{V}_{PCC}$ is determined by both $\vec{Z}_{Lf}$ and $\vec{Z}_{Lg}$. Therefore, the voltage level and voltage harmonic profile at PCC of the weak grid is more vulnerable to the impact of inverter system than in the stiff grid at fundamental frequency.

At high frequency ranges, the voltage at PCC is approximated as shown in Equation (4.15). It shows that low value of L_g in stiff grid suppresses the term $\vec{Z}_{Lf}\vec{Z}_{Lg}$ with increasing frequency. As the term $\vec{Z}_{Cf}\vec{V}_X\vec{Z}_{Lg}$ is negligible due to the low value of L_g, $\vec{V}_{PCC}$ is dependent on the term $\vec{Z}_{Cf}\vec{V}_G\vec{Z}_{Lf}$ and determined by the term $\vec{Z}_{Lf}\vec{Z}_{Lg}$. For a weak grid, $\vec{V}_{PCC}$ relies on both the terms $\vec{Z}_{Cf}\vec{V}_X\vec{Z}_{Lg}$ and $\vec{Z}_{Cf}\vec{V}_G\vec{Z}_{Lf}$, while attenuated by the term $\vec{Z}_{Lf}\vec{Z}_{Lg}$.

Figure 4.11 shows the RMS magnitude of the voltage at PCC for stiff grid (with 100µH of L_g) and weak grid (with 700µH of L_g) over a range of frequencies when 43V RMS and 46V RMS of 50Hz fundamental background grid voltage and inverter bridge output voltage are substituted into Equation (4.7) respectively. These values of voltage are taken directly from measurements obtained from the practical experimental hardware. The figure shows that the magnitude of the voltage at PCC for weak grid is slightly higher than stiff grid over the low frequency range (lower than 100 Hz) due to higher values of grid impedance. The voltage at PCC of both the weak grid and stiff grid then start to attenuate around the parallel resonant frequency of the LCL branch at approximately 1.009 kHz and 1.157 kHz respectively. This is reflected in the value of the term $\vec{Z}_{Lf}\vec{Z}_{Lg}$ in Equation (4.7). The voltage at PCC of weak grid is determined by the high value of the term $\vec{Z}_{Lf}\vec{Z}_{Lg}$, while low value of L_g in stiff grid suppresses this term leading to lower attenuation.

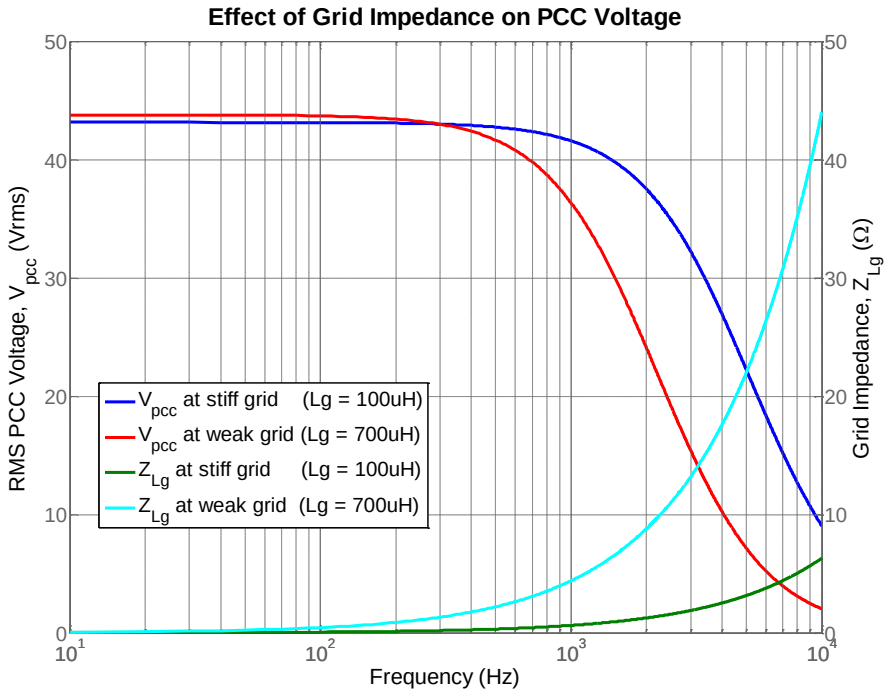

Figure 4.11 Effect of grid impedance on PCC voltage over range of frequencies.
(V_G = 43V RMS, V_X = 46V RMS.)

The output current of inverter system (I_O) can be approximated as shown by Equation (4.13). At low frequency, the inverter system output current is approximated as shown in Equation (4.16). In this equation, the inverter system output current term $\vec{I}_O$ corresponds to the difference between the inverter bridge output voltage ($\vec{V}_X$) and the background grid voltage ($\vec{V}_G$), and attenuated by $\vec{Z}_{Lf}$ in a stiff grid (L_g is negligible), or attenuated by both $\vec{Z}_{Lf}$ and $\vec{Z}_{Lg}$ in a weak grid (L_g becomes more competitive with L_f).

Figure 4.12 shows the RMS magnitude of the inverter system output current for stiff grid (with 100μH of L_g) and weak grid (with 700μH of L_g) over range of frequencies, when 43V RMS and 46V RMS of 50Hz fundamental background grid voltage and inverter bridge output voltage are substituted into Equation (4.13) respectively. Again, these values of voltage are taken directly from measurements obtained from the practical experimental hardware. It shows that the magnitude of inverter system output current in stiff grid is higher than output current in weak grid at low frequency range due to lower grid impedance. This imply that for the same value of fundamental background grid voltage, the controller of the inverter system has to create higher value of fundamental inverter bridge output voltage in weak grid in order to inject same amount of the fundamental current into the grid as in stiff grid. If the DC link voltage of the inverter system connected to weak grid and stiff grid are the same magnitude, then the controllability margin of the inverter system digital controller in weak grid is less than in stiff grid due to higher transformation ratio of DC to AC conversion for higher magnitude in fundamental inverter bridge output voltage required by weak grid.

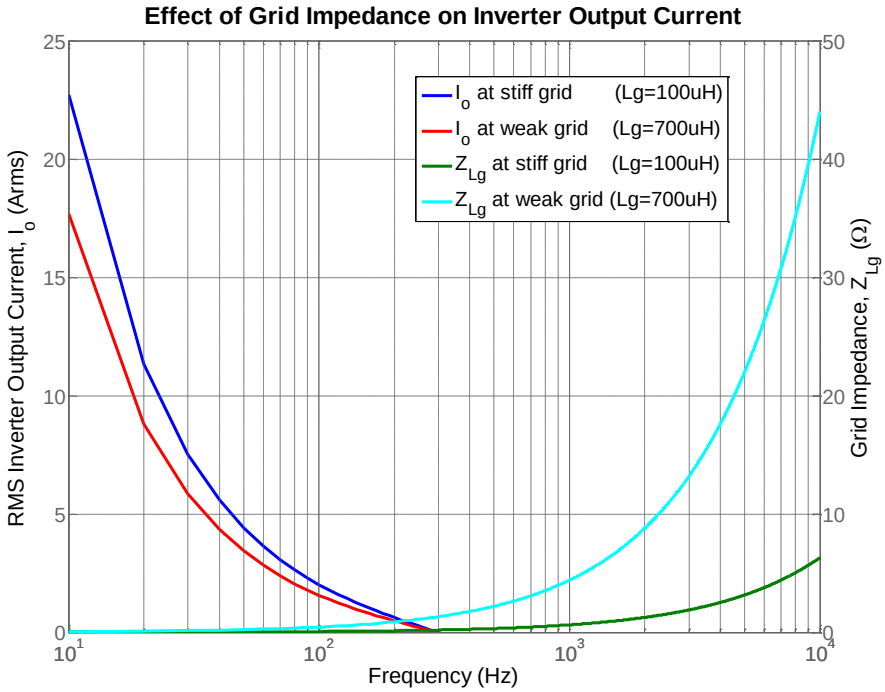

Figure 4.12 Effect of grid impedance on the fundamental inverter system output current over range of frequencies.
(V_G = 43V RMS, V_X = 46V RMS.)

To investigate the frequency response of the inverter output current at LCL branch as shown in Figure 4.6, the transfer function model of LCL branch need to be used. Equation (4.18) shows the function of the LCL branch obtained in Section 2.2.1. It can be manipulated to obtain the open loop transfer function of LCL branch as shown in

Transfer Function (4.19), where $^{V_G(s)}/_{V_X(s)}$ term can be treated as disturbance to the system.

$$\frac{I_O(s)}{V_X(s)(R_{Cf}C_fs+1)-V_G(s)[C_fL_fs^2+C_f(R_{Cf}+R_{Lf})s+1]} = \frac{1}{C_fL_fL_gs^3+C_f[L_g(R_{Cf}+R_{Lf})+L_f(R_{Cf}+R_g)]s^2+[L_g+L_f+C_f(R_gR_{Cf}+R_{Lf}R_{Cf}+R_{Lf}R_g)]s+(R_g+R_{Lf})} \quad \textbf{(4.18)}$$

$$G_{OL-LCL}(s)=\frac{I_O(s)}{V_X(s)} = \frac{(R_{Cf}C_fs+1)-\frac{V_G(s)}{V_X(s)}[C_fL_fs^2+C_f(R_{Cf}+R_{Lf})s+1]}{C_fL_fL_gs^3+C_f[L_g(R_{Cf}+R_{Lf})+L_f(R_{Cf}+R_g)]s^2+[L_g+L_f+C_f(R_gR_{Cf}+R_{Lf}R_{Cf}+R_{Lf}R_g)]s+(R_g+R_{Lf})} \quad \textbf{(4.19)}$$

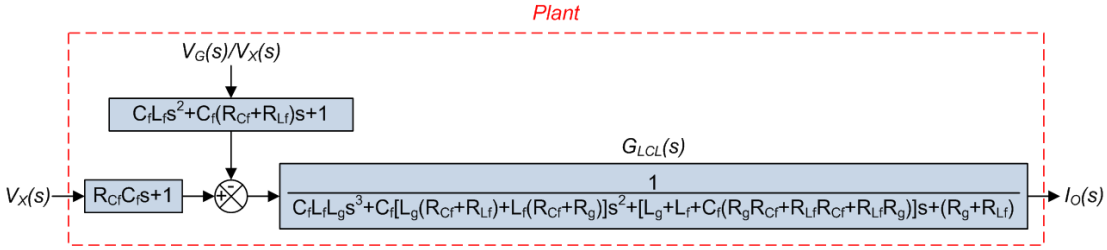

Figure 4.13 Open loop block diagram of LCL branch

Figure 4.13 shows the block diagram of the open loop LCL transfer function given by Transfer Function (4.19). As shown in the figure that the only output of the system is affected by two of its inputs, this will form the system into a Multi Input Single Output (MISO) system that gives two transfer function responses that corresponding to particular input, which are the open loop response when the disturbance ($^{V_G(s)}/_{V_X(s)}$) is zero, as shown by Transfer Function (4.20), and open loop response when the system input ($V_X(s)$) is zero, as shown by Transfer Function (4.21).

$$G_{OL-LCL}(s)|_{\frac{V_G(s)}{V_X(s)}=0} = \left.\frac{I_O(s)}{V_X(s)}\right|_{\frac{V_G(s)}{V_X(s)}=0} = \frac{(R_{Cf}C_fs+1)}{C_fL_fL_gs^3+C_f[L_g(R_{Cf}+R_{Lf})+L_f(R_{Cf}+R_g)]s^2+[L_g+L_f+C_f(R_gR_{Cf}+R_{Lf}R_{Cf}+R_{Lf}R_g)]s+(R_g+R_{Lf})} \quad \textbf{(4.20)}$$

$$G_{OL-LCL}(s)|_{V_X(s)=0} = \left.\frac{I_O(s)}{V_X(s)}\right|_{V_X(s)=0} = \frac{-\frac{V_G(s)}{V_X(s)}[C_fL_fs^2+C_f(R_{Cf}+R_{Lf})s+1]}{C_fL_fL_gs^3+C_f[L_g(R_{Cf}+R_{Lf})+L_f(R_{Cf}+R_g)]s^2+[L_g+L_f+C_f(R_gR_{Cf}+R_{Lf}R_{Cf}+R_{Lf}R_g)]s+(R_g+R_{Lf})} \quad \textbf{(4.21)}$$

Hence, to analyse the combined effect of the command and disturbance response, Transfer Function (4.19) must be used as the model of the system. The analysis can be

simplified by substituting the term $^{V_G(s)}/_{V_X(s)}$ by a fixed input-output voltage ratio when the inverter output current ($I_O(s)$) is assumed constant. The frequency response of inverter output current gain with respect to inverter bridge output voltage for given input-output voltage ratio current can then be obtained by Bode plot.

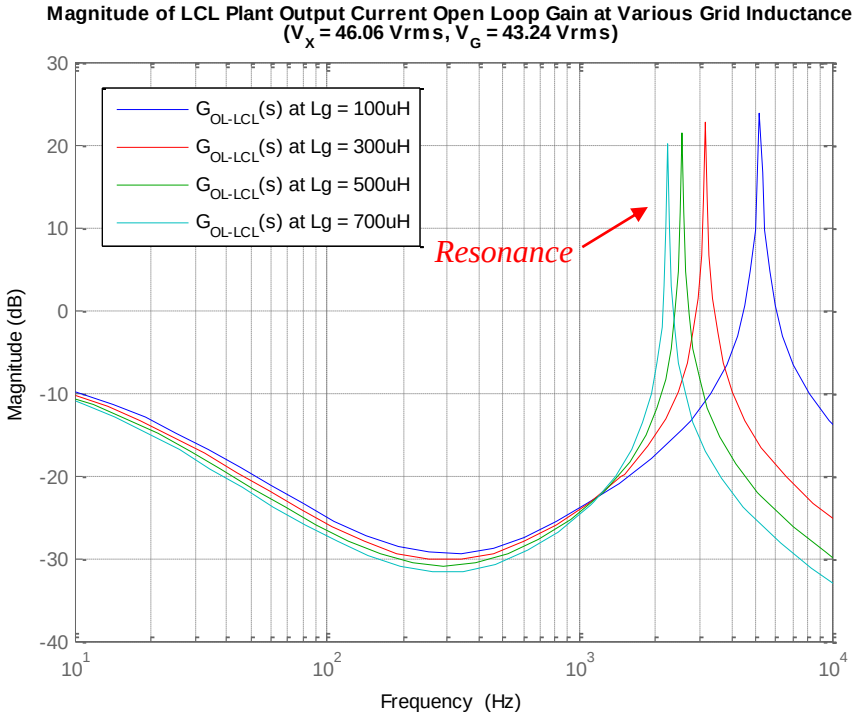

Figure 4.14 Open loop frequency response of LCL branch inverter output current gain at various grid inductances.

(V_X = 46.06V RMS, V_G = 43.24V RMS, L_f = 1.8mH, C_f = 10μF.)

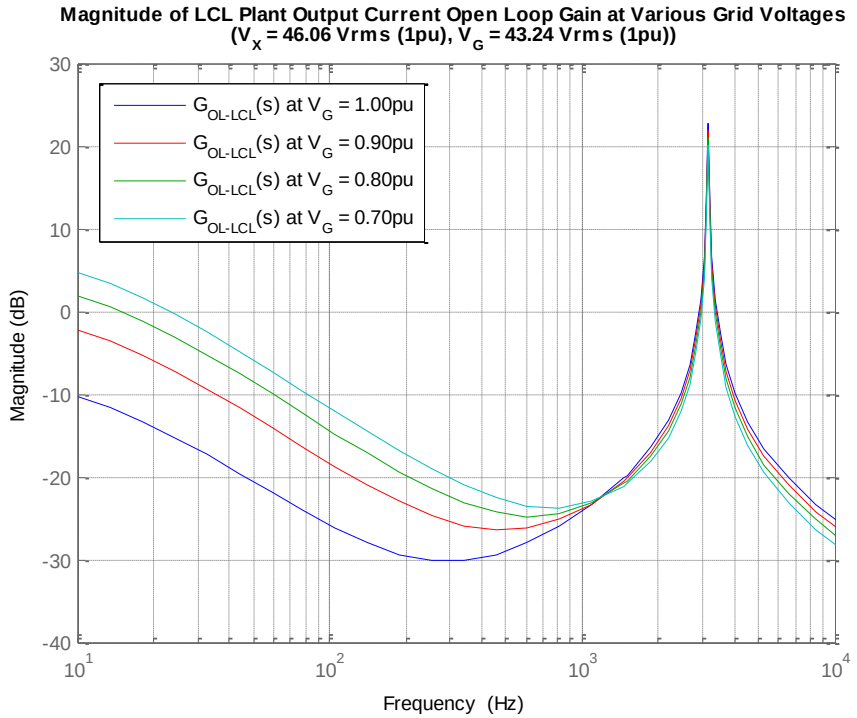

Figure 4.15 Open loop frequency response of LCL branch inverter output current gain at various background grid voltages.

(V_X = 46.06V RMS, V_G = 43.24V RMS, L_f = 1.8mH, C_f = 10μF, L_g = 300μH.)

Figure 4.14 and Figure 4.15 show the open loop frequency response of inverter output current gain of LCL branch at various grid inductances and background grid voltage respectively. As shown in Figure 4.14, increase in grid inductance caused more attenuation on inverter output current gain at low frequency range (>1 kHz), and shifted the resonant peak of LCL branch to the lower frequency significantly. In Figure 4.15, variation in background grid voltage magnitude does not affect the resonant frequency of LCL branch, but the inverter output current gain is inversely proportional to the magnitude of background grid voltage at low frequency range (<1 kHz), and directly proportional to the magnitude of background grid voltage at frequency higher than resonant point. Note that the detail discussion of resonance phenomenon is presented in Chapter 5.

4.5.3 *Effect of Grid Conditions on the Current Control Loop of Inverter System*

Most of the grid-connected inverters employ the current feedback controller to control the current inject into distribution grid. These inverter systems measure the current injected into the grid and feeding it back into the Proportional-Integral (PI) control loop of the digital controller. As the grid inductance and voltage magnitude are dependent on the operating condition of distribution grid which change over time, the variation in grid inductance and background grid voltage magnitude can affect the output current gain of PI controller. To investigate the grid inductance effect on output current gain, model of grid-connected inverter system based on the cascaded transfer function at each part of the system is developed. Figure 4.16 shows the block diagram of continuous system model with current feedback PI control. Detailed discussion on modelling of the individual block is presented in Section 2.2.

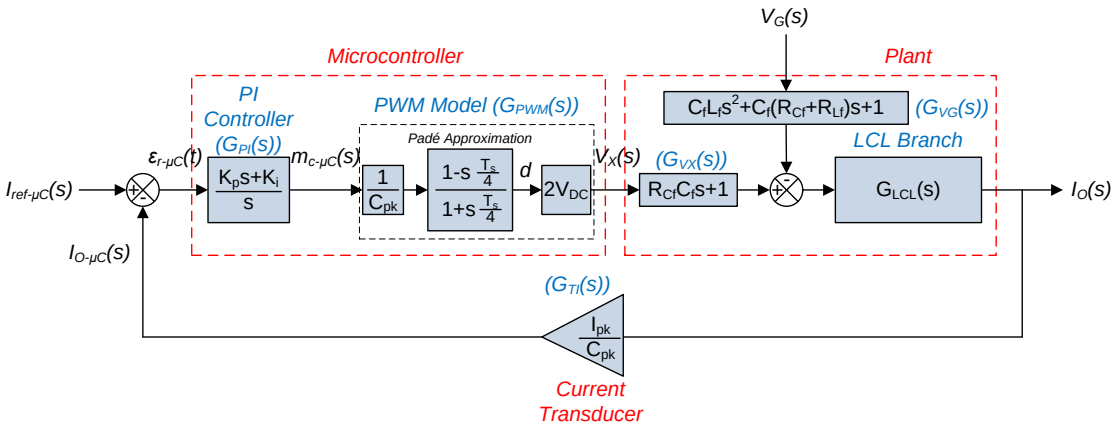

Figure 4.16 Model of grid-connected inverter system with current feedback PI control.

As shown in Figure 4.16, the inverter system output current ($I_O(s)$) is dictated by two inputs, which are the microcontroller reference current ($I_{ref\text{-}\mu C}(s)$), and the background grid voltage ($V_G(s)$) that can be treated as disturbance to the system. Similar to the transfer function for LCL branch discussed in Section 4.5.2, this forms the system into a MISO system that gives two transfer function responses that corresponding to its particular input, which are the command response when the disturbance ($V_G(s)$) is zero, as shown by Transfer Function (4.22), and disturbance response when the demand input ($I_{ref\text{-}\mu C}(s)$) is zero, as shown by Transfer Function (4.24).

By setting $V_G(s) = 0$,

$$I_{O-\mu C}(s) = \left[I_{ref-\mu C}(s) - I_{O-\mu C}(s)\right] G_{PI}(s) G_{PWM}(s) G_{VX}(s) G_{LCL}(s) G_{TI}(s)$$

$$I_{O-\mu C}(s) = I_{ref-\mu C}(s) G_{PI}(s) G_{PWM}(s) G_{VX}(s) G_{LCL}(s) G_{TI}(s) - I_{O-\mu C}(s) G_{PI}(s) G_{PWM}(s) G_{VX}(s) G_{LCL}(s) G_{TI}(s)$$

$$I_{O-\mu C}(s)[1 + G_{PI}(s) G_{PWM}(s) G_{VX}(s) G_{LCL}(s) G_{TI}(s)] = I_{ref-\mu C}(s) G_{PI}(s) G_{PWM}(s) G_{VX}(s) G_{LCL}(s) G_{TI}(s)$$

$$G_{Command}(s) = \left.\frac{I_{O-\mu C}(s)}{I_{ref-\mu C}(s)}\right|_{V_G(s)=0} = \frac{G_{PI}(s) G_{PWM}(s) G_{VX}(s) G_{LCL}(s) G_{TI}(s)}{1 + G_{PI}(s) G_{PWM}(s) G_{VX}(s) G_{LCL}(s) G_{TI}(s)} \quad \textbf{(4.22)}$$

By re-arranging Transfer Function (4.22),

$$I_{O-\mu C}(s)\big|_{V_G(s)=0} = I_{ref-\mu C}(s) \frac{G_{PI}(s) G_{PWM}(s) G_{VX}(s) G_{LCL}(s) G_{TI}(s)}{1 + G_{PI}(s) G_{PWM}(s) G_{VX}(s) G_{LCL}(s) G_{TI}(s)} \quad \textbf{(4.23)}$$

By setting $I_{ref-\mu C}(s) = 0$,

$$I_{O-\mu C}(s) = \left\{I_{O-\mu C}(s)[-G_{PI}(s) G_{PWM}(s) G_{VX}(s)] - V_G(s) G_{VG}(s)\right\} G_{LCL}(s) G_{TI}(s)$$

$$I_{O-\mu C}(s) = -I_{O-\mu C}(s) G_{PI}(s) G_{PWM}(s) G_{VX}(s) G_{LCL}(s) G_{TI}(s) - V_G(s) G_{VG}(s) G_{LCL}(s) G_{TI}(s)$$

$$I_{O-\mu C}(s)[1 + G_{PI}(s) G_{PWM}(s) G_{VX}(s) G_{LCL}(s) G_{TI}(s)] = -V_G(s) G_{VG}(s) G_{LCL}(s) G_{TI}(s)$$

$$G_{Disturbance}(s) = \left.\frac{I_{O-\mu C}(s)}{V_G(s)}\right|_{I_{ref-\mu C}(s)=0} = -\frac{G_{VG}(s) G_{LCL}(s) G_{TI}(s)}{1 + G_{PI}(s) G_{PWM}(s) G_{VX}(s) G_{LCL}(s) G_{TI}(s)} \quad \textbf{(4.24)}$$

By re-arranging Transfer function (4.24),

$$I_{O-\mu C}(s)\big|_{I_{ref-\mu C}(s)=0} = -V_G(s) \frac{G_{VG}(s) G_{LCL}(s) G_{TI}(s)}{1 + G_{PI}(s) G_{PWM}(s) G_{VX}(s) G_{LCL}(s) G_{TI}(s)} \quad \textbf{(4.25)}$$

By re-arranging Transfer function (4.22) and Transfer Function (4.24), the output current of the inverter system in microcontroller domain ($I_{O\text{-}\mu C}(s)$) that corresponding to command response and disturbance response can be obtained, as shown by Expression (4.23) and Expression (4.25) respectively. The overall closed loop response of the inverter system, expressed as the relationship between the inverter output current and

current demand in microcontroller domain, can then be obtained by adding Expression (4.23) and Expression (4.25), given the Closed Loop Response (4.26).

By adding Expression (4.23) and Expression (4.25),

$$I_{O-\mu C}(s) = I_{O-\mu C}(s)\big|_{V_G(s)=0} + I_{O-\mu C}(s)\big|_{I_{ref-\mu C}(s)=0}$$

$$I_{O-\mu C}(s) = I_{ref-\mu C}(s)\frac{G_{PI}(s)G_{PWM}(s)G_{VX}(s)G_{LCL}(s)G_{TI}(s)}{1+G_{PI}(s)G_{PWM}(s)G_{VX}(s)G_{LCL}(s)G_{TI}(s)} - V_G(s)\frac{G_{VG}(s)G_{LCL}(s)G_{TI}(s)}{1+G_{PI}(s)G_{PWM}(s)G_{VX}(s)G_{LCL}(s)G_{TI}(s)}$$

$$I_{O-\mu C}(s) = I_{ref-\mu C}(s)\left[\frac{G_{PI}(s)G_{PWM}(s)G_{VX}(s)G_{LCL}(s)G_{TI}(s)}{1+G_{PI}(s)G_{PWM}(s)G_{VX}(s)G_{LCL}(s)G_{TI}(s)} - \frac{\left[\frac{V_G(s)}{I_{ref-\mu C}(s)}\right]G_{VG}(s)G_{LCL}(s)G_{TI}(s)}{1+G_{PI}(s)G_{PWM}(s)G_{VX}(s)G_{LCL}(s)G_{TI}(s)}\right]$$

$$G_{CL}(s) = \frac{I_{O-\mu C}(s)}{I_{ref-\mu C}(s)} = \frac{G_{PI}(s)G_{PWM}(s)G_{VX}(s)G_{LCL}(s)G_{TI}(s) - \left[\frac{V_G(s)}{I_{ref-\mu C}(s)}\right]G_{VG}(s)G_{LCL}(s)G_{TI}(s)}{1+G_{PI}(s)G_{PWM}(s)G_{VX}(s)G_{LCL}(s)G_{TI}(s)} \quad \textbf{(4.26)}$$

The closed loop frequency responses of discrete controller output current gain at various grid inductances and background grid voltage magnitude are shown in Figure 4.17 and Figure 4.18 respectively. As shown in Figure 4.17, higher value of grid inductances give more attenuation on the current gain at low frequency range (lower than 1 kHz). At fundamental frequency, the discrete control loop requires higher closed loop gain for higher grid inductance in order to inject the same amount of current into distribution grid as for low grid inductance. Moreover, higher value of grid inductance shifts the resonant peak of controller output current gain to lower frequency, as shown by the red arrow in Figure 4.17. Resonance at lower frequency will cause the lower frequency oscillation that will affect the stability of the current control loop, zero crossing detection and hence the power quality of the inverter system, detailed discussion of resonance phenomenon is presented in Chapter 5. In Figure 4.18, the controller output current gain at low frequency range (lower than 1 kHz) does not affect by variation in background grid voltage magnitude, as the feedback control loop is controlling its command response to cope with the change in background grid voltage magnitude.

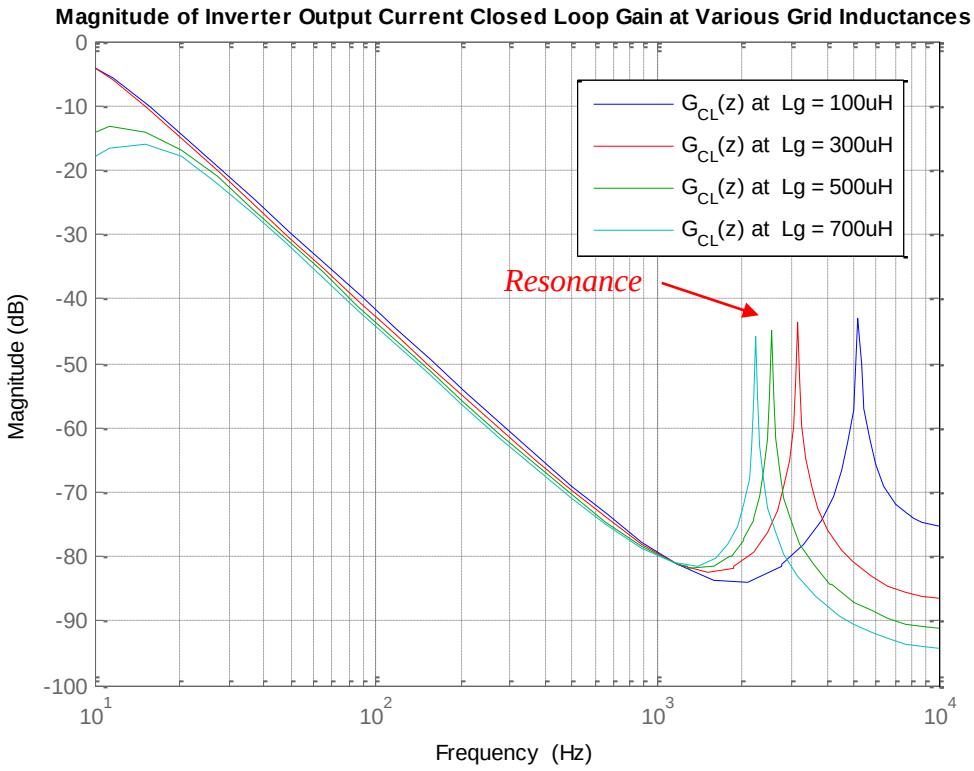

Figure 4.17 Closed loop frequency response of discrete controller output current gain at various grid inductances.

(V_{DC} = 100V, V_G = 43.24V RMS, L_f = 1.8mH, C_f = 10µF, K_p = 1.1, K_i = 0.6, T_s = 50µs.)

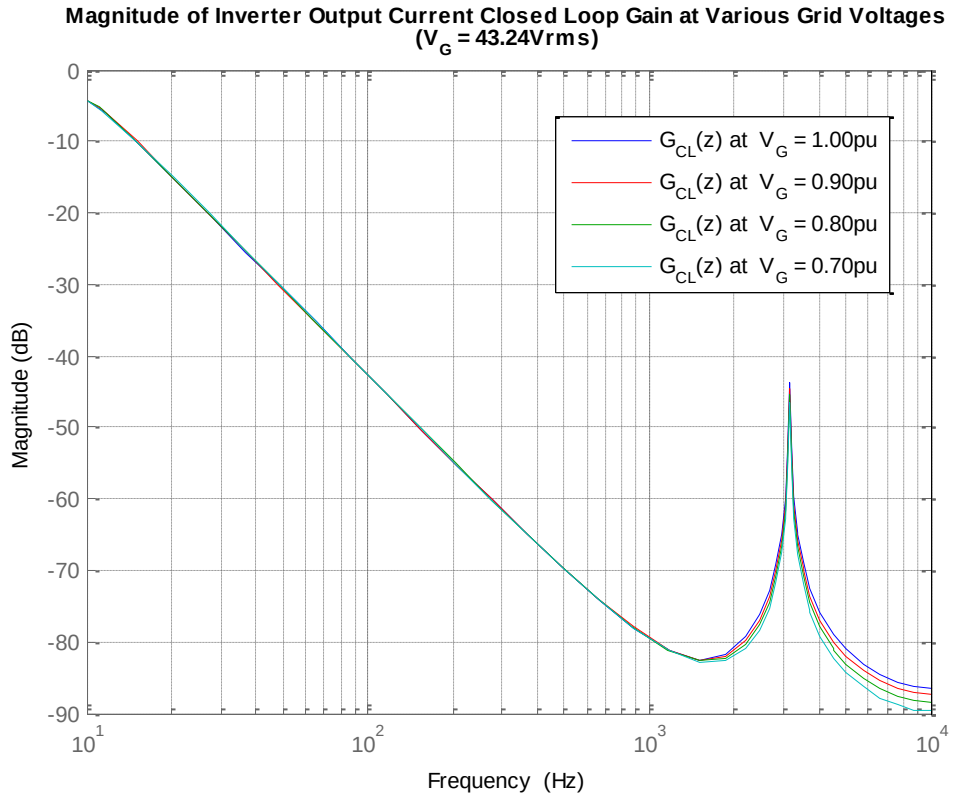

Figure 4.18 Closed loop frequency response of discrete controller output current gain at various background grid voltages.

(V_{DC} = 100V, V_G = 43.24V RMS, L_f = 1.8mH, C_f = 10µF, K_p = 1.1, K_i = 0.6, T_s = 50µs.)

4.6 Effects of Grid Operating Conditions on the Harmonic Performance of Inverter System Output Current

Unwanted interactions arise when power electronic inverters are connected to the distribution network. It has been shown that grid-connected PV inverters affect the operating condition of the distribution grid under certain circumstances. Verhoeven [10] suggested that harmonic currents injected into the distribution grid by PV inverters will affect the power quality of the distribution grid; and in areas of high PV system penetration, potentially may cause unwanted islanding. It is also known that the harmonic currents generated by PV inverters can cause malfunctioning of grid side protection devices [11]. Further problems, such as local voltage rise and network voltage fluctuations, are mentioned by Povlsen [12], Hacker, Thornycroft, et al. [13] and Canova, Spertino, et al. [14].

Despite of the distribution grid is affected by power electronic inverter, the operating conditions of the grid can contrary have an impact on the performance of the grid-connected inverter system. Simmons and Infield [15] demonstrated an increase in current total harmonic distortion (THD) at the output of a grid-connected inverter, and linked this to the distortion present in the grid voltage waveform. It was also suggested that the current waveform is more sinusoidal at increasing power levels, due to the finite resolution and discretisation of the ADC devices used for current measurement. As the number of grid-connected installations continues to increase, the effect of these interactions is likely to be magnified.

The current control performance of a grid-connected inverter is sensitive to grid operating conditions; such as the power quality and phase angle of the grid voltage waveform, and the grid impedance. These conditions vary continuously, which makes it difficult to ensure the inverter system is tuned for optimum performance over long periods of time. It has been shown in Section 4.3 and Figure 4.5 of this chapter that the output current of inverter system is affected by the variation in grid operating condition over time. The linearity and zero crossing interference of harmonic current and voltage between the distribution grid and linear/non-linear load were explained by Cobben [81], while Bosman, Cobben, et al. [82] suggest the linearity and frequency decoupling behaviour of interaction between the distribution grid and solar inverter.

An additional issue is the occurrence of resonance between the distribution grid and the PV inverter [16]. Resonance occurs over a narrow frequency range and lead to significant harmonics to be produced when the grid impedance is coupled to the grid-connected inverter system impedance. The detail of resonance phenomenon is discussed in Chapter 5.

To assess the effect of grid operating conditions on the harmonic performance of inverter system output current, a constant background grid voltage with tuneable magnitude and phase angle for specific harmonic components is essential. The practical test of interaction between the inverter system and the grid utilising programmable grid simulator is demonstrated by Heskes and Enslin [83]. However, as AC voltage source that is able to sink the current is not available in the laboratory and the voltage of distribution grid in real-life practically vary over time, the assessment involving the effect of variation in distribution grid operating condition on the harmonic performance of grid-connected inverter system is carried out through simulation in Matlab/Simulink®. A high fidelity simulation models of grid-connected PV inverter system and distribution grid in Matlab/Simulink®, as discussed in Section 2.3, is recalled in Figure 4.19. To simulate the system response which is very close to real-life, signal based Simulink® and electrical based SimPower blocks are utilised in the system models. For the high fidelity of the model, the real-life value of passive components that measured by Fluke© PM6304 RCL Meter is employed in the simulation, while the background grid voltage model is built based on the background grid voltage harmonic data (magnitude and phase angle of harmonics up to 50^{th}) that measured by Yokogawa® PZ4000 Power Analyser in practical test and analysed by FFT function in Matlab/Simulink®.

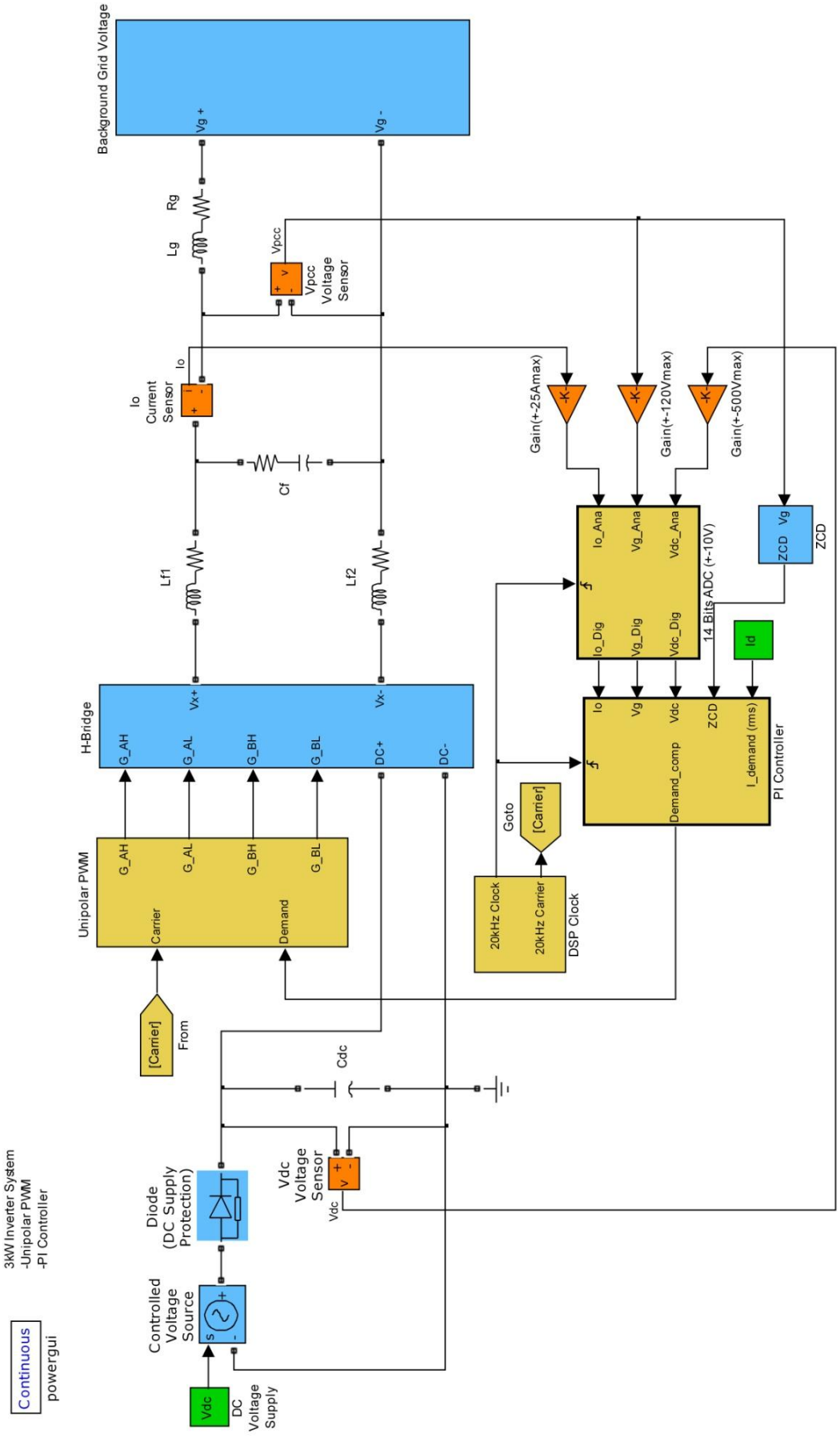

Figure 4.19 Simulation model of grid-connected PV inverter system and distribution grid.

The simulation model is verified by comparing the simulation result to the practical measurement. Figure 4.20 shows the comparisons of PCC voltage and inverter system output current harmonic profile in practical and simulation respectively. As shown in Figure 4.20(a) that harmonic profile of PCC voltage in simulation is very close to the PCC voltage harmonic profile in practical. In Figure 4.20(b) the inverter system output current harmonic profile in simulation has higher harmonic magnitude than in experimental data. This is due to the damping effect of parasitic impedance in practical experiment which is very difficult to include in simulation, such as the ESR of the filter inductor and inductor used to simulate the grid impedance. In real-life, the inductor ESR varies with frequency and has its own self-resonant frequency (Bartoli, Reatti, et al. [64]). However, the harmonic profile of inverter system output current in simulation still give the similar trend to the harmonic profile in practical.

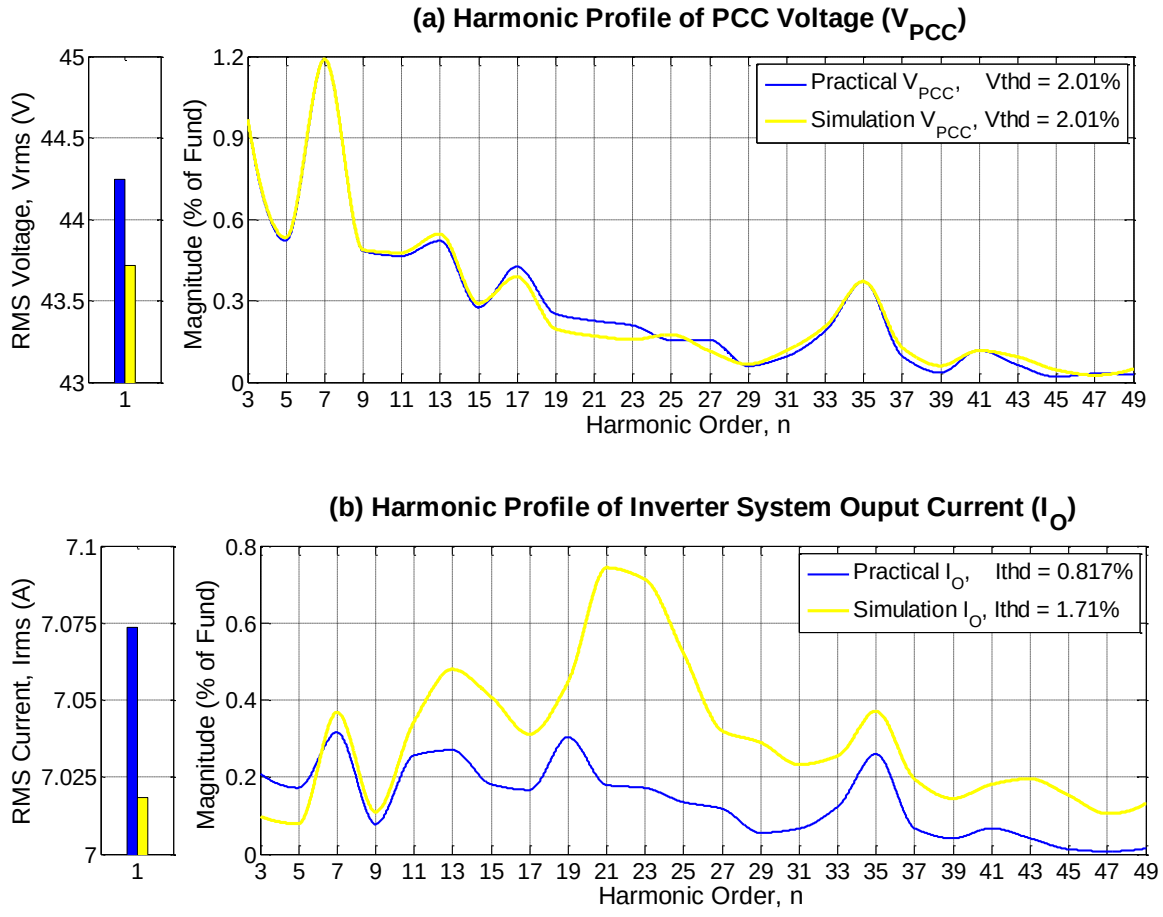

Figure 4.20 Comparisons of harmonic profile in practical experiment and simulation, for PCC voltage (V_{PCC}) and inverter system output current (I_O).
(V_{DC} = 100V, V_G = 43V RMS, L_f = 1.8mH, C_f = 10µF, L_g = 92.2µH grid inductance, K_p = 1.1, K_i = 0.6, F_s = 20kHz.)

4.6.1 *Effect of Background Grid Voltage Magnitude*

To assess the sensitivity of the inverter current controller to the variation in the harmonic magnitude of background grid voltage, the grid-connected inverter system model in Figure 4.19 is applied to interface with the variable background grid voltage model in simulation via a 100μH grid inductance. In the simulation, the phase angle of the background grid voltage harmonics and the series resistance of passive components will have a cancelling effect and damping effect on the inverter system output current respectively. To ensure that only the effect of variation in background grid voltage magnitude is depicted in the simulation result, the phase angle of the background grid voltage harmonics and series resistance of passive component are offset to zero. The magnitude of an individual harmonic component of background grid voltage is then manually adjusted in a controlled manner, and the effect on the overall current control is observed. Figure 4.21 to Figure 4.24 show the low order harmonic profile of inverter system output current when the magnitude of the 3^{rd}, 5^{th}, 7^{th}, or 9^{th}, harmonics of the background grid voltage are varied in turn by up to ±20%, whilst all other harmonics remain constant in magnitude. The effect on the low order harmonic spectrum of the inverter system output current is shown in Figure 4.21(b) to Figure 4.24(b). By altering a single magnitude of the background grid voltage harmonic (as shown by the red dashed box of Figure 4.21(a) to Figure 4.24(a)), it is apparent that each harmonic component of the inverter system output current is affected. There is also a directly proportional change in the magnitude of the 3^{rd}, 5^{th}, 7^{th}, or 9^{th}, harmonic of the inverter system output current when the magnitude of the 3^{rd}, 5^{th}, 7^{th}, or 9^{th}, harmonic of the background grid voltage is varied respectively (as shown by the red dashed box of Figure 4.21(b) to Figure 4.24(b)).

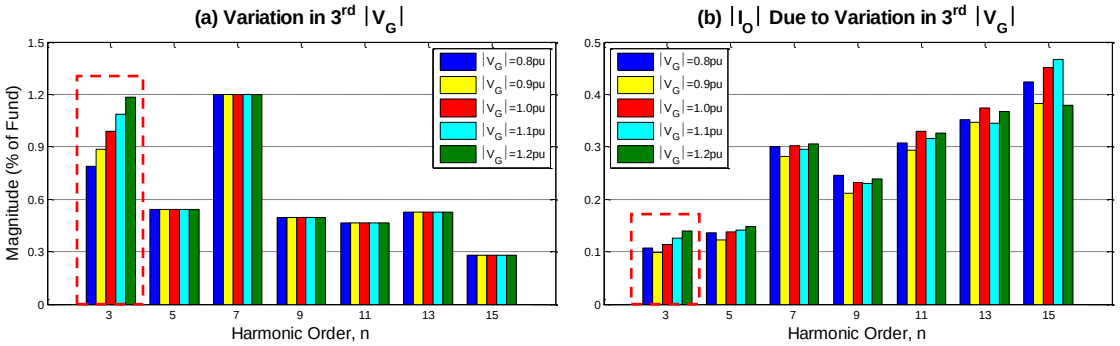

Figure 4.21 Effect of variation in the 3rd harmonic magnitude of background grid voltage (V_G) on the harmonic magnitude of inverter system output current (I_O).

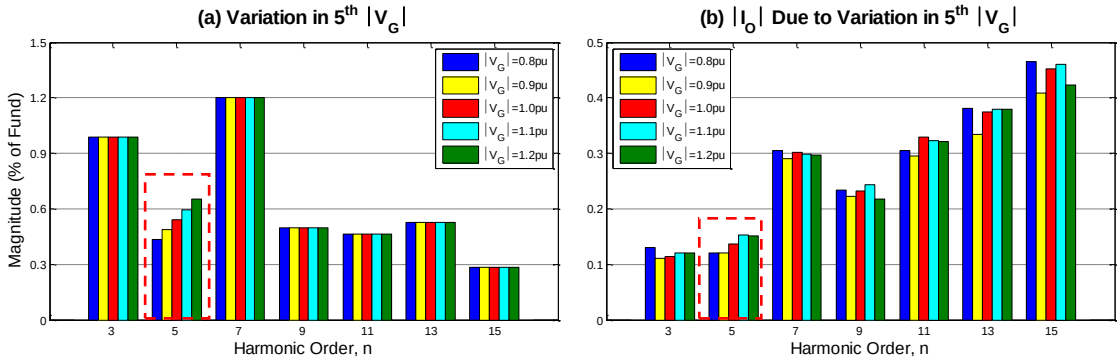

Figure 4.22 Effect of variation in the 5th harmonic magnitude of background grid voltage (V_G) on the harmonic magnitude of inverter system output current (I_O).

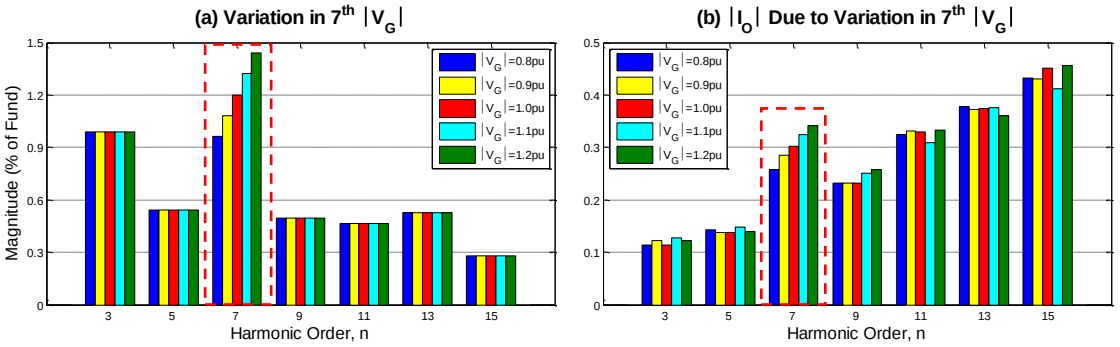

Figure 4.23 Effect of variation in the 7th harmonic magnitude of background grid voltage (V_G) on the harmonic magnitude of inverter system output current (I_O).

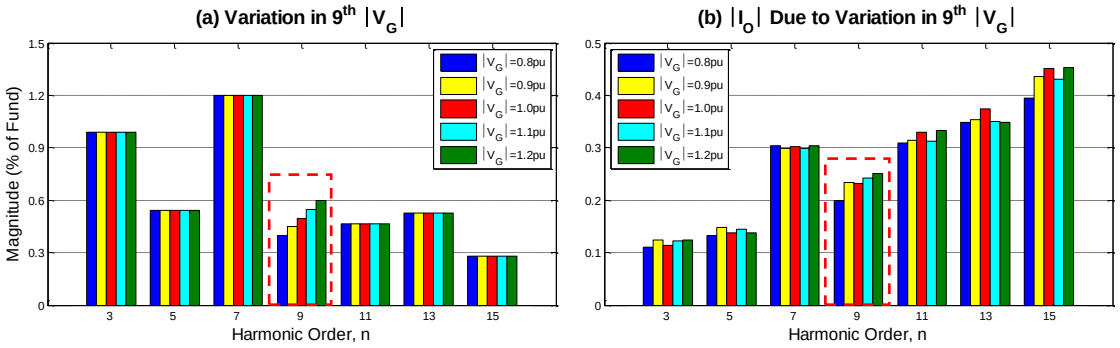

Figure 4.24 Effect of variation in the 9th harmonic magnitude of background grid voltage (V_G) on the harmonic magnitude of inverter system output current (I_O).

Figure 4.25 shows the phase angle of the inverter system output current due to variation in the magnitude of the 3rd, 5th, 7th, or 9th, harmonic of the background grid voltage. As shown by Figure 4.25 that the variation in the magnitude of background grid voltage harmonic component will not cause the significant effect on the phase angle of inverter system output current harmonic. Therefore, neglecting the effect of the phase angle, the magnitude of inverter system output current harmonic is directly proportional to the magnitude of background grid voltage harmonic.

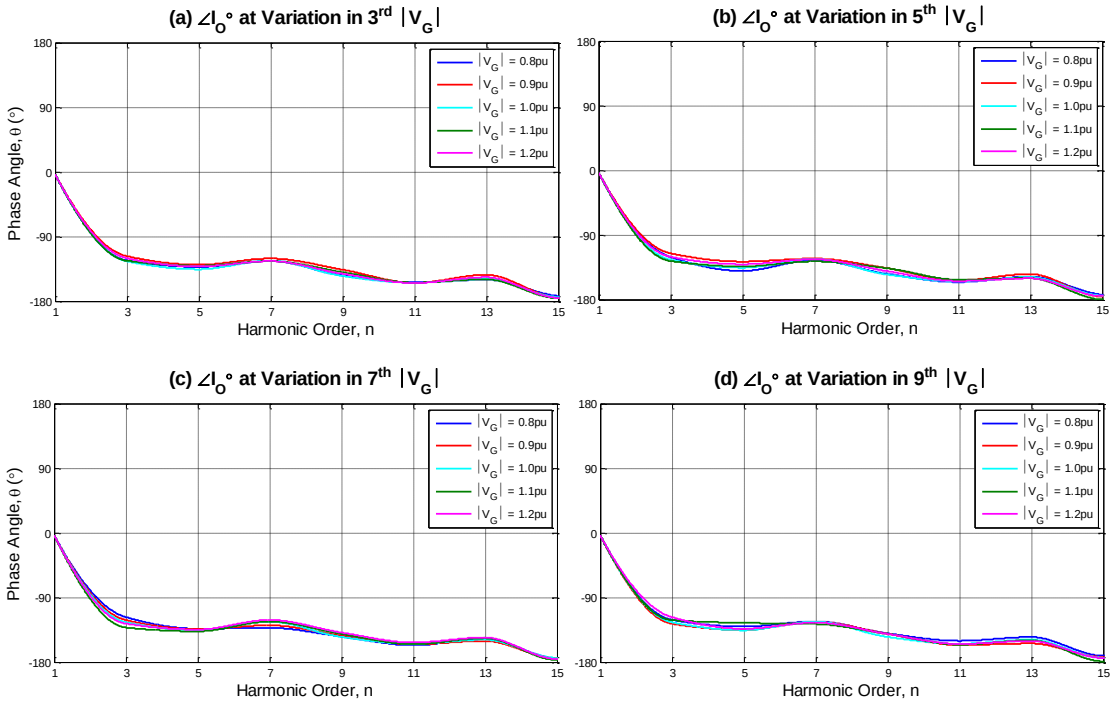

Figure 4.25 Variation in the harmonic phase angle of inverter system output current (I_O) due to variation in the harmonic magnitude of background grid voltage (V_G).

4.6.2 *Effect of Background Grid Voltage Phase Angle*

As the inverter system output current is related to the vector of background grid voltage, hence variation in the phase angle of background grid voltage harmonics will have certain effect on inverter system output current. To assess the sensitivity of the inverter current controller to the variation in the harmonic phase angle of background grid voltage, the grid-connected inverter system model in Section 4.6.1 is applied in the simulation. The phase angle of an individual harmonic component of background grid voltage is then manually offset in a controlled manner, and the effect on the overall current control is observed. It should be noted that the magnitude of background grid voltage harmonics are remain unchanged throughout the simulation.

Figure 4.26 to Figure 4.29 show the low order harmonic phase angle of inverter system output current when the phase angle of the 3^{rd}, 5^{th}, 7^{th}, or 9^{th}, harmonics of the background grid voltage are varied in turn by up to 270° lagging (as shown by the red dashed ellipse of Figure 4.26(a) to Figure 4.29(a)), whilst all other harmonics remain zero in phase angle. The effect on the low order harmonic phase angle of the inverter system output current is shown in Figure 4.26(b) to Figure 4.29(b). By altering a single-phase angle of the background grid voltage harmonic, it is apparent that the phase angle of the corresponding harmonic component of inverter system output current is affected. As shown on the figures that there is a directly proportional change in the phase angle of the 3^{rd}, 5^{th}, 7^{th}, or 9^{th}, harmonics of the inverter system output current when the phase angle of the 3^{rd}, 5^{th}, 7^{th}, or 9^{th}, harmonic of the background grid voltage is varied respectively (as shown by the red dashed ellipse of Figure 4.26(b) to Figure 4.29(b)).

Figure 4.30 shows the magnitude of the inverter system output current due to variation in the phase angle of the 3^{rd}, 5^{th}, 7^{th}, or 9^{th}, harmonic of the background grid voltage. As shown by Figure 4.30 that the variation in the phase angle of background grid voltage harmonic component will have the apparent effect on the magnitude of inverter system output current harmonic. Moreover, as shown by the red dashed box in Figure 4.30, the magnitude of the 3^{rd}, 5^{th}, 7^{th}, or 9^{th}, harmonic of inverter system output current is at maximum when the corresponding 3^{rd}, 5^{th}, 7^{th}, or 9^{th} harmonic of the background grid voltage is 90° lagging at the positive cycle zero crossing of the fundamental harmonic (50Hz). Vice-versa, the magnitude of the 3^{rd}, 5^{th}, 7^{th}, or 9^{th}, harmonic of inverter system output current is at minimum when the corresponding 3^{rd}, 5^{th}, 7^{th}, or 9^{th} harmonic of the background grid voltage is 90° leading (270° lagging) at the positive cycle zero crossing of the fundamental harmonic (50Hz). This is due to the change in the magnitude of inverter bridge output voltage in order to cope with the variation in the phase angle of background grid voltage harmonic, as shown in red dashed box in Figure 4.31.

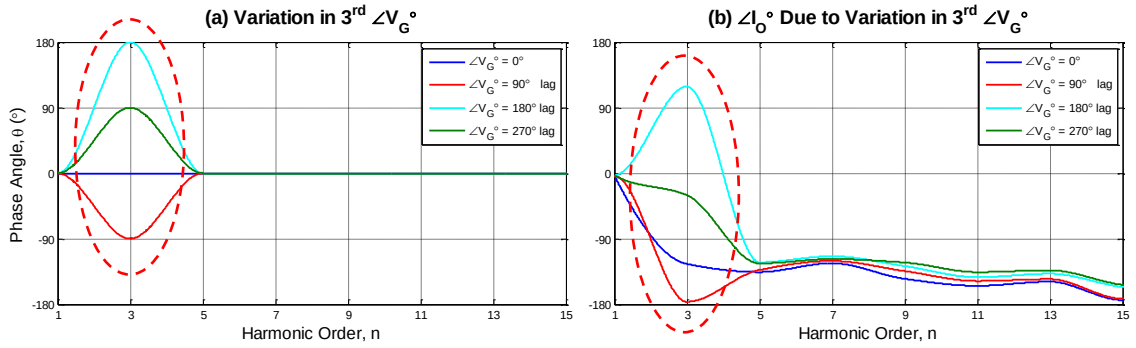

Figure 4.26 Effect of variation in the 3rd harmonic phase angle of background grid voltage (V_G) on the harmonic phase angle of inverter system output current (I_O).

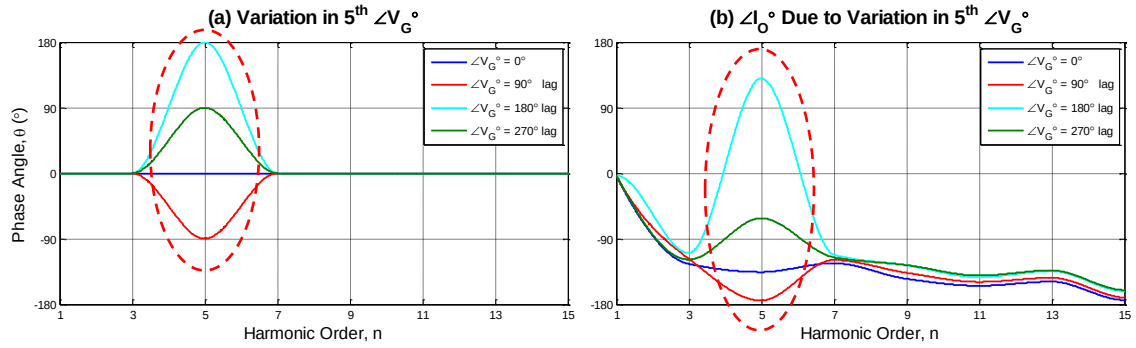

Figure 4.27 Effect of variation in the 5th harmonic phase angle of background grid voltage (V_G) on the harmonic phase angle of inverter system output current (I_O).

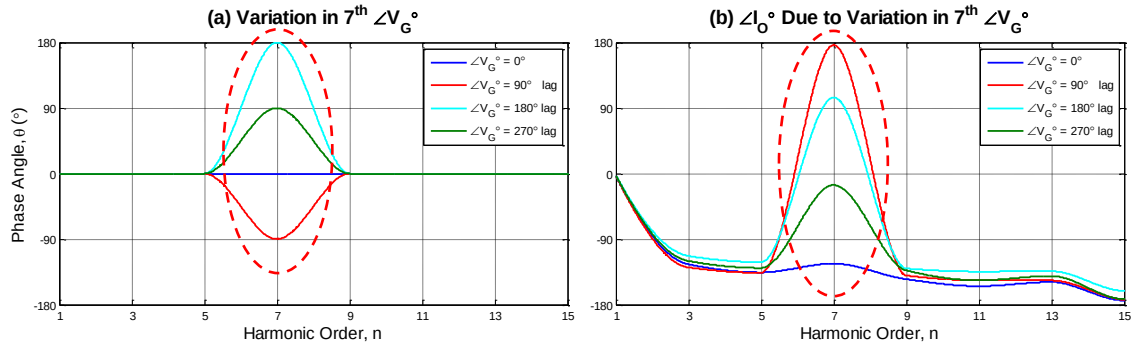

Figure 4.28 Effect of variation in the 7th harmonic phase angle of background grid voltage (V_G) on the harmonic phase angle of inverter system output current (I_O).

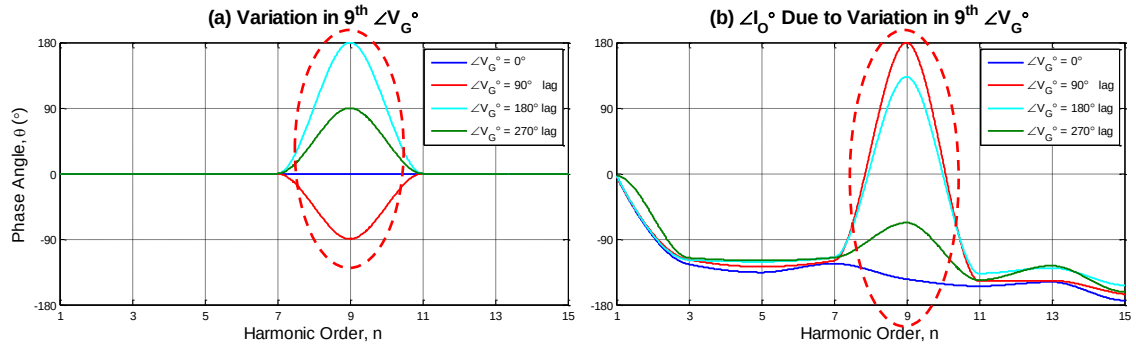

Figure 4.29 Effect of variation in the 9th harmonic phase angle of background grid voltage (V_G) on the harmonic phase angle of inverter system output current (I_O).

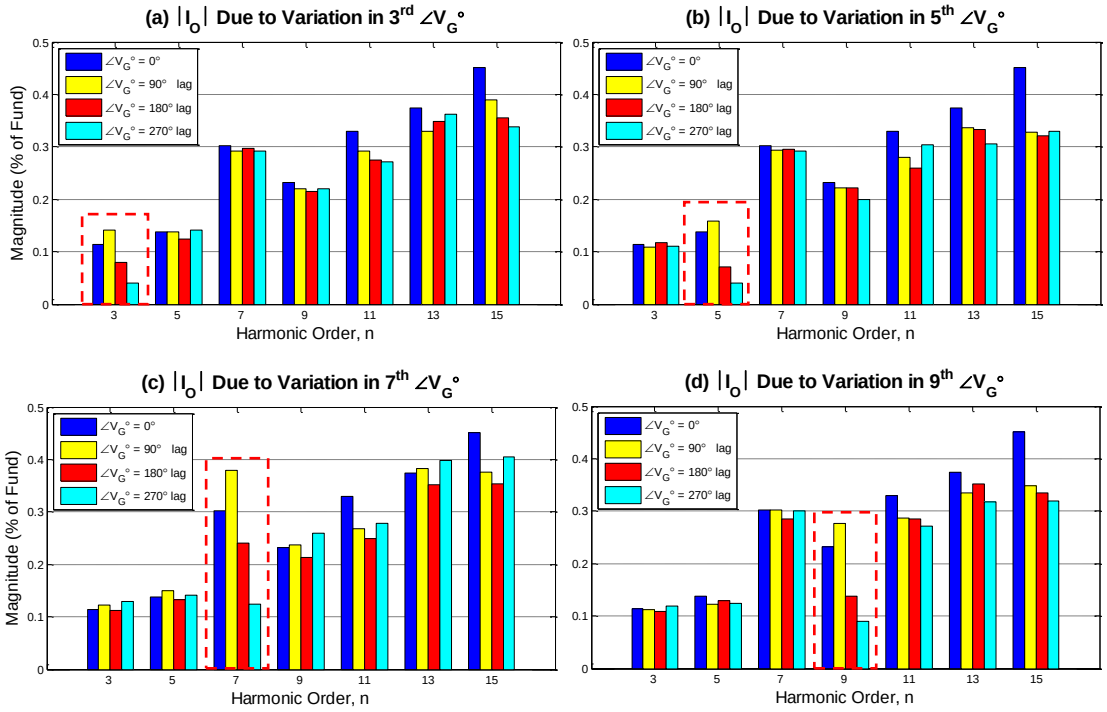

Figure 4.30 Variation in the harmonic magnitude of the inverter system output current (I_O) due to variation in the harmonic phase angle of background grid voltage (V_G).

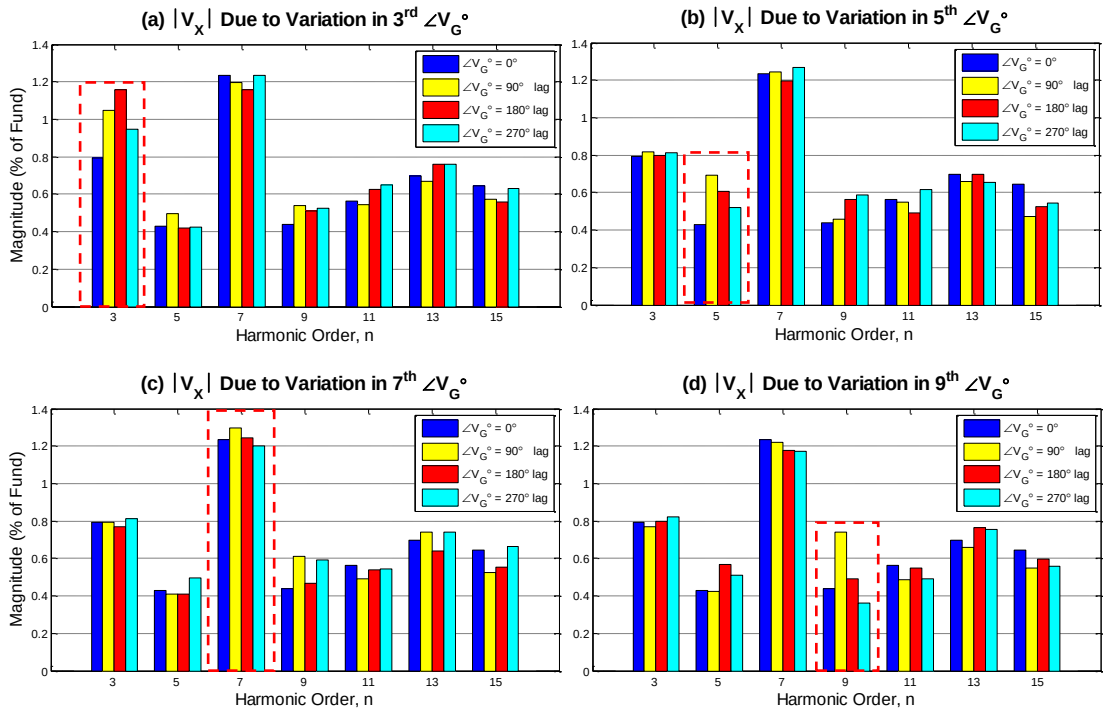

Figure 4.31 Variation in the harmonic magnitude of the inverter bridge output voltage (V_X) due to variation in the harmonic phase angle of background grid voltage (V_G).

4.6.3 *Frequency Decoupling of Harmonic Interference*

The linearity behaviour between the magnitude and phase angle of background grid voltage harmonic and inverter system output current harmonic is given in Section 4.6.1 and Section 4.6.2. Another important aspect of harmonic interference is the frequency decoupling of interfered harmonic between the distribution grid and inverter system, as suggested by Bosman, Cobben, et al. [82]. However, the impact of the individual harmonic magnitude and phase angle of background grid voltage on the inverter system output current harmonics is not clearly demonstrated and explained.

Frequency decoupling of interfered harmonic depict that the magnitude and phase angle of the n^{th} background grid voltage harmonic will only interfere with the magnitude and phase angle of the n^{th} inverter system output current harmonic. To assess this frequency decoupling behaviour, the grid-connected inverter system model in Figure 4.19 is applied to interface with the variable background grid voltage model in simulation via a 100μH grid inductance. In the simulation, the magnitude and phase angle of background grid voltage based on the practical measurement is used as the reference model, then the magnitude and phase angle of the 3^{rd}, 5^{th}, 7^{th}, or 9^{th}, harmonic of the background grid voltage harmonic are increased to 2pu and offset by 180° respectively.

The simulation results are presented in Figure 4.32 to Figure 4.35. They show the low order harmonic magnitude and harmonic phase angle of background grid voltage and inverter system output current when the 3^{rd}, 5^{th}, 7^{th}, or 9^{th}, background grid voltage is varied. As shown from the figures, there is a significant change in the magnitude and phase angle of the 3^{rd}, 5^{th}, 7^{th}, or 9^{th}, harmonic of the inverter system output current when the magnitude and phase angle of the 3^{rd}, 5^{th}, 7^{th}, or 9^{th}, harmonic of the background grid voltage is varied respectively (as shown by the red dashed box of Figure 4.32(b) to Figure 4.35(b), and the red dashed ellipse of Figure 4.32(d) to Figure 4.35(d)). Moreover, it is also apparent that the variation in the 3^{rd}, 5^{th}, 7^{th}, or 9^{th}, harmonic of background grid voltage does not caused the significant change in others harmonics apart from the corresponding interfered harmonic. It should be noted that the small change in the magnitude of the 7^{th} harmonic of the inverter system output current (7^{th} in Figure 4.34(b)) is due to the variation in the 7^{th} harmonic of the background grid voltage (7^{th} in Figure 4.34(a)), and is possibly due to the phase angle of the other harmonics which lead to the cancellation effect on the background grid voltage seen by the inverter system current controller.

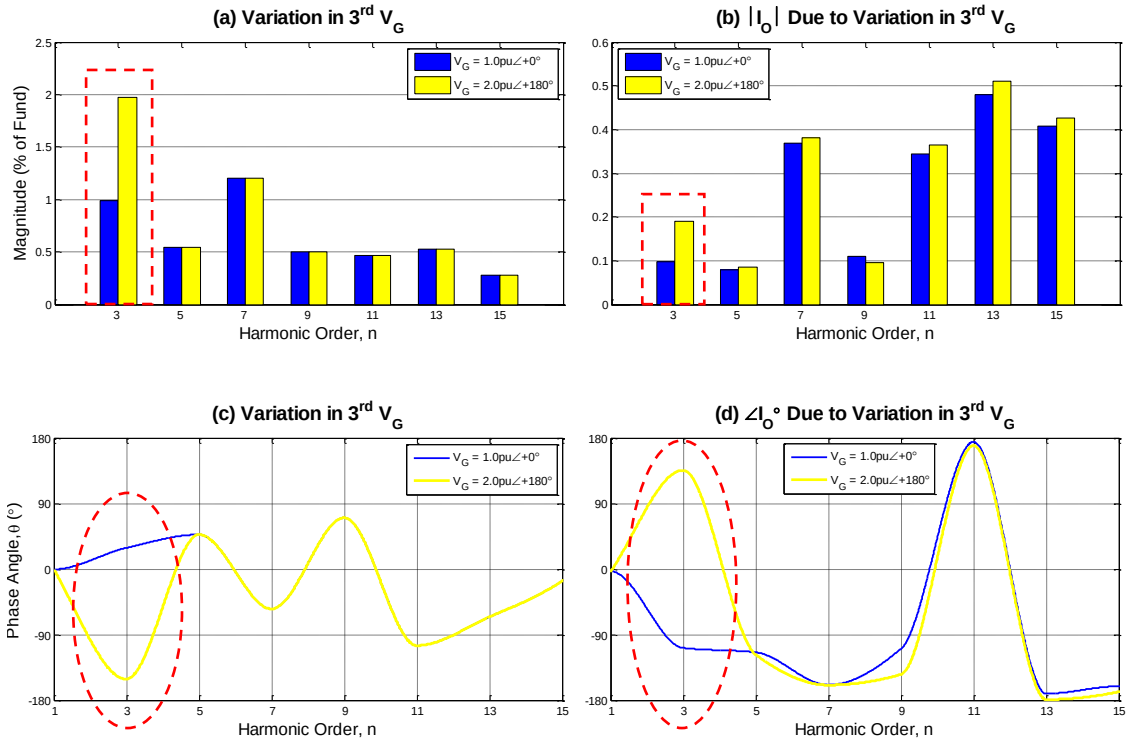

Figure 4.32 Effect of variation in the 3rd harmonic magnitude and phase angle of background grid voltage (V_G) on the harmonic of inverter system output current (I_O).

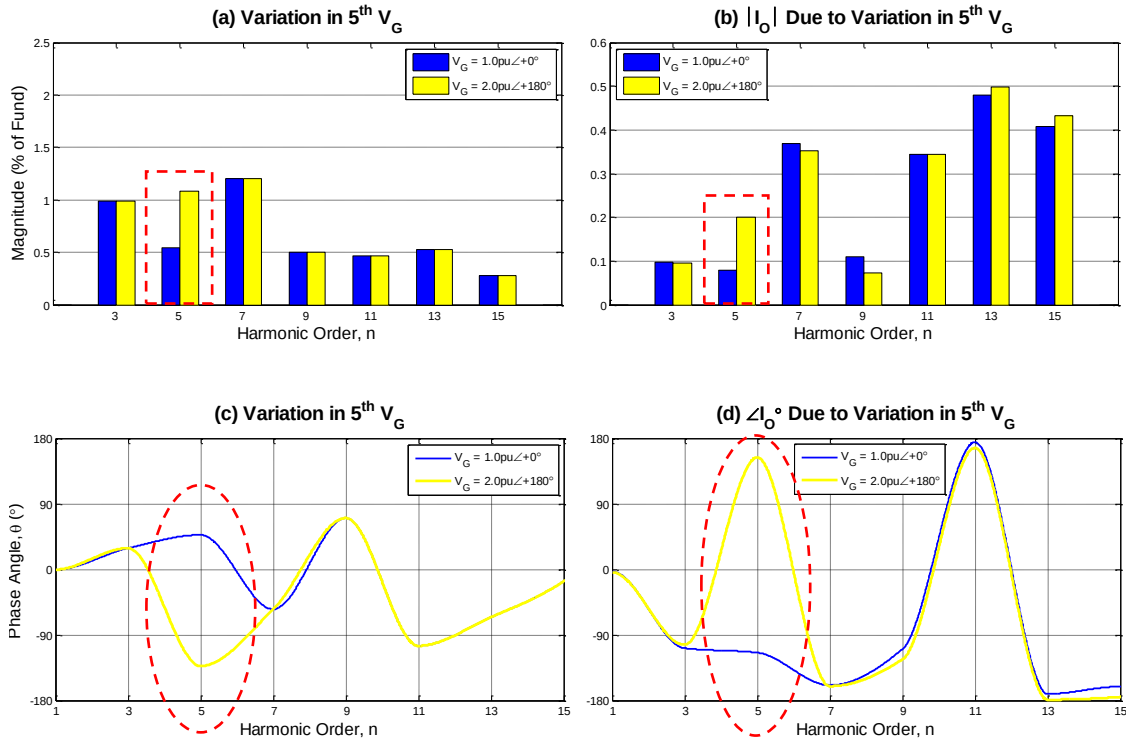

Figure 4.33 Effect of variation in the 5th harmonic magnitude and phase angle of background grid voltage (V_G) on the harmonic of inverter system output current (I_O).

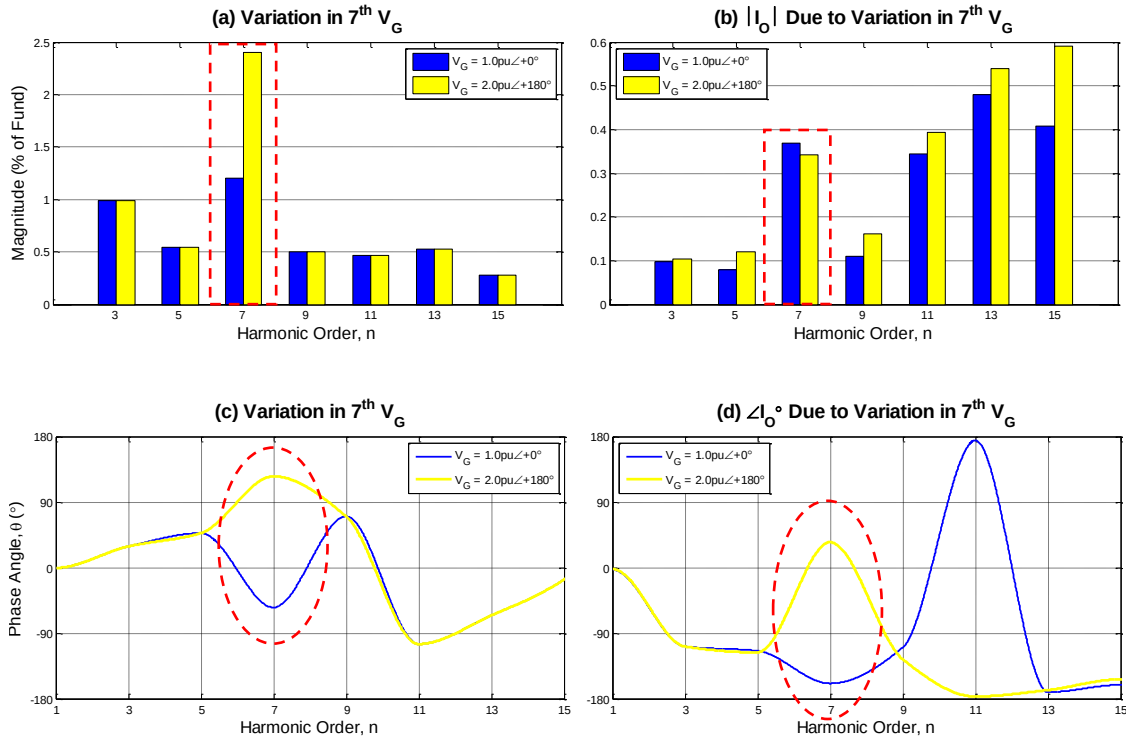

Figure 4.34 Effect of variation in the 7th harmonic magnitude and phase angle of background grid voltage (V_G) on the harmonic of inverter system output current (I_O).

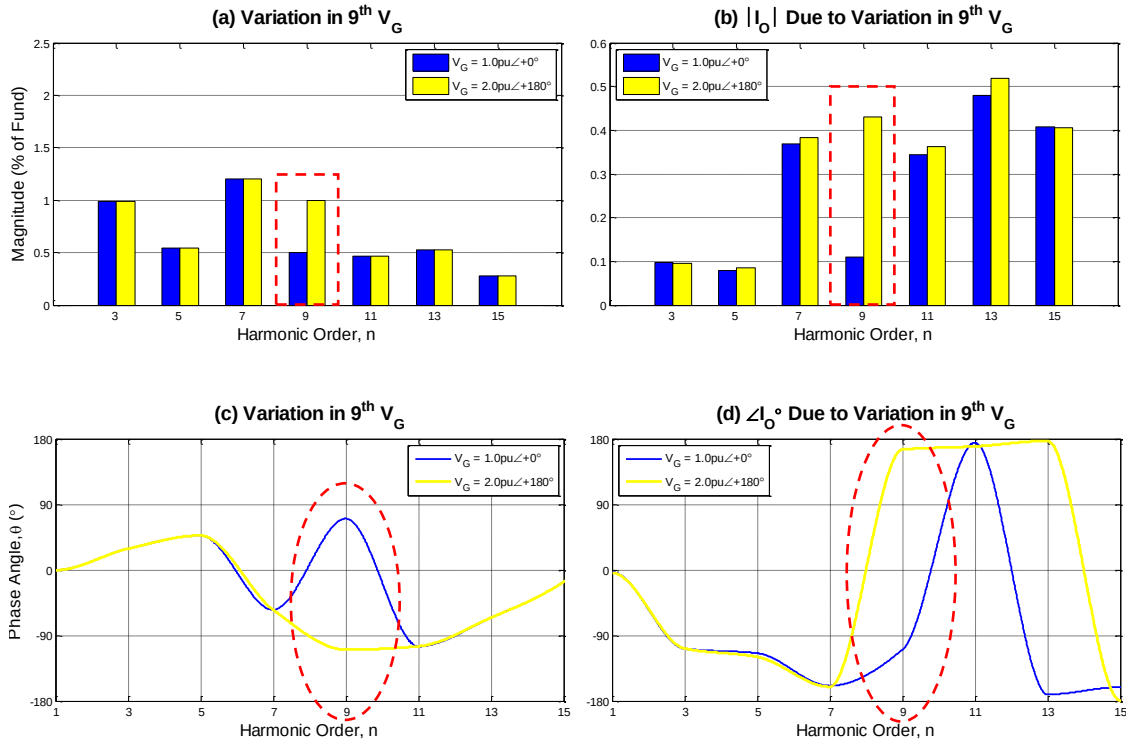

Figure 4.35 Effect of variation in the 9th harmonic magnitude and phase angle of background grid voltage (V_G) on the harmonic of inverter system output current (I_O).

4.7 Summary

This chapter has presented the harmonic interaction of the grid-connected PV inverter and the distribution grid involved with the variation in grid operating conditions, such as the variation in the value of grid impedance, as well as harmonic magnitude and phase angle of background grid voltage. It has been shown in the chapter that the operating conditions of the distribution grid led to variation in the harmonic profile of PCC voltage. To understand the effect of the variation on the PCC voltage and system output current of PV inverter, the harmonic mechanism of the interaction is analysed and understood through the employed LCL model. For a stiff grid (low grid impedance), the PCC voltage is prone to the harmonics of background grid voltage. In contrast, the harmonic profile of PCC voltage is vulnerable to the harmonics of PV inverter system in a weak grid (high grid impedance). For the simulation results presented with the effect the background grid voltage, the low order output current harmonics of a grid-connected PV inverter system are sensitive to even small variation in the harmonics of background grid voltage (magnitude and phase angle). It has been shown that the low order harmonic magnitude (from 3^{rd} to 15^{th} harmonics) of inverter system output current is increased with harmonic magnitude of background grid voltage. Likewise for the harmonic phase angle of inverter system output current, it is shown that there is proportional variation in the harmonic phase angle of inverter system output current when the harmonic phase angle of background grid voltage is varied. This also causes the variation in the harmonic magnitude of inverter system output current. Besides this, the results have shown the harmonic magnitude and phase angle of the n^{th} background grid voltage will significantly interfere with the corresponding harmonic magnitude and phase angle of inverter system output current.

Chapter 5. Resonance of PV Inverter and Distribution Grid

5.1 Introduction

This chapter consider the resonance phenomenon due to the interaction between the grid-connected PV inverter system and distribution grid. In particularly, it is concerned with the cause of the resonance excitation and its effect on the current control loop of the grid-connected PV inverter system. Initially, the interaction mechanism that causes the excitation of resonance is explained with particular interest in the effect of variation in grid impedance. It is shown that variation in grid impedance excites the resonance in the network. The second part of this chapter presents the resonance mitigation measures that are proposed in this research. The outcomes of the test are compared and presented in this chapter.

5.2 Background of Resonance Phenomenon in the Distribution Network

As the electrical frequency in a circuit is increased, capacitive reactance ($X_C = -\frac{1}{\omega C}$) decreases and inductive reactance ($X_L = \omega L$) increases. Eventually, a frequency is reached where the capacitive and inductive reactance of the circuit impedance are very closely matched to each other. At this point, resonance is observed in the circuit. Electrical resonance is a phenomenon where a large quantity of energy oscillates (exchanging energy) between the inductive and capacitive components in the circuit (Alexander and Sadiku [75], Hughes [76]). This will cause the response of the circuit at resonant frequency to be significantly different to other frequencies, and hence the instability issues might arise as the consequence of this undesired response.

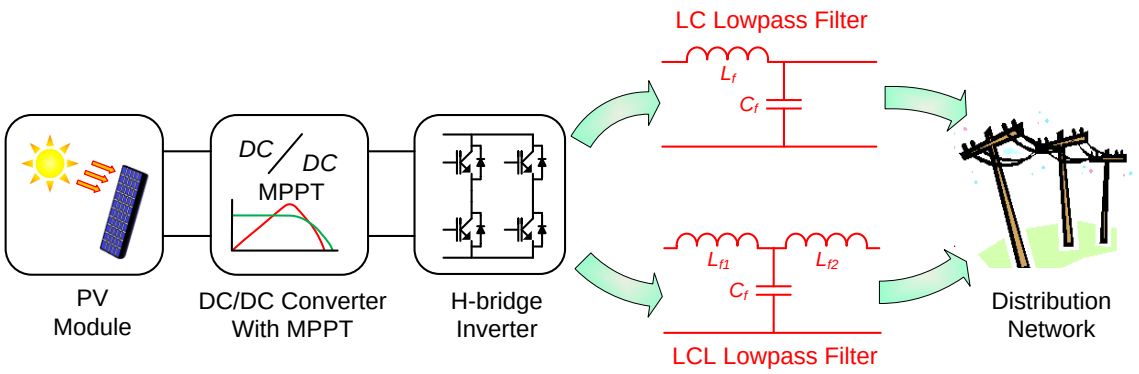

Figure 5.1 Typical arrangement of the lowpass filter use to interface the grid-connected PV system to the distribution network.

Grid-connected PV inverters are normally interfaced with the distribution network via a lowpass filter, which is normally an LC filter or LCL filter arrangement, as shown by the lowpass filter arrangement in Figure 5.1. Typically, these filters are coupled with the impedance of the distribution network to form a resonant circuit. At the resonant frequency, significant voltage and current distortion is observed at the Point of Common Coupling (PCC). The impedance of the distribution network includes source transformers, cable reactance, effect of connected loads (linear and non-linear), and the impact of distributed generation connected at the PCC.

In distribution networks with high penetration of grid-connected PV systems, the resonance may be excited by the large number of grid-connected PV inverters connected in parallel at the PCC (Enslin, Hulshorst, et al. [16]). Problems of harmonic distortion, which arise from the interaction between grid-connected PV inverters and the distribution grid, such as voltage rise caused by the grid impedance and increase in the inverter output current harmonics as a result of the increase in grid voltage harmonics, are discussed by Simmons and Infield [15], Enders, Halter, et al. [84], and Bosman, Cobben, et al. [82]. Furthermore, the interaction problems, such as current harmonics and DC current injection of PV inverter, are extensively presented in PV UPSCALE Publication Review Report [85], ETSU Research Report [13], and IEA PVPS Report [10].

In distribution networks with more than one grid-connected PV inverter connected in parallel at the PCC, Armstrong, Atkinson, et al. [67], and Infield, Onions, et al. [86], suggest that the magnitude of PV inverter output current low order harmonics increases as the number of similar paralleled PV inverters increase. Besides that, the interaction between the grid-connected PV inverter and non-linear loads connected at the same PCC in the low voltage distribution network is discussed by Benhabib, Myrzik, et al. [87].

Although the problems of the interaction and the impact of the PV inverters on the distribution network are extensively analysed, the problems associated with the network resonance with the penetration of grid-connected PV inverter rarely assessed, especially the effects of the resonance phenomenon on the harmonic performance of the PV inverter current controller are hardly evaluated. Furthermore, current harmonic standards such as IEEE Std 929, 2000 [17], IEC 61000-3-2 [19], ENA G83/1-1 [22], and the distribution network voltage characteristic standard EN50160 [18], could be

exceeded under excitation of resonance phenomenon due to the interaction between grid-connected PV inverters and the distribution grid, even if each of the grid-connected PV inverter in the network has individually complied with those standards. For this reason, the effect of this resonance and its excitation mechanism are analysed and investigated in this chapter. This is carried out through the frequency response of the PV inverter current control loop and excitation of the resonance in practical experiment via variation in grid impedance.

5.3 Resonance Effect on Harmonic Distortion of Voltage and Current

In distribution network with various devices and loads connected to the PCC, two types of resonance commonly exist: parallel resonance which is caused by the parallel arrangement of capacitive and inductive network reactance, and series resonance which is caused by the series arrangement of capacitive and inductive network reactance (Enslin, Hulshorst, et al. [16]). The typical circuit arrangement of parallel resonance and series resonance are shown in Figure 5.2(a) and Figure 5.2(b) respectively.

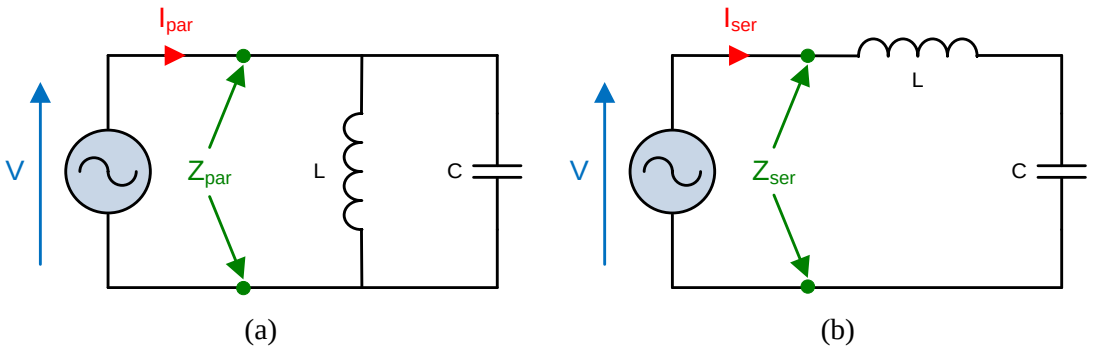

Figure 5.2 Common resonance in distribution network. (a) Parallel resonant circuit; (b) Series resonant circuit.

At parallel resonance, the energy of the resonant circuit oscillates between the inductive and capacitive reactance which are connected in parallel. At resonant frequency (f_{res}), the impedance of the circuit (Z_{par}) is at a maximum. This leads to a very small magnitude of current (I_{par}) flowing into the resonant circuit at the resonant frequency. Conversely, at series resonance, the energy of the resonant circuit oscillates between the inductive and capacitive reactance which are connected in series. At resonant frequency, the impedance of the circuit (Z_{ser}) is at a minimum. This leads to very high magnitude current (I_{ser}) flow into the resonant circuit at the resonant frequency. The actual resonant frequency of the circuit can be calculated via the well-known equation as given by Equation (5.1) (Alexander and Sadiku [75], Hughes [76]).

$$f_{res} = \frac{1}{2\pi\sqrt{LC}} \tag{5.1}$$

Figure 5.3 clearly shows the impedance characteristics of both the series and parallel circuit as a function of frequency. In this example, a 100mH inductor and 10µF capacitor is used. Using Equation (5.1), the resonant frequency is 159 Hz.

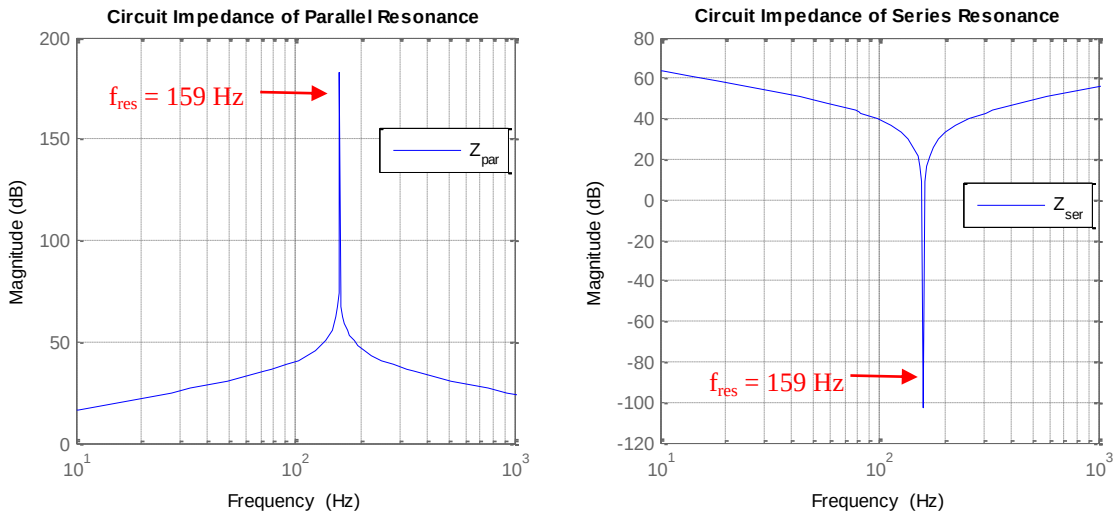

(a) (b)

Figure 5.3 Frequency response of the circuit impedance at resonance. (a) Circuit impedance at parallel resonance; (b) Circuit impedance at series resonance.
(L = 100mH , C = 10µF.)

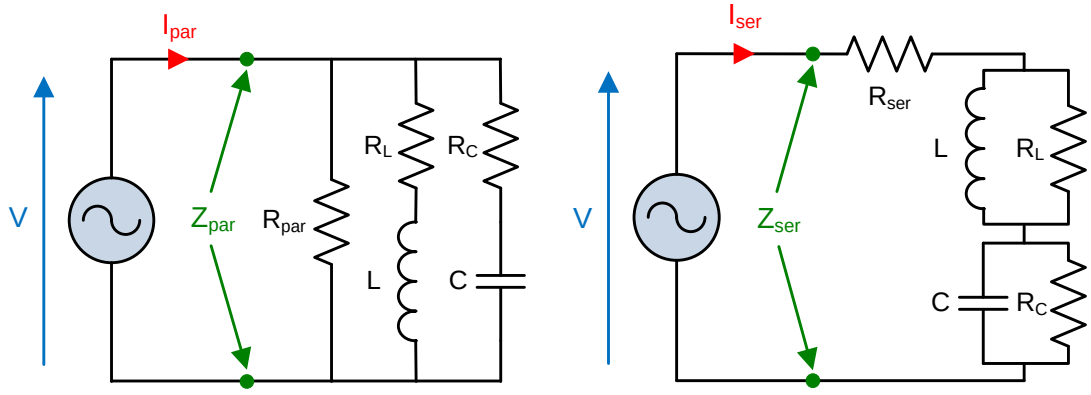

(a) (b)

Figure 5.4 Possible resistance presence in the distribution network. (a) Parallel resonant circuit; (b) Series resonant circuit.

In practice, the distribution network consists of resistance despite of it is predominantly inductive or capacitance. This resistance can be the resistance of the loads that connected in parallel with the inductive and/or capacitive loads, or the equivalent series resistance (ESR) of the cables, loads or transformer that connected in series with their inductive or capacitive reactance. Figure 5.4 illustrates the possible location of the

resistance that presence in the parallel and series LC resonant circuit. Depending on the location of the resistance in this LC resonant circuit (shown in Figure 5.4), it has the tendency to shift the resonant frequency or to damp the peak of the resonance. This phenomenon is commonly referred to as anti-resonance (Kuphaldt [88]). Figure 5.5(a) shows the effect of the resistance on the circuit impedance of the parallel LC resonant circuit as shown in Figure 5.4(a). As shown by the blue line in the figure that the resistance (R_{par}) in parallel with inductance and capacitance has the damping effect on the very high peak of circuit impedance at resonant frequency (compare to Figure 5.3(a)). Moreover, the red and cyan lines show that the resistance in series with inductance (R_L) or capacitance (R_C) damped the circuit impedance while shifting the resonant frequency down and up respectively. Contrary, Figure 5.5(b) shows the effect of the resistance on the circuit impedance of the series LC resonant circuit as shown in Figure 5.4(b). As shown by the blue line in the figure that the resistance (R_{ser}) in series with inductance and capacitance increased the circuit impedance at resonant frequency (compare to Figure 5.3(b)). Moreover, the red and cyan lines show that the resistance in parallel with inductance (R_L) or capacitance (R_C) increased the circuit impedance while shifting the resonant frequency up and down respectively.

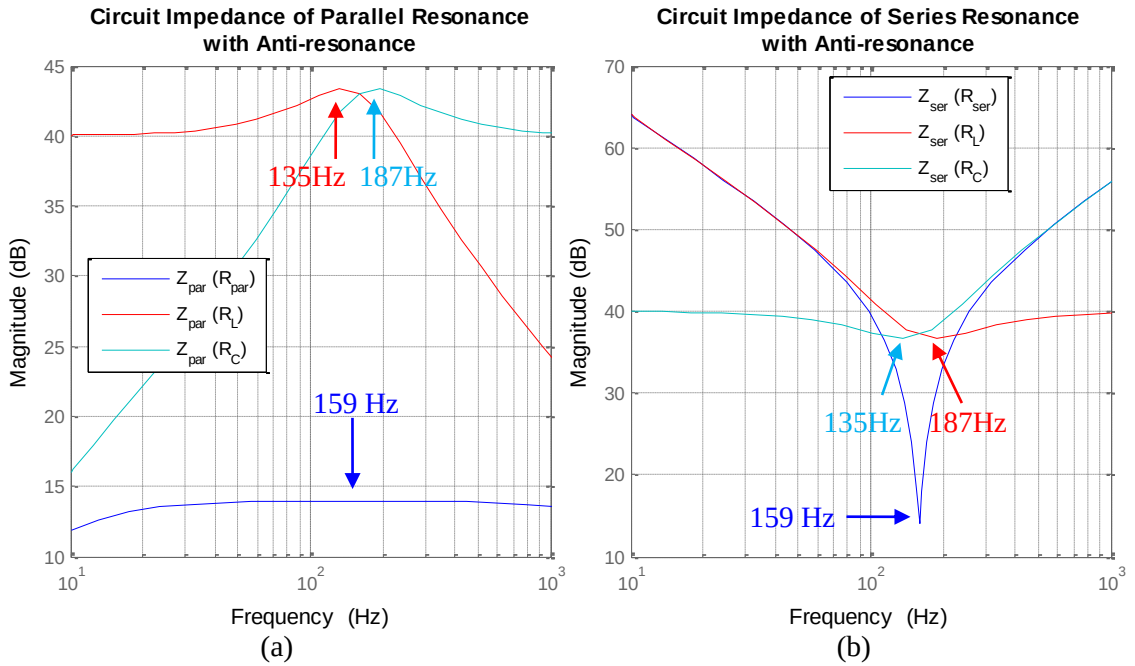

Figure 5.5 Anti-resonance of LC resonant circuit. (a) Anti-resonance in parallel resonant circuit; (b) Anti-resonance in series resonant circuit.
(L =100mH, C = 10μF, R_{par} = R_{ser} = 5Ω, R_L = R_C = 100Ω.)

In practice, a grid-connected PV system is often connected in parallel with various loads and/or generators at the PCC. In some cases it might even have several PV systems

connected in parallel with these loads and generators. Figure 5.6 shows the typical connection of grid-connected PV system coupled to the PCC of the distribution grid via an LC filter (L_f and C_f). For the purpose of keeping the analysis simple, the output of the PV system inverter bridge can be represented by a current (I_X) which consists of harmonics. In Figure 5.6, the network impedance is the lumped resistance (R_{net}), inductance (L_{net}) and capacitance (C_{net}) of all loads, generators, cables, and even other PV systems connected in parallel to the PCC. The source inductance (L_s) is predominantly the leakage inductance of the supply transformer at source substation of the distribution grid, series inductance of cables, and transfer reactance of supply generators etc. The harmonic impedance (Z_{har} in Figure 5.6), which is the relationship between a harmonic voltage disturbance into the system and the resultant injected grid current harmonic component [89], provides a simple measure to evaluate the sensitivity of voltage and current harmonics in the distribution network.

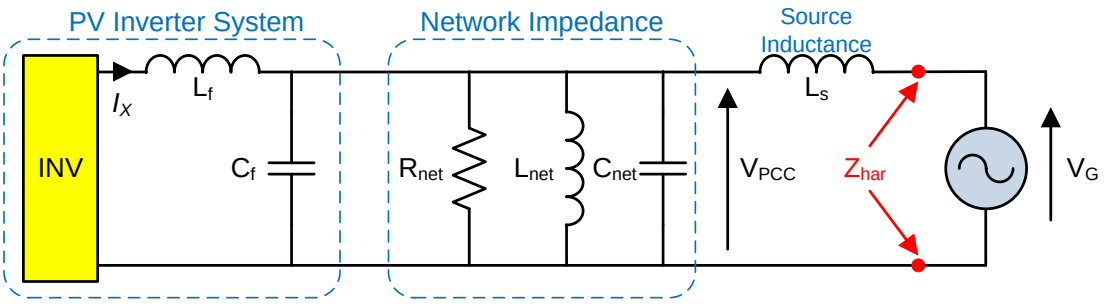

Figure 5.6 Single-phase circuit diagram of typical distribution grid with connection of grid-connected PV system at PCC.

In practice, the resonance phenomenon in a distribution network interfaced with PV systems (as shown in Figure 5.6) is a complex combination of parallel and series resonance. The effect of parallel and series resonance on distribution grid is explained by Enslin, Hulshorst, et al. [16]. They suggest that parallel resonance can be excited by parallel connection of the circuit capacitance (such as network capacitance of loads, generations, or cables and filter capacitance of PV systems) and the circuit inductance (such as network inductance of loads, generations, cables, or transformers). In this case, harmonic impedance at resonant frequency is very high. If the current harmonic generated by the grid-connected PV inverter (harmonic below 50^{th} typically) coincides with the resonant frequency in this parallel resonance mechanism, a large resonant voltage, that is only damped by the associated network resistance (R_{net}), will arise on the network voltage at the PCC and lead to voltage distortion at the PCC (V_{PCC}) (Enslin, Hulshorst, et al. [16]). Excessive distortion of the PCC voltage may violate the harmonic standards [17, 18, 90] and can affect the operation of equipment. It can also

cause problems for grid-connected PV inverter systems connected to the PCC; especially devices equipped with Zero Crossing Detection (ZCD) or Phase-Locked Loop (PLL) can suffer from synchronisation issues. Furthermore, the effects are more severe in weak grid conditions as higher value of source inductance (L_s) in weak grid shift the resonant point of the network to lower frequency. This is referred as low frequency parallel resonance of distribution grid.

For the same distribution grid as shown in Figure 5.6, series resonance can be excited by series connection of the circuit capacitance (such as network capacitance of loads, generations, or cables and filter capacitance of PV systems) and source inductance (such as leakage inductance of supply transformer, series inductance of cables, or transfer reactance of supply generator). In this case, harmonic impedance at resonant frequency is very low in magnitude. If the background grid voltage (V_G) from the source is distorted and consists of the harmonic coincides with the resonant frequency in this series resonance mechanism, a high magnitude of resonant current which only damped by associated series resistance of the cables or passive components etc., will flow in the network and hence resulting in higher current distortion through the loads and PV inverter filter capacitor [16]. The output current of PV inverter may exceed the limit of harmonic standards [17, 19, 22] in this circumstance.

In conclusion, it can be said that with parallel resonance, the PV inverter is the source of the harmonic distortion as the harmonic impedance is high. Hence the current harmonic is generated internally, and leads to distortion of the PCC voltage. With series resonance, the background grid voltage is the source of harmonic distortion as the harmonic impedance is low. Here, the distortion is injected externally leading to distortion in the PV system output current and other current in the network. Furthermore, in high capacity PV plants, the distortion in the current injected into the supply can be severe. The low frequency resonance will become more problematic with an increase in the number of PV systems connected to the same PCC as the resonant frequency is reduced with higher values of capacitance and inductance. It is also mentioned by Enslin, Hulshorts, et al. [16] that the resonant frequency can be as low as the 5^{th} harmonic (250Hz) for a single-phase 400V cable feeder with 10 to 30 households which equipped with grid-connected PV system.

5.4 Excitation of Resonance in Distribution Grid with PV Inverter

For analysis purpose, the network of distribution grid is simplified by only considering a single grid-connected PV inverter connected to the PCC. In addition, as the loads connected at PCC are predominantly inductive load or purely resistive load (e.g. induction motor is the typical inductive load that commonly connected at everywhere in distribution network, while capacitive load such as power factor correction capacitors is only installed at specific location of distribution network that require voltage regulation), the network impedance at the PCC and source impedance in Figure 5.6 can be lumped into a single inductive impedance, named as grid impedance (L_g and R_g), as shown in Figure 5.7. For a single-phase, two-wire, 230V, 50 Hz supply (United Kingdom), the reference impedance of 0.4+j0.25 Ω (equivalent to 0.4Ω and 0.796mH of grid resistance and grid inductance respectively) are given by IEC standard IEC 60725 [56] as the maximum grid impedance of the distribution grid. The possible calculation of the grid impedance is demonstrated by Heskes, Rooij, et al. [57] via simple calculation of the cable and source transformer impedance if their parameters are available.

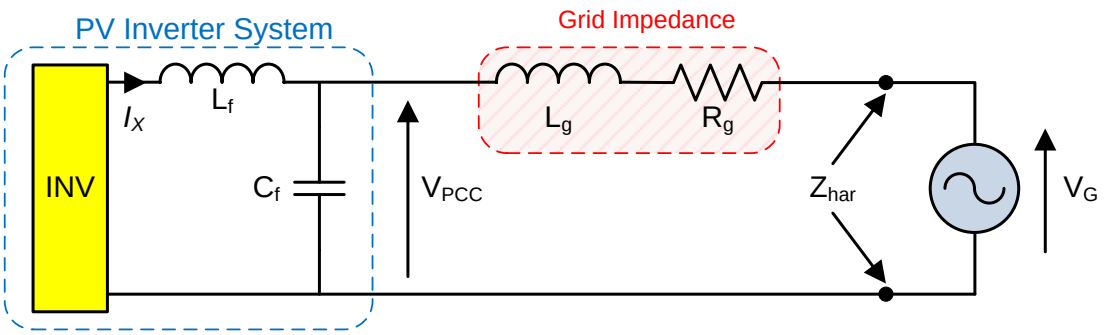

Figure 5.7 Single-phase circuit diagram of a PV inverter system connected to the PCC with lumped grid impedance.

Typical grid-connected PV inverter operates at high switching frequency; 20+ kHz switching frequency is typical for a commercial PV inverter (Armstrong, Atkinson, et al. [21, 67]). Due to this high switching frequency, a lowpass filter with inductor and capacitor arrangement is normally connected at the output of inverter bridge (as shown by L_f and C_f in Figure 5.7) to filter out the switching harmonics and any unwanted harmonics (e.g. harmonic outside of the fundamental). As the cut-off frequency ($f_{cut\text{-}off}$) of the lowpass filter is dictated by both the inductance and capacitance, which is identical to the resonance equation as given in Equation (5.1), the inductance of the lowpass filter can be increased or decreased by decrease or increase the capacitance

respectively while maintaining the same cut-off frequency. In this research, the LC lowpass filter of the experimental PV inverter system is designed for 1125Hz of cut-off frequency as the trade-off between the current control bandwidth and attenuation of the harmonics. This LC lowpass filter is made up by 2mH inductor (2-off 1mH) and a 10μF of capacitor. However, it is measured by RCL meter in practical that the exact value of the inductor and capacitor are 1.808mH (approximately 1.8mH) and 9.9252μF (approximately 10μF) respectively, and hence the actual cut-off frequency of the LC lowpass filter is approximately 1188Hz instead of the designed 1125Hz. To reduce the power losses caused by the inductor, and also make the PV inverter system cost effective, light weight and smaller in size, manufacturers tend to reduce the inductance of the lowpass filter by increasing the capacitance value. However, suggested by Enslin, Hulshorst, et al. [16], this higher value of filter capacitance strongly reduces the current source behaviour of the PV inverter (as higher capacitance provide lower impedance path for current to flow through the filter capacitor) and can also be responsible for creating a resonance circuit together with network impedance. A conventional PV inverter not optimised for this resonance effect will not respond to these resonant phenomena and hence it will not be compensated by the current control loop of the PV inverter. Figure 5.8 shows the range of lowpass filter capacitance and inductance (in per unit) for 1125Hz of cut-off frequency applied on experimental system. It shows that the inductance can be reduced by half, provided the filter capacitance is doubled.

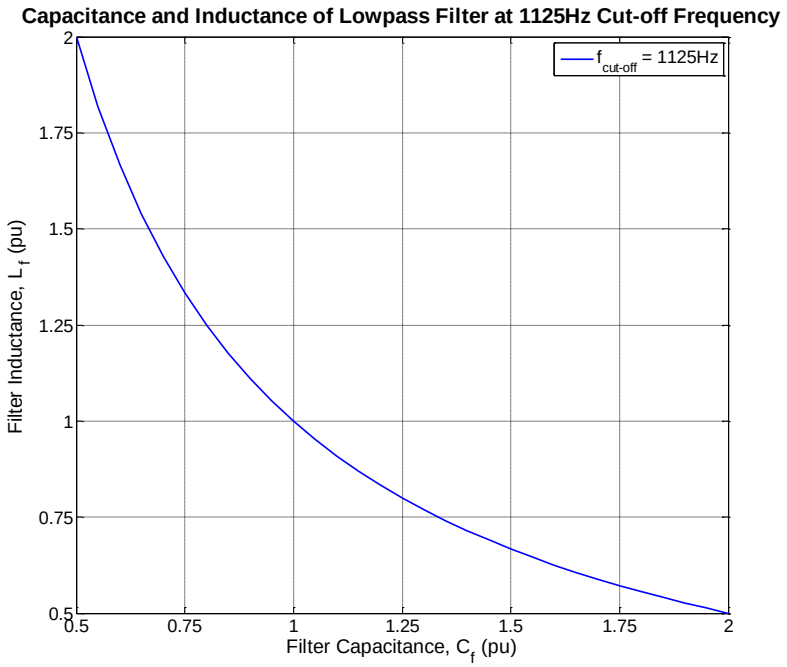

Figure 5.8 Capacitance and inductance of LC lowpass filter for 1125Hz of cut-off frequency.
(C_f = 10μF = 1pu, L_f = 2mH = 1pu.)

Conventional grid networks, which have traditionally been fed by centralized power generation, such as coal power plants, have a reasonably stiff grid impedance value. However, the grid impedance of networks with a high penetration of distributed generation and many sources of non-linear loads, often dispersed throughout the network, is much more volatile and likely to change over time (Liserre, Teodorescu, et al. [91], Enslin, Hulshorst, et al. [16]). Resonance can be excited in these systems when a variation in the grid impedance causes a shift in the system resonant frequency. This will interact with the switching behaviour and filter component (predominantly filter capacitor) of the PV inverter. In turn, this may lead to distortion in the network voltage and current. Such a situation may be possible, even though the PV inverter controller was initially configured to avoid the resonant frequency during installation and commissioning.

To evaluate the variation in the resonant frequency due to the interaction between the PV inverter filter and network impedance, the well-known resonant frequency equation for LCL filter as given by Equation (5.2) (Ahmed, Finney, et al. [38]), can be applied to calculate the resonant frequency for LCL arrangement in Figure 5.7.

$$f_{res\_LCL} = \frac{1}{2\pi}\sqrt{\frac{L_g + L_f}{L_g L_f C_f}} \tag{5.2}$$

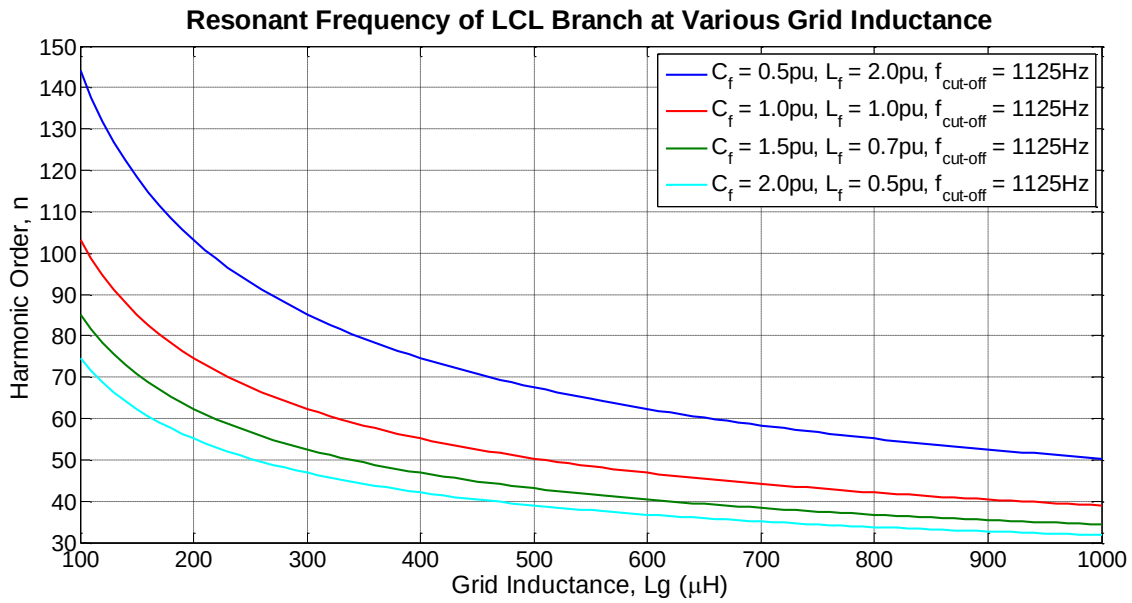

Figure 5.9 Resonant frequency of LCL branch at various grid inductances (L_g) with fixed 1125Hz lowpass filter cut-off frequency ($f_{cut\text{-}off}$).
(C_f = 10μF = 1pu, L_f = 2mH =1pu.)

Figure 5.9 shows the resonant frequency of the LCL arrangement in Figure 5.7 at various grid inductances with fixed PV inverter lowpass filter cut-off frequency of 1125Hz. As shown in the figure that the resonant frequency reduces significantly by higher value of grid inductance, especially when the PV inverter is connected to the weak grid (high grid inductance). Furthermore, the resonant frequency decreases significantly with an increase in PV inverter lowpass filter capacitance. As shown in the figure, the resonant frequency can be as low as 33rd harmonic in the worst case scenario. The resonant frequency can be even lower when multiple PV inverters are connected in parallel as the capacitance is increased with the number of PV inverters, as demonstrated by Kotsopoulos, Heskes, et al. [92].

Furthermore, zero crossing distortion is commonly observed on the output current waveform of grid-connected PV inverter system. This is demonstrated by the output current waveform of a high fidelity simulation model of inverter system (Matlab/Simulink®) in Figure 5.10. As shown in the figure, the distortion in the form of a notch taken out of the sine wave is occurred at zero crossing of inverter system output current. Suggested by Kotsopoulos, Heskes, et al. [92], this zero crossing distortion (shown by the notch at the zero crossing of I_O in Figure 5.10), is due to the practical limitations in the PWM generation that interrupt the current flow near the zero crossing.

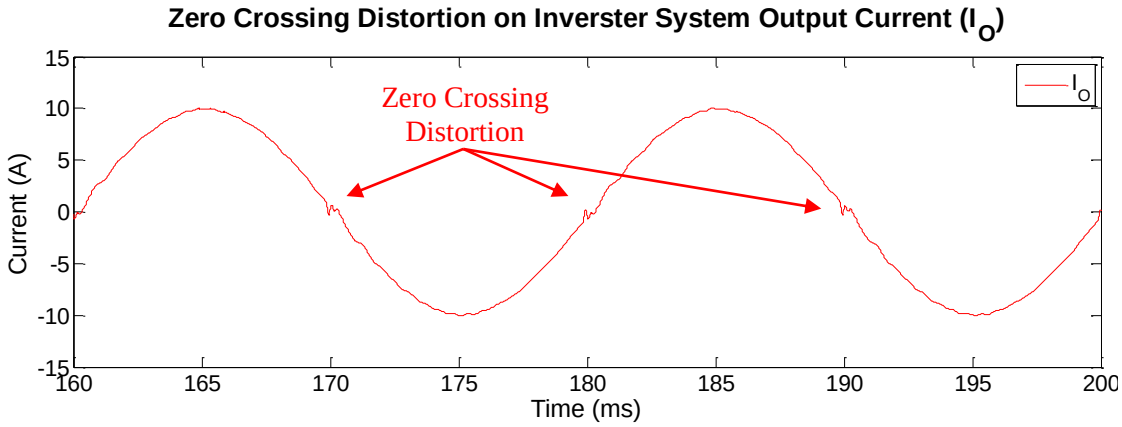

Figure 5.10 Zero crossing distortion on inverter system output current.
(I_{demand} = 7A RMS, V_{DC} = 100V, V_G = 39V RMS, K_p = 1.1, K_i= 0.6, L_f = 1.8mH, C_f = 10µF, L_g = 92.2µH.)

In addition, it has been demonstrated by Kotsopoulos, Heskes, et al. [92] that this zero crossing distortion has the tendency to increase the harmonics of inverter current, in particularly the increase on the harmonics below the 50th are relatively significant. If the resonant frequency of the LC circuit (shown in Figure 5.7) that formed by the inverter filter capacitor and grid inductance is low enough to coincide with these current

harmonics that increased by zero crossing distortion, the resonance can be excited in this circumstance which lead to high magnitude of the inverter system output current harmonic at resonant frequency. This excited resonance can be observed on the output current waveform of inverter system where the oscillation occurs at zero crossing of the current waveform. To demonstrate this, a 300µH of grid inductance is inserted into the model to reduce the resonant frequency of LC circuit and the excitation of resonance due to zero crossing distortion is observed in the simulation. The output current waveform of the inverter system in the simulation is shown in Figure 5.11(a). It shows that the oscillation has occurred at zero crossing of current waveform due to excitation of resonance. This resonance occurs at zero crossing can also be observed in the PCC voltage waveform as shown in Figure 5.11(b).

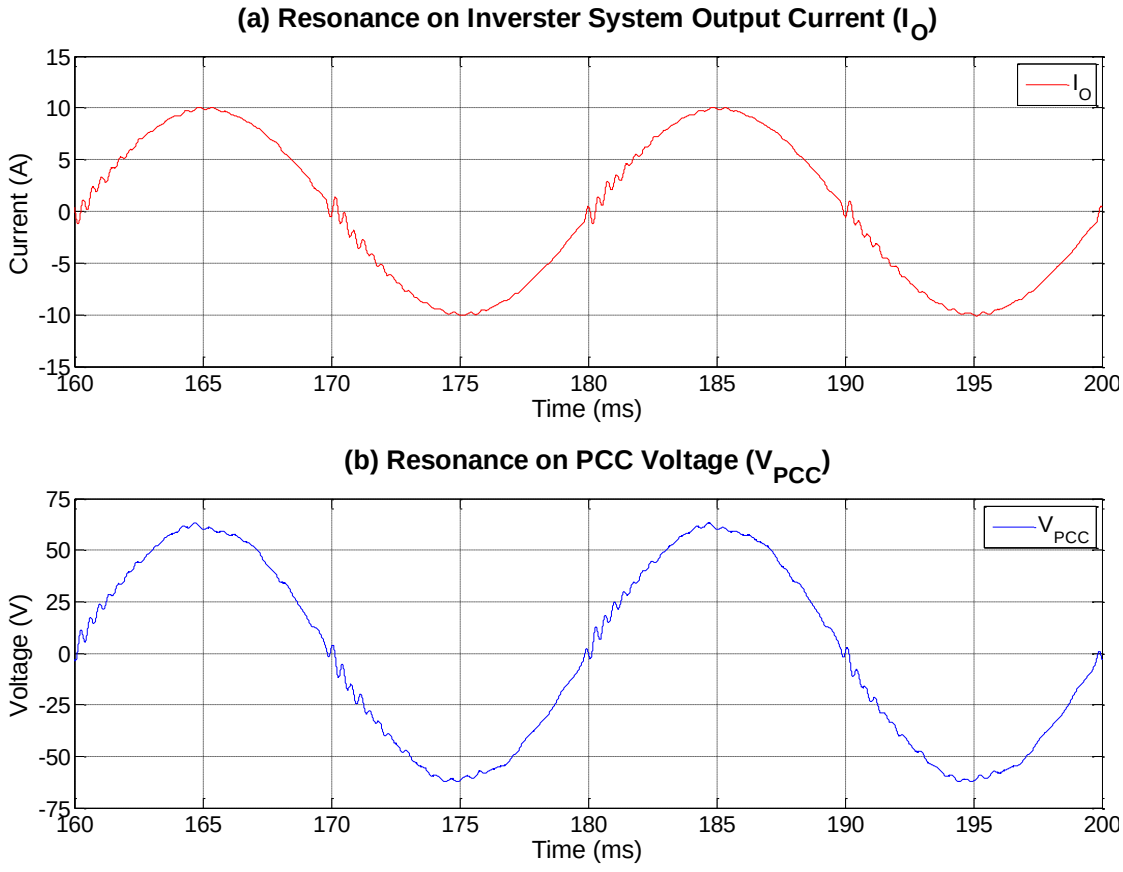

Figure 5.11 Resonance excited by zero crossing distortion at 300µH of grid inductance. (I_{demand} = 7A RMS, V_{DC} = 100V, V_G = 39V RMS, K_p = 1.1, K_i= 0.6, L_f = 1.8mH, C_f = 10µF, L_g = 300µH.)

5.5 Effect of Resonance on PV Inverter Current Control Loop

The output current of the grid-connected PV inverter system is controlled by the microprocessor based current controller. When resonance is excited in the circuit, it interacts with the current control loop and further contributes to this resonant excitation.

Although the resonance phenomenon is widely discussed in previous studies [16, 58, 84, 91], the effect of resonance on the current control loop of grid-connected PV inverter is hardly explained. For this reason, the study involved with the variation in grid impedance that causes the excitation of resonance and their effect on the current control loop of grid-connected PV inverter is carried out in this research. As the study is concerned with the frequency response of the resonance loop, the transfer function based grid-connected PV inverter system model is required for the analysis. It has been shown by Abeyasekera, Johnson, et al. [58] that the model of grid-connected PV inverter can be represented by a simple PI control transfer function with PWM gain and transfer function of LCL branch. However, the fidelity of the controller response to the resonance for this simplified model is not sufficient to represent the practical system. Hence, a high fidelity transfer function based grid-connected PV inverter system model as presented in Section 2.2.4 is developed for the analysis. It is recalled in Figure 5.12 to show the linkage of inverter current controller and distribution grid components, such as background grid voltage (V_G) and grid inductance (L_g).

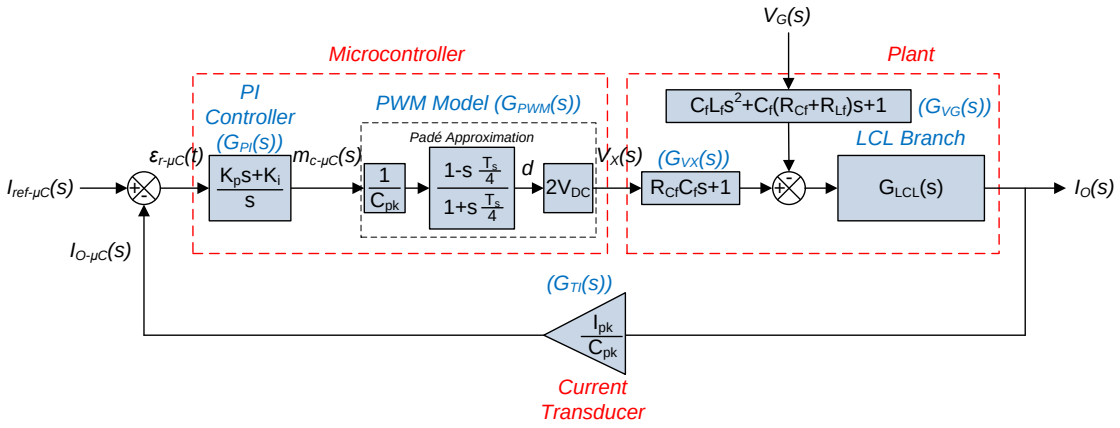

Figure 5.12 Model of grid-connected inverter system with output current feedback PI control.

In addition, the closed loop transfer function of PV inverter current controller presented in Section 4.5.3 that recalled as in Equation (5.3), further shows that the distribution grid components (background grid voltage and grid inductance) form a part of current control loop. This implies the excitation of resonance, depends on the level of resonance effect, might cause the instability of the current controller or have the operational effect on PV inverter system.

$$G_{CL}(s) = \frac{I_{O-\mu C}(s)}{I_{ref-\mu C}(s)} = \frac{G_{PI}(s)G_{PWM}(s)G_{VX}(s)G_{LCL}(s)G_{TI}(s) - \left[\frac{V_G(s)}{I_{ref-\mu C}(s)}\right]G_{VG}(s)G_{LCL}(s)G_{TI}(s)}{1 + G_{PI}(s)G_{PWM}(s)G_{VX}(s)G_{LCL}(s)G_{TI}(s)} \quad \textbf{(5.3)}$$

The grid-connected PV inverter is designed with high output impedance to minimize the harmonic current pollution. Suggested by Enslin, Hulshorst, et al. [16], the output impedance has to be high up to the 40th harmonic to avoid the harmonic current pollution. However, as shown by Figure 5.12 and Equation (5.3), grid characteristics such as grid voltage and grid inductance form a part of the current control loop and closed loop response of inverter current controller. This implies the variation in grid inductance will has the significant effect on the output impedance of the inverter system which in turn varies the current gain of the inverter system and the resonant frequency of the distribution grid. Figure 5.13 shows the closed loop gain of a grid-connected PV inverter designed with lowpass filter cut-off frequency of 1188Hz (with 1.8mH and 10µF of lowpass filter inductance and capacitance respectively), interfaced with various grid inductance. One of the significant effects on the figure is the resonant frequency of the closed loop response, in which the resonant frequency is shifted to lower frequency with higher value of grid inductance.

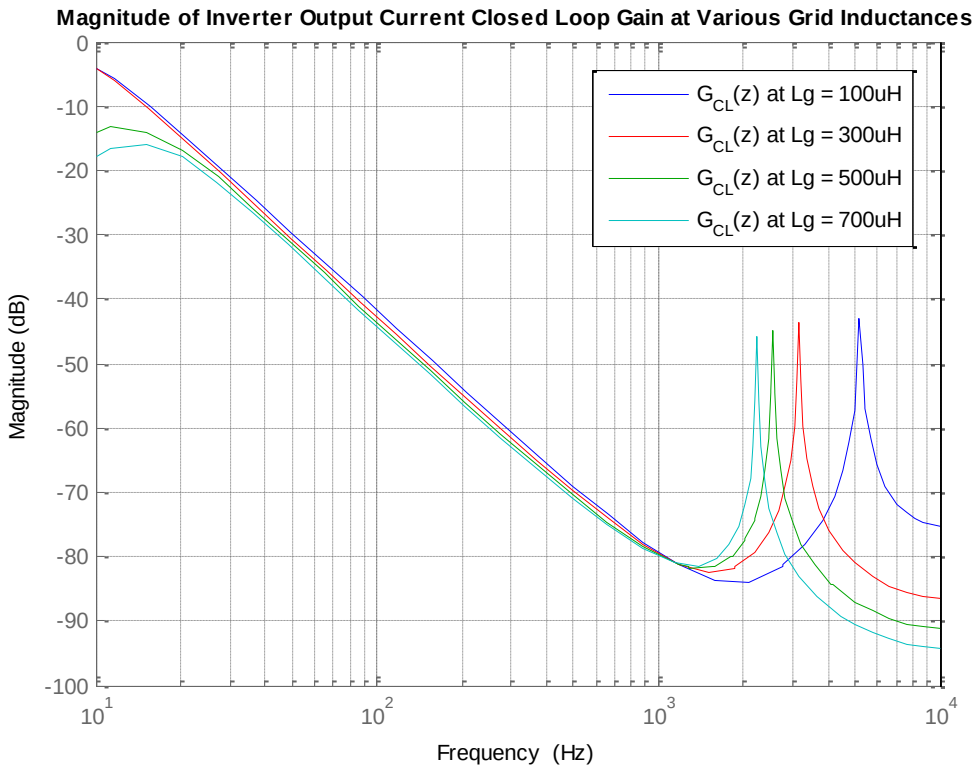

Figure 5.13 Closed loop frequency response of discrete controller output current gain at various grid inductances.
(V_{DC} = 100V, V_G = 43.24V RMS, L_f = 1.8mH, C_f = 10µF, K_p = 1.1, K_i = 0.6, T_s = 50µs.)

To assess the sensitivity of the PV inverter current controller to the background grid voltage distortion, the harmonic impedance suggested by Twining and Holmes [89] can be used to investigate the relationship between the background grid voltage disturbance,

and the resultant inverter system output current injected into the distribution grid, as denoted by Z_{har} in Figure 5.7. As current is inversely proportional to impedance, higher harmonic impedance will result in lower PV inverter system output current harmonic in response to the corresponding external disturbance causes by background grid voltage, and hence higher disturbance rejection capability of the inverter current controller. The harmonic impedance of the PV inverter system can be obtained through the disturbance response of the current control loop in Figure 5.12 with zero current demand. The expression for harmonic impedance is given by Equation (5.4).

If $I_{ref-\mu C}(s) = 0$,

$$I_O(s) = \{I_O(s)G_{TI}(s)[-G_{PI}(s)G_{PWM}(s)G_{VX}(s)] - V_G(s)G_{VG}(s)\}G_{LCL}(s)$$

$$I_O(s) = -I_O(s)G_{TI}(s)G_{PI}(s)G_{PWM}(s)G_{VX}(s)G_{LCL}(s) - V_G(s)G_{VG}(s)G_{LCL}(s)$$

$$I_O(s)[1 + G_{TI}(s)G_{PI}(s)G_{PWM}(s)G_{VX}(s)G_{LCL}(s)] = -V_G(s)G_{VG}(s)G_{LCL}(s)$$

$$Z_{har}(s) = \left.\frac{V_G(s)}{I_O(s)}\right|_{I_{ref-\mu C}(s)=0} = -\frac{1 + G_{TI}(s)G_{PI}(s)G_{PWM}(s)G_{VX}(s)G_{LCL}(s)}{G_{VG}(s)G_{LCL}(s)} \quad \textbf{(5.4)}$$

Furthermore, the robustness of the current controller to the disturbance caused by background grid distortion can be assessed through the dynamic stiffness of the system suggested by Ryan, Brumsickle, et al. [93]. The dynamic stiffness of the inverter current controller can be obtained via inverse of harmonic impedance expression, as given by Equation (5.5).

$$Y_{out}(s) = \left.\frac{I_O(s)}{V_G(s)}\right|_{I_{ref-\mu C}(s)=0} = -\frac{G_{VG}(s)G_{LCL}(s)}{1 + G_{TI}(s)G_{PI}(s)G_{PWM}(s)G_{VX}(s)G_{LCL}(s)} \quad \textbf{(5.5)}$$

Figure 5.14 shows the effect of grid inductance on the harmonic impedances of PV inverter system, when interfaced with the distribution grid. By comparing the harmonic impedances without grid inductance (0μH of L_g) and with 100μH of grid inductance as shown in the figure, an undesirable resonant point (at f_{res2}) with low impedance is introduced when a 100μH of grid inductance is included. This is because by introducing the grid inductance into the system transforms the 2nd order LC arrangement of the PV inverter lowpass filter into a 3rd order LCL system with additional resonant point that very low in impedance (shown by f_{res2} in Figure 5.14).

As the resonant point that very high in impedance (shown by f_{res1} in Figure 5.14) is due to the interaction between the PV inverter lowpass filter inductance (L_f) and capacitance (C_f), the energy provided by the PV inverter is oscillating between the inverter filter inductance and capacitance at the resonant frequency. This leads to very high impedance at the output side of the inverter filter and hence the resultant harmonic current injected into the grid source in response to the resonance is actually small. The frequency at this resonant point can be calculated by the resonant frequency equation of an LC circuit in Equation (5.1).

Furthermore, the resonant point that very low in impedance (shown by f_{res2} in Figure 5.14) is due to the interaction between the PV inverter lowpass filter impedance (L_f and C_f) and grid inductance (L_g). Here, a large amount of energy oscillates between the inverter filter capacitance and grid inductance at the resonant point. This leads to very low impedance at the grid side of the grid inductance and hence the resultant harmonic current injected into the grid in response to the resonance is high. The resonant frequency at this resonant point can be calculated by the resonant frequency equation of LCL circuit in Equation (5.2).

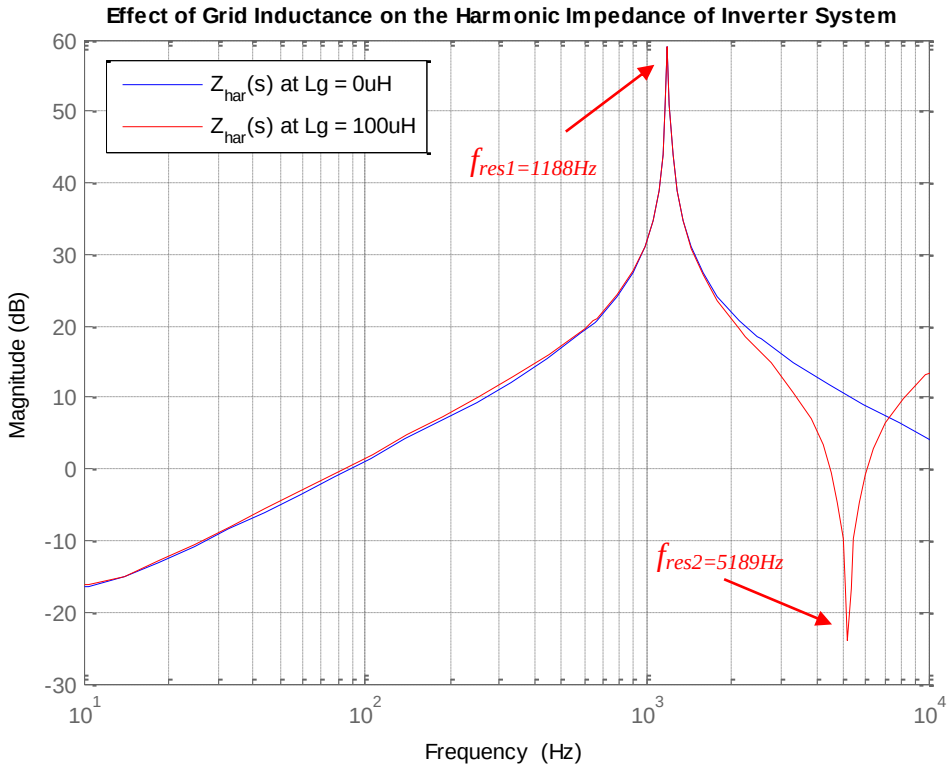

Figure 5.14 Difference in harmonic impedance (Z_{har}) of grid-connected PV inverter system without and with the grid inductance (L_g).
(V_{DC} = 100V, V_G = 43.24V RMS, L_f = 1.8mH, C_f = 10μF, K_p = 1.1, K_i = 0.6.)

As shown in Equation (5.2), the resonant frequency of the low impedance resonant point is a function of the grid inductance. Any variation in grid inductance will cause a shift in the resonant frequency. This shifting effect is shown in Figure 5.15, where the low impedance resonant peak (at f_{res2}) is shifted to lower frequency when the grid inductance value is increased. It is very apparent in the figure that the resonant frequency of low impedance resonant peak is shifted from 5189Hz to 2249Hz when the grid inductance is increased from 100µH up to 700µH with 200µH step. It is noted that the resonant peak that very high in impedance is remained at 1188Hz over the grid impedance range (shown by f_{res1} in Figure 5.15) as it is the resonant point of inverter LC lowpass filter and hence not affected by the grid inductance.

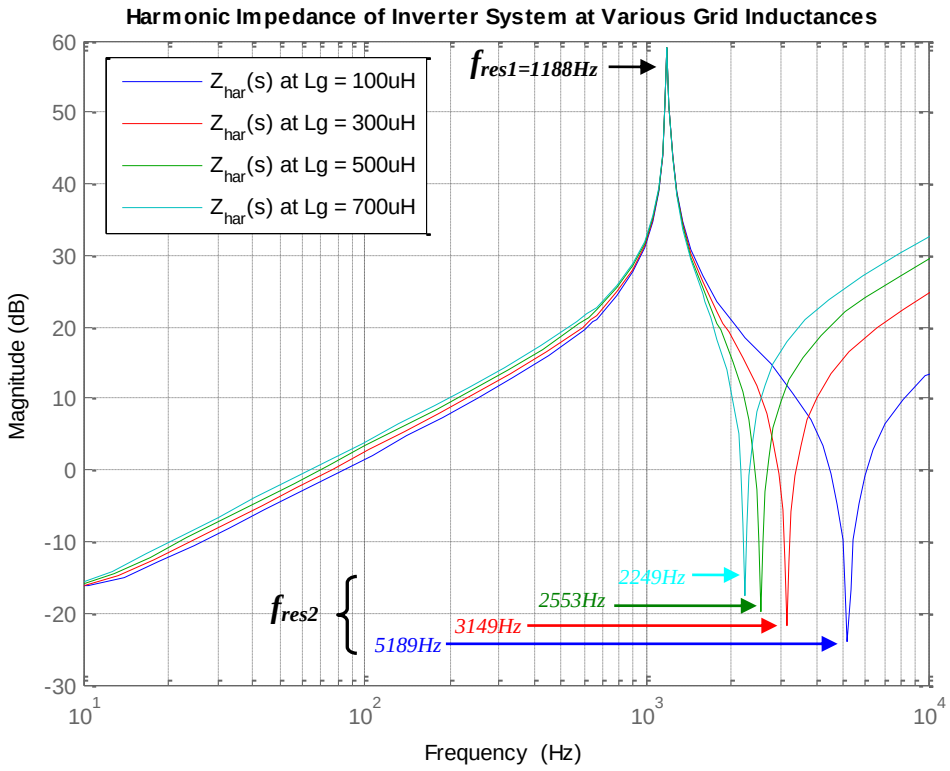

Figure 5.15 Effect of grid inductance (L_g) on the harmonic impedance (Z_{har}) of grid-connected PV inverter system.
(V_{DC} = 100V, V_G = 43.24V RMS, L_f = 1808µH, C_f = 9.9252µF, K_p = 1.1, K_i = 0.6.)

5.6 Effect of Resonance on Harmonic Performance of Current Controller in Practical

Although the effect of the resonance on PV inverter current control loop is assessed in Section 5.5, the harmonic performance of inverter current controller in response to the specific value of grid inductance and background grid voltage in reality are hardly shown on the frequency response chart. Hence the practical experiment is carried out to interface the experimental grid-connected PV inverter system with the distribution grid

in the laboratory. The detail of the test rig setup and implementation of the experimental grid-connected inverter system is discussed in Chapter 3.

In practical experiment, the background grid voltage is emulated by the isolation transformer and the variac that used to provide the isolation and step down the 230V AC mains voltage in the laboratory respectively, while variable inductor is placed in between the experimental grid-connected PV inverter system and the isolation transformer to represent the variable grid inductance. The voltage waveform of inverter bridge output voltage (V_X), PCC voltage (V_{PCC}), and background grid voltage (V_G), as well as current waveform of inverter bridge output current (I_X) and inverter system output current injected into the grid (I_O), are recorded throughout the experiment utilising Yokogawa© PZ4000 Power Anaylzer and analysed by Matlab/Simulink®. A conventional PI current control loop without voltage feedforward is implemented in the practical experiment in order to study the performance of PI controller in response to the resonance, and both the proportional gain (K_p = 1.1) and integral gain (K_i = 0.6) remain unchanged throughout the experiment. A recorded waveform of the practical experiment without added grid inductance (emulated L_g = 0uH) is shown in Figure 5.16.

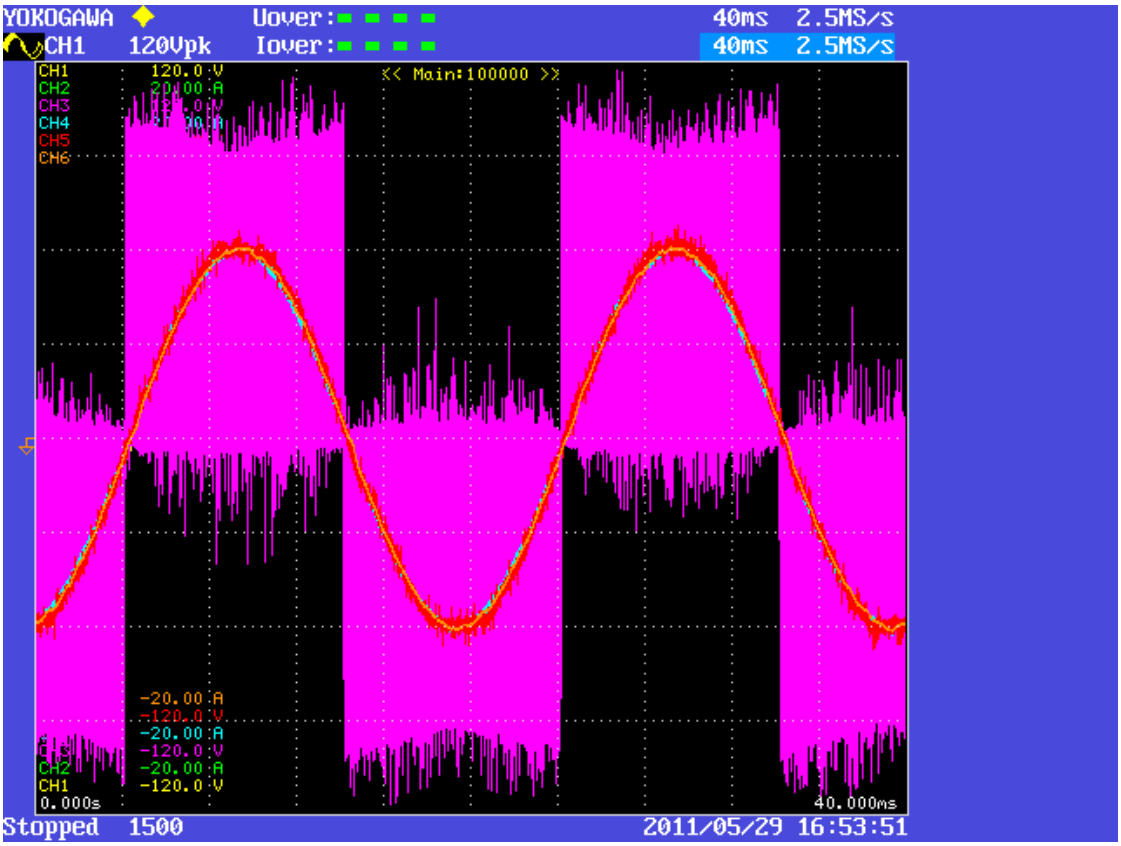

Figure 5.16 Waveform of the practical experiment without added grid inductance.
(CH1 = V_{PCC}, CH2 = I_O, CH3 = V_X, CH4 = I_X, CH5 = V_G, CH6 = I_O;
I_{demand} = 7A RMS, V_{DC} = 100V, V_G = 39V RMS, f_1 = 50Hz, K_p = 1.1, K_i = 0.6, L_g = 0μH.)

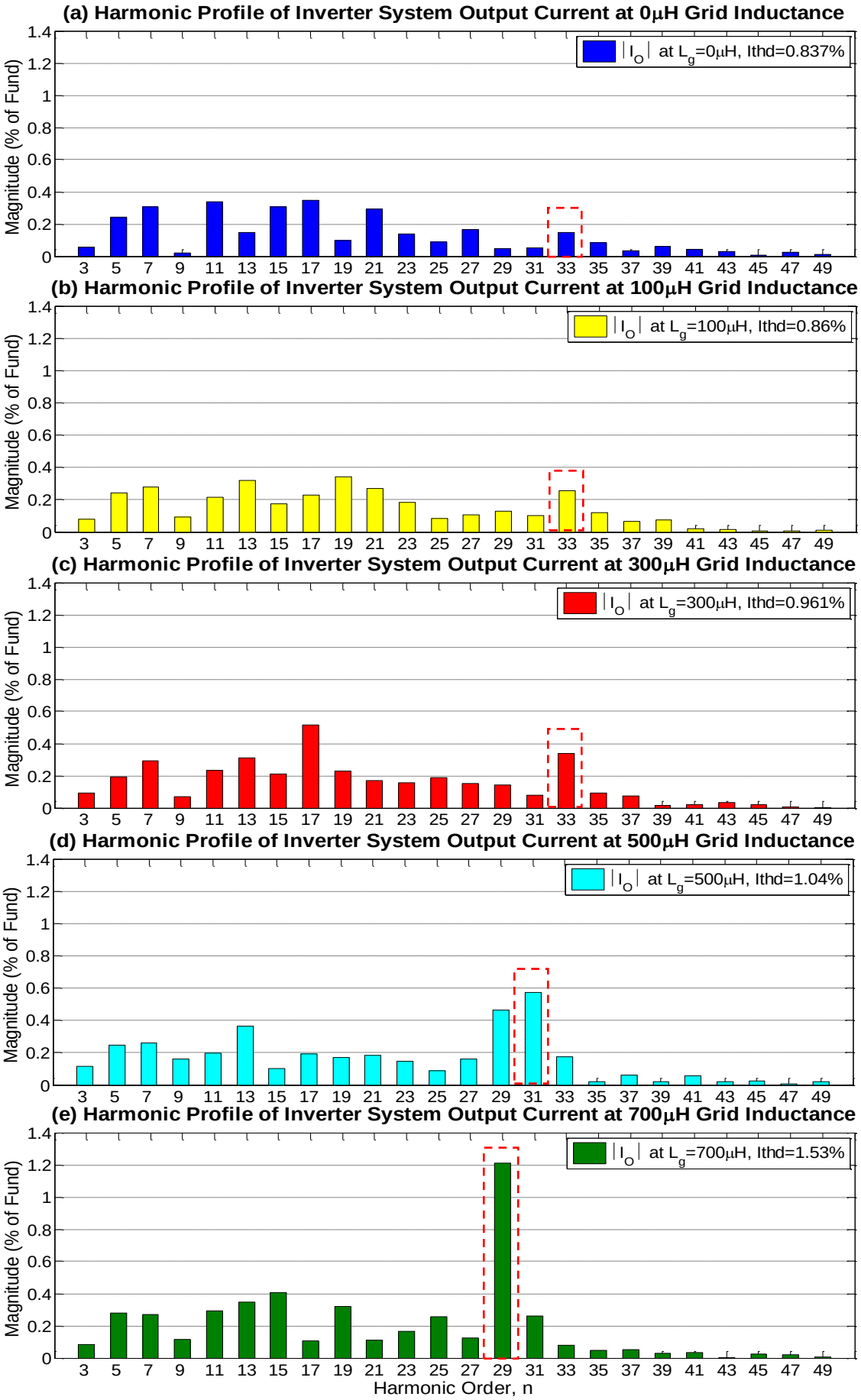

Figure 5.17 Effect of the grid inductance (L_g) on the frequency of resonance and the output current harmonic profile (I_O) of grid-connected PV inverter system.
(I_{demand} = 7A RMS, V_{DC} = 100V, V_G = 39V RMS, f_1 = 50Hz, K_p = 1.1, K_i = 0.6.)

The harmonic profiles of the inverter system output current in the practical experiment at the emulated grid inductance of 0µH up to 700µH are shown in Figure 5.17. As shown by Figure 5.17(a) to Figure 5.17(e), the current harmonics between 29th and 33rd are sensitive to the variation in grid inductance. This shows that increasing the grid inductance by 700µH leads to the resonance excitation between the 29th and the 33rd harmonics (as shown by red boxes in Figure 5.17), as these are the resonant frequencies of the low impedance resonant point of LCL system at specific grid inductance as shown by Figure 5.14. By comparing the low impedance resonant frequency point of the LCL system in the theoretical analysis (Figure 5.15 (f_{res2})) to the practical experiment (Figure 5.17), the frequency of the low impedance resonant point in the practical case is much lower. This is due to the contribution of leakage and magnetizing reactance of the isolation transformer and variac installed in the practical experiment; these can be lumped to form a high value of grid inductance that shifts the frequency of low impedance resonant point to between 33rd and 29th harmonics in practical experiment.

The trends of inverter system output current harmonic profile for specific grid inductances are compared as shown in Figure 5.18. These show that the excitation of low impedance resonance due to the rise in grid inductance led to significant increase in the magnitude of current harmonic at corresponding low impedance resonant frequency. Furthermore, there are also significant increases in the magnitude of the neighbouring harmonic around the resonant point. As a result, there is a noticeable rise in the inverter system output current THD.

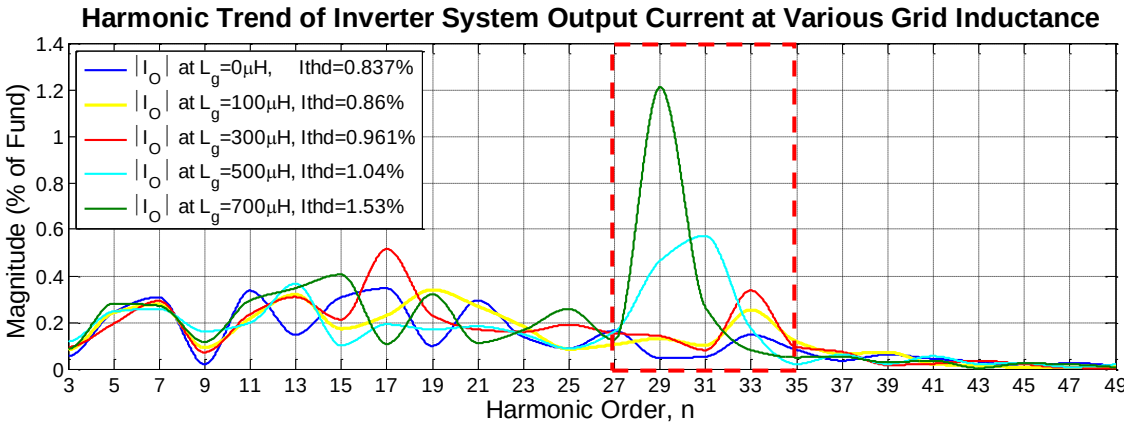

Figure 5.18 Harmonic trend comparison of grid-connected PV inverter system output current (I_O) at various grid inductances (L_g).
(I_{demand} = 7A RMS, V_{DC} = 100V, V_G = 39V RMS, f_1 = 50Hz, K_p = 1.1, K_i = 0.6.)

For conventional PI controller implemented in practical experiment, the proportional gain (K_p) is responds to the command of the error signal while the integral gain (K_i) is aimed to respond the disturbance, hence the proportional term and integral term are referred to as command response and disturbance response respectively (Ellis [60]). Although both the command response and disturbance response are improved by high loop gains, Ellis [60] suggested that a high proportional gain provides a higher bandwidth and better ability to reject disturbances with high frequency content, while a high integral gain helps the control system reject lower frequency disturbances. Furthermore, Twining and Holmes [59, 94] suggested that the absolute magnitude of the system harmonic impedance increases with a high value of proportional gain and hence the harmonic current caused by the background grid distortion and resonance will decrease for higher proportional gain. All of these suggestions have led to the concept of higher proportional gain will improve the harmonic performance of current controller in response to background grid voltage distortion and resonance phenomenon.

The harmonic impedance expression of PV inverter system interfaced with the grid inductance can be simplified by substituting a constant gain (K_{PWM}) for PWM model ($G_{PWM}(s)$) in Figure 5.12, as shown by derivation below. The simplified harmonic impedance expression of the system is given by Equation (5.6), neglecting the damping effect of circuit resistance. It shows that the harmonic impedance of the system increases with respect to the proportional gain (K_p) of current controller.

By substituting K_{PWM} for $G_{PWM}(s)$,

$$I_O(s) = \{I_O(s)G_{TI}(s)[-G_{PI}(s)G_{PWM}(s)G_{VX}(s)] - V_G(s)G_{VG}(s)\}G_{LCL}(s)$$

$$I_O(s) = \left\{-I_O(s)K_{TI}\left(\frac{K_p s + K_i}{s}\right)K_{PWM}(R_{Cf}C_f s + 1) - V_G(s)\left[C_f L_f s^2 + C_f(R_{Cf} + R_{Lf})s + 1\right]\right\}G_{LCL}(s)$$

$$I_O(s) = \left\{\frac{-I_O(s)K_{TI}K_{PWM}(K_p s + K_i)(R_{Cf}C_f s + 1) - V_G(s)\left[C_f L_f s^3 + C_f(R_{Cf} + R_{Lf})s^2 + s\right]}{s}\right\}G_{LCL}(s)$$

$$\frac{s}{G_{LCL}(s)} = \frac{-I_O(s)K_{TI}K_{PWM}(K_p s + K_i)(R_{Cf}C_f s + 1) - V_G(s)\left[C_f L_f s^3 + C_f(R_{Cf} + R_{Lf})s^2 + s\right]}{I_O(s)}$$

$$\frac{s}{G_{LCL}(s)} = -K_{TI}K_{PWM}(K_p s + K_i)(R_{Cf}C_f s + 1) - \frac{V_G(s)}{I_O(s)}\left[C_f L_f s^3 + C_f(R_{Cf} + R_{Lf})s^2 + s\right]$$

$$\frac{V_G(s)}{I_O(s)}\left[C_f L_f s^3 + C_f(R_{Cf} + R_{Lf})s^2 + s\right] = -K_{TI}K_{PWM}(K_p s + K_i)(R_{Cf}C_f s + 1) - \frac{s}{G_{LCL}(s)}$$

$$\frac{V_G(s)}{I_O(s)} = \frac{-K_{TI}K_{PWM}(K_p s + K_i)(R_{Cf}C_f s + 1) - \frac{s}{G_{LCL}(s)}}{C_f L_f s^3 + C_f(R_{Cf} + R_{Lf})s^2 + s}$$

$$\frac{V_G(s)}{I_O(s)} = \frac{-K_{TI}K_{PWM}K_p R_{Cf}C_f s^2 - K_{TI}K_{PWM}K_p s - K_{TI}K_{PWM}K_i R_{Cf}C_f s - K_{TI}K_{PWM}K_i - \frac{s}{G_{LCL}(s)}}{C_f L_f s^3 + C_f(R_{Cf} + R_{Lf})s^2 + s}$$

$$\frac{V_G(s)}{I_O(s)} = \frac{-K_{TI}K_{PWM}K_pR_{Cf}C_fs^2 - K_{TI}K_{PWM}\left(K_p + K_iR_{Cf}C_f\right)s - K_{TI}K_{PWM}K_i - \frac{s}{G_{LCL}(s)}}{C_fL_fs^3 + C_f\left(R_{Cf} + R_{Lf}\right)s^2 + s}$$

$$\frac{V_G(s)}{I_O(s)}$$

$$= \frac{-K_{TI}K_{PWM}K_pR_{Cf}C_fs^2 - K_{TI}K_{PWM}\left(K_p + K_iR_{Cf}C_f\right)s - K_{TI}K_{PWM}K_i - C_fL_fL_gs^4 - C_f\left[L_g\left(R_{Cf} + R_{Lf}\right) + L_f\left(R_{Cf} + R_g\right)\right]s^3 - \left[L_g + L_f + C_f\left(R_gR_{Cf} + R_{Lf}R_{Cf} + R_{Lf}R_g\right)\right]s^2 - \left(R_g + R_{Lf}\right)s}{C_fL_fs^3 + C_f\left(R_{Cf} + R_{Lf}\right)s^2 + s}$$

$$Z_{har}(s) = \frac{V_G(s)}{I_O(s)}$$

$$= -\left\{\frac{C_fL_fL_gs^4 + C_f\left[L_g\left(R_{Cf} + R_{Lf}\right) + L_f\left(R_{Cf} + R_g\right)\right]s^3 + \left[L_g + L_f + C_f\left(R_gR_{Cf} + R_{Lf}R_{Cf} + R_{Lf}R_g\right) + K_{TI}K_{PWM}K_pR_{Cf}C_f\right]s^2 + \left[R_g + R_{Lf} + K_{TI}K_{PWM}\left(K_p + K_iR_{Cf}C_f\right)\right]s + K_{TI}K_{PWM}K_i}{C_fL_fs^3 + C_f\left(R_{Cf} + R_{Lf}\right)s^2 + s}\right\}$$

By neglecting the resistance damping effect, $R_{Lf} = R_{Cf} = R_{Lg} = 0$,

$$Z_{har}(s) = \frac{V_G(s)}{I_O(s)} = -\left[\frac{C_fL_fL_gs^4 + \left(L_g + L_f\right)s^2 + \left(K_{TI}K_{PWM}K_p\right)s + K_{TI}K_{PWM}K_i}{C_fL_fs^3 + s}\right] \quad \textbf{(5.6)}$$

However, increase the proportional gain (K_p) of current controller has increased the level of oscillation and ripples at the output of inverter system, as demonstrated by Twining and Holmes [59, 94]. Furthermore, it is observed in the practical experiment of the research that the level of oscillation and ripples tend to be more severe at higher value of grid inductance as higher value of grid inductance shift the low impedance resonance to lower frequency. These oscillation and ripple could coincide with this low impedance resonance at resonant frequency and hence cause the excitation of low impedance resonance.

Figure 5.19 shows the waveforms of PCC voltage and inverter system output current at grid inductance up to 700μH in practical experiment. As shown from Figure 5.19(a) to Figure 5.19(e) that the oscillation and ripples on PCC voltage waveform is increased with higher value of grid inductance. This causes the distortion of inverter system output current and hence an increase in both the PCC voltage and inverter system output current THD. It is noted that although the THD value of the inverter system output current is considered low compared to the limits of harmonic standards [17, 19, 22], increase in PV inverter power level and the number of PV inverters connected to the same PCC are likely to increase the oscillation and ripples on PCC voltage waveform. Hence, THD of inverter system output current increases and the limits of harmonic standards might be exceeded (as distortion on PCC voltage increases when higher current flowing through the grid inductance, which in turn affects the harmonic performance of inverter system current controller). This interaction has also been shown by Equation (5.6) in which the harmonic impedance is inversely proportional to inverter system output current.

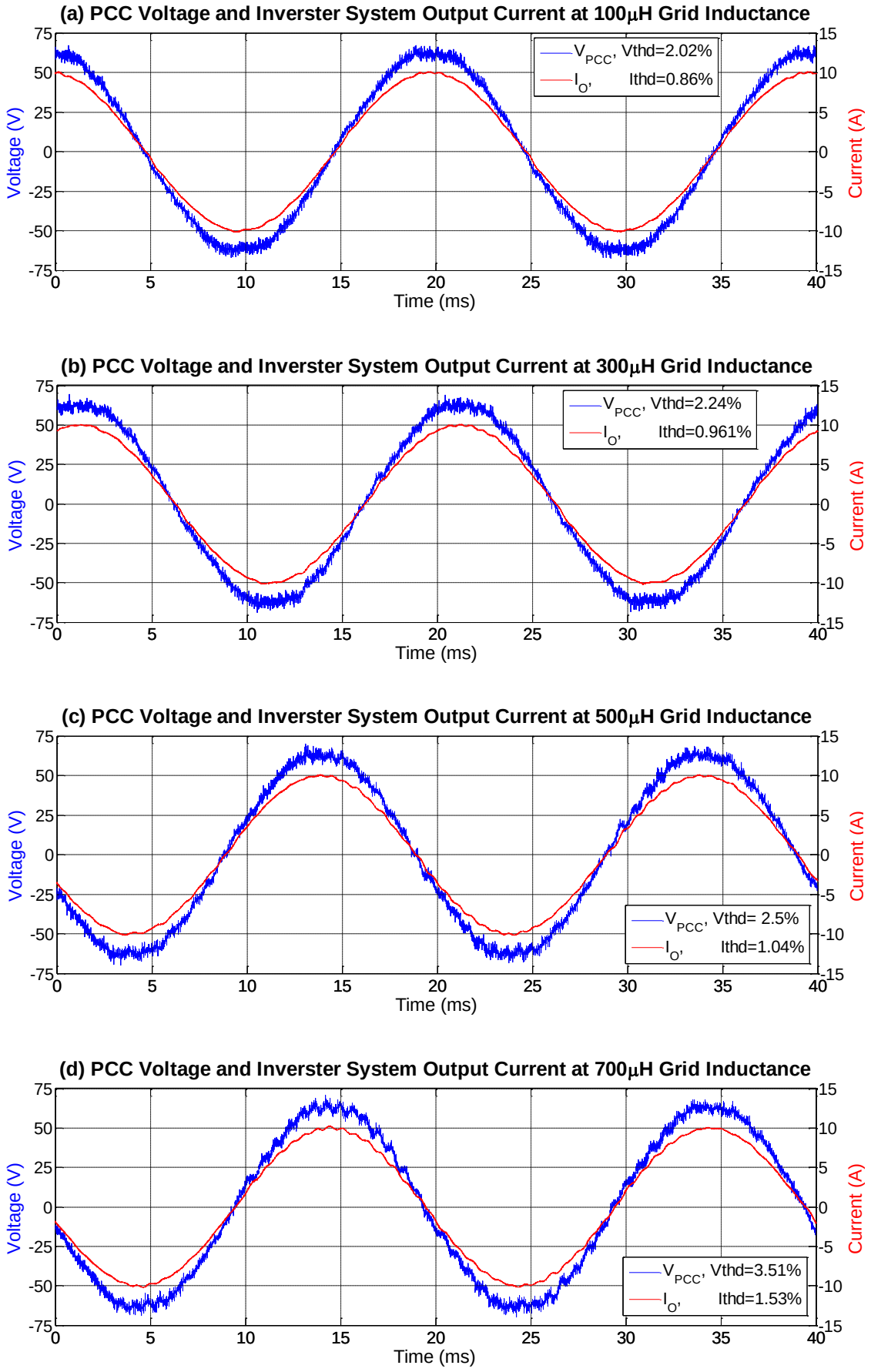

Figure 5.19 Waveforms of PCC voltage (V_{PCC}) and inverter system output current (I_O) at various grid inductances (L_g).

(I_{demand} = 7A RMS, V_{DC} = 100V, V_G = 39V RMS, f_1 = 50Hz, K_p = 1.1, K_i = 0.6.)

In Figure 5.19(d), there is noticeable oscillation in waveforms of PCC voltage and inverter system output current due to high level of resonance. This resonance is excited by the oscillation and ripples that caused by excessive PI control proportional gain (K_P) at high grid inductance value. The mechanism of this resonance is shown in Figure 5.20. During this resonance, large amount of energy is oscillating from inverter filter capacitance (C_f) to both inverter filter inductance (L_f) and grid inductance (L_g), this in turn causing the oscillation in the PCC voltage (V_{PCC}), inverter bridge output current (I_X) and inverter system output current (I_O). As the harmonic impedance is very low at resonant frequency (as shown by Z_{har} in Figure 5.20), the oscillating inverter system output current that very high in its harmonics magnitude and only damped by the circuit resistance, is injected into the distribution grid source. This also implies the increase in inverter system output current THD.

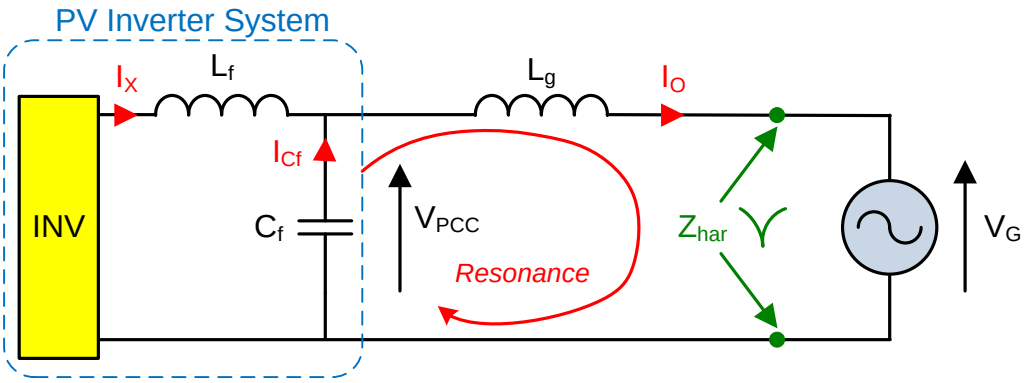

Figure 5.20 Mechanism of low impedance resonance due to the interaction between inverter filter inductance (L_f), inverter filter capacitance (C_f) and grid inductance (L_g).

To show the mechanism of low impedance resonance due to the interaction between PV inverter filter capacitance and grid inductance, the voltage and current waveforms of the practical experiment with 700µH of grid inductance are analysed via FFT function in Matlab/Simulink®. The harmonic profile comparison (in RMS magnitude) of the PCC voltage (V_{PCC}) and background grid voltage (V_G) is shown in Figure 5.21, while Figure 5.22 shows the harmonic comparison (in RMS magnitude) of inverter bridge output current (I_X) and inverter system output current (I_O). As shown in Figure 5.21, the excitation of low impedance resonance has caused the oscillation in PCC voltage which led to high voltage harmonic at resonant frequency (29^{th} harmonic). As this resonance is caused by interaction between PV inverter filter capacitance and grid inductance, high value of current is released by filter capacitance and then flows through the low impedance path (distribution grid source) at resonant frequency. This is shown by the

high magnitude of inverter system output current compared to the relatively low inverter bridge output current at the resonant frequency in Figure 5.22.

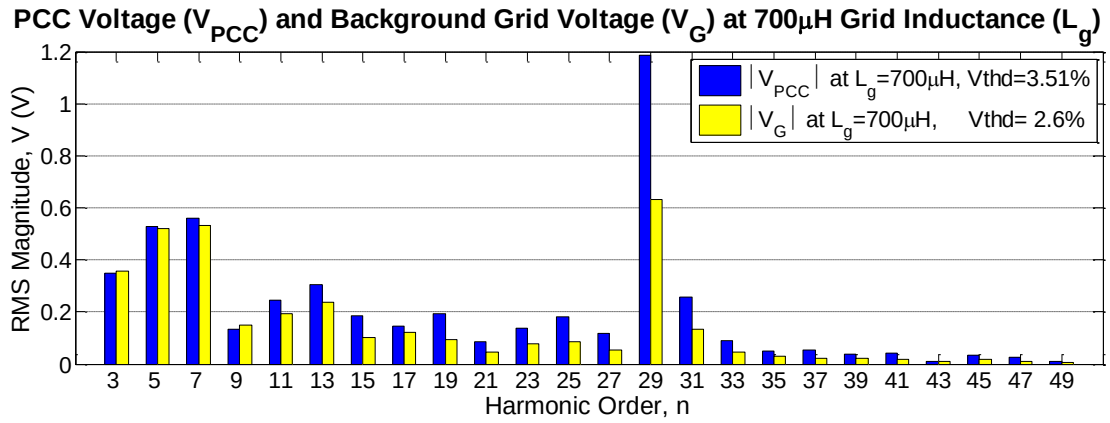

Figure 5.21 Harmonic profile comparison of PCC voltage (V_{PCC}) and background grid voltage (V_G) at 700µH of grid inductance (L_g).
(I_{demand} = 7A RMS, V_{DC} = 100V, V_G = 39V RMS, f_1 = 50Hz, K_p = 1.1, K_i = 0.6, L_g = 700µH.)

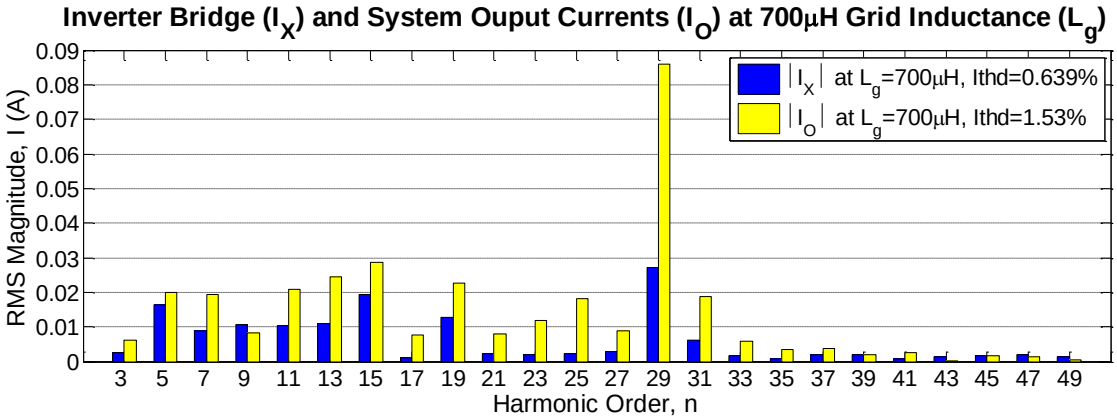

Figure 5.22 Harmonic profile comparison of inverter bridge output current (I_X) and inverter system output current (I_O) at 700µH of grid inductance (L_g).
(I_{demand} = 7A RMS, V_{DC} = 100V, V_G = 39V RMS, f_1 = 50Hz, K_p = 1.1, K_i = 0.6, L_g = 700µH.)

Ideally, the typical grid-connected PV inverter system is desired to inject the current into the distribution grid with the same phase angle as the PCC voltage. In other words, the PV inverter is designed to always operate at unity power factor. In practice, the inverter system output current and PCC voltage can be synchronized through a Phased Locked Loop (PLL) device or Zero Crossing Detector (ZCD). These synchronization devices require the PCC voltage waveform for synchronism and hence any distortion of the PCC voltage may compromise the accuracy of these devices. Excessive oscillations or ripples on PCC voltage, caused by resonance, may lead to mal-functioning of these synchronization equipments. Figure 5.23 shows the severe oscillation on PCC voltage and inverter system output current due to the mal-functioning of ZCD in practical experiment caused by high level of resonance at 1000µH of grid inductance.

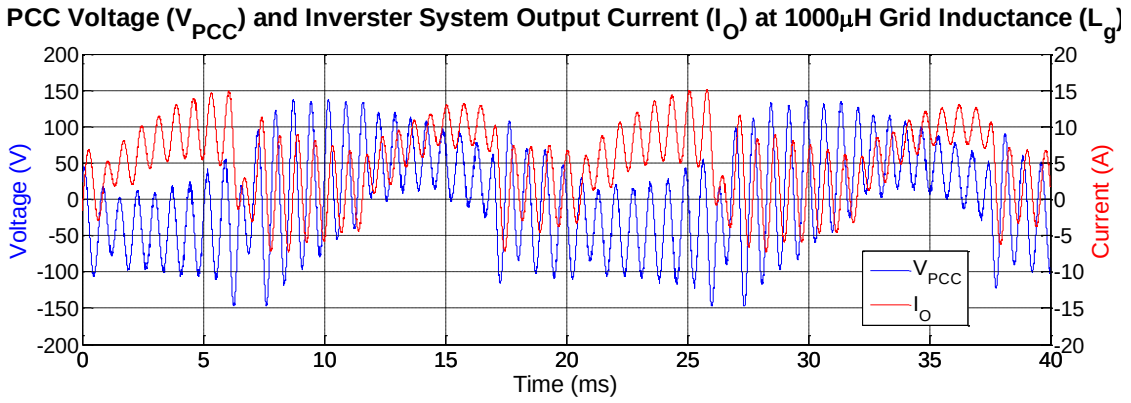

Figure 5.23 Oscillation in PCC voltage (V_{PCC}) and inverter system output current (I_O) at 1000µH of grid inductance (L_g).
(I_{demand} = 7A RMS, V_{DC} = 100V, V_G = 39V RMS, f_1 = 50Hz, K_p = 1.1, K_i = 0.6, L_g = 1000µH.)

5.7 Mitigation of Resonance

As the impedance of distribution grid changes over time due to variation in operating conditions, the resonant frequency of the network is dynamically changing in response to the impedance variation. Resonance can be excited in the distribution grid when the harmonics of the grid-connected PV inverter output coincides with the resonant frequency created by the change in the grid impedance. Such a situation may be possible, even though the PV inverter is initially configured to avoid the resonant frequency during installation and commissioning.

However, it is observed in the practical experiment (shown in Section 5.6) that the experimental grid-connected PV inverter system with conventional PI control does not effectively suppress the oscillation cause by resonance and hence high level of harmonic distortion can be measured on inverter output current or PCC voltage. Based on this point of view, it is desired to design a robust grid-connected PV inverter which remain stable and with reasonably good harmonic performance at resonance. The robustness of the grid-connected PV inverter on resonance is particularly important in Smart Grid [95] which is becoming increasingly popular. As Smart Grid might consist of various sources of distributed generation connected to, or indeed disconnected from, the PCC at any time, the resonant frequency of the network is more volatile than a traditional grid system fed by centralized power generation. Hence, resonance is more likely to be excited in Smart Grid if the PV inverter is not designed to suppress, or ideally avoid, resonance.

From the aspect of the grid-connected PV inverter, resonance can be suppressed by means of passive and/or active damping. With simple passive damping, a resistor is

placed in series with the PV inverter filter capacitor or inductor to damp the resonance. Due to the additional power losses and voltage drops (controller operates in higher modulation depth to compensate the voltage drops across additional resistances) caused by the additional resistance, it is advantageous and more flexible to make use of control algorithm to actively damp the resonance. This has been demonstrated by Wessels, Dannehl, et al. [96], by adding a virtual resistor into the control loop to damp the resonance of an LCL filter. For three-phase voltage source converters (VCS), the active damping of LCL resonance can be achieved by implementing voltage oriented control (VOC) together with the virtual flux and virtual resistor, as demonstrated by Gullvik, Norum, et al. [97]. Another measure of damping the resonance for three-phase VSC is suggested by Blasko and Kaura [98], by applying the lead-lag element in the synchronous reference frame to the feedback of the filter capacitor voltage. Furthermore, in terms of feedback control, Twining and Holmes [59] present the damping of resonance by means of filter capacitor current feedback, while suppression of resonance by filter inductor current feedback is suggested by Abeyasekera, Johnson, et al. [58], and Engel, Rigbers, et al. [99]. However, the methods to damp the resonance discussed above require additional voltage or current sensors, which might increase the cost of the converter system. Based on this reason, an approach to damp the resonance without an additional sensor is proposed by Dick, Richter, et al. [100]. They propose the damping of resonance by placing an Infinite Impulse Response (IIR) filter on the current feedback of LCL output. Although the number of sensors is reduced in this approach, additional computational power, or computational time, is essential for proper implementation of the digital IIR filter and hence a higher specification microcontroller may be needed.

Despite the different measures of damping resonance in the literature above, most devote attention on the stability of the current controller under excitation of resonance. The overall harmonic performance of the current control loop is hardly assessed. Therefore, various types of control measure on grid-connected PV inverter system are implemented and assessed in this research in order to develop a PV inverter which will remain robust and with reasonably good harmonic performance under excitation of resonance. Three different types of control are considered in this research. Among these control measures, terminal voltage feedforward and fundamental sine wave feedfoward are discussed in this chapter, while proposed adaptive PI current control is discussed extensively in Chapter 6.

5.7.1 *Terminal Voltage Feedforward*

As the operating condition of the distribution grid is change over time, this change can be measured by the sensors and seen by the PI control loop of the grid-connected PV inverter controller as the disturbances. To counter with the disturbances, terminal voltage feedforward topology that feed the terminal voltage signal of grid-connected PV inverter system (PCC voltage) into the control loop can be implemented to improve the response of the controller. This terminal voltage feedforward term unburdens the control loop as most of the inverter excitation can be generated in the feedforward path, hence the command response become less dependent on the control loop bandwidth and the control law is required to provide only corrections and to respond to disturbances (Ellis [60]). In other words, a portion of control signal to counter with the PCC voltage (V_{PCC}) at the terminal voltage of PV inverter is provides by feedforward path, while the PI controller only need to compensate and control the voltage drops across the inductance of inverter LC lowpass filter (V_{Lf}), and hence control the inverter system output current injects to the distribution grid. This is depicted by the terminal voltage feedforward control structure of PI controller as shown in Figure 5.24.

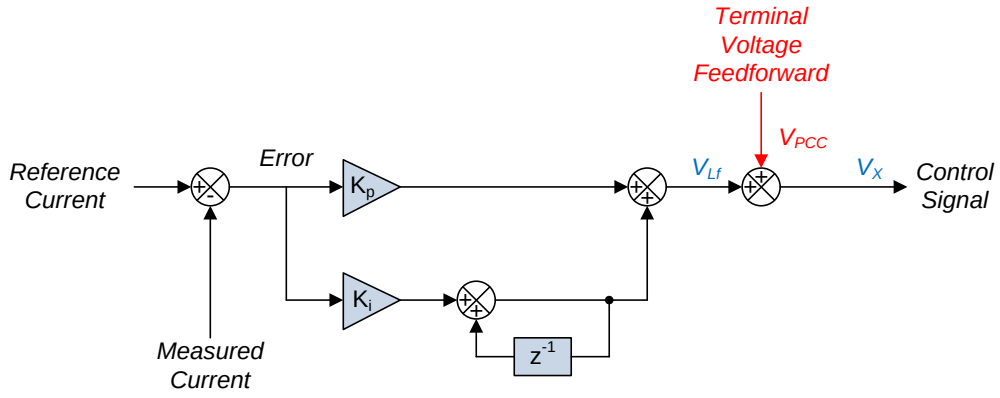

Figure 5.24 Block diagram of PI current controller with terminal voltage feedforward.

Considering harmonics, there is no harmonic current injected into the distribution grid if the corresponding voltage harmonics of inverter bridge output voltage (V_X) and the PCC voltage (V_{PCC}) are exactly the same in magnitude and phase angle, as explained in Section 4.4. In practice, the waveform of PCC voltage that consists range of harmonics (including the resonant harmonics) is instantaneously feedforwards to the current control loop to generate the voltage harmonics (including the resonant harmonics) with the same magnitude and phase angle as PCC voltage at the output of inverter bridge, in order to prevent the harmonic current flow. Eventually, any oscillation on the PCC voltage will be compensated by the feedforward term and hence no excitation of resonance.

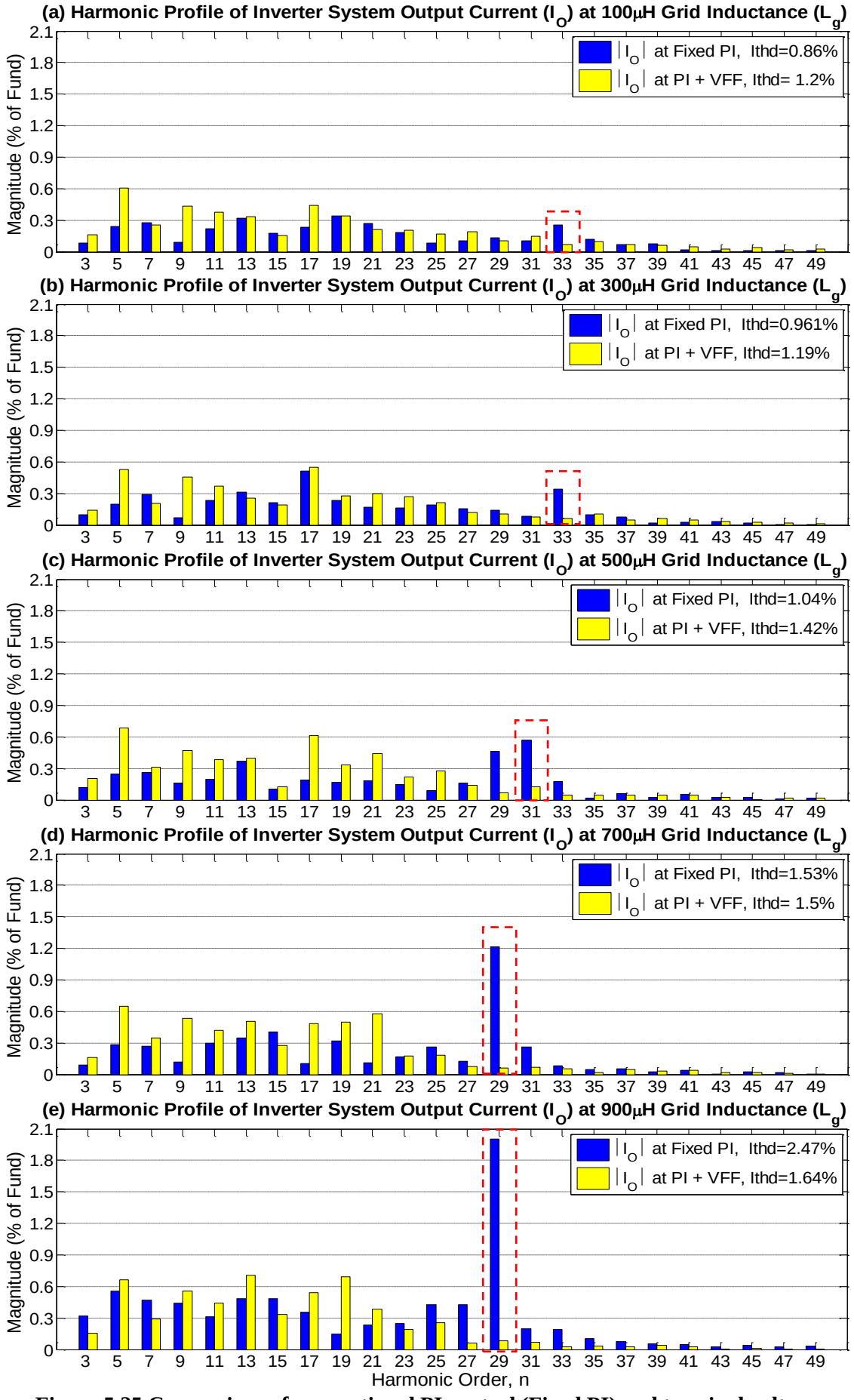

Figure 5.25 Comparison of conventional PI control (Fixed PI) and terminal voltage feedforward PI control (PI+VFF) at various grid inductances (L_g).

(I_{demand} = 7A RMS, V_{DC} = 100V, V_G = 39V RMS, K_p = 1.1, K_i = 0.6(Fixed PI) = 0.18(PI+VFF).)

To assess the performance of terminal voltage feedforward scheme, the experimental grid-connected PV inverter system is operated with conventional PI control (Fixed PI only) and PI control with terminal voltage feedforward (PI+VFF) at various grid inductances (from 100μH up to 900μH with 200μH step) in practical experiment. During the experiment, the integral gain (K_i) of PI controller is varied between the two proposed schemes (0.6 for Fixed PI, 0.18 for PI+VFF) as the disturbance response of terminal voltage feedforward scheme is compensated by feedforward term. However, the proportional gain (K_p) is kept the same on both schemes (1.1 for Fixed PI and PI+VFF) to compare their performance in response to the resonance. The harmonic profiles of inverter system output current (I_O) in the two proposed schemes are compared and presented as in Figure 5.25.

As shown in Figure 5.25(a) to Figure 5.25(e), the high magnitude of inverter system output current harmonics between the 29th and the 33rd (shown by red boxes in Figure 5.25) due to the excitation of resonance are measured on inverter system with conventional PI control (Fixed PI) only but not observed on PI control with terminal voltage feedforward (PI+VFF) when the grid inductance is increased. This is because the oscillation in PI control with terminal voltage feedforward (PI+VFF) is compensated by feedforward term and hence no excitation of resonance even at very high value of grid inductance (shown by Figure 5.25(e) with 900μH of grid inductance).

However, it is observed in Figure 5.25(a) to Figure 5.25(e) that PI control with terminal voltage feedforward (PI+VFF) exhibits typically higher low order harmonic content (from 3rd to 21st harmonics) of inverter system output current (I_O) across complete range of grid inductance due to inevitable errors of measurement circuits. Ideally, the magnitude of current harmonics in PI control with terminal voltage feedforward (PI+VFF) should be lower than in conventional PI control (Fixed PI) as the harmonics of the PCC voltage are feed into the control loop for compensation. However, the practical system in real-life which employs the sensing circuit, amplifier circuit, analogue to digital conversion, and digital control etc., will have the error, offset or computational delay in the signal route or gain which could deviate the measurement of PCC voltage waveform from original. The combinational effects of these are the main factor that causes the higher low order harmonic in inverter system output current when terminal voltage feedforward is implemented, and hence the rise in current THD.

In addition, the comparison of PCC voltage harmonic profile in PI control with terminal voltage feedforward PI (PI+VFF) at various grid inductances is shown in Figure 5.26, in which huge variation on PCC voltage harmonic at resonant frequency (between the 29th and the 33rd harmonics) is not measured when the grid inductance is varied, although there are some variations in the low order harmonics (from 3rd to 21st harmonics) of PCC voltage.

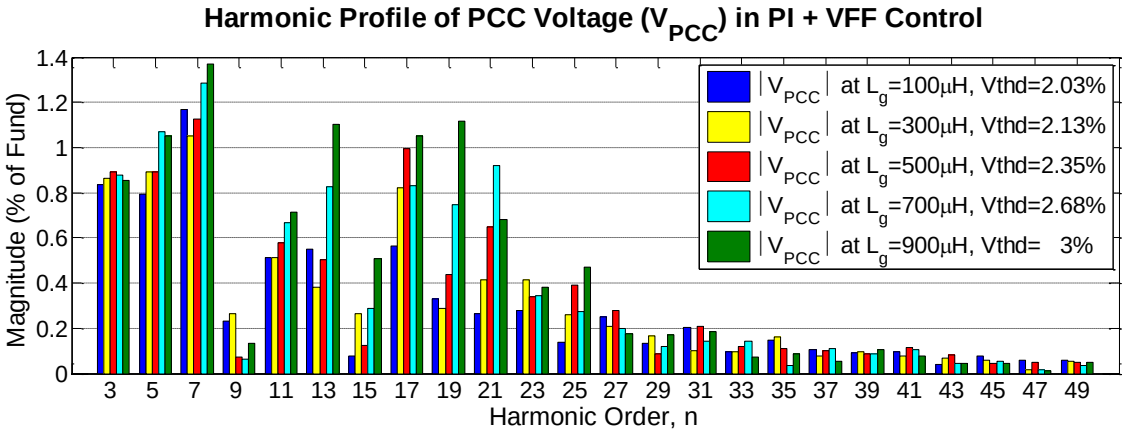

Figure 5.26 Comparison of PCC voltage (V_{PCC}) in PI control with terminal voltage feedforward (PI+VFF) at various grid inductances (L_g).
(I_{demand} = 7A RMS, V_{DC} = 100V, V_G = 39V RMS, K_p = 1.1, K_i = 0.18.)

By concluding the practical results as shown in Figure 5.25 and Figure 5.26, PI control with terminal voltage feedforward (PI+VFF) is proved to be robust to the resonance and the variation in grid inductance up to 900μH (weak grid). Although higher magnitude of low order harmonic content is observed in the inverter system output current (I_O), this drawback could be outweighed by its robustness in controller performance and superior stability under disturbances.

5.7.2 *Fundamental Sine Wave Feedforward*

As demonstrated in Section 5.7.1, PI control with terminal voltage feedforward (PI+VFF) is robust to the resonance but exhibits typically higher low order harmonic content (from 3rd to 21st harmonics) in inverter system output current (I_O) across the complete range of grid inductance. Nevertheless, it is the aim of this research to develop a control measure that robust to the resonance while exhibit the low magnitude characteristic of the low order harmonics across complete range of grid inductance. For this reason, the idea of PI control with fundamental sine wave feedforward (PI+SFF) is proposed to test its performance in response to resonant excitation. In PI control with fundamental sine wave feedforward, same voltage transducer and ADC that employed in terminal voltage feedforward scheme (as demonstrated in Section 5.7.1) are

employed to measure the magnitude of PCC voltage (V_{PCC}) over a cycle. A fundamental (50Hz) sine wave signal (V_{f1}), synchronised with PCC voltage via ZCD and corresponding to the magnitude of PCC voltage, is then generated by the sine look-up table of the microcontroller and feedforwarded to the output of the conventional PI control loop, as shown by Figure 5.27.

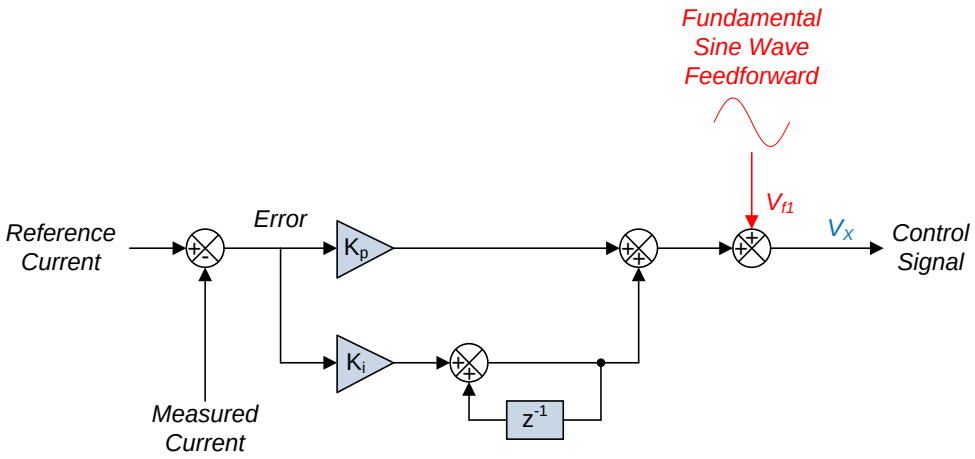

Figure 5.27 Block diagram of PI current controller with fundamental sine wave feedforward.

In theory, only the fundamental harmonic on PCC voltage (50Hz harmonic) is compensates by the feedforward term in PI control with fundamental sine wave feedforward scheme, while the rest of the harmonics on PCC voltage as well as the voltage drops across the inverter LC lowpass filter inductance (and hence current control) have to be calculated by PI controller. This could unburdens the PI controller while preventing the low order harmonics of PCC voltage being feedforwarded to the current control loop, and hence low magnitude characteristic of the low order harmonics as in conventional PI control (shown by Fixed PI in Figure 5.25) can be achieved.

Likewise to the terminal voltage feedforward scheme (demonstrated in Section 5.7.1), the performance of PI control with fundamental sine wave feedforward is assessed through the practical experiment with various grid inductance values in the laboratory, and its inverter system output current (I_O) harmonic profiles is then compared to as in conventional PI control (Fixed PI) and PI control with terminal voltage feedforward (PI+VFF). As the disturbance response of PI controller is unburdens by feedforward term in terminal voltage and fundamental sine wave feedforward schemes, 0.18 of integral gain (K_i) is applied in these control schemes (PI+VFF and PI+SFF) while 0.6 of integral gain is applied in conventional PI control. It is noted that the proportional gain (K_p) is kept the same on all tested schemes (1.1 in Fixed PI, PI+VFF and PI+SFF) to compare their performance in response to resonant excitation.

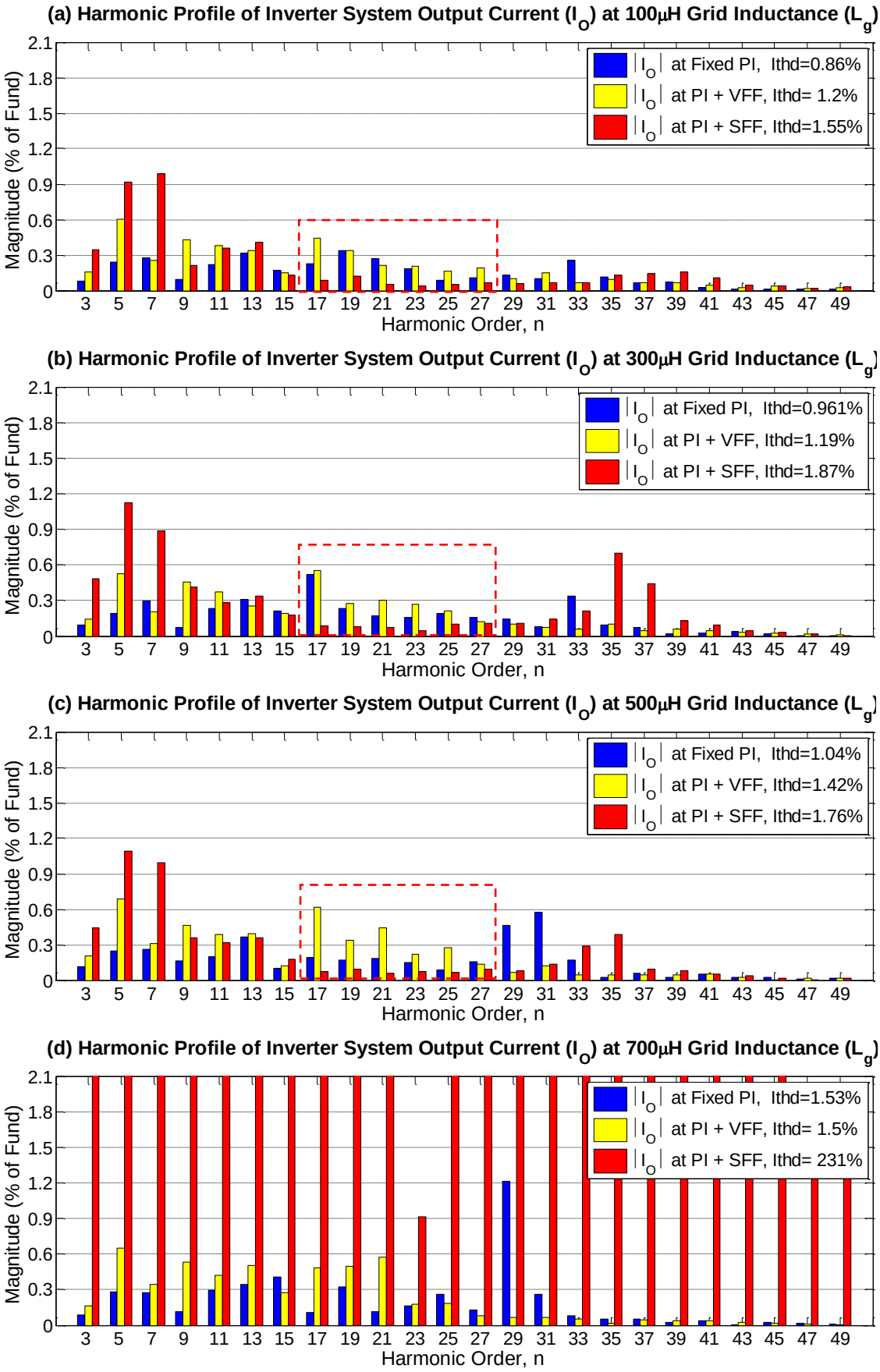

Figure 5.28 Comparison of conventional PI control (Fixed PI), terminal voltage feedforward PI control (PI+VFF), and fundamental sine wave feedforward PI control (PI+SFF) at various grid inductances (L_g).

(I_{demand} = 7A RMS, V_{DC} = 100V, V_G = 39V RMS, K_p = 1.1, K_i = 0.6(Fixed PI) = 0.18(PI+VFF, PI+SFF).)

The harmonic profiles of inverter system output current (I_O) in practical experiment of the three proposed schemes are compared and presented as in Figure 5.28. As shown by the red boxes in Figure 5.28(a) to Figure 5.28(c), the harmonic magnitude of inverter system output current (I_O) from the 17^{th} to 27^{th} harmonics are reduced significantly in PI control with fundamental sine wave feedforward (PI+SFF).

Nevertheless, it is also shown in Figure 5.28(a) to Figure 5.28(c) that the very low order harmonics (the 3^{rd}, 5^{th} and 7^{th} harmonics) of inverter system output current (I_O) in PI control with fundamental sine wave feedforward (PI+SFF) are increased significantly. This is related to the high magnitude of the 3^{rd}, 5^{th} and 7^{th} harmonics in the typical PCC voltage of distribution grid that caused by the harmonic nature of loads connected to the PCC and synchronous generator at power plant (Zaneta, Anton, et al. [101], Hershey Energy Systems [102]). As the integral gain (K_i) is reduced to 0.18 in PI control with fundamental sine wave feedforward, there is insufficient integral gain to compensate the very low frequency disturbance from the PCC voltage (such as the 3^{rd}, 5^{th} and 7^{th} harmonics) in PI control with fundamental sine wave feedforward and hence high magnitude in its very low order harmonics of inverter system output current (shown by 3^{rd}, 5^{th} and 7^{th} harmonics in Figure 5.28(a) to Figure 5.28(b). It is noted that the harmonics of PCC voltage in PI control with terminal voltage feedforward (PI+VFF), including the 3^{rd}, 5^{th} and 7^{th} harmonics, are compensated by feedforward term and hence not suffered from very low frequency disturbance.

Furthermore, it is observed in Figure 5.28(b) and Figure 5.28(c) that the resonance is excited in PI control with fundamental sine wave feedforward (PI+SFF) at resonant frequency around 1750Hz (35^{th} harmonics) when the grid inductance (L_g) is increased to 300μH and 500μH respectively. Also, it is very apparent in Figure 5.28(d) that very high level of resonance is excited in PI control with fundamental sine wave feedforward and has led to significant current harmonics in inverter system output current (I_O), when the grid inductance is increased to 700μH. This resonance is excited by the oscillation and ripples in the PCC voltage and inverter system output current that caused by the excessive proportional gain (K_P) of PI controller when the grid inductance is varied. As only the fundamental harmonic (50Hz harmonic) is fedforward to the control loop of fundamental sine wave feedforward scheme, these oscillation and ripples which tend to increase with grid inductance value are not compensated in PI control with fundamental sine wave feedfoward. Hence, the experimental grid-connected PV inverter system is become unstable at 700μH of grid inductance. Significant oscillation can be observed

on the waveforms of PCC voltage (V_{PCC}) and inverter system output current (I_O) of PI control with fundamental sine wave feedforward, when the experimental system is became unstable at 700µH of grid inductance, as shown in Figure 5.29.

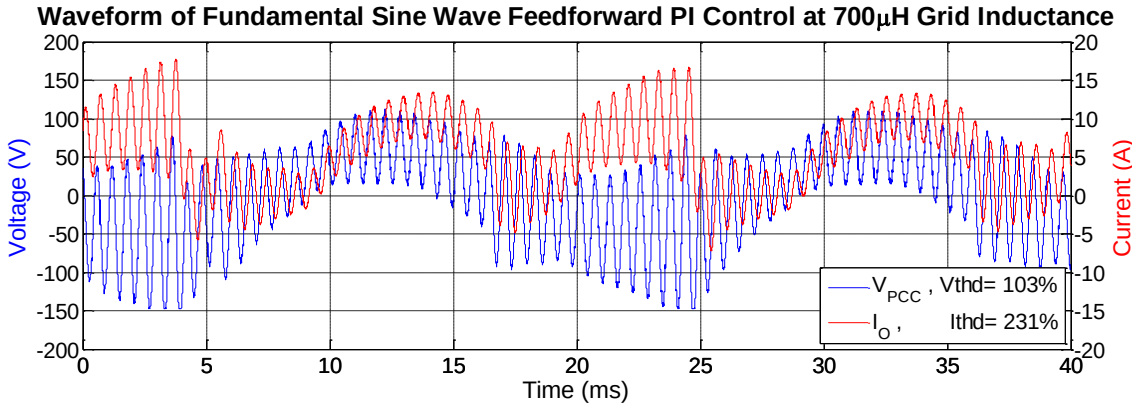

Figure 5.29 Significant oscillation in the PCC voltage (V_{PCC}) and inverter system output current (I_O) of PI control with fundamental sine wave feedforward (PI+SFF), due to high level of resonant excitation at 700µH of grid inductance (L_g).
(I_{demand} = 7A RMS, V_{DC} = 100V, V_G = 39V RMS, K_p = 1.1, K_i = 0.18, L_g = 700µH.)

By concluding the practical results as shown in Figure 5.28 and Figure 5.29, PI control with fundamental sine wave feedforward (PI+SFF) is proved not to help in damping the excitation of the resonance nor maintaining low magnitude in very low order harmonics as the rise in the 3rd, 5th and 7th current harmonics have been measured in practical experiment and the PV inverter system is became unstable at 700µH of grid inductance.

5.8 Summary

This chapter has discussed the resonance phenomenon caused by the interaction between the grid-connected PV inverter system and distribution grid. It has been shown that by connecting the PV inverter system to the PCC, the LC lowpass filter of inverter system is coupled to the grid inductance to form a 3rd order LCL system with additional low impedance resonant point that did not exist in the 2nd order LC system. At the frequency of this low impedance resonance, the inverter filter capacitance is interacting with the grid inductance to inject the resonant current into distribution grid. This resonant current is measured by current transducer and feedbacks to the PI current control loop which in turn causing the instability of PV inverter system. Moreover, it has also shown in the analysis that the background grid voltage and grid inductance form a part of current control loop and hence they contribute to the excitation of this low impedance resonance. The analysis has shown that the frequency of the low impedance resonance is reduced when the grid inductance is increased. In practice, this

low impedance resonance could be excited by the oscillation and ripples that caused by excessive PI controller proportional gain (K_P) when the grid inductance is increased, and hence the resonant frequency is reduced. To suppress the resonant excitation, three different types of control measures are proposed. Amongst these control measures, terminal voltage feedforward and fundamental sine wave feedforward have been presented in this chapter. The experimental results show that, although terminal voltage feedfoward PI control exhibits higher low order harmonic content of inverter system output current, it is advantageous in suppression of the resonant excitation and robust to the variation in grid inductance. In addition, fundamental sine wave feedforward PI control is not to help in damping the resonant excitation. Another innovative adaptive PI control technique that proposed in this research to suppress the resonance is presented in Chapter 6.

Chapter 6. Adaptive Proportional Gain for Suppression of Resonance

6.1 Introduction

This chapter presents an innovative adaptive control technique to suppress the resonance caused by the interaction between the PV inverter system and the grid. The first part of the chapter concentrates on the effect of PI controller tuning on the harmonic performance of the inverter system. Initially, the effect of proportional gain on the resonance excited system is studied with various grid inductance values. It is shown that the PCC voltage oscillation can be reduced by proper tuning of the proportional gain and hence the resonance can be suppressed. As the value of the grid inductance must be known to optimally tune the proportional gain, a band-pass filter and signal processing technique is developed for adaptive tuning of the PI controller proportional gain. The performance of the proposed adaptive PI controller is experimentally verified by comparing its performance with a conventional PI controller with terminal voltage feed-forward scheme. Finally, the PV inverter with adaptive PI controller is setup to interface with distribution grid continuously over a longer period of time. The variation in grid impedance is observed via the proposed estimation technique and the adaption of the adaptive PI controller is assessed.

6.2 Excitation of Resonance

As the distribution grid impedance changes over time, due to variation in operating conditions, the resonant frequency of the network dynamically changes in response to this. Resonance can be excited in the distribution grid when the harmonics of the grid-connected PV inverter output coincide with the resonant frequency of the grid. Such a situation is possible even though the PV inverter is initially configured to avoid resonant characteristics during installation and commissioning. The cause and effect of this resonance has already been discussed extensively in Chapter 5.

Conventional grid-connected PV inverters, with only PI control loops do not effectively suppress the oscillation cause by resonance and hence high level of harmonic distortion can be measured on inverter output current or PCC voltage. For this reason, terminal voltage feedforward can be added to the output of PI current controller to compensate the oscillation and hence no excitation of resonance. This terminal voltage feedforward scheme is demonstrated in Section 5.7.1. The comparison of inverter system output

current for conventional PI control (Fixed PI) and PI control with terminal voltage feedforward (PI+VFF) at a grid inductance of 100µH, 300µH, 500µH and 700µH are shown in Figure 6.1.

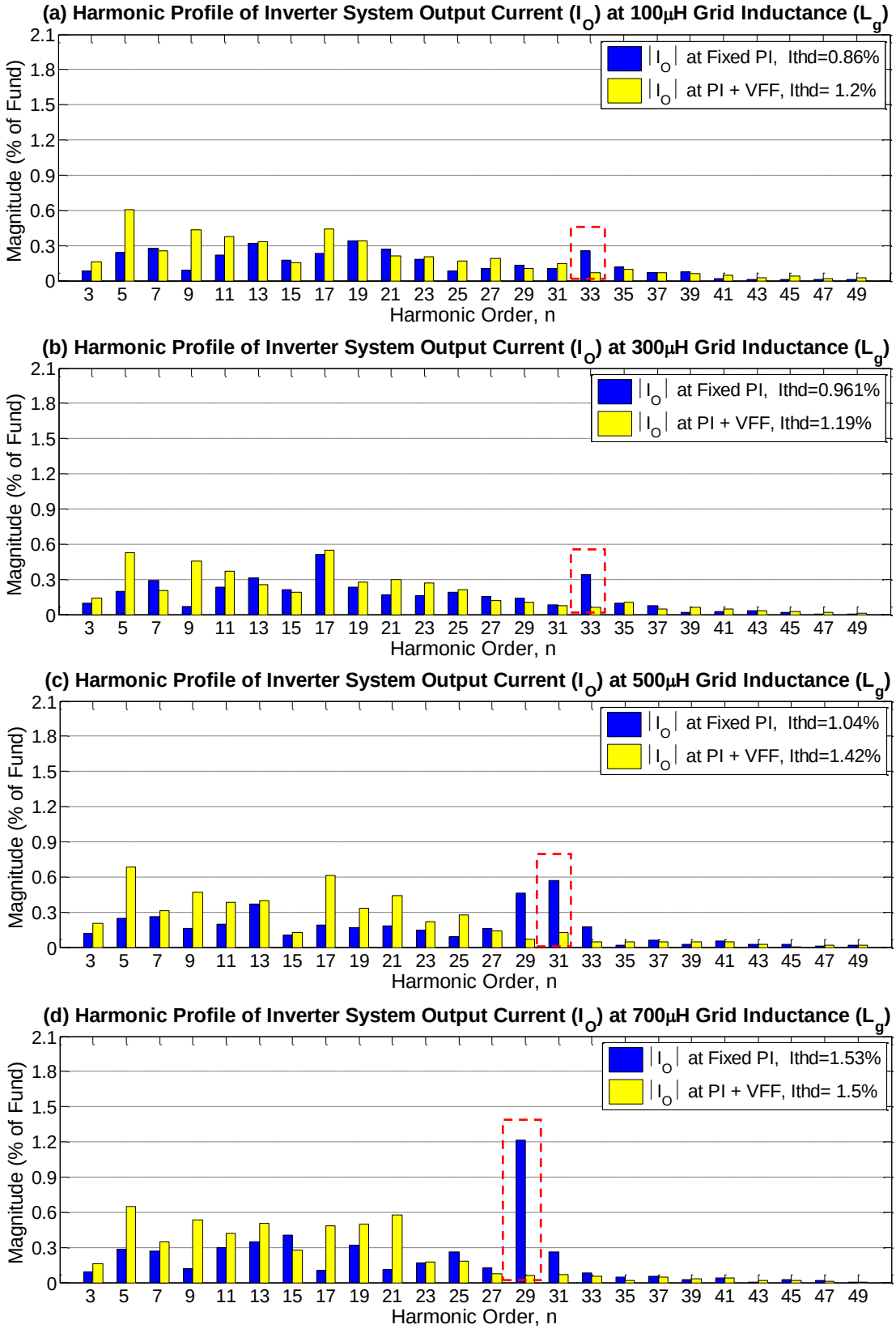

Figure 6.1 Comparison of conventional PI control (Fixed PI) and terminal voltage feedforward PI control (PI+VFF) at various grid inductances (L_g).
(I_{demand} = 7A RMS, V_{DC} = 100V, V_G = 39V RMS, K_p = 1.1, K_i = 0.6(Fixed PI) = 0.18(PI+VFF).)

In spite of the excitation of resonance can be suppressed by implementing terminal voltage feedforward, as shown by the red boxes in Figure 6.1, it has the tendency to increase the low order harmonics (harmonics from the 3rd to 21st) of inverter system output current irrespective of the excitation of resonance, and hence lead to higher current THD than conventional PI control at low grid inductance (as shown in Figure 6.1(a)). Glance through the current harmonic profiles in Figure 6.1, the current THD of conventional PI control can be improved significantly if the current harmonics at the resonance can be suppressed as the grid inductance increases. This has led to the idea on the suppression of resonance via adaptively tune the PI controller gain based on the grid inductance change.

6.3 Suppression of Resonance in PI Control by Varying K_P

As first explained in Section 5.6, resonant excitation of the inverter system output current when applying conventional PI control (as shown in Figure 6.1) is due to the PCC voltage oscillation that coincides with the resonant frequency when the grid inductance is increases. The oscillation in the PCC voltage is observed when excessive proportional gain (K_P) is applied (Twining and Holmes [59, 94]). From this point of view, the oscillation on the PCC voltage can be reduced by reducing the proportional gain accordingly when the grid inductance increases; hence the excitation of resonance can be suppressed.

To assess the effect of proportional gain on the suppression of resonance, the experimental grid-connected PV inverter system is setup to interface with the distribution grid in the laboratory via 700μH of emulated grid inductance, isolation transformer and variac. A conventional PI controller without terminal voltage feedforward is implemented. During the experiment, the proportional gain (K_p) of the PI control is progressively reduced from the nominal value of 1.1 to 0.8 with a step size of 0.1, while the integral gain (K_i) is fixed at 0.6 throughout the experiment.

The harmonic profile of the PCC voltage and the inverter system output current at different value of proportional gain in practical experiment are presented in Figure 6.2 and Figure 6.3 respectively. As shown by the red box in Figure 6.2, the voltage harmonics at the resonant frequency (from the 29th to 33rd harmonics) are significantly reduced when the proportional gain is reduced from 1.1 to 0.9, then increased again when the proportional gain is reduced further to 0.8. This implies the oscillation on the PCC voltage is reduced to a minimum when the proportional gain is set to 0.9.

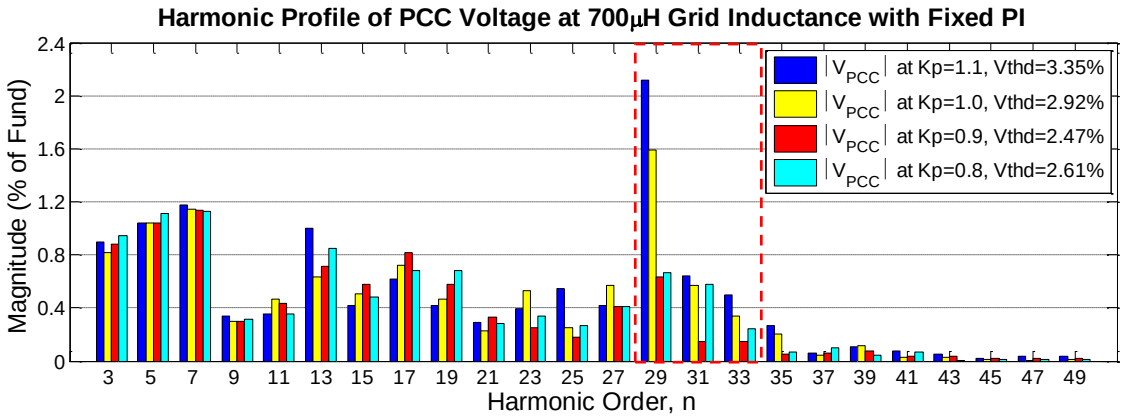

Figure 6.2 Effect of PI control proportional gain (K_P) on resonant excitation, harmonic profile of PCC voltage (V_{PCC}) at 700μH of grid inductance (L_g).
(I_{demand} = 7A RMS, V_{DC} = 100V, V_G = 39V RMS, f_1 = 50Hz, K_i = 0.6, L_g = 700μH.)

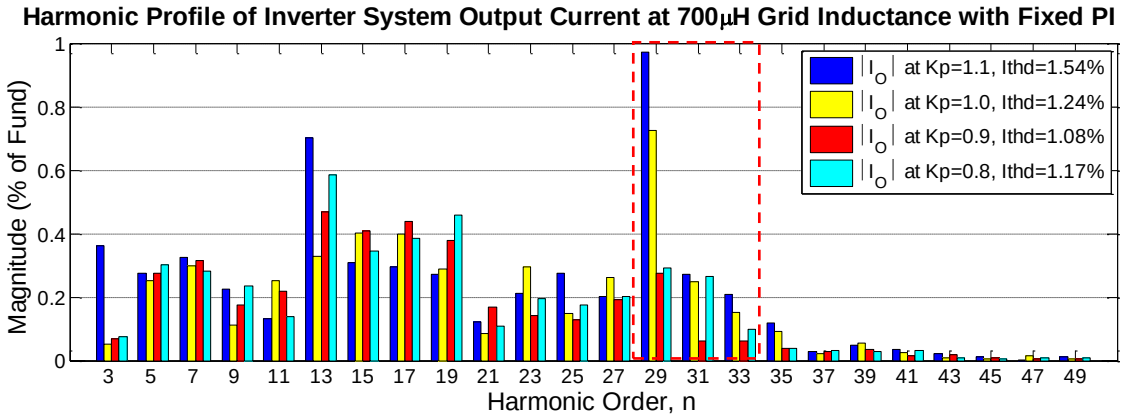

Figure 6.3 Effect of PI control proportional gain (K_P) on resonant excitation, harmonic profile of inverter system output current (I_O) at 700μH of grid inductance (L_g).
(I_{demand} = 7A RMS, V_{DC} = 100V, V_G = 39V RMS, f_1 = 50Hz, K_i = 0.6, L_g = 700μH.)

A similar effect is observed in the harmonic profile of the inverter system output current, as shown in Figure 6.3. The current harmonics at the resonant frequency (from 29th to 33rd harmonics) are significantly reduced when the proportional gain is reduced from 1.1 to 0.9, and then increased again when the proportional gain is reduced further to 0.8. As the oscillation of PCC voltage is reduced to a minimum at K_p = 0.9, the resonance is suppressed the most; hence, lowest current harmonics at the resonant frequency.

Further experiment is carried out to assess the effect of proportional gain (K_p) on resonance over a range of different grid inductance values (from 100μH up to 900μH). Three sets of tests are carried out for each grid inductance value:

- fixed gain PI control (Fixed PI),
- PI control with terminal voltage feedforward (PI+VFF),
- manually tuned K_P PI control (PI Kp).

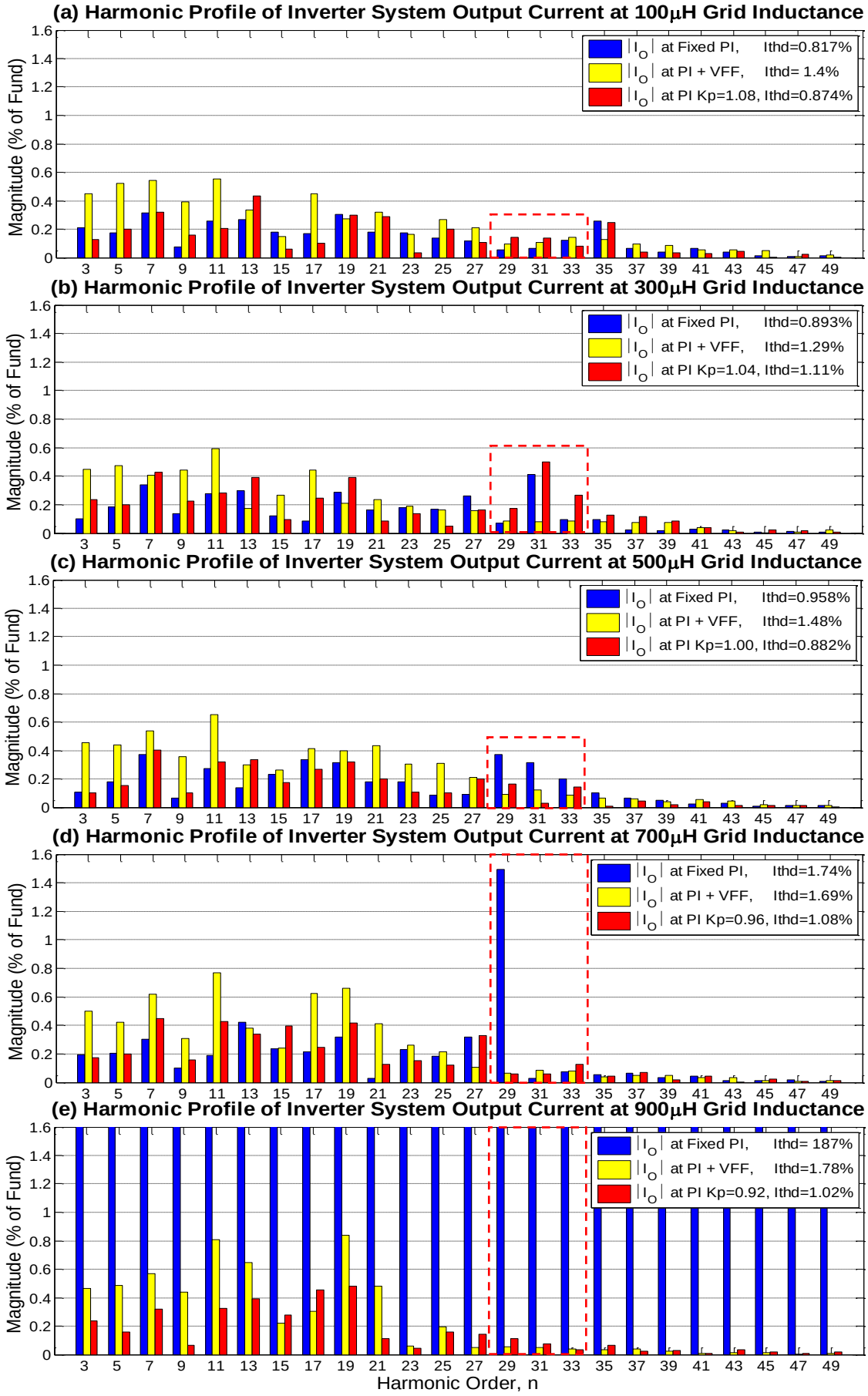

Figure 6.4 Comparison of fixed gain PI control (Fixed PI), terminal voltage feedforward PI control (PI+VFF), and manually tuned K_P PI control (PI Kp).
(I_{demand} = 7A RMS, V_{DC} = 100V, V_G = 39V RMS, f_1 = 50Hz, K_p = 1.1(Fixed PI, PI+VFF), K_i = 0.6(Fixed PI, PI Kp) = 0.18(PI+VFF).)

For the manually tuned K_P PI control test, the proportional gain is reduced as the effective grid inductance (L_g) is increased. The harmonic profile comparison for inverter system output current (I_O) with different control schemes is presented in Figure 6.4. As shown in Figure 6.4(a) to Figure 6.4(e), with manually tuned K_P PI control the inverter system output current harmonics around the resonant frequency (29^{th} to 33^{rd} harmonics) are suppressed by reducing the K_P value as the grid inductance is increased. However, with fixed PI control there is a significant increase in the current harmonics at the resonant frequency.

At low order current harmonics (from 3^{rd} to 21^{st} to harmonics), the manually tuned K_P PI controller retains the low harmonic magnitude characteristics of fixed PI control. The terminal voltage feedforward PI controller exhibits typically higher low order harmonic content across the complete range of grid inductance. It is apparent that with fixed PI control at 900μH effective grid inductance instability of the controller occurred (as shown by Figure 6.4(e)). Under the same grid conditions, the manually tuned K_P PI controller and terminal voltage feedforward PI controller remain robust. All of these have caused the current THD of manually tuned K_P PI control significantly lower than fixed PI control and terminal voltage feedforward PI control at high grid inductance value (500μH up to 900μH), while just slightly higher than fixed PI control at low grid inductance value (100μH up to 300μH).

Therefore, the experimental results show the robustness and stability of the grid-connected PV inverter PI controller under disturbances, such as grid inductance change and resonance, can be guaranteed by proper tuning of the PI controller proportional gain over a wide range of grid inductance values. Furthermore, it is possible to maintain relatively low magnitude in low order harmonics of inverter system output current. This also implies that the THD of inverter system output current can be maintained at a low value even when the PV inverter system is interfaced with high grid inductance.

6.4 Grid Inductance Estimation of PV Inverter System

The technique on suppression of the resonance based on proper tuning of PI control proportional gain proposed in Section 6.3 require value of the grid inductance. Moreover, as discussed in Section 5.4 that the grid inductance is change over time due to the variation in operating conditions, it is not possible to continuously monitor the grid inductance by measuring equipment and manually tune the proportional gain of PI controller. Based on this reason, grid impedance estimation technique that is able to

interface with the microcontroller is essential to adaptively tune the controller for corresponding grid inductance.

There are different ways to measure or estimate the impedance of distribution grid, in which the conventional ways of measurement are probe signal injection, harmonic injection and Discrete Fourier Transform (DFT). Visscher and Heskes [103] present a method to measure the grid impedance without altering the electric properties of the distribution grid. In this method, a probe signal is injected to the grid and to the load under normal working condition, and a double phase locked amplifiers which consist of a sine and cosine wave is simultaneously multiplied with the reference signal and averaged over a relatively long period. However, the periodic disturbance signal, which is close to the fundamental frequency, cannot be measured instantaneously as it requires an averaging process over time. Another measurement technique that provides instantaneous estimation of grid impedance is proposed by Ciobotaru, Teodorescu, et al. [104]. The technique produces a perturbation on the output of the power converter that is in the form of periodical injection of one or two voltage harmonic signals, and the current response for the corresponding injected frequency measured during the perturbation is then analysed through DFT (for one voltage harmonic method) or statistical technique (for two harmonic method) in order to estimate the grid impedance. As DFT is calculated by vector approach in this technique, the DSP can be overloaded if careful attention is not paid to the relatively long calculation time of DFT. In contrast to long computational time of DFT using vector approach, a running-sum approach to calculate the DFT by accumulators is proposed by Asiminoaei, Teodorescu, et al. [105]. The estimation method that estimates the grid impedance by injecting an interharmonic current and determines the voltage drop caused by the grid impedance is presented together with this approach [105]. Moreover, as the typical grid-connected PV inverter has the low pass filter with LC or LCL arrangement installed at the output of inverter bridge, the grid impedance estimation can be achieved by excitation of the filter resonance, as proposed by Lisserre, Blaabjerg, et al. [106].

The proposed estimation methods discussed above either require a long response time, injection of the harmonic, or excitation of resonance which affect the voltage and current characteristic of distribution grid. Therefore, in this research, a method that provides the PI control loop with a simple signal corresponding to the grid impedance is proposed. Figure 6.5 shows the harmonic trend of PCC voltage at various grid inductances when the fixed PI control is implemented on the experimental grid-

connected PV inverter. As shown, very high voltage harmonics can be observed around the resonant frequency and the magnitude of these harmonics is with respect to the grid inductance value. Hence, the excitation level of the resonance can be used to estimate the value of grid inductance if the voltage harmonics within the resonance range (from 29th to 33rd harmonics) can be trapped and measured by the appropriate filter circuit.

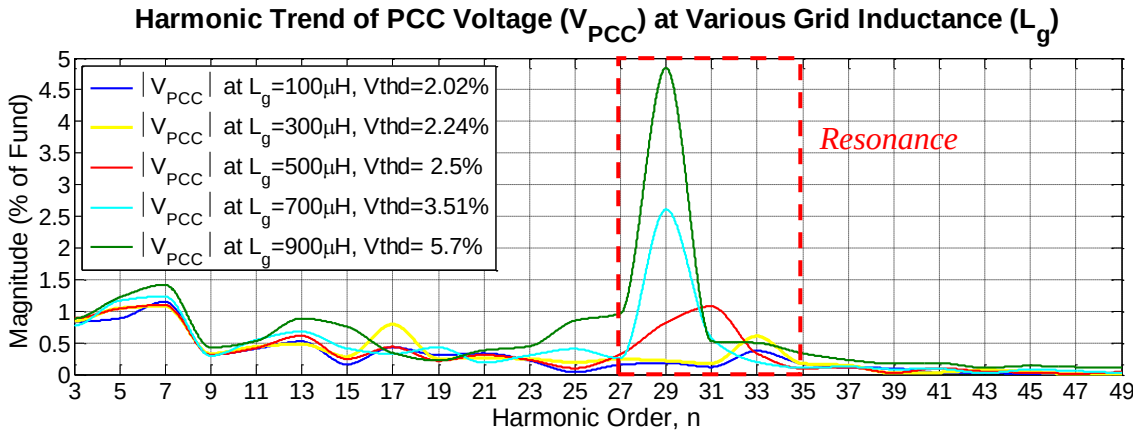

Figure 6.5 Comparison of PCC voltage (V_{PCC}) harmonic trend at various grid inductances (L_g) with fixed gain PI control (Fixed PI).
(I_{demand} = 7A RMS, V_{DC} = 100V, V_G = 39V RMS, f_1 = 50Hz, K_p = 1.1, K_i = 0.6.)

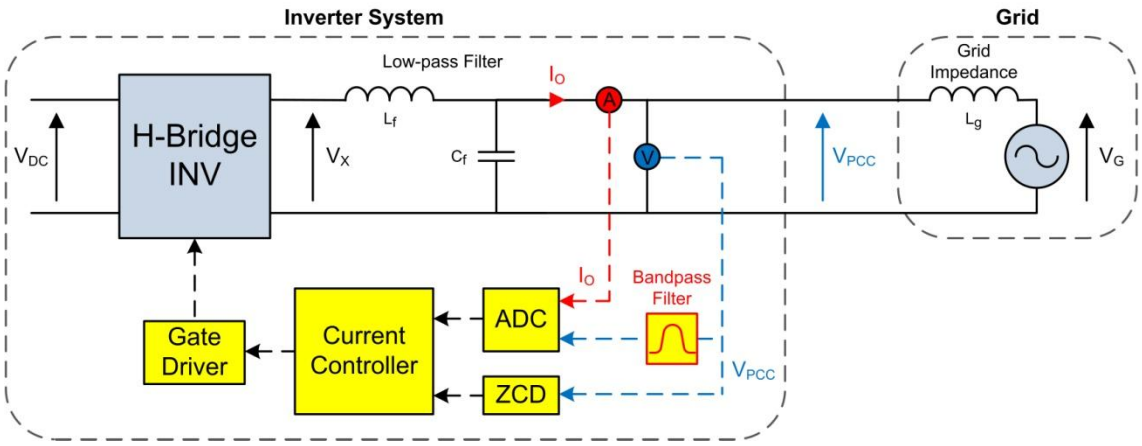

Figure 6.6 System arrangement of the grid-connected PV controller with resonance detection.

To trap and the voltage harmonics at resonance range, same voltage sensor that employed in terminal voltage feedforward scheme (as demonstrated in Section 5.7.1) is employed. Same as terminal voltage feedforward scheme, the voltage sensor is placed across the output terminal of PV inverter system to measure the PCC voltage waveform. From the measured voltage waveform, a bandpass filter is proposed to filter out the voltage harmonics outside of a narrow band setup around the resonant frequency. The resultant voltage waveform that only consists of voltage harmonics at resonance range is then measured by digital controller via digital to analogue converter (ADC). The

arrangement of the system with proposed bandpass filter for resonance detection is shown in Figure 6.6. Depending upon the grid inductance range and the specific application, the bandpass filter can be designed to pass a wide, or very tight, resonant frequency range.

6.5 Bandpass Filter Design for Resonance Detection

Bandpass filter is commonly used in communication and signal processing application to capture the frequency component at designed frequency range. It can be achieved by either analogue circuit, or in discretized system via microprocessor. Careful attention should be paid if the discretized bandpass filter is implemented in the digital current control loop of inverter controller as high attenuation rate of discretized bandpass filter require relatively long duration of computational time. For this reason, analogue bandpass filter is employed in this research to ensure the performance of digital current control loop is not compromised. This is particularly important for grid-connected PV inverter controllers as they are mostly operate at very high frequency (typically 20 kHz of sampling frequency) [27] to reduce the switching noises and current harmonics, the addition discretized bandpass filter processing could overload the microcontroller easily in this case.

For resonance detection purposes, the bandpass filter with high corner frequency attenuation rate is desired to pass the harmonic components at resonance frequency and attenuate any harmonic components out of the filter passband. This implies higher order of bandpass filter is essential to damp the harmonic components out of the passband effectively, including the fundamental component. Moreover, the harmonic components at resonance that cause the oscillation on PCC voltage are relatively small in magnitude compare to fundamental components, high gain of harmonic component at the passband will magnify the resonance components and hence ease the detection of resonance. Therefore, due to the intrinsic limitation on the passive filter passband gain and the Q-factor [107], the requirements are easier to achieve by active bandpass filter via operational-amplifier (op-amp).

Active bandpass filter with Sallen-Key topology is proposed for resonance detection due to its simplicity. Another valued advantage of Sallen-Key active filter are it allows high Q-factor and passband gain without the use of inductor [66, 108]. The design technique of Sallen-Key active bandpass filter is discussed extensively in previous studies [108-111]. For the proposed Sallen-Key active bandpass filter used for

resonance detection, 4th order Sallen-Key filter provides enough attenuation at corner frequency. Moreover, Butterworth filter response is chosen in filter design to ensure minimum ripple at the filter passband [107, 112]. As the resonance is observed in the practical experiment that the resonant frequency is likely to locate at the frequency range in between the 25th and 55th harmonics, 2 kHz of bandpass filter centre frequency with 1 kHz passband bandwidth are decided for the proposed active bandpass filter. The final requirements of the proposed active bandpass filter are summarised in Table 6.1.

Bandpass Filter Specification	
Circuit Topology	*Sallen-Key*
Response	*Butterworth*
Order	*4th*
Stage	*2*
Passband Gain	*26.02 dB (20 V/V)*
Centre Frequency	*2 kHz*
Passband Bandwidth	*1 kHz*
Corner Frequency Attenuation	*23.02 dB*

Table 6.1 Specification of bandpass filter for resonance detection.

However, the Sallen-Key bandpass filter is a 2nd order filter. Therefore, two Sallen-Key bandpass filters are cascaded to form a 2-stage 4th order active bandpass filter. Circuit diagram in Figure 6.7 shows the cascaded arrangement of proposed 4th order active bandpass filter fulfilled the specification as shown in Table 6.1.

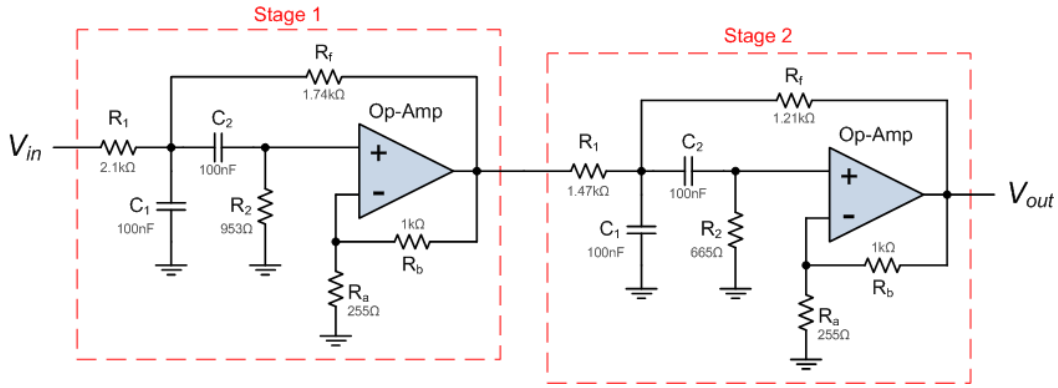

Figure 6.7 Circuit diagram of 2 stages cascaded active bandpass filter.

The open loop transfer function ($H_{OL}(s)$) of the 2nd order Sallen-Key bandpass filter is provided in literature by previous studies [108, 109] and shown in Equation (6.1). As 4th order of cascaded active bandpass filter is proposed, the resultant open loop transfer function of the bandpass filter ($G_{OL\text{-}BP}(s)$) is the multiplication of the 1st stage ($H_{OL1}(s)$) and 2nd stage ($H_{OL2}(s)$) transfer functions, yield Equation (6.2).

$$H_{OL}(s) = \frac{\left(1+\frac{R_b}{R_a}\right)\frac{s}{R_1C_1}}{s^2 + \left(\frac{1}{R_1C_1}+\frac{1}{R_2C_1}+\frac{1}{R_2C_2}-\frac{R_b}{R_aR_fC_1}\right)s + \frac{R_1+R_f}{R_1R_fR_2C_1C_2}} \quad \textbf{(6.1)}$$

$$G_{OL-BP}(s) = H_{OL1}(s)H_{OL2}(s) \quad \textbf{(6.2)}$$

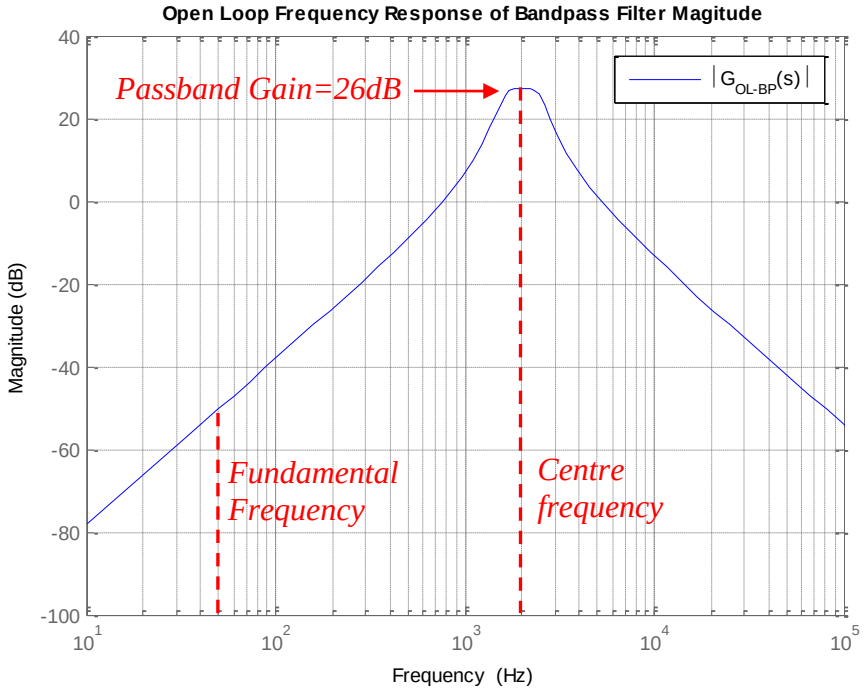

Figure 6.8 Magnitude frequency response of the 4th order active bandpass filter for resonance detection.

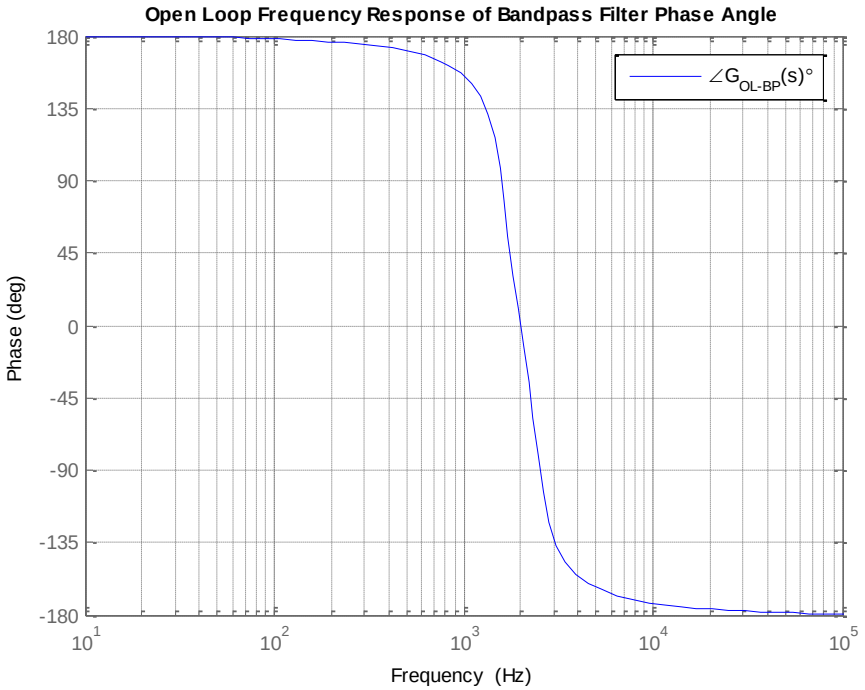

Figure 6.9 Phase angle frequency response of the 4th order active bandpass filter for resonance detection.

The frequency responses of the active bandpass filter magnitude and phase angle (obtained through Equation (6.1) and Equation (6.2)) are show in Figure 6.8 and Figure 6.9 respectively. In Figure 6.8, the filter passband gain is magnified to 26dB (19.95 V/V) and the centre frequency is set to 2 kHz, while the fundamental component (50 Hz) is attenuated to around -50dB (0.0032 V/V). In practice, an Analog Devices® AD822 precision op-amp with very high unity-gain bandwidth (1.8 MHz) is employed in the bandpass filter circuit, the frequency response as shown in Figure 6.8 is not noticeably affected by the bandwidth of the op-amp.

The analogue active bandpass filter proposed in Figure 6.7 is built and shown in Figure 6.10. The printed circuit board (PCB) is powered by a 9V battery and the bandpass filter is made up by a dual op-amp IC (Analog Devices® AD822). To ensure the minimum noise on the input and output signal of bandpass filter, co-axial cable with BNC connector are used for the connection between the PCC voltage sensor and bandpass filter, as well as the connection between the bandpass filter and microcontroller ADC unit. Detail discussion of test rig setup and equipments for experimental grid-connected PV inverter system, including bandpass filter connection, are presented in Chapter 3, while the schematic diagram of the analogue active bandpass filter is presented in Appendix II.

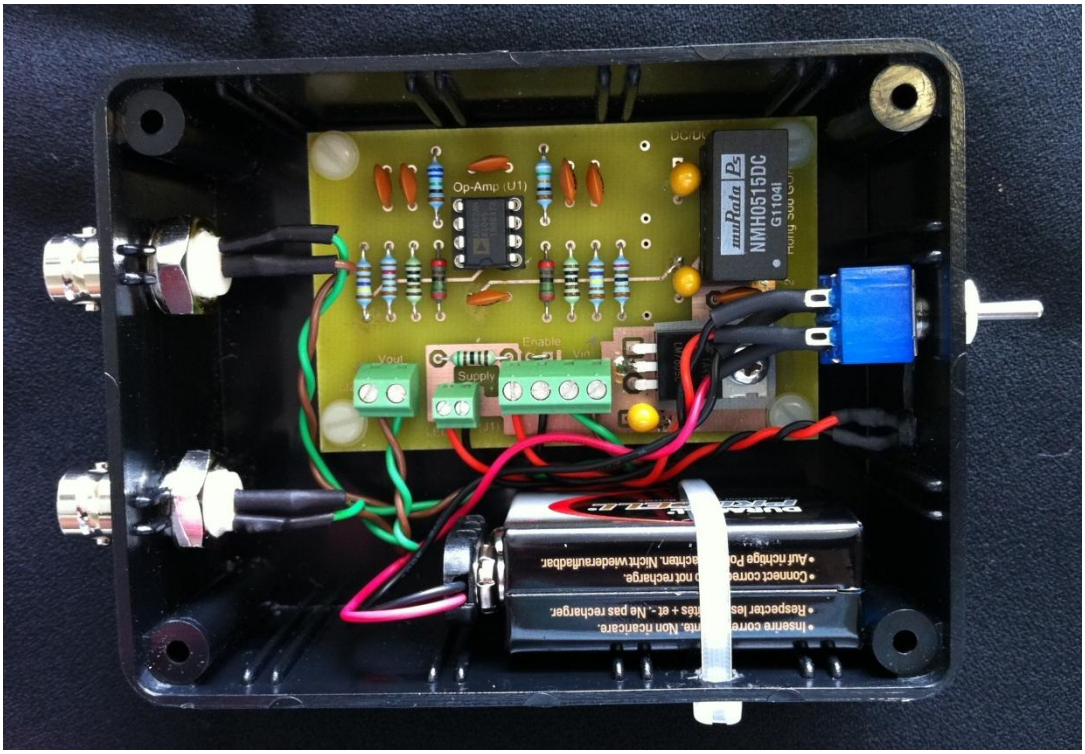

Figure 6.10 Analogue active bandpass filter for resonance detection.

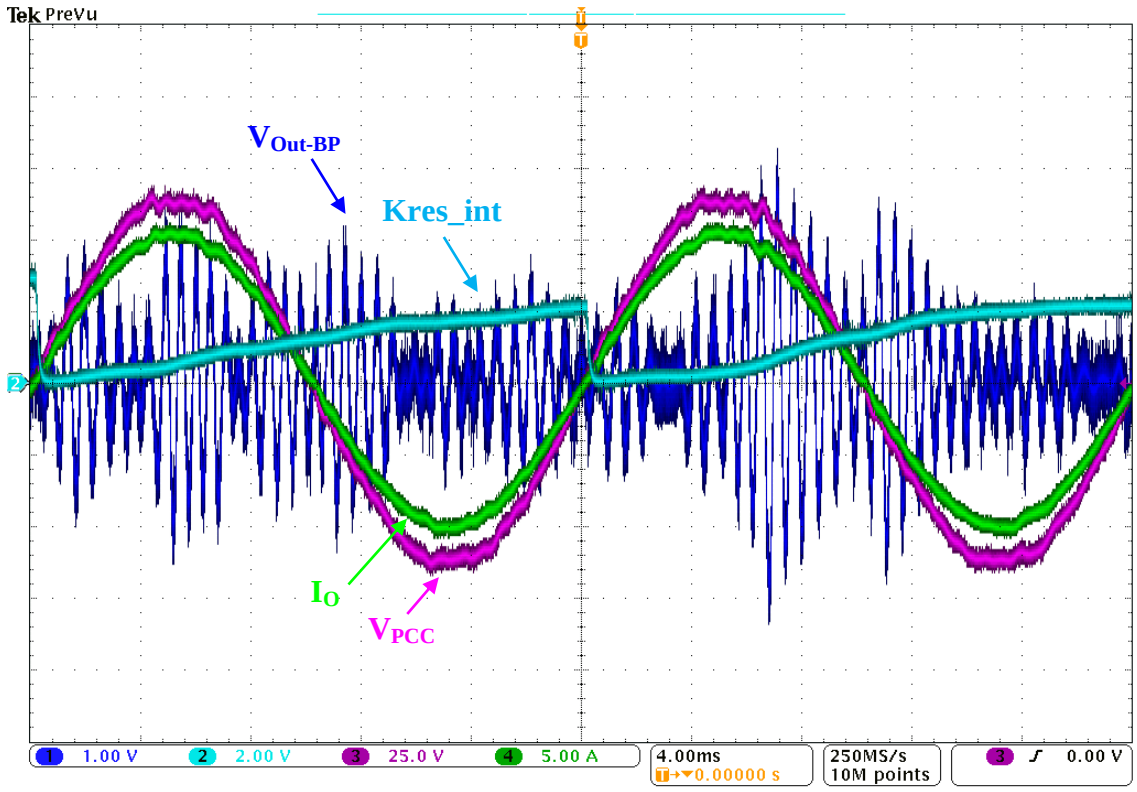

Figure 6.11 Waveform of PCC voltage (V_{PCC}), inverter system output current (I_O), bandpass filter output voltage (V_{Out-BP}) and microcontroller resonance detection integration signal (Kres_int) with fixed gain PI control at 100µH of grid inductance (L_g). (I_{demand} = 7A RMS, V_{DC} = 100V, V_G = 39V RMS, f_1 = 50Hz, K_p = 1.1, K_i = 0.6, L_g = 100µH.)

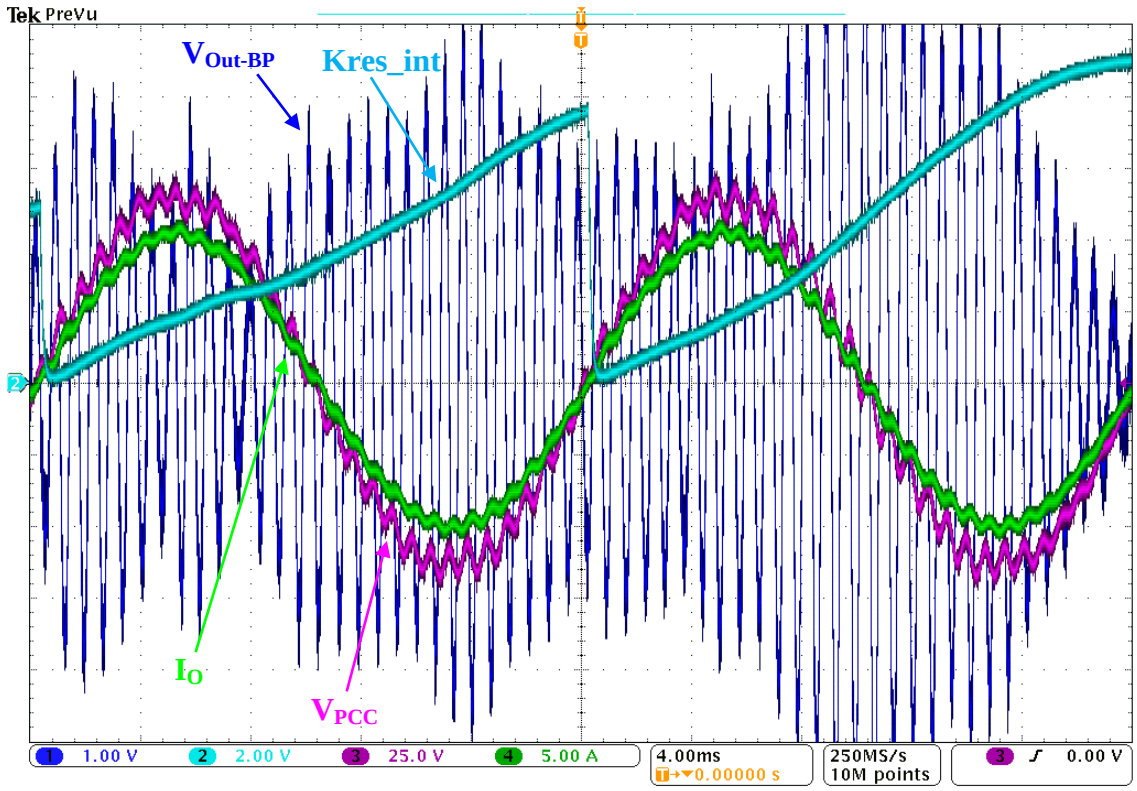

Figure 6.12 Waveform of PCC voltage (V_{PCC}), inverter system output current (I_O), bandpass filter output voltage (V_{Out-BP}) and microcontroller resonance detection integration signal (Kres_int) with fixed gain PI control at 900µH of grid inductance (L_g). (I_{demand} = 7A RMS, V_{DC} = 100V, V_G = 39V RMS, f_1 = 50Hz, K_p = 1.1, K_i = 0.6, L_g = 100µH.)

Figure 6.11 and Figure 6.12 show the filtering effect of the active bandpass filter for resonance detection at 100μH and 900μH of grid inductance respectively. In Figure 6.11, the PCC voltage (V_{PCC}) is sensed by the voltage sensor to create a scaled PCC voltage signal. To detect the resonance, the bandpass filter captured the harmonic components of scaled PCC voltage that located at the designed bandpass filter passband (in the frequency range of the 25^{th} and 55^{th} harmonics). The captured harmonics are shown by the bandpass filter output voltage waveform ($V_{Out\text{-}BP}$) in Figure 6.11. Although the oscillation on PCC voltage is not apparent due to low value of grid inductance (100μH), the filter passband harmonics are still magnified by high passband gain as designed. It should be noted that the trace "Kres_int" in Figure 6.11 and Figure 6.12 are the resonance detection integration signals which will be discussed later of this section.

In Figure 6.12, high level of oscillation is observed on the PCC voltage (V_{PCC}) due to the excitation of resonance within the passband frequency range of the bandpass filter with the high value of grid inductance (900μH). These high values of harmonics at the resonant frequency are captured by bandpass filter and hence high magnitude of voltage waveform is observed at the output of bandpass filter ($V_{Out\text{-}BP}$).

To analyse the filtering effect of the designed bandpass filter further, the input and output voltage waveform of the bandpass filter is measured by Yokogawa® PZ4000 Power Analyser and analysed by Fast Fourier Transform (FFT) function in Matlab/Simulink®. Figure 6.13 and Figure 6.14 show the comparison of the scaled PCC voltage (also referred as bandpass filter input voltage) and the bandpass filter output voltages harmonic profiles at 100μH and 900μH of grid inductance respectively. It should be noted that the harmonic magnitude of bandpass filter output voltage is scaled to the absolute magnitude of scaled PCC voltage fundamental harmonic to produce the bandpass filter output voltage harmonic profile expressed in percentage, as shown in Figure 6.13 and Figure 6.14.

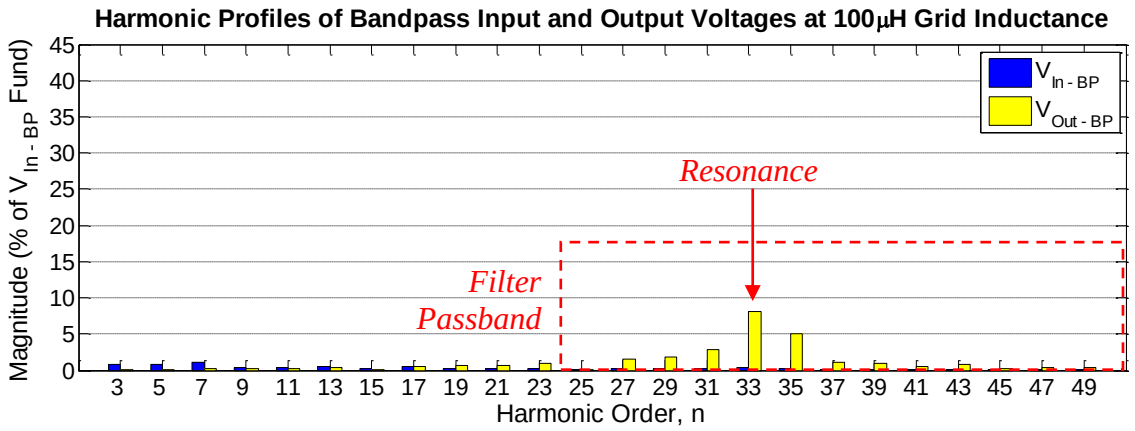

Figure 6.13 Harmonic profile comparison of the scaled PCC voltage (V_{In-BP}) and bandpass filter output voltage (V_{Out-BP}) at 100μH of grid inductance (L_g).
(I_{demand} = 7A RMS, V_{DC} = 100V, V_G = 39V RMS, f_1 = 50Hz, K_p = 1.1, K_i = 0.6, L_g = 100μH.)

Although the harmonic components within the filter passband are small in magnitude in Figure 6.13, they are still detected and magnified by designed bandpass filter. This is particularly apparent on the harmonic magnitude at the resonance, as pointed by the red arrow in the figure.

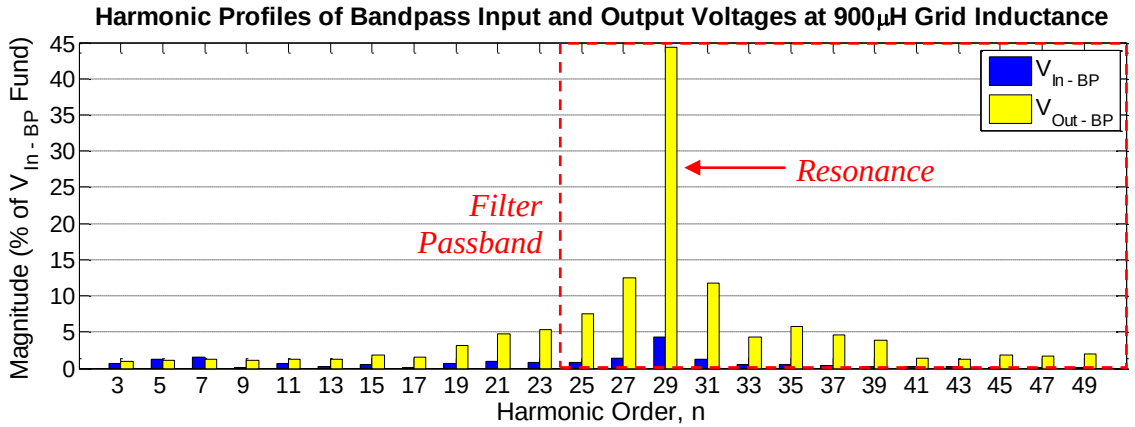

Figure 6.14 Harmonic profile comparison of the scaled PCC voltage (V_{In-BP}) and the bandpass filter output voltage (V_{Out-BP}) at 900μH of grid inductance (L_g).
(I_{demand} = 7A RMS, V_{DC} = 100V, V_G = 39V RMS, f_1 = 50Hz, K_p = 1.1, K_i = 0.6, L_g = 900μH.)

With resonance excited at high value of grid inductance (900μH), high value of harmonic components at resonant frequency (as pointed by the red arrow in Figure 6.14) are detected and magnified by the bandpass filter, while the harmonic components out of the filter passband are attenuated more, as shown by Figure 6.14.

6.6 Adaptive Proportional Gain Technique for Suppression of Resonance

Resonance can be suppressed by proper tuning of PI control proportional gain (K_P) as discussed in Section 6.3. This will need the information of the grid inductance to be known in order to tune the proportional gain accordingly. To measure the variation in grid inductance, the 4th order active bandpass filter is proposed to capture the harmonic components of PCC voltage at resonant frequency and hence the variation in grid inductance can be determined by measuring the magnitude of the harmonic components captured by the bandpass filter.

However, the harmonic components captured by the bandpass filter are expressed at the output of bandpass filter in a form of oscillating voltage signal that oscillates at the resonant frequency, as shown by the bandpass filter output waveform in Figure 6.12. This has led to the need of FFT or specialised technique to transform this waveform to the form that readable by the current control loop for proportional gain tuning. To avoid complex calculation of FFT, a signal processing technique that rectify and integrate the oscillating waveform is proposed to transform the output voltage waveform of bandpass filter, as shown by the control structure of the proposed adaptive tuning technique for the suppression of resonance in Figure 6.15. It consists of the signal processing process that transforms and averaging the oscillating signal to a form that readable by the look-up table for proportional gain tuning. The waveform for each of these signal processing steps are shown in Figure 6.16 and Figure 6.17 for grid inductance of 100µH and 900µH respectively.

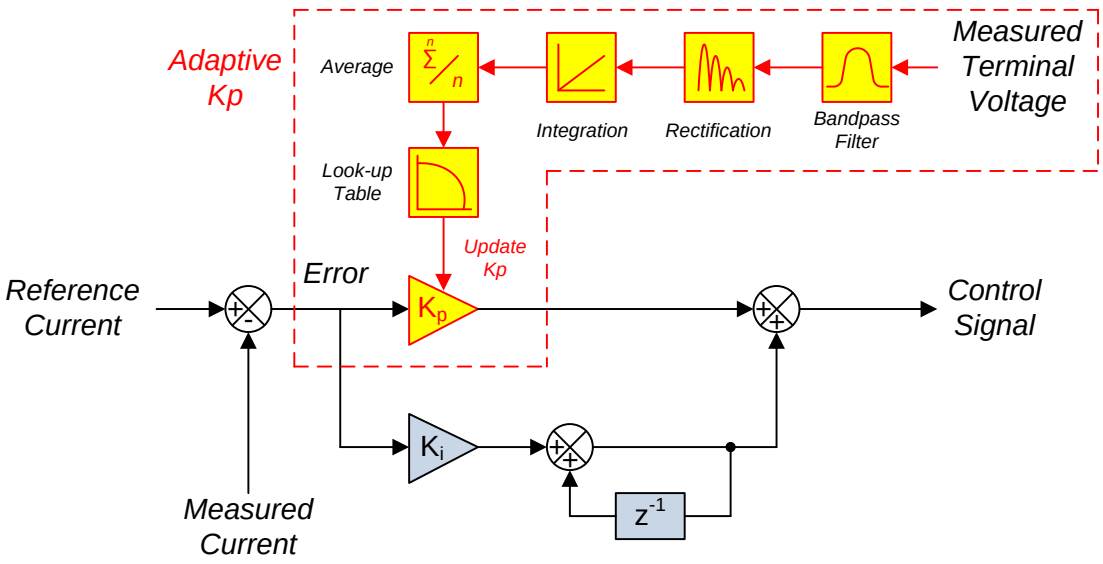

Figure 6.15 Adaptive tuning technique for proportional gain (K_P) of PI current control.

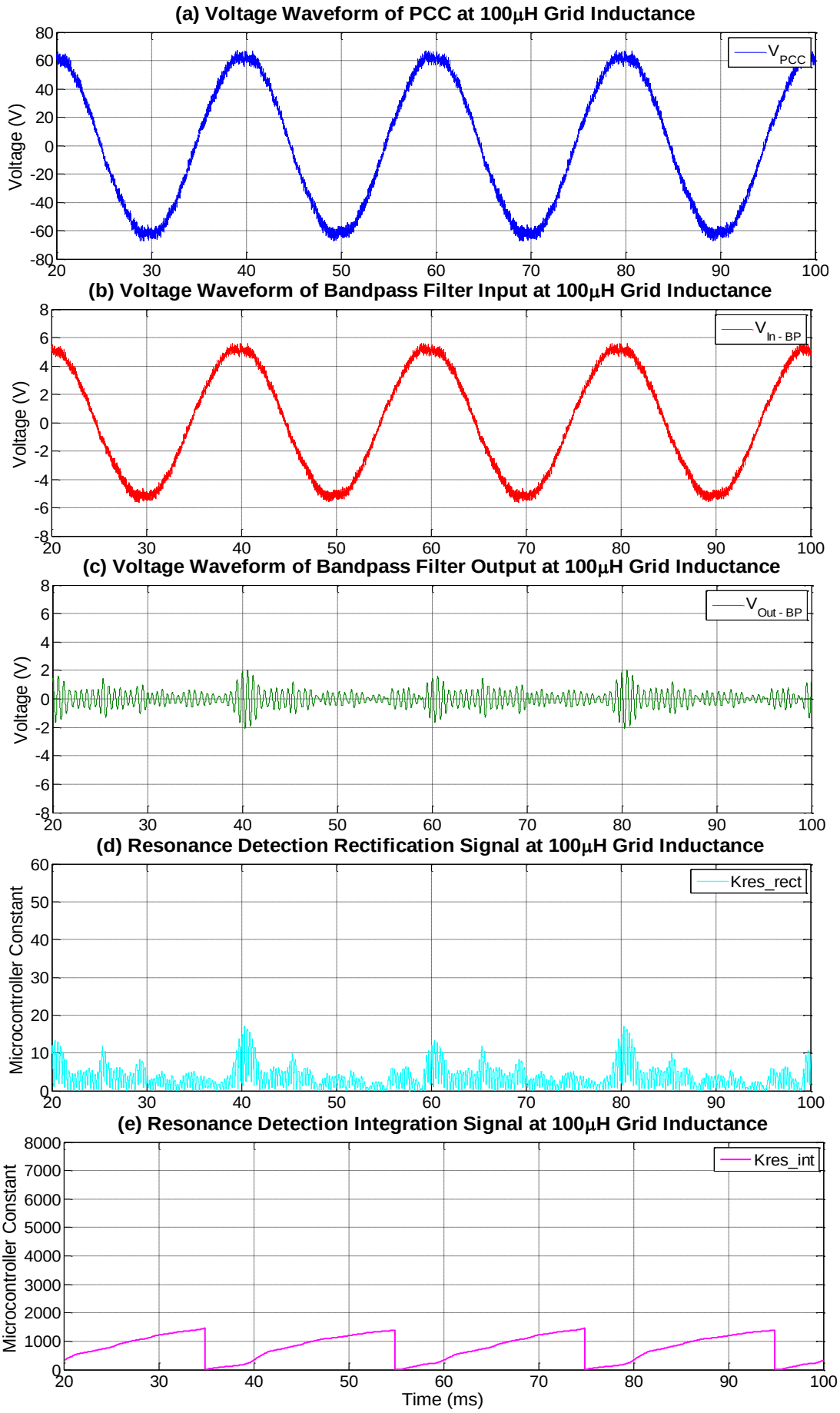

Figure 6.16 Signal processing of PCC voltage signal for resonance detection at 100μH of grid inductance (L_g).

(I_{demand} = 7A RMS, V_{DC} = 100V, V_G = 39V RMS, f_1 = 50Hz, K_p = 1.1, K_i = 0.6, L_g = 100μH.)

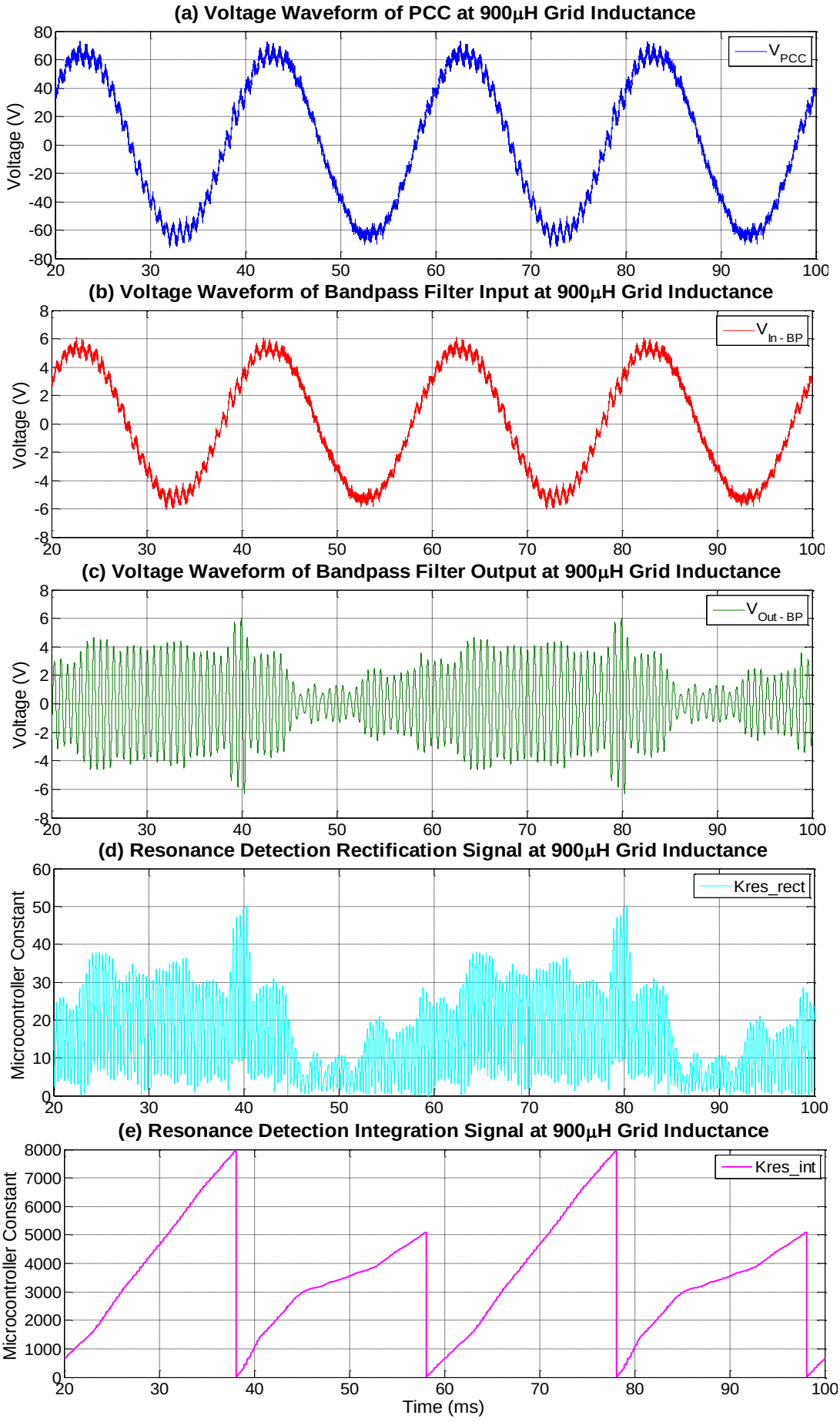

Figure 6.17 Signal processing of PCC voltage signal for resonance detection at 900µH of grid inductance (L_g).

(I_{demand} = 7A RMS, V_{DC} = 100V, V_G = 39V RMS, f_1 = 50Hz, K_p = 1.1, K_i = 0.6, L_g = 900µH.)

As shown by the control structure in Figure 6.15, the harmonic components at resonant frequency that captured by bandpass filter in the form of an oscillating signal ($V_{Out\text{-}BP}$, as shown in Figure 6.16(c) and Figure 6.17(c)) is convert to digital signal and read by microcontroller via ADC unit. As this converted digital signal asymmetrically oscillates along the zero point of vertical axis, rectification is applied on the digital signal to offset the negative part, yield the rectified signal (Kres_rect) as shown in Figure 6.16(d) and Figure 6.17(d). This process is achieved by the expressions as shown in Equation (6.3) and Equation (6.4), where *VOut_BP(k)* and *Kres_rect(k)* are the discretized bandpass filter output voltage and the rectification signal in microcontroller domain respectively.

If $VOut\_BP(k) \geq 0$,

$$Kres\_rect(k) = VOut\_BP(k) \tag{6.3}$$

If $VOut\_BP(k) < 0$,

$$Kres\_rect(k) = -VOut\_BP(k) \tag{6.4}$$

The rectification signal is then integrated by summing up the rectification signal at every control cycle and reset to zero at the end of the PCC voltage fundamental cycle, yield the integration signal (Kres_int) as shown in Figure 6.16(e) and Figure 6.17(e). This process is achieved by the expression as shown in Equation (6.5), where *Kres_int(k)* is the integration signal in microcontroller domain.

$$Kres\_int(k) = Kres\_rect(k) + Kres\_rect(k-1) \tag{6.5}$$

Besides that, the integration signal (Kres_int) is regenerated by the digital to analogue converter (DAC) in practical experiment and shown in Figure 6.11 and Figure 6.12 for grid inductance of 100μH and 900μH respectively. As shown on the figures that the maximum value of the integration signal (Kres_max) reflects the level of the oscillation on PCC voltage and hence the variation in grid inductance, the PI control proportional gain can then be tuned according to the maximum value of the integration signal.

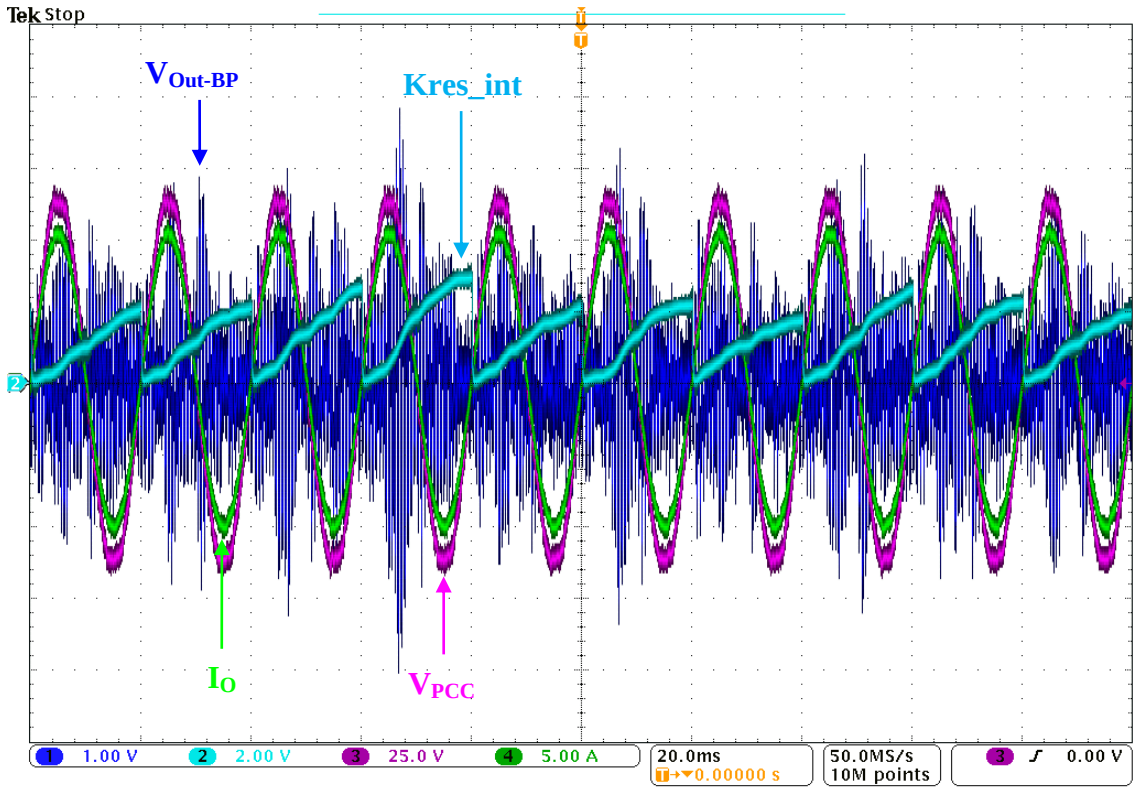

Figure 6.18 10 cycles of PCC voltage (V_{PCC}), inverter system output current (I_O), bandpass filter output voltage (V_{Out-BP}) and microcontroller resonance detection integration signal (Kres_int) with fixed PI control at 100µH of grid inductance (L_g).
(I_{demand} = 7A RMS, V_{DC} = 100V, V_G = 39V RMS, f_1 = 50Hz, K_p = 1.1, K_i = 0.6, L_g = 100µH.)

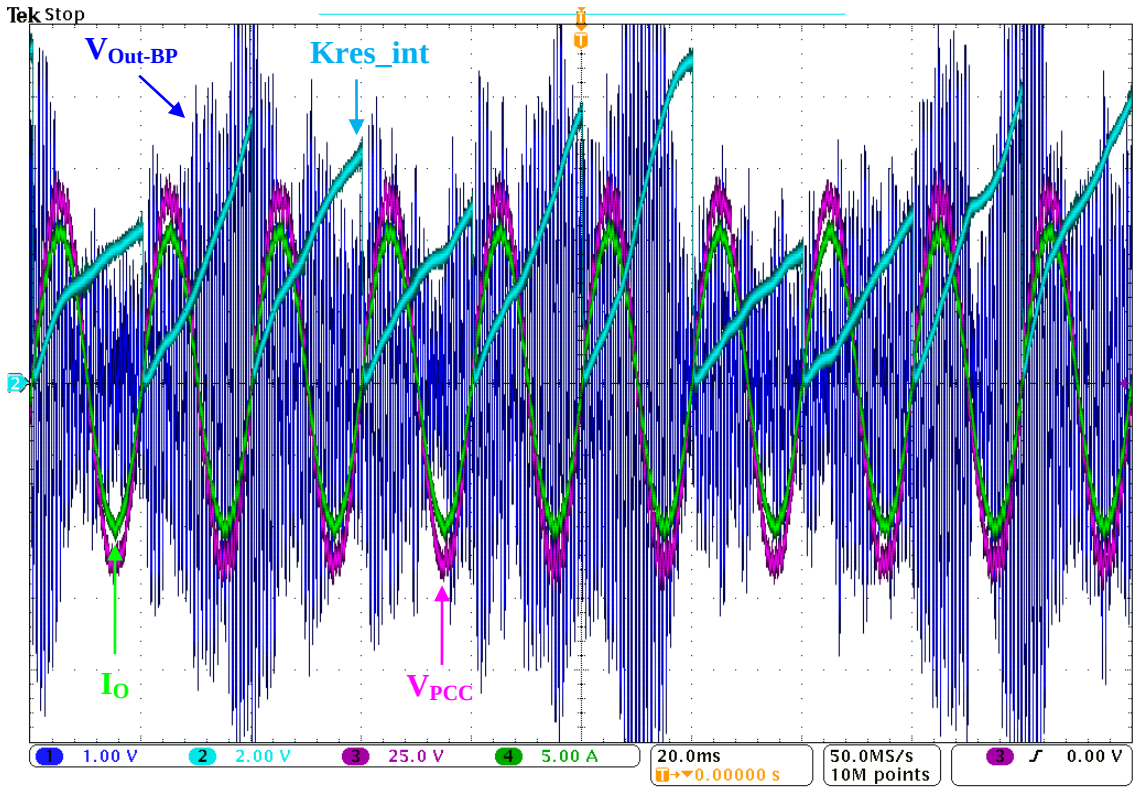

Figure 6.19 10 cycles of PCC voltage (V_{PCC}), inverter system output current (I_O), bandpass filter output voltage (V_{Out-BP}) and microcontroller resonance detection integration signal (Kres_int) with fixed PI control at 900µH of grid inductance (L_g).
(I_{demand} = 7A RMS, V_{DC} = 100V, V_G = 39V RMS, f_1 = 50Hz, K_p = 1.1, K_i = 0.6, L_g = 100µH.)

However, the maximum value of the integration signal is observed in practical experiment that not to be consistent but in fact fluctuate over time, as shown in Figure 6.18 and Figure 6.19 that record the waveform of the integration signal (Kres_int) over 10 PCC voltage fundamental cycles. Furthermore, it is observed on the practical experiment that the fluctuation is more severe on higher grid inductance value, as shown in Figure 6.19 where the grid inductance is increased to 900μH.

To cope with the fluctuation on the maximum value of integration signal, average of the maximum value of integration signal over the latest 10 cycles are used to tune the PI control proportional gain, as shown by the expression in Equation (6.6), where *Kres_max(k)* and *Kres_max_avg(k)* are the maximum value of integration signal and the average of its 10 latest cycles in microcontroller domain respectively.

$$Kres\_\max\_avg(k) = [Kres\_max(k-9) + \cdots + Kres\_max(k-1) + Kres\_max(k)]/10 \quad \textbf{(6.6)}$$

At the end of the signal processing stage where the average of the maximum value of integration signal over 10 latest cycles is obtained, this value is then fed into the pre-set look-up table as shown in Figure 6.15 to obtain its correlated proportional gain which will be updated and used by PI current control loop. Therefore, the proportional gain of the PI current control loop is adaptively tuned for corresponding grid inductance value to suppress the resonance.

6.7 Tuning of Adaptive Proportional Gain Look-up Table

Look-up table forms the core of the proposed adaptive control technique for resonance suppression as it dictates the level of suppression on resonance. The resonance might be over-suppressed or under-suppressed without proper tuning of look-up table. The proportional gain of PI control is lower than desired when the resonance is over-suppressed. This could lead to distortion on inverter system current waveform which increases the current THD as the command response of PI control loop is not sufficient, and harmonic standards [17, 19, 22] might be exceed in the case of heavily over-suppressed resonance. Contrary, oscillation on the PCC voltage is occurred when the resonance is under-suppressed. Higher oscillation on PCC voltage will cause the oscillation on output current of inverter system too and hence increase in current THD. Moreover, heavily under-suppressed resonance will cause excessive oscillation on the PCC voltage which could lead to malfunctioning of PV inverter synchronisation devices, such as Zero Crossing Detector (ZCD) and Phase-Locked Loop (PLL), and instability of

current controller. Hence, the tuning of the adaptive proportional gain look-up table is particularly important to effectively suppression the resonance while maintaining the best harmonic performance of current control loop.

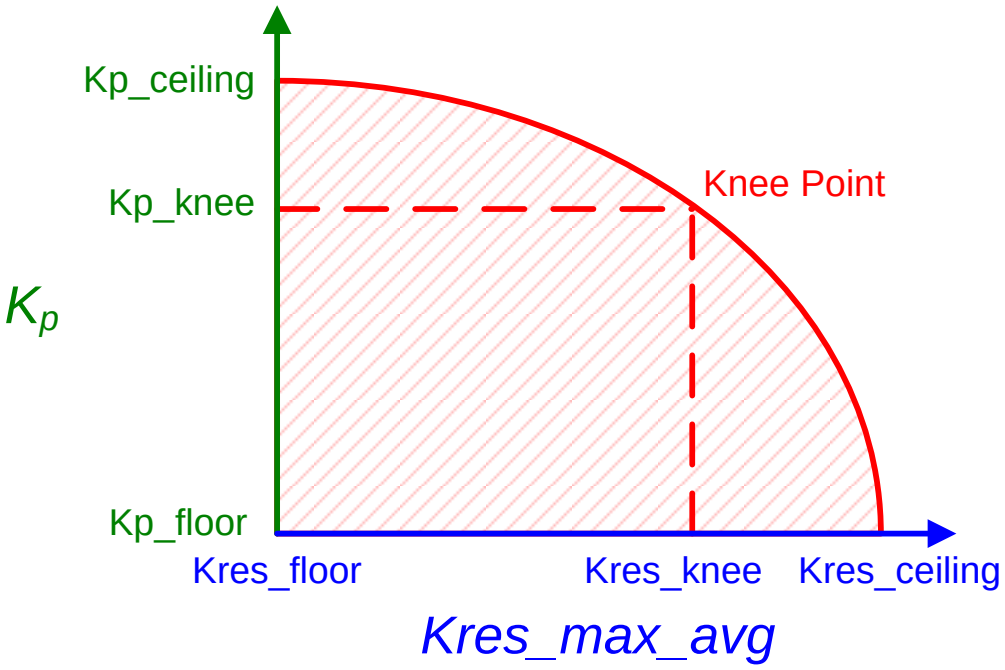

Figure 6.20 Look-up table for adaptive proportional gain PI control.

The proposed look-up table to correlate the average of maximum integration signal (Kres_max_avg) and PI control proportional gain (K_P) for resonance suppression is shown in Figure 6.20. In the figure, constants Kres_ceiling and Kres_floor represent the maximum and minimum value of Kres_max_avg that reflecting the highest and lowest expected grid inductance values respectively, which are the worst case and best case scenarios. Correlated to Kres_ceiling and Kres_floor are the Kp_floor and Kp_ceiling respectively, which are the allowable minimum K_P for most severe resonance and allowable maximum K_P for most trivial resonance. Another constant that reflects the mid-point condition between the worst case and best case scenarios (scenario when the grid inductance value is at the centre of the expected highest and lowest grid inductance), Kres_knee, and its correlated Kp_knee dictate the knee point of the curve.

In mathematical term, the curve of the adaptive proportional gain look-up table as shown in Figure 6.20 can be expressed as shown by Equation (6.7) to Equation (6.9).

$$res\_x = \frac{Kres\_\max\_avg - Kres\_floor}{Kres\_ceiling - Kres\_floor} \tag{6.7}$$

$$res\_y = -m(res\_x - Kx)^{pow} + Ky \tag{6.8}$$

$$K_p = res\_y(Kp\_ceiling - Kp\_floor) + Kp\_ceiling \tag{6.9}$$

Among Equation (6.7) to Equation (6.9), Equation (6.7) is more related to scale the Kres_max_avg value to match the normalized horizontal axis of look-up table, while Equation (6.9) is more related to rescale the K_P value from the correlated normalized vertical axis of look-up table. Moreover, the characteristic of the curve in the adaptive proportional gain look-up table is dictated by the curve characteristic equation as shown in Equation (6.8). This equation consists of four variables that vary the curve characteristic in different ways, as shown by Figure 6.21.

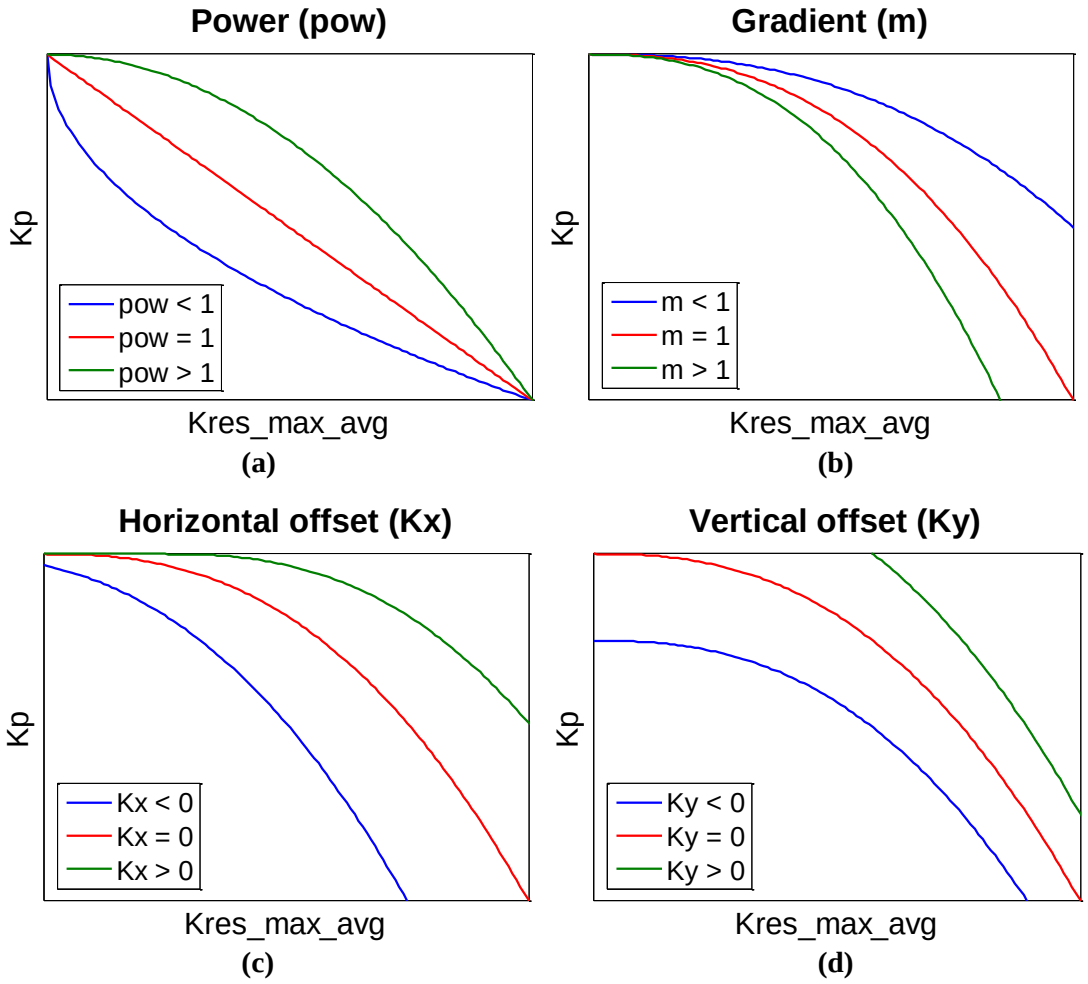

Figure (a)	Effect of the variable pow on the look-up table characteristic.
Figure (b)	Effect of the variable m on the look-up table characteristic.
Figure (c)	Effect of the variable Kx on the look-up table characteristic.
Figure (d)	Effect of the variable Ky on the look-up table characteristic.

Figure 6.21 Effect of the curve characteristic equation variables on the characteristic of the look-up table curve.

As shown by the effects in Figure 6.21(a) and Figure 6.21(b), the variables pow and m dictate the exponential level and gradient of the curve. The exponential decay rate of the curve is inversely proportional to variable pow, while the gradient of the curve is proportional to the variable m. In Figure 6.21(c) and Figure 6.21(d), the variables Kx and Ky offset the curve along the horizontal axis and vertical axis respectively. Positive and negative values of Kx shift the curve to the right and left respectively, while positive and negative value of Ky shift the curve up and down respectively.

The tuning of adaptive proportional gain look-up table must be carried out by simulating the different test cases, such as worst case scenario, best case scenario and knee point scenario, in practice to ensure the look-up table is match to the actual grid inductance range in real-life with all of the equipment errors and offsets taking into account. The procedure of look-up table tuning is shown by the flow chart in Figure 6.22.

Figure 6.23 shows the different test cases simulated in practical experiment. It show the value of Kres_max_avg that recorded over 10 minutes time with proportional gain tuned for lowest inverter system output current THD at best case scenario without any grid inductance (Figure 6.23(a)), knee point scenario with 400μH of grid inductance placed (Figure 6.23(b)), and worst case scenario with 1000μH of grid inductance placed (Figure 6.23(c)). The trend of the Kres_max_avg value as shown in the figure is obtained by the 8^{th} order of Fourier series via Matlab/Simulink®. From the trend of Kres_max_avg, the minimum trend value of best case scenario, mean trend value of knee point scenario and maximum trend value of worst case scenario are determined from the figures. The outcomes from different test cases are summarized as in Table 6.2.

Test Case	Grid Inductance (L_g)	K_p for lowest Output Current THD	Output Current THD	Kres_max_avg Trend Data
Best Case	*0μH*	*1.1*	*0.881%*	*1000 (Minimum)*
Knee Point	*400μH*	*1.05*	*1.178%*	*1700 (Mean)*
Worst Case	*1000μH*	*0.95*	*1.18%*	*2200 (Maximum)*

Table 6.2 Summary of the simulated test cases.

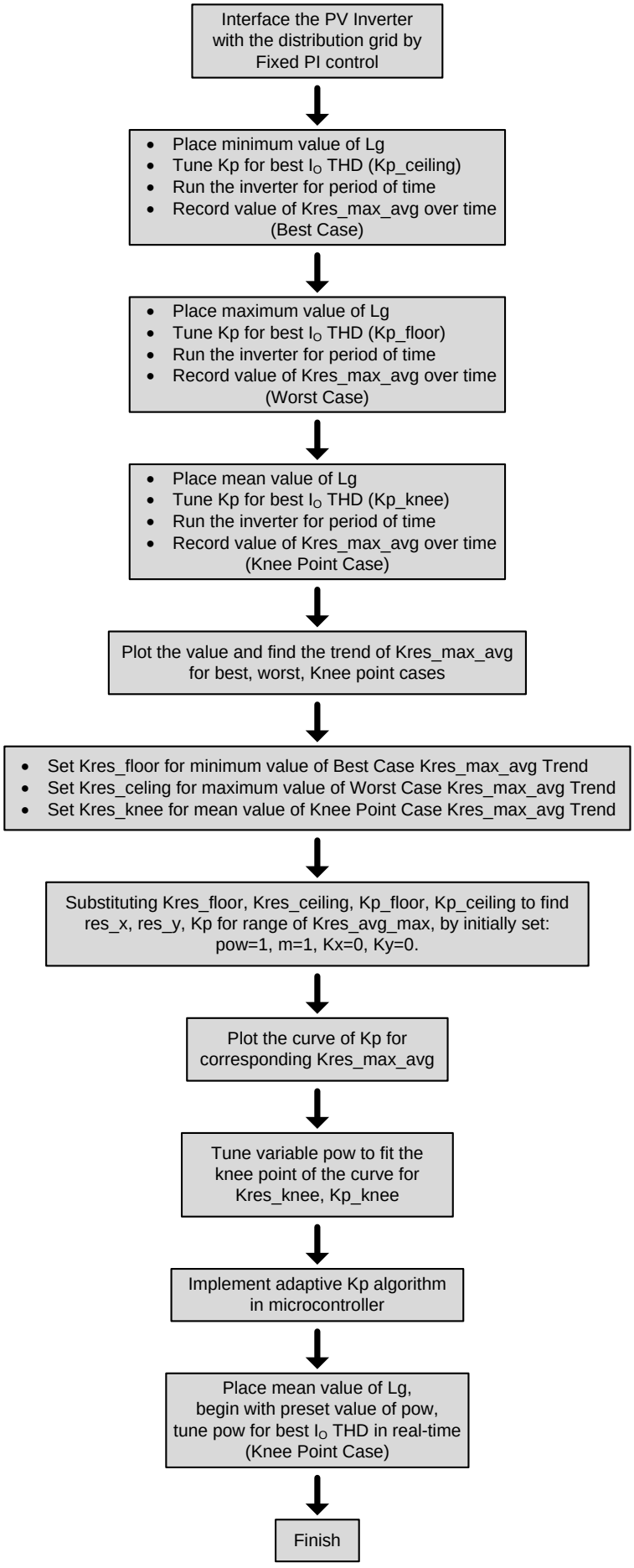

Figure 6.22 Flow chart of adaptive proportional gain look-up table tuning in practice.

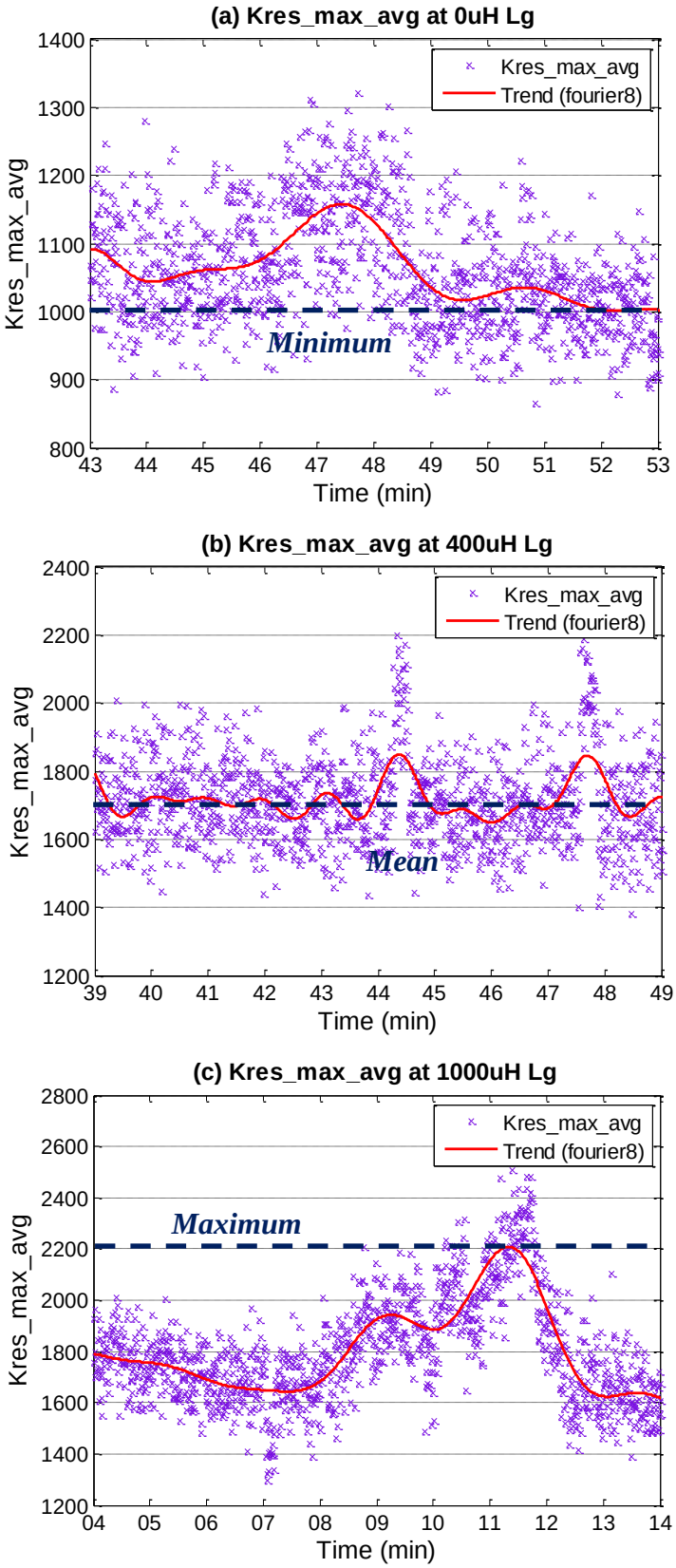

Figure (a)	Kres_max_avg at simulated best case scenario.
Figure (b)	Kres_max_avg at simulated knee point scenario.
Figure (c)	Kres_max_avg at simulated worst case scenario.

Figure 6.23 Recorded Kres_max_avg value over 10 minutes time and its trend at various test cases with proportional gain (K_P) tuned for lowest inverter system output current (I_O) THD.

As the values shown in Table 6.2 are obtained from the simulated three critical test cases, these values reflect the limit on Kres_max_avg and K_P in proposed adaptive proportional gain look-up table and also the knee point of the curve. Hence, the values in Table 6.2 for simulated test cases are substituted to match with look-up table as shown in Figure 6.20. In this process, the minimum value of Kres_max_avg trend and its corresponding K_P in best case scenario are substituted for Kres_floor and Kp_ceiling respectively, while the maximum value of Kres_max_avg trend and its corresponding K_P in worst case scenario are substituted for Kres_ceiling and Kp_floor respectively. By substituting these values into Equation (6.7) to Equation (6.9), the look-up table for a range of Kres_max_avg with unmatched knee point is plotted by initially set the variables pow and m equal to 1, Kx and Ky equal to 0, as shown by the linear look-up table in Figure 6.24.

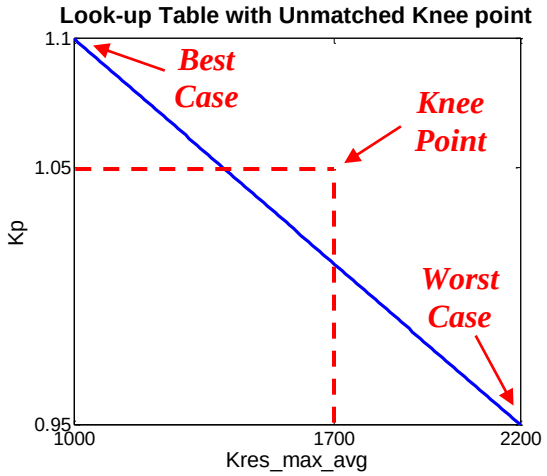

Figure 6.24 Look-up table with unmatched knee point.

To tune the knee point of look-up table, variable pow in Equation (6.8) is adjusted to match the knee point of the curve with the mean value of Kres_max_avg trend and its corresponding K_P for knee point case in Table 6.2. 2.1 of pow is obtained to match the look-up table knee point at this step and the preliminary adaptive proportional gain look-up table is plotted as shown in Figure 6.25.

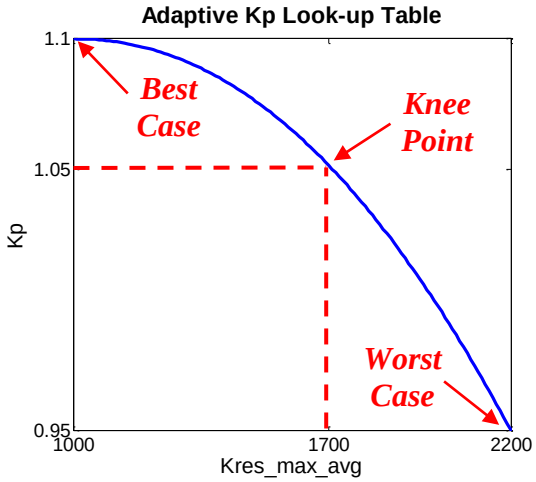

Figure 6.25 Preliminary adaptive proportional gain look-up table with all test cases matched.

The tuning of adaptive proportional gain look-up table is done by mathematical expression so far. It has to be refined by real-time tuning of the look-up table to match the condition in practice. For this purpose, Equation (6.7) to Equation (6.9) are implemented in Texas Instrument® TMS320F2812 DSP together with PI control loop in practical experiment. In real-time control aspect, LabVIEW™ software package from National Instruments® is used to control and communicate with DSP in real-time via RS232 serial communication interface. Figure 6.26 show the graphical user interface (GUI) in LabVIEW™ for real-time tuning of adaptive proportional gain look-up table.

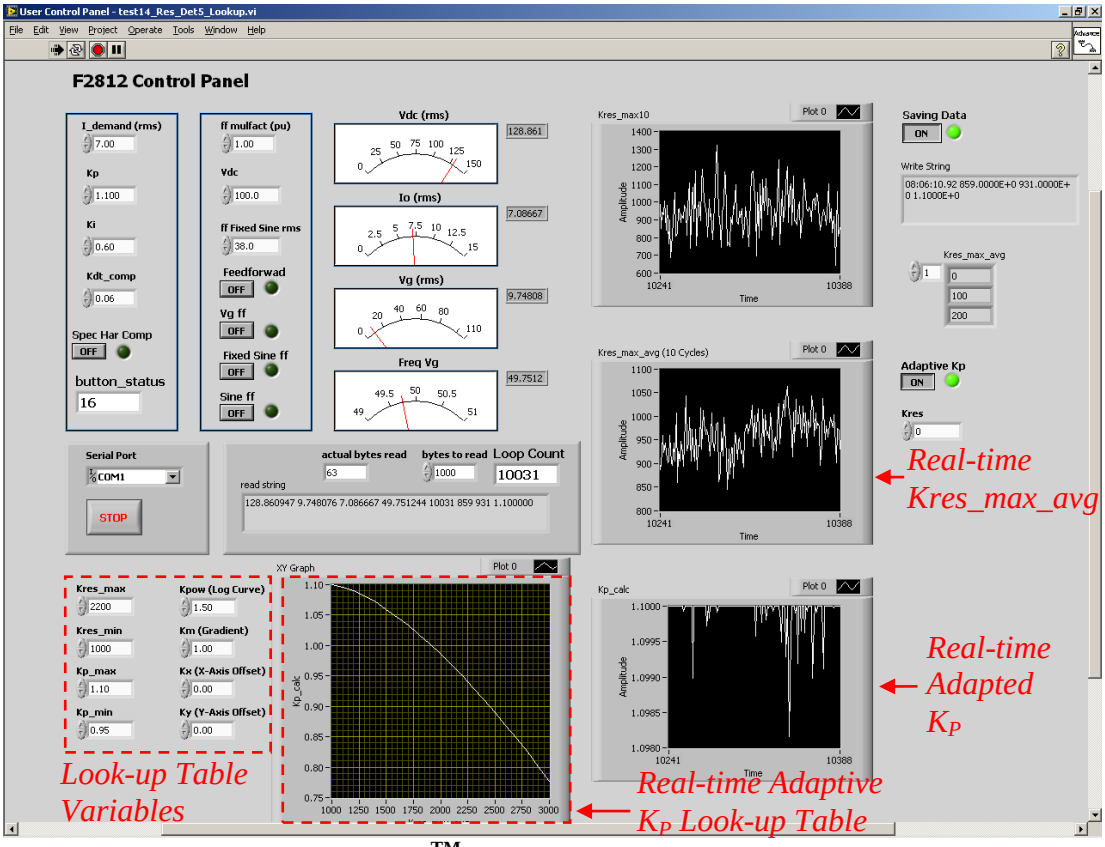

Figure 6.26 GUI in LabVIEW™ for DSP real-time control and communication.

To refine the preliminary look-up table, three cases as in Table 6.2 are simulated by inserting 0μH, 400μH and 1000μH of grid inductance in practical experiment. The proposed adaptive proportional gain PI control is implemented and the variable values used in preliminary look-up table (a shown in Figure 6.25) are used as the base value before refining taking place. The refining step is carried out by simulating the test cases in order. The variables of Equation (6.8) that dictate the characteristic of the look-up table curve, pow, m, Kx and Ky, are then adjusted in real-time to match the proportional gain in Table 6.2 for corresponding test cases. Table 6.3 shows the finalized value for adaptive proportional gain look-up table that refined in practical experiment.

Variable	Value
Kres_ceiling	*2200*
Kres_floor	*1000*
Kp_celing	*1.1*
Kp_floor	*0.95*
pow	*1.5*
m	*1*
Kx	*0*
Ky	*0*

Table 6.3 Finalized value for adaptive proportional gain look-up table.

In microcontroller point of view, executing equation which consists of complicated mathematical calculation, such as fraction or exponential term, is very complicated and hence longer computational time is needed to complete the calculation. Especially for the equations used for adaptive proportional gain look-up table as shown in Equation (6.7) and Equation (6.8), huge increase in the computational time of microcontroller is observed in practical experiment when the equations are implemented. The effective solution for this is to generate the look-up table based on Equation (6.7) to Equation (6.9) by applying the values in Table 6.3, then store the generated look-up table into the memory of microcontroller (either RAM or flash) prior the current control loop began. Therefore, the adaptive proportional gain of PI control can be correlated from its corresponding Kres_max_avg value that reflecting the value of grid inductance, without implementing the complicated equation. Figure 6.27 shows the adaptive proportional gain look-up table stored in the memory of TMS320F2812 DSP. In the figure, Kres_ceiling of look-up table is extended to 3000 from 2200 in Table 6.3 to provide additional suppression for higher level of resonance. Moreover, any Kres_max_avg value fall outside of the look-up table is clamped to Kres_floor or kres_ceiling to prevent overflow.

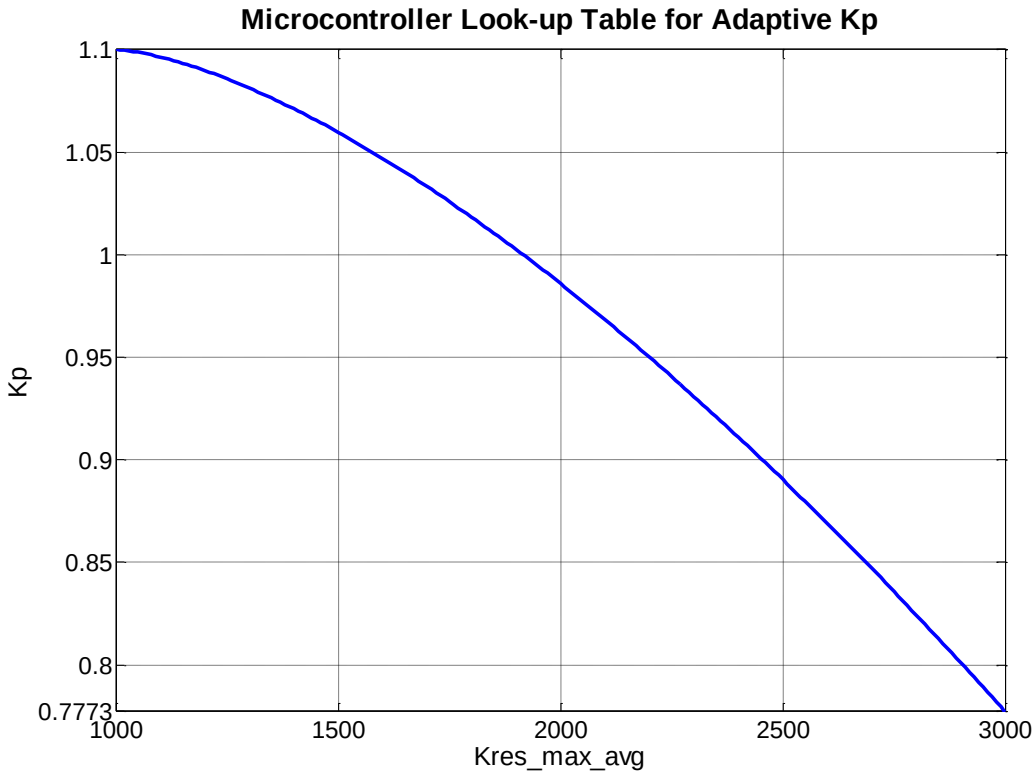

Figure 6.27 Adaptive proportional gain (K_P) look-up table stored in the memory of TMS320F2812 DSP.

6.8 Harmonic Performance and Resonance Suppression of Adaptive Proportional Gain PI Control

To assess the harmonic performance and the resonance suppression ability of the proposed adaptive proportional gain PI control, three different scheme of control topology are implemented on the microcontroller of the same grid-connected PV inverter system in practical experiment, which are conventional PI control with fixed gain (Fixed PI), PI control with terminal voltage feedforward (PI+VFF), and proposed adaptive proportional gain PI control (Adaptive Kp). The value of grid inductance is varied in order during the experiment to simulate the variation in grid inductance which led to excitation of resonance with increases value of grid inductance. Moreover, the inverter system output current for three different control schemes is recorded by Yokogawa® PZ4000 Power Analyser. By using FFT function in Matlab/Simulink®, the inverter system output current for the three different schemes at various grid inductances is analysed, and their harmonic profiles are they compared as shown in Figure 6.28. It should be noted that the detail practical experiment setup is extensively discussed in Chapter 3.

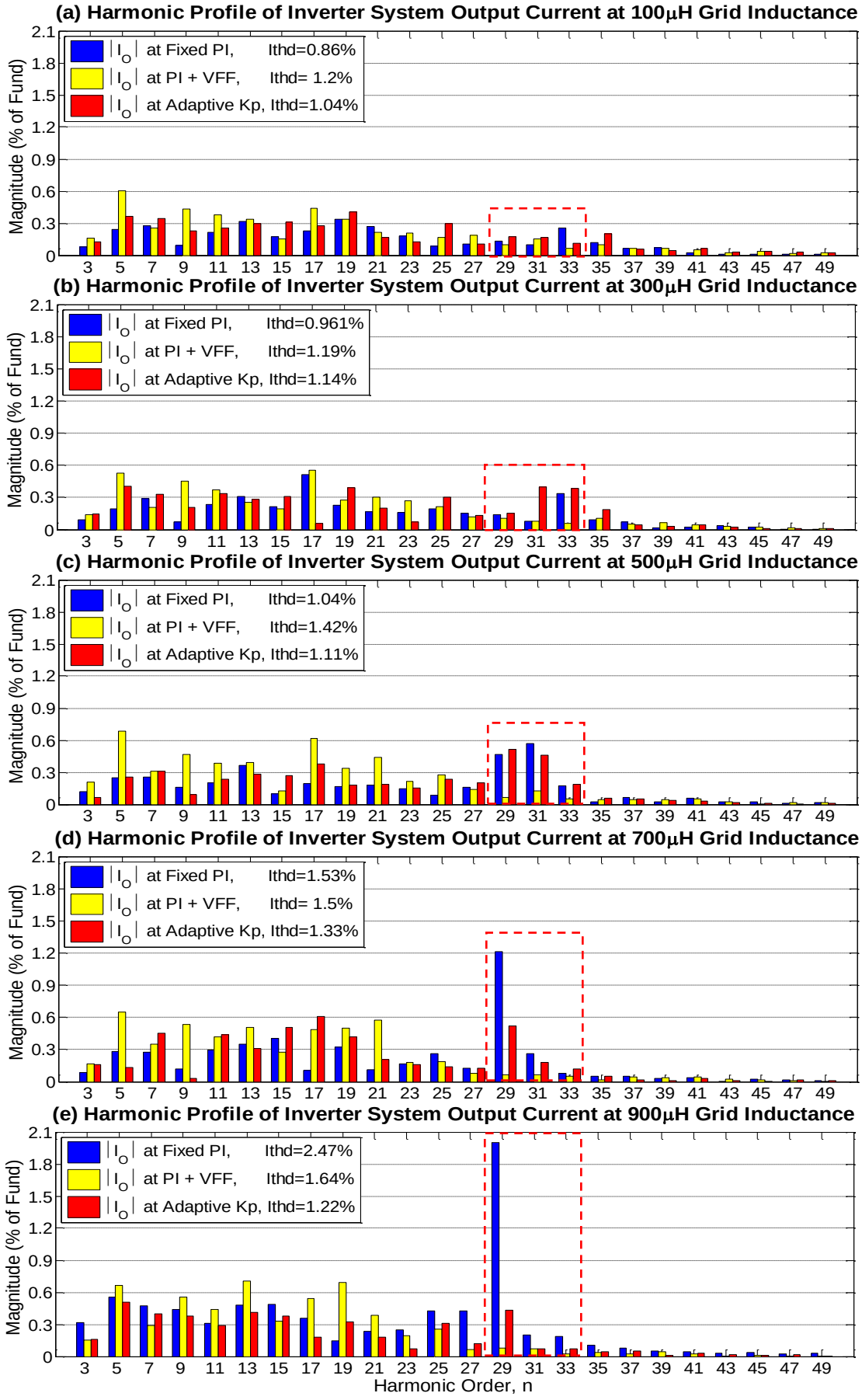

Figure 6.28 Comparison of fixed gain PI control (Fixed PI), terminal voltage feedforward PI control (PI + VFF), and adaptive proportional gain PI control (Adaptive Kp).
(I_{demand} = 7A RMS, V_{DC} = 100V, V_G = 39V RMS, f_1 = 50Hz, K_p = 1.1(Fixed PI, PI+VFF), K_i = 0.6(Fixed PI, Adaptive Kp) = 0.18(PI+VFF).)

By comparing the red boxes in Figure 6.28(a) to Figure 6.28(e) where the resonance is excited, very high magnitude of the current harmonic at resonant frequency is observed on fixed PI control scheme, while no excitation of the resonance is observed on terminal voltage feedforward PI control scheme even at very high value of grid inductance (900μH). For adaptive proportional gain PI control, although the magnitude of the current harmonics at resonant frequency is similar to the magnitude in fixed PI control at low value of grid inductance (100μH to 500μH), high magnitude of the current harmonics at resonant frequency with high value of grid inductance (700μH and 900μH) are suppressed significantly as the proportional gain is lower to cope with higher grid inductance value, as shown by Figure 6.28(d) and Figure 6.28(e). This also reflects effective suppression of the resonance at high value of grid inductance with adaptively tuned proportional gain.

As shown by the low order harmonics profile (from 3^{rd} to 21^{st} harmonics) of inverter system output current (I_O) in Figure 6.28, the low order harmonics trend of adaptive proportional gain PI control scheme slightly higher than or similar to the low order harmonics trend of fixed PI control scheme, while the low order harmonics trend of terminal voltage feedforward PI control scheme always the highest among the three control scheme.

By comparing the three control scheme in Figure 6.28, it is apparent that the fixed PI control has superior performance in the low order harmonics of the inverter system output current but susceptible to the excitation of resonance, while terminal voltage feedforward PI control is advantageous in suppression of the resonance and robust to the disturbance, but its drawback on high low order harmonics that cause the higher current THD offsetting its advantage. In adaptive proportional gain PI control scheme, it inherit the superior performance of fixed PI control in low order harmonic and adaptively tune its proportional gain to suppress the current harmonics at resonant frequency. Therefore, as shown by the current THD value in Figure 6.28, although the current THD of adaptive proportional gain PI control scheme is slightly higher than fixed PI control scheme at low grid inductance value which can be outweigh by its robustness and performance in resonance suppression, its current THD is always lower than terminal voltage feedforward PI control scheme even at high value of grid inductance value. Furthermore, the performance of adaptive proportional gain PI control can be further improved through more accurate design of bandpass filter centre frequency for the frequency of resonance and better tuning of the look-up table.

6.9 Interaction Test of Adaptive Proportional Gain PI Controller

As the grid inductance vary over time due to the change in grid operating condition, the proposed adaptive proportional gain PI controller should adaptively tune the proportional gain according to the variation in grid inductance. To assess the interaction between the grid inductance and the adaptive proportional gain of PI control, the adaptive proportional gain PI control is implemented on the grid-connected PV inverter current controller in practical experiment to interface with the emulated low voltage distribution grid in the laboratory over long period of time. To assess the interaction of the proposed adaptive proportional gain PI controller in response to the variation in operating condition of the actual grid, the emulated grid inductance (tapped inductor) is not employed in the experiment. During the experiment, the value of Kres_max_avg and K_P for adaptive proportional gain PI control are continuously monitored and recorded via LabVIEW^{TM} GUI over 12 hours a day. These values are then plotted and their trend are obtained by 8th order of Fourier series, as shown by the value of Kres_max_avg and its trend from 7am to 7pm of a day on 25/05/2011 in Figure 6.29, and its corresponding K_P value and trend as shown in Figure 6.30. It is also apparent on Figure 6.29 and Figure 6.30 that the proportional gain (K_P) of PI control is adaptively tuned for corresponding variation in Kres_max_avg that reflects the change in actual grid inductance. Another three days of test results are shown in Figure 6.31 and Figure 6.32, Figure 6.33 and Figure 6.34, Figure 6.35 and Figure 6.36.

As shown in Figure 6.29, Figure 6.31, Figure 6.33 and Figure 6.35, the instantaneous value of Kres_max_avg (purple cross in the figures) is continuously fluctuated throughout the monitoring interval. This fluctuation reflects the instantaneous change in the actual grid inductance that caused by variation in the grid operating condition (e.g. connection/disconnection of the loads). In response to this variation, the proportional gain (K_p) of PI control is adaptively tuned to suppress the resonant excitation and hence exhibiting the optimal harmonic performance of PV inverter system, as shown in Figure 6.30, Figure 6.32, Figure 6.34 and Figure 6.36. In addition, the red boxes in these figures show the maximum variation in the PI control proportional gain (K_p) in response to the highest Kres_max_avg value over 12 hours of a day (shown in the red boxes of Figure 6.29, Figure 6.31, Figure 6.33 and Figure 6.35 respectively). It is noted that the proportional gain (K_p) in Figure 6.30, Figure 6.32, Figure 6.34 and Figure 6.36 is varied by 18%, 13.3%, 12.7% and 10.7% of proposed K_p range (shown in Figure 6.25, K_p=1.1~ 0.95) at maximum respectively.

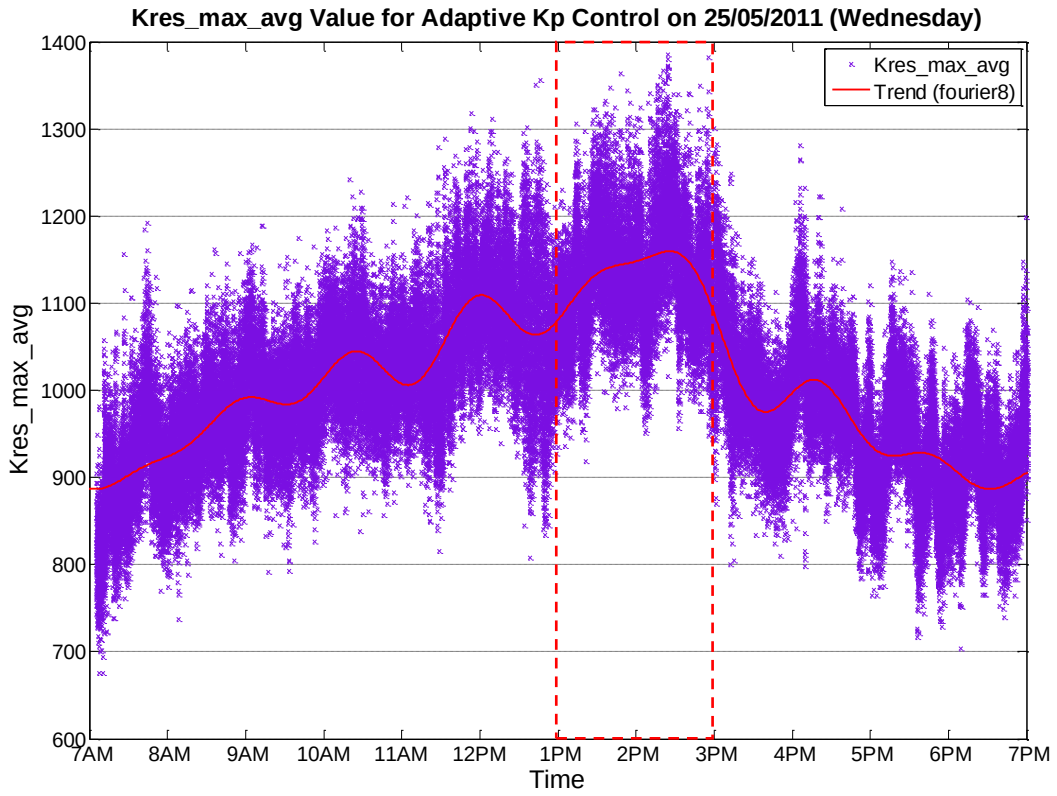

Figure 6.29 Kres_max_avg value for adaptive proportional gain (K_P) PI control on 25/05/2011.
(I_{demand} = 7A RMS, V_{DC} = 100V, V_G = 39V RMS, f_1 = 50Hz, K_i = 0.6, L_g = 0μH.)

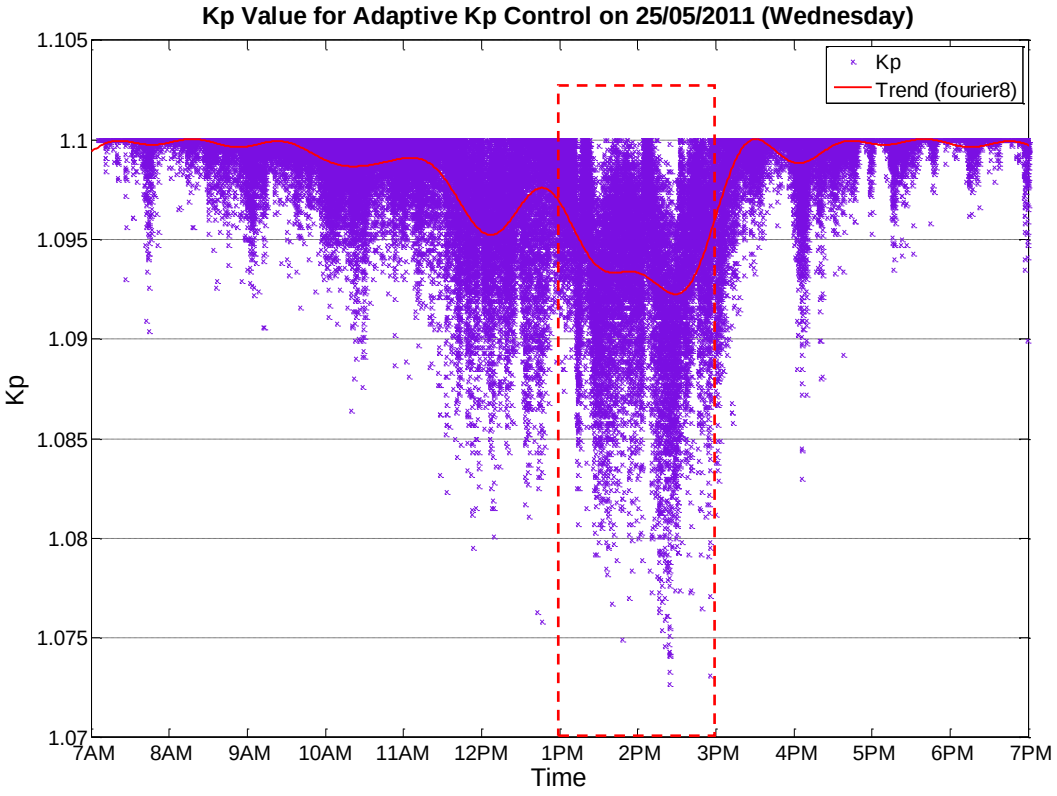

Figure 6.30 K_P value for adaptive proportional gain (K_P) PI control on 25/05/2011.
(I_{demand} = 7A RMS, V_{DC} = 100V, V_G = 39V RMS, f_1 = 50Hz, K_i = 0.6, L_g = 0μH.)

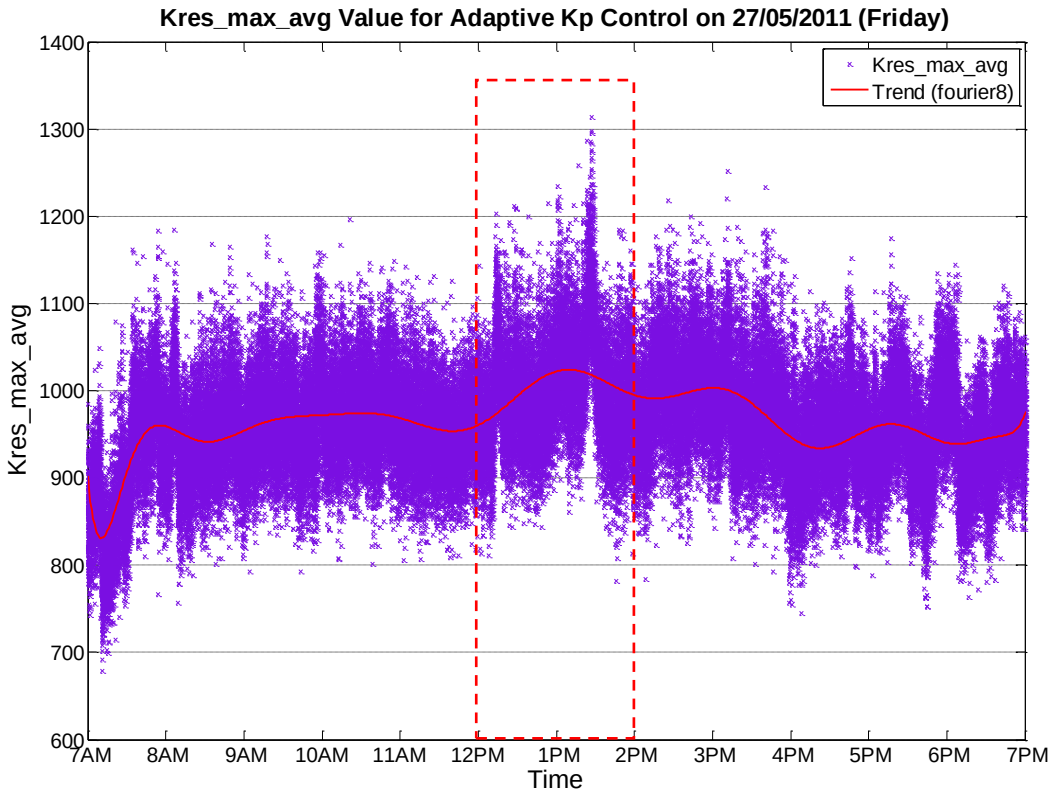

Figure 6.31 Kres_max_avg value for adaptive proportional gain (K_P) PI control on 27/05/2011.

(I_{demand} = 7A RMS, V_{DC} = 100V, V_G = 39V RMS, f_1 = 50Hz, K_i = 0.6, L_g = 0μH.)

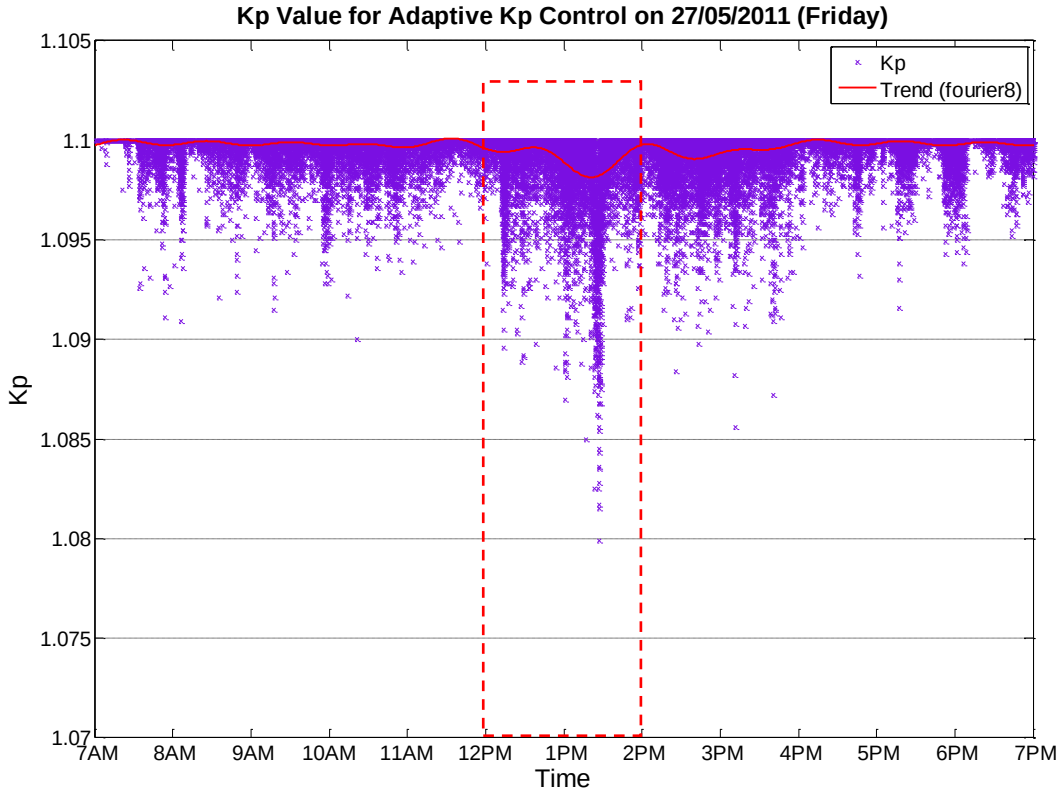

Figure 6.32 K_P value for adaptive proportional gain (K_P) PI control on 27/05/2011.

(I_{demand} = 7A RMS, V_{DC} = 100V, V_G = 39V RMS, f_1 = 50Hz, K_i = 0.6, L_g = 0μH.)

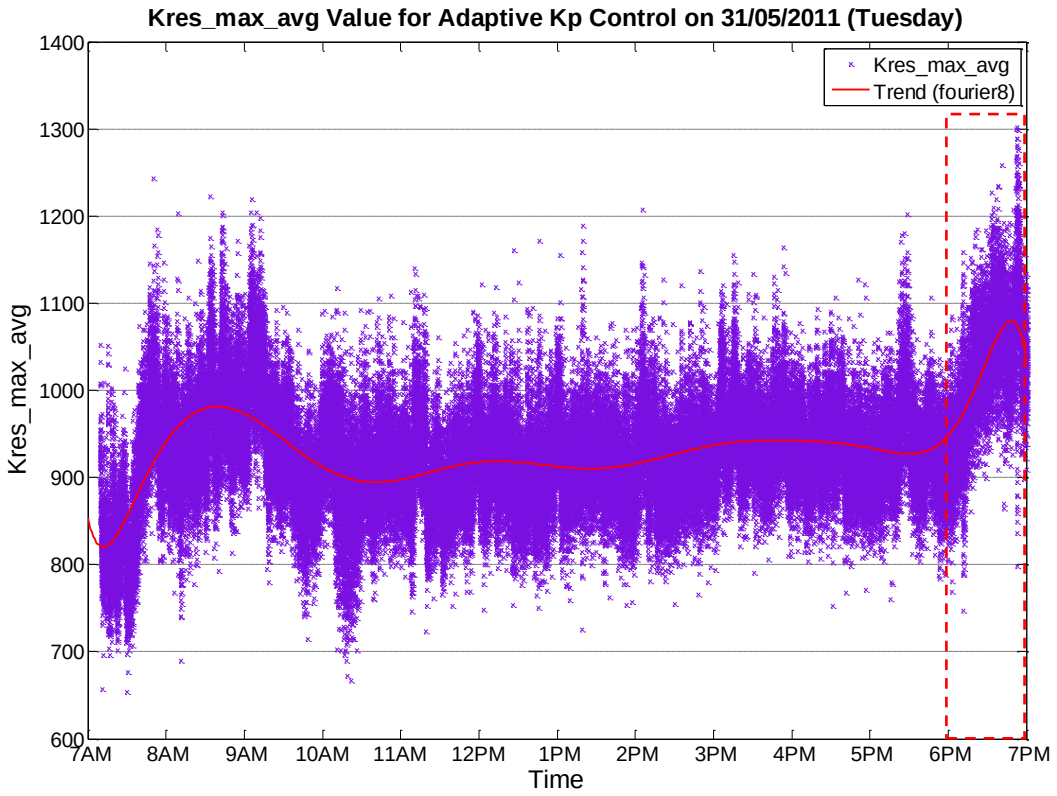

Figure 6.33 Kres_max_avg value for adaptive proportional gain (K_P) PI control on 31/05/2011.
(I_{demand} = 7A RMS, V_{DC} = 100V, V_G = 39V RMS, f_1 = 50Hz, K_i = 0.6, L_g = 0μH.)

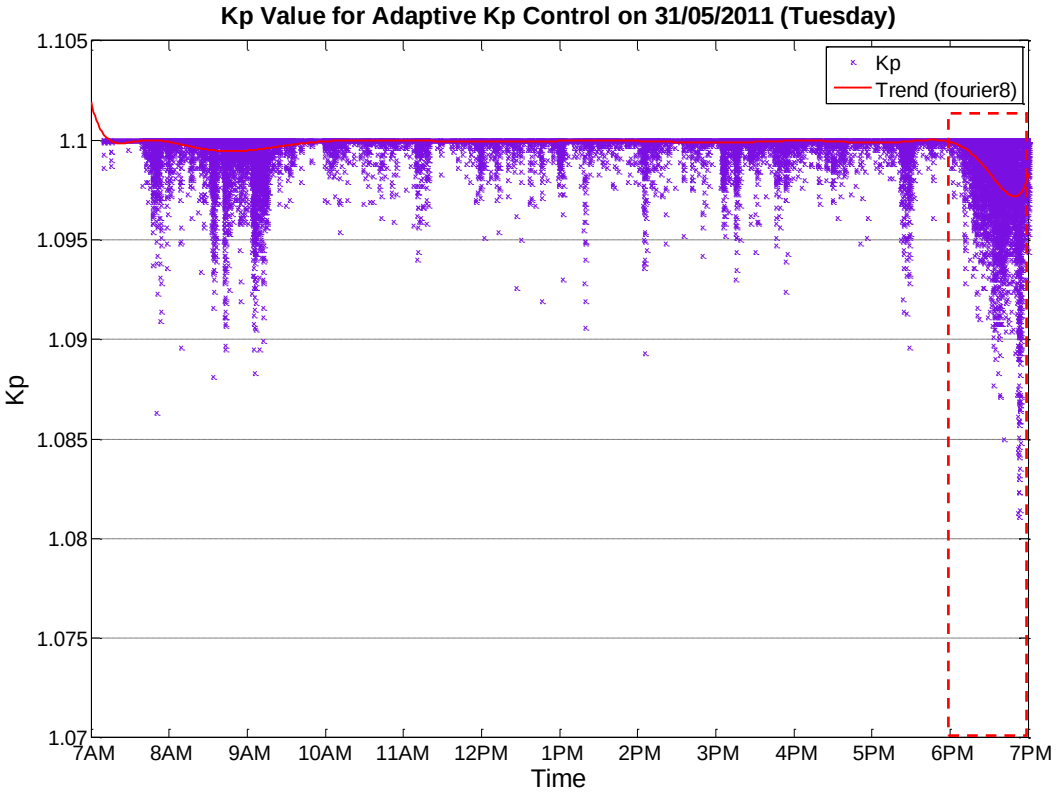

Figure 6.34 K_P value for adaptive proportional gain (K_P) PI control on 31/05/2011.
(I_{demand} = 7A RMS, V_{DC} = 100V, V_G = 39V RMS, f_1 = 50Hz, K_i = 0.6, L_g = 0μH.)

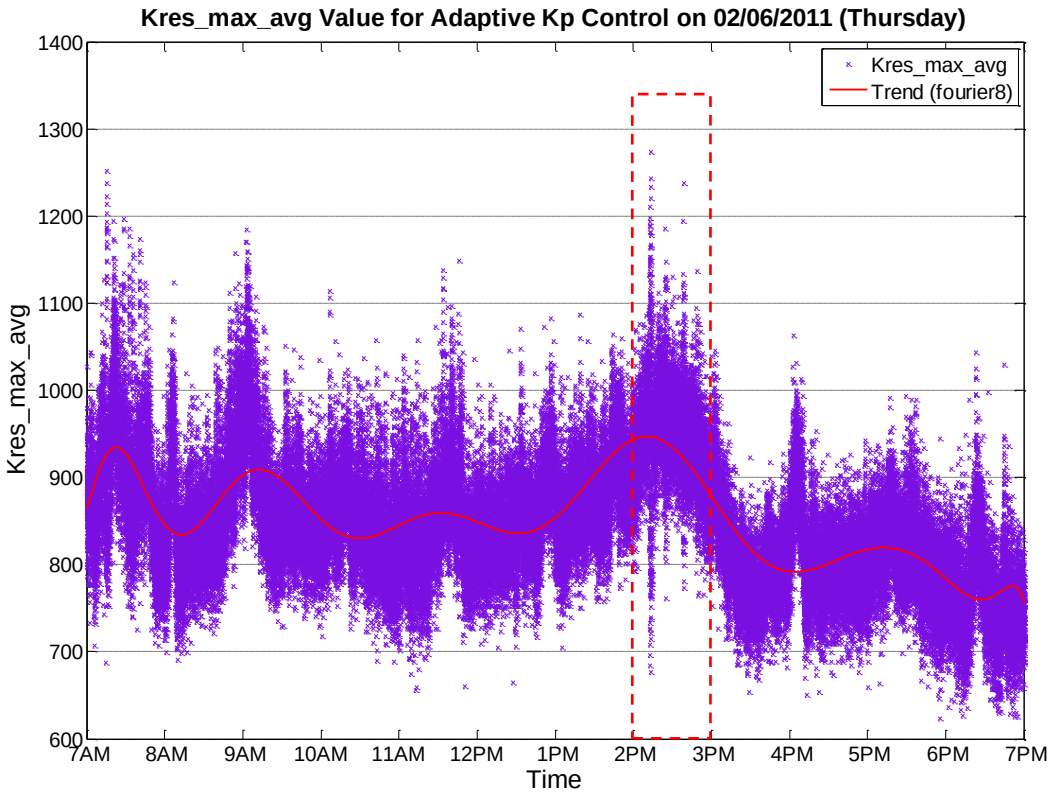

Figure 6.35 Kres_max_avg value for adaptive proportional gain (K_P) PI control on 02/06/2011.

(I_{demand} = 7A RMS, V_{DC} = 100V, V_G = 39V RMS, f_1 = 50Hz, K_i = 0.6, L_g = 0μH.)

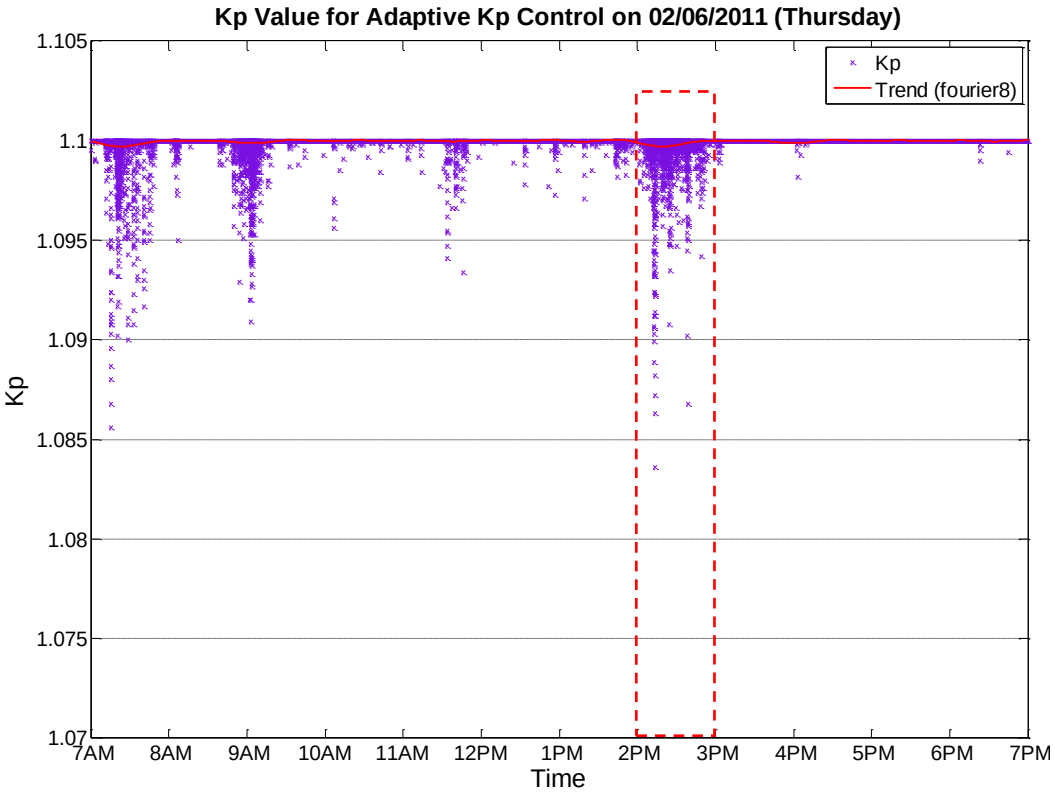

Figure 6.36 K_P value for adaptive proportional gain (K_P) PI control on 02/06/2011.

(I_{demand} = 7A RMS, V_{DC} = 100V, V_G = 39V RMS, f_1 = 50Hz, K_i = 0.6, L_g = 0μH.)

6.10 Summary

This chapter discussed the effect of PI control proportional gain on the excitation resonance and the adaptive tuning technique of proportional gain to suppress the resonance. It has been shown on the practical result that the resonance can be suppressed by proper tuning of proportional gain. For this reason, a technique to adaptively tune the proportional gain by capturing the harmonics at resonance frequency via active bandpass filter is developed. A look-up table is used in the adaptive tuning to correlate the variable that reflects the grid inductance value with its corresponding proportional gain for PI control. Tuning of this look-up table is particular important to effectively adapt the proportional gain for grid inductance variation, and hence proper tuning procedure is developed and discussed. Furthermore, inverter system current harmonic profile of the proposed adaptive proportional gain PI control, fixed gain PI control and terminal voltage feedforward PI control from practical experiment are compared. The comparison show that the proposed adaptive proportional gain PI control inherit the superior harmonic performance of fixed PI control on low order harmonic while remain robust at high value of grid inductance as the resonance is suppressed by adaptively tuned proportional gain. This has led to lower inverter system output current THD with adaptive proportional gain PI control than terminal voltage feedforward PI control even at high value of grid inductance.

Chapter 7. Thesis Conclusions

7.1 Conclusions for Interaction of Grid-Connected PV Inverter and Distribution Grid

Typically, grid-connected PV inverter systems employ closed loop output current control to inject unity power factor current into the distribution grid. For this reason, the interaction between the distribution grid and the current controller of the PV inverter system is important. To help understand the interactions which take place, an experimental grid-connected PV inverter system has been connected to the laboratory supply and the power quality of the system has been recorded at various times across the day. It is observed that the harmonic profile of the inverter system output current is affected by the variation in the harmonic profile of the background grid voltage. This effect and linkage between the background grid voltage and inverter system output current has been further analysed in simulation and mathematically explained in Section 4.4.

To study the harmonic effect of background voltage on the harmonic performance of inverter current controller in more detail, a high fidelity grid-connected PV inverter system model is developed in Matlab/Simulink®. This model offers more flexibility and repeatability of testing than is possible from a fixed laboratory supply where predictable, or controllable, characteristics cannot be guaranteed. Experimentally obtained harmonic data from the laboratory grid voltage is used to generate the distribution grid model in Matlab/Simulink®. The simulation results are compared to the practical results for verification purposes, and the similarity in harmonic performance of each has been confirmed. In the simulation the individual background grid voltage harmonics are varied; the results confirm that by altering a single magnitude of the background grid voltage harmonic, each harmonic component of the inverter system output current is affected. There is also a directly proportional change in the magnitude of the respective inverter system output current harmonic when the magnitude of the corresponding background grid voltage harmonic is varied. In addition to the effect of background grid voltage harmonic, the simulation has confirmed that there is also a direct proportional change in the phase angle of the respective inverter system output current harmonic when the phase angle of the corresponding background grid voltage harmonic is varied. Moreover, it is shown that the magnitude of the respective inverter system output

current harmonic is at maximum when the corresponding background grid voltage harmonic is lagging the fundamental harmonic by 90° and vice-versa when the corresponding background grid voltage harmonic is leading the fundamental harmonic by 90° (270° lagging). This is due to the change in the magnitude of the inverter bridge output voltage in order to cope with the variation in the phase angle of background grid voltage harmonic.

In conclusion, the result confirm that the low order output current harmonics of a grid-connected PV inverter are sensitive to even small changes in the magnitude and phase angle of background grid voltage harmonic. A modest change in the background grid voltage over time can result in significantly different current control performance of the grid-connected PV inverter.

7.2 Conclusions for Resonance and Adaptive Control for Suppression of Resonance

Typical grid-connected PV inverters interface with the electrical network via a lowpass filter. This filter couples with the impedance of the distribution grid to form an LCL resonant circuit and introduce an additional low impedance resonance which leads to voltage and current distortion at the resonant frequency. In the network with a high penetration of distributed generation and many sources of non-linear loads, the grid impedance is much more volatile and likely to change over time which causes a shift in the frequency of the low impedance resonance. It is shown in the practical research that this low impedance resonance is excited by the PCC voltage oscillation that coincides with the resonant frequency that shifted with increased grid inductance. Such a situation is possible, even though the PV inverter controller is initially configured to avoid the resonant frequency during installation and commissioning.

It has been experimentally proven that the PCC voltage oscillation is caused by excessive values of PI control proportional gain (K_P). One way to reduce this oscillation is by employing a terminal voltage feedforward scheme. This unburdens the PI control by feedforwading the terminal voltage waveform of PV inverter to the output of PI control. However, it is also shown by practically that this feedforward scheme has a tendency to increase the low order harmonics of the inverter output current due to the measurement error and offset of the voltage sensor and conversion circuits. For this reason, a novel approach to suppressing the resonance is proposed in this thesis. As this oscillation is caused by excessive K_P within the PI controller, the resonant oscillation

can be minimised by simply reducing the proportional gain as the grid inductance increases. Practical results clearly demonstrate that the resonance is suppressed by reducing K_P as the grid inductance is increased.

In the proposed resonance suppression scheme, a 4^{th} order active bandpass filter is employed and tuned to capture the harmonic components at the resonant frequency. This can be used as a simple detector for variation in grid impedance.

The proportional gain of the PI controller is then adaptively tuned by processing the bandpass filter output signal and correlating the result to a preset look-up table value. This proposed scheme has been successfully implemented on the experimental grid-connected inverter system. The harmonic performance of the scheme is compared with conventional PI control and the terminal voltage feedforward scheme. Results confirm that the proposed Adaptive K_P scheme effectively suppresses the resonance while providing superior low order harmonic performance in the inverter output current.

7.3 Further Work

Other areas of investigation have been identified that might help the robustness of the grid-connected PV system in response to distribution grid disturbances. For example, the performance of the current controller can be significantly improved if the grid synchronisation method is more robust to highly distorted grid voltages. Literature review has shown that significant work has been carried out in the area of grid synchronisation algorithms. However, many of these methods are concerned with low levels of grid distortion. Synchronisation with highly distorted voltage waveforms caused by resonance is an area for further investigation, such as implementation of a robust PLL instead of ZCD for synchronisation.

Improvement in the design of the passive lowpass filter at the output of the inverter bridge is also possible. Although the filter design is not a new topic in the field, it can easily interact with the grid impedance to excite the resonance if special attention is not given in the design process. Moreover, it is hard to find guidelines on lowpass filter design for grid-connected applications that take into account the variation in grid impedance and interactions with the grid. Hence, the robustness of the grid-connected PV inverter system can be improved if the lowpass filter is designed in such a way that the input impedance is very high for a wide range of grid impedance to reject the disturbance from the grid, whilst providing very high attenuation to the unwanted

harmonics. So far the investigation on the effect of variation in background grid voltage harmonic on the harmonic performance of PV inverter is carried out through simulation in Matlab/Simulink®. This is primarily because a programmable AC source able to sink current is not available in the laboratory. A step further would be to acquire such a piece of equipment and conduct this investigation experimentally for greater understanding of this interaction in practice.

From a control point of point, there is still plenty of room to improve the robustness of the grid-connected PV inverter current controller. With regards to the proposed adaptive K_P scheme to suppress resonance, further improvement can be made by more accurate design of the bandpass filter and more precise tuning of the look-up table. Here, a more powerful microprocessor might be used to implement a digital bandpass filter with better response. Moreover, the work carried out on grid-connected PV inverter system could also be extended to 3 phase applications with flexible real/reactive power control. Flexible control is emerging as an important area in the field of Smart Grid systems where power flow and reactive power compensation are relevant.

7.4 Research Outcomes

This work has yielded the following research output:

- H. S. Goh, M. Armstrong, and B. Zahawi, "The effect of grid operating conditions on the current controller performance of grid connected photovoltaic inverters," in *13th European Conference on Power Electronics and Applications* 2009, pp. 1-8.

In addition, at the time of submission, two papers presenting the outcomes from the practical research have been submitted for review to IEEE Transaction on Power Electronics and IEEE Transaction on Industrial Electronics respectively.

- H. S. Goh, M. Armstrong, and B. Zahawi, "Effect of grid operating conditions on the harmonic performance of grid-connected PV inverters."
- H. S. Goh, M. Armstrong, and B. Zahawi, "Adaptive proportional gain (K_P) PI control for suppression of resonance on grid-connected PV inverters."

Appendix I. Verification of LCL Branch Transfer Function

Open Loop Frequency Response of LCL branch:

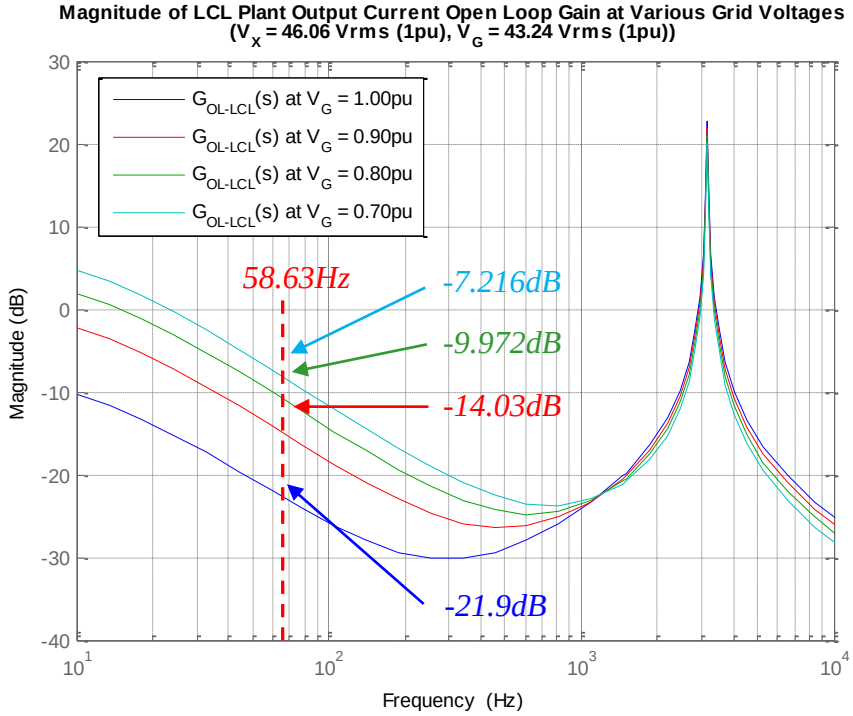

Figure: Magnitude of LCL plant output current open loop gain at various grid voltages.

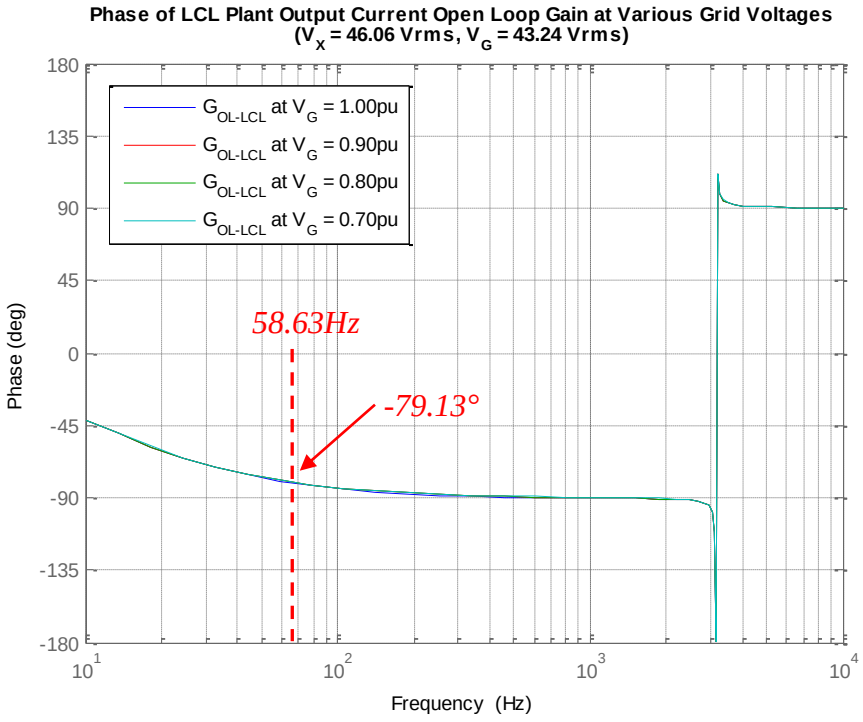

Figure: Phase angle of LCL plant output current open loop gain at various grid voltages.

V_G	1.0pu	0.9pu	0.8pu	0.7pu
I_O/V_X (dB)	-21.9dB	-14.03dB	-9.972dB	-7.216dB
I_O/V_X (A/V)	0.0804	0.1988	0.3172	0.4357
Phase Angle	-79.13°	-79.13°	-79.13°	-79.13°
I_O (V_X=46.0641 V)	3.70A	9.16A	14.61A	20.07A

Table: Values of LCL branch output current open loop gain at frequency of 58.63Hz with various grid voltages by transfer function model.

V_X (1pu)	46.0641V
V_G (1pu)	43.2423V
L_f	1808μH
R_{Lf}	0.15Ω
C_f	9.9252μH
R_{Cf}	0.0566Ω
L_g	300μH
R_g	0Ω

Table: Parameters for LCL branch.

As filter capacitive reactance is high at low frequency, it has less effect on output current of LCL branch and hence can be neglected to simplify the verification. Figure below show the equivalent circuit of LCL branch neglecting the filter capacitance.

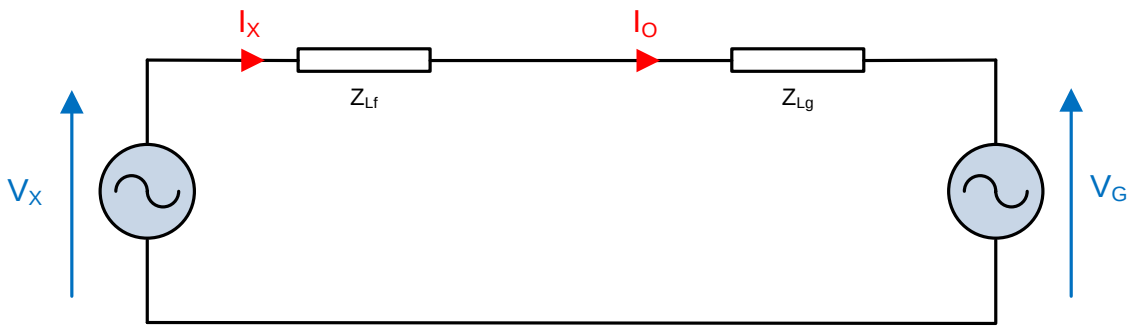

Figure: Equivalent circuit of LCL branch neglecting the filter capacitance.

At frequency of 58.63Hz,

$$Z_{Lf} = R_{Lf} + j2\pi f L_f = 0.15 + j(2\pi \times 58.63 \times 1808\mu H) = (0.15 + j0.666)\Omega$$

$$Z_{Lg} = R_g + j2\pi f L_g = 0 + j(2\pi \times 58.63 \times 300\mu H) = j0.1105\Omega$$

From the figure,

$$I_O = \frac{V_X - V_G}{Z_{Lf} + Z_{Lg}}$$

For V_G=1.0pu,

$$I_O = \frac{46.0641 - 43.2423}{0.15 + j0.666 + j0.1105} = (0.6766 - j3.5032)A = (3.57\angle - 79.07°)A$$

For V_G=0.9pu,

$$I_O = \frac{46.0641 - 43.2423 \times 0.9}{0.15 + j0.666 + j0.1105} = (1.7138 - j8.8718)A = (9.04\angle - 79.07°)A$$

For V_G=0.8pu,

$$I_O = \frac{46.0641 - 43.2423 \times 0.8}{0.15 + j0.666 + j0.1105} = (2.7509 - j14.2403)A = (14.50\angle - 79.07°)A$$

For V_G=0.7pu,

$$I_O = \frac{46.0641 - 43.2423 \times 0.7}{0.15 + j0.666 + j0.1105} = (3.7879 - j19.6089)A = (19.97\angle - 79.07°)A$$

V_G	Transfer Function Model	Equivalent Circuit Calculation
1.0pu	*3.70∠-79.13°A*	*3.57∠-79.07°A*
0.9pu	*9.16∠-79.13°A*	*9.04∠-79.07°A*
0.8pu	*14.61∠-79.13°A*	*14.50∠-79.07°A*
0.7pu	*20.07∠-79.13°A*	*19.97∠-79.07°A*

Table: Comparison of LCL branch output current gain at 58.63Hz with transfer function model and equivalent circuit calculation.

Appendix II. Schematics of Measurement Boards, Zero Crossing Detector and Active Bandpass Filter

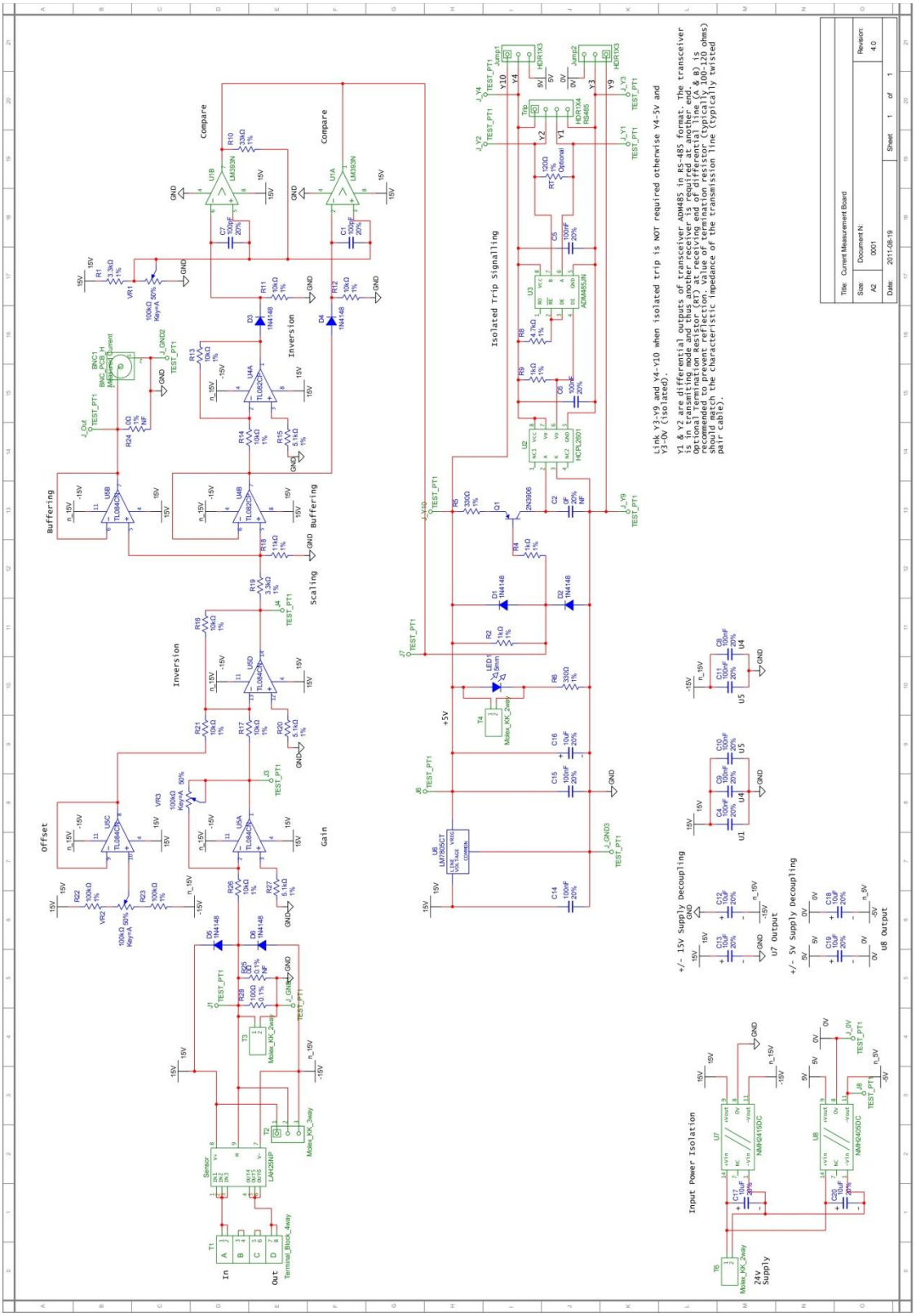

Figure A: Schematics of current measurement board.

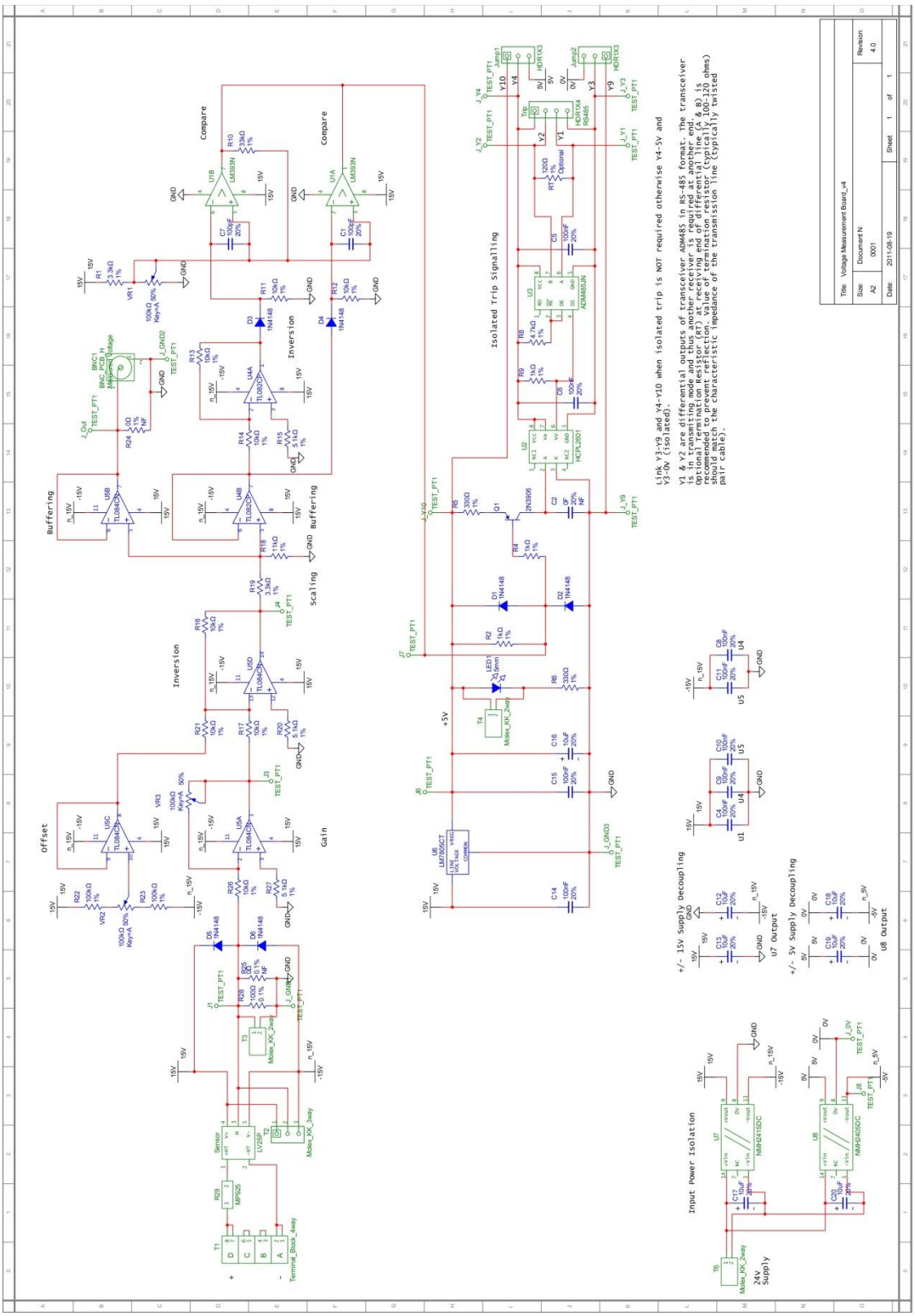

Figure B: Schematics of voltage measurement board.

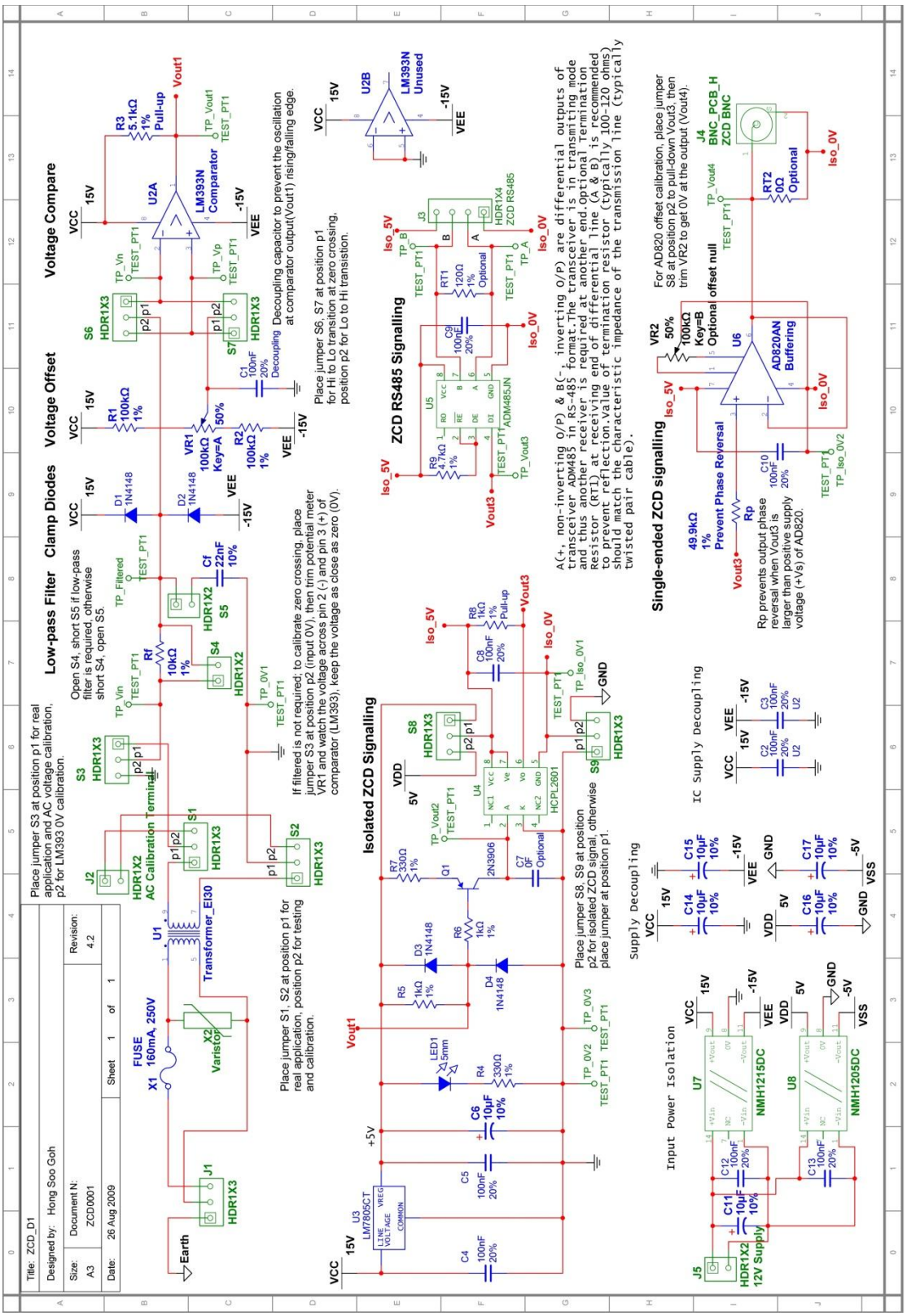

Figure C: Schematic of zero crossing detector (ZCD).

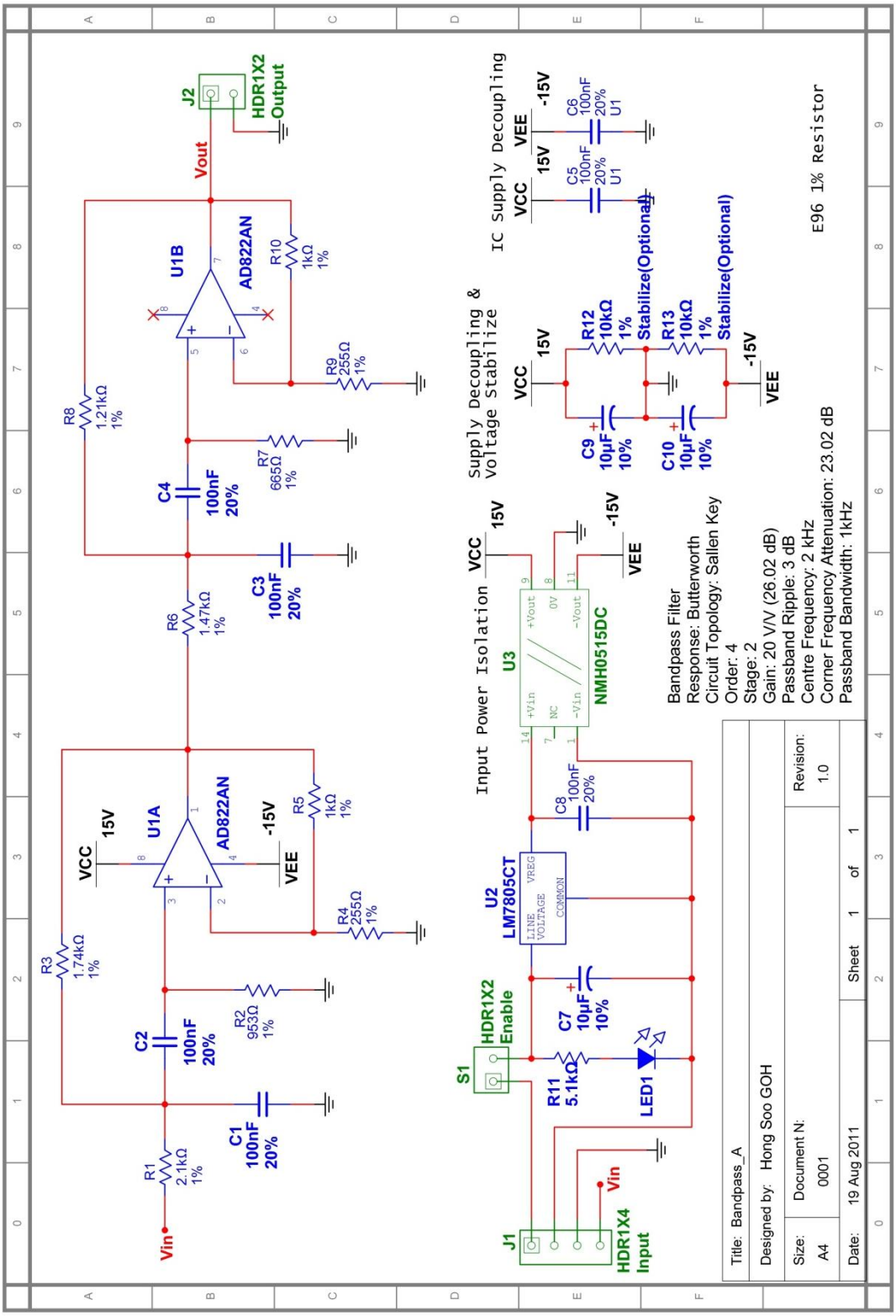

Figure D: Schematic of the 4th order active bandpass filter for resonance detection.

Appendix III. Peripheral Experimental Components and Measurement Equipment

A. Variac and Isolation Transformer

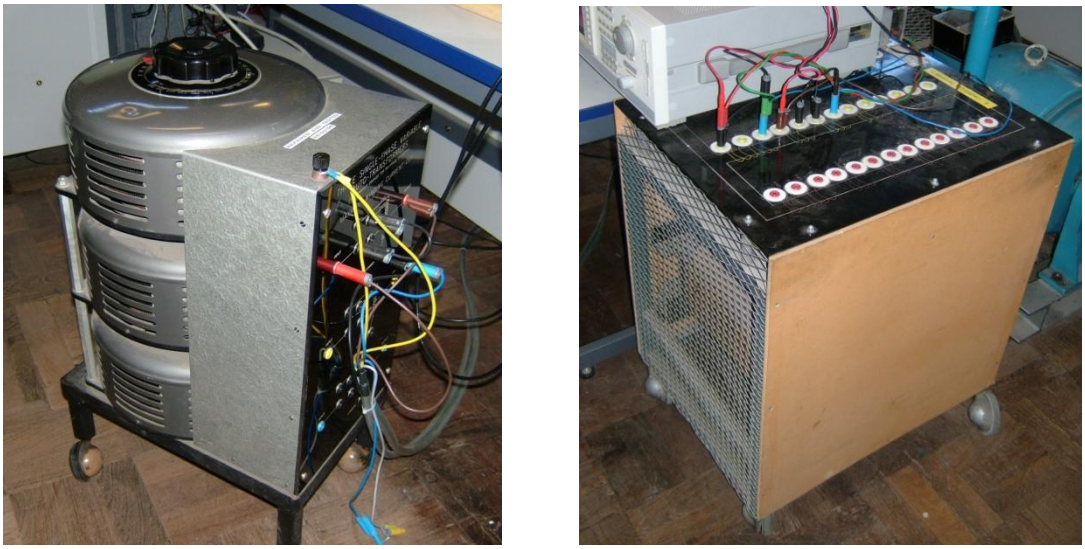

(a) **(b)**

Figure A: Variac and isolation transformer employed in experimental grid-connected PV inverter system, (a) variac, (b) isolation transformer.

In Figure A, the experimental PV inverter system is interfaced to the laboratory 230V mains supply via a variac and isolation transformer, as shown in Figure A(a) and Figure A(b) respectively. These devices are standard lab equipment, and are chosen on the grounds of equipment availability and cost effectiveness of the project. Note that only one phase of the variac and isolation transformer is utilised; although three-phase connection is possible. The variac is included to adjust the effective mains supply voltage observed by the experimental grid-connected PV inverter system. By lowering the mains supply voltage, it is possible for a lower DC link voltage to be used on the experimental system without changing the DC/AC conversion ratio that applied on real system in practice. The variac is a non-isolated autotransformer. As a result, it does not provide any protection against the flow of DC current into the laboratory supply. However, in accordance with UK recommendations, and the more immediate concern of protecting the PEDM laboratory supply, DC current injection must be prevented. The risk of DC current injection into the distribution grid may be completely eliminated through the use of a mains frequency isolation transformer. For this reason, the isolation

transformer shown in Figure A(b) is inserted between the variac and the inverter system (as shown in Figure 3.2).

In a conventional system, the isolation transformer forms part of the overall PV inverter system that connects to the distribution network at a point of common coupling (PCC). Whilst the aim of this research is to investigate the effect of grid operating conditions on the harmonic performance of the PV inverter current controller, the use of an isolation transformer is neglected in the experimental system to simplify the analysis. For this purpose, the isolation transformer is moved to the simulated distribution grid side (between grid impedance and variac) in experimental system as shown in Figure 3.2, as the impedance of the isolation transformer can be seen by the PV inverter system as a part of supply substation source impedance. Note that the parameters of the isolation transformer, such as winding and magnetising impedances etc., are obtained through open-circuit and short-circuit tests as presented in Appendix V.

B. Earthed Cage with Interlocking Protection

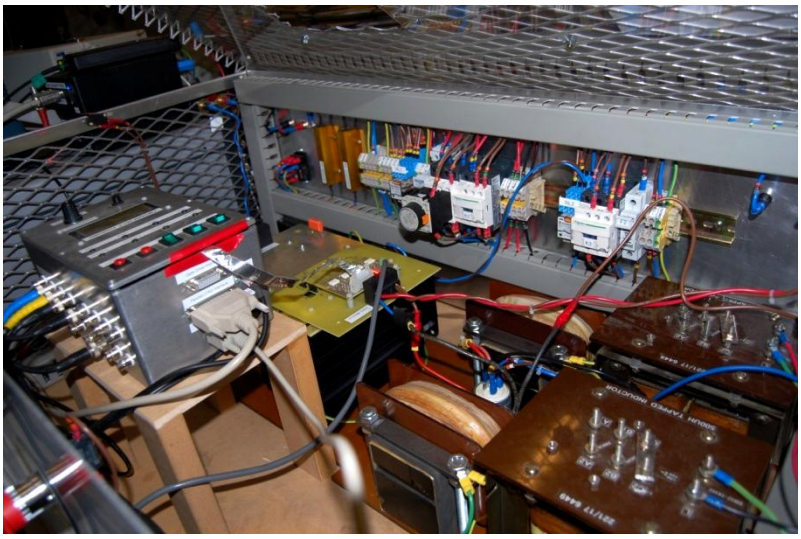

Figure B: Experimental system components encased in the earth cage.

The experimental PV inverter system (including H-bridge inverter, gate driver and lowpass filter) is encased in a metal cage connected to the mains supply earthing system to prevent any access of live terminals. This is shown in Figure B. In the event of any earth fault, the fault current will trip the earth fault protection relay of the mains supply and all sources of power (such as the DC power supply and 230V mains supply) will rapidly be turned off. For additional safety, the cage is equipped with an interlocking system that isolates the experimental PV inverter system from all power sources when the cage lid is opened.

C. Measurement of Waveform Harmonics

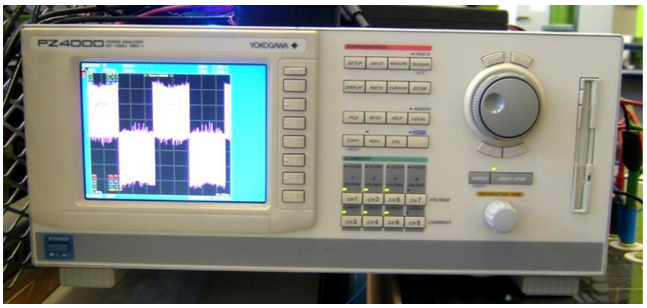

Figure C: Yokogawa® PZ4000 Power Analyser.

The waveforms of the experimental grid-connected PV inverter system in Figure 3.2 are recorded via a Yokogawa® PZ4000 Power Analyser as shown in Figure C. As the PZ4000 Power Analyser utilises a resistive shunt (10mΩ) for the current measurement, it does not suffer from the offset drift issues and the switching noises induced by inductive circuit and associated with hall-effect current sensors (Armstrong [27]). During the practical experiment, the power analyser is set to record 100k samples (2.5 MHz sampling frequency) over 2 cycles of fundamental frequency (50Hz). The recorded waveform is then imported into Matlab/Simulink® software package for FFT analysis and hence the harmonic data of the recorded waveform can be obtained. For simulation purpose, this harmonic data analysed by FFT is imported into the simulation model to re-construct the background grid voltage in Simulink®. An example of the experimental grid-connected PV inverter system waveforms, recorded by Yokogawa® PZ4000 Power Analyser, is shown in Figure D.

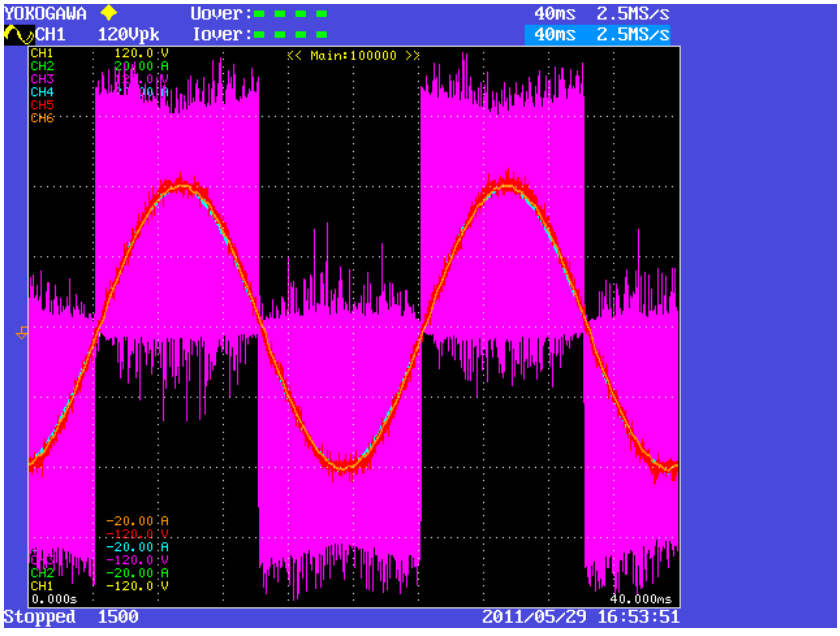

Figure D: Waveforms of the test circuit of experimental grid-connected PV inverter system recorded by Yokogawa® PZ4000 Power Analyser.
(CH1 = V_{PCC}, CH2 = I_O, CH3 = V_X, CH4 = I_X, CH5 = V_G, CH6 = I_O.)

Appendix IV. Grid Connection Sequence

To help prevent large transient voltages, or inrush current, when the experimental grid-connected PV inverter system is initially connected to the distribution grid, special attention must be paid on the connection procedure. Connection of the experimental system to the distribution network is made by the following procedure:

(1) **Variac is set to zero volts and the inverter IGBT gate signals are all set to low.** In this way, no voltage is seen at the inverter system output (zero voltage on inverter lowpass filter capacitor) and no current can flow from the DC link to the grid side through the inverter bridge.

(2) **Switch on the DC power supply to power up DC link.** Inrush current is suppressed by soft start protection circuit installed on the DC link.

(3) **Set the current demand of the inverter current controller to zero. Initialise the switching of the inverter bridge.** The PWM modulation depth should be practically zero under this condition and virtually no current will be flowing through the power electronic inverter.

(4) **Variac is gradually wound up and the effective PCC voltage (voltage across inverter lowpass filter capacitor) is increased. The current demand of current controller is sustained at zero at this stage.** The modulation depth should increase as the inverter current controller attempts to counteract the applied PCC voltage. The PCC voltage is steadily increased until it reaches the rated output voltage for the DC link voltage of the inverter. With 380V DC link voltage, the full 230V voltage of distribution grid may be applied to the inverter system output.

(5) **The current demand of the inverter current controller is ramped up to the full current demand of the inverter system.** All-out effort is now given by the inverter current controller to inject the reference current into the distribution grid. At this point, the inverter is now fully operational as a grid-connected inverter system.

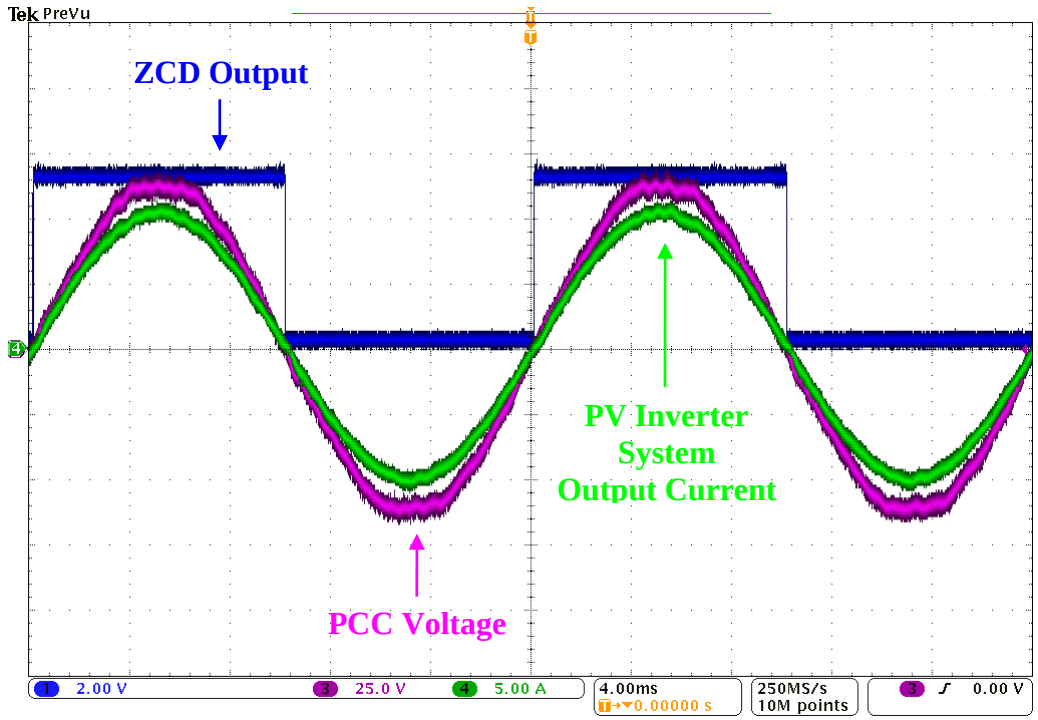

Figure A: Output current waveform of experimental grid-connected PV inverter system synchronised to the PCC voltage.
(I_{demand} = 7A RMS, V_{DC} = 100V, V_G = 43.24V RMS, L_f = 2mH, C_f = 10μF, K_p = 1.1, K_i = 0.6.)

An example waveform of the proposed experimental grid-connected PV inverter system in practical experiment is shown in Figure A. It is shown in the figure that the output current of the experimental grid-connected PV inverter system is synchronised to the PCC voltage through the ZCD output signal that triggering at zero crossing of PCC voltage. It is noted that the experimental grid-connected PV inverter system is operated at unity power factor as the output current is in-phased with the PCC voltage.

Appendix V. Transformer Tests for Parameter Estimation

The parameter of the transformer, such as winding and core impedance, are normally not available and does not provided with the transformer itself, unless it is specially requested from the manufacture. This is not the case for the old transformer which sits in the laboratory for ages with all of the manufacture information lost. For analysis purpose, the parameter of the transformer is always required in the laboratory test and experiment. To obtain the parameter of the transformer, open-circuit test and short-circuit test can be implemented to estimate its winding and magnetising parameters, as demonstrated by Ayasun and Nwankpa [113]. The equivalent circuit of an ideal transformer is shown in Figure A.

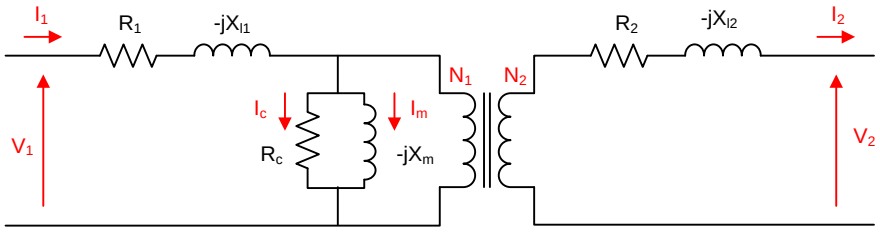

Figure A: Ideal transformer equivalent circuit.

where,
V_1 and V_2 are the terminal voltage of primary winding and secondary winding respectively;
I_1 and I_2 are the input current of primary winding and output current of secondary winding respectively;
R_1 and X_{l1} are the resistance and leakage reactance of primary winding;
R_2 and X_{l2} are the resistance and leakage reactance of secondary winding;
R_c and X_m are the core resistance and magnetising reactance of excitation branch.

A. Transformer Open-circuit Test

In open-circuit test, no load is connected to secondary winding of the transformer, which leads to zero current flow in secondary winding of the transformer. Hence, the current flow into primary winding is dominates by the excitation branch of transformer during open-circuit test. For this reason, open-circuit test is use to determine some common parameter of transformer such as parameters of excitation branch (R_c and X_m), no-load current, no-load power factor and no-load loss of the transformer. Figure B shows the test setup for transformer open-circuit test. EAC-3P AC power source that manufactured by ET Power System Ltd is used as the AC source and Yokogawa® WT1600 Power Meter was used to measure the current, voltage and power of the test

circuit. The test is carried out by slowly increase the voltage of AC source to rated voltage of transformer (240Vrms), then the power meter is used to measure the power level. Figure C shows the voltage and current waveform of transformer open-circuit test with the input current at primary winding (I1) saturated during open-circuit test. The test value of the measurements is shown in Table A.

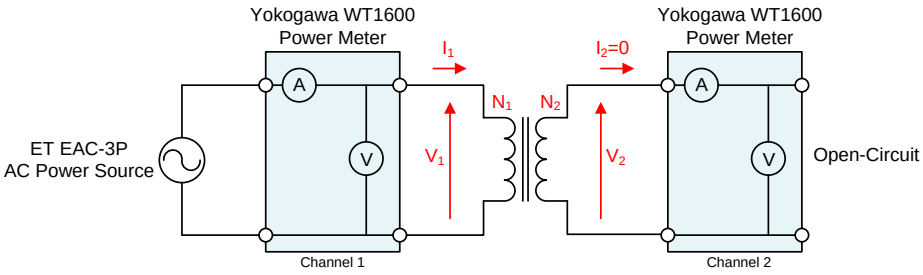

Figure B: Test setup for transformer open-circuit test.

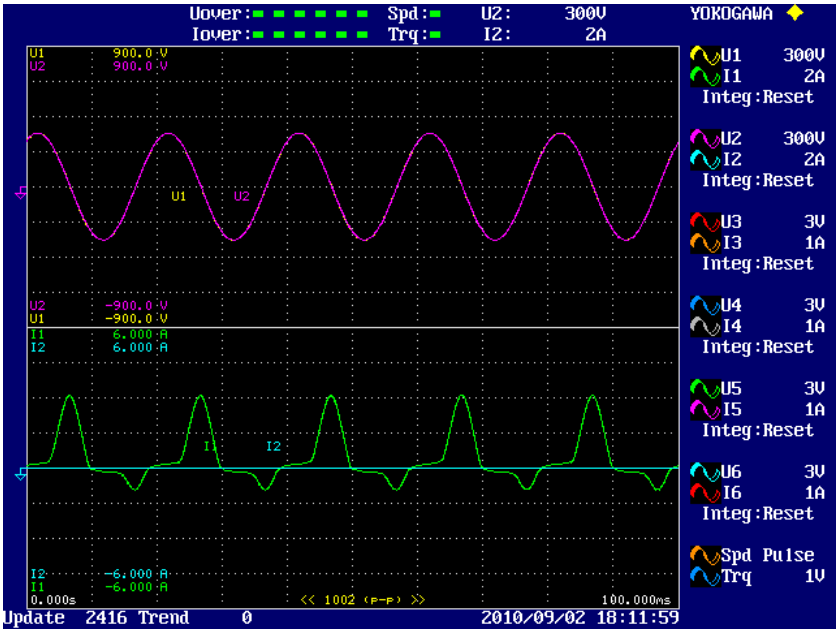

Figure C: Voltage and current waveform of transformer open-circuit test. Trace U1: Terminal voltage of primary winding; Trace I1: Input current of primary winding; Trace U2: Terminal voltage of secondary winding; Trace I2: Output current of secondary winding.

Terminal voltage of primary winding, V_1 (V_{oc})	*241.76 V (rms)*
Input current at primary winding, I_1 (I_{oc})	*1.0927 A (rms)*
Measured power at primary winding, P_1 (P_{oc})	*34.029 W*
Terminal voltage of secondary winding, V_2	*241.49 V (rms)*
Output current at secondary winding, I_2	*0 A (rms)*
Measured power at secondary winding, P_2	*0 W*

Table A: Test value measured by WT1600 for open-circuit test.

As the impedance of the primary winding branch (R_1 and jX_{l1}) is trivial compare to excitation branch, and the current flow across primary winding is tiny during open-circuit test, the equivalent circuit of the transformer (Figure A) can be simplified by neglecting the impedance of winding branch, as shown in Figure D.

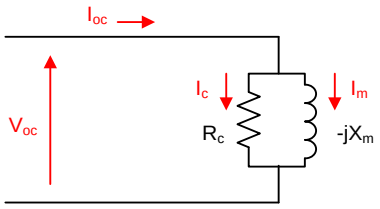

Figure D: Equivalent circuit of transformer open-circuit test

The excitation branch in figure D can be lump into a single quantity and notated by admittance (Y), which known as the inverse of impedance (Z). The parameter of the excitation branch can then be obtained via well-known Ohm's Law and power factor expressions below.

$$V_{oc} = I_{oc}Z_e = \frac{I_{oc}}{Y_e}$$
$$|Y_e| = \frac{I_{oc}}{V_{oc}} = \frac{1.0927A}{241.76V} = 4.5198 \times 10^{-3}S$$
$$PF_{oc} = \cos\theta_{oc} = \frac{P_{oc}}{S_{oc}} = \frac{P_{oc}}{I_{oc}V_{oc}} = \frac{34.029W}{1.0927A \times 241.76V} = 0.128814$$
$$\theta_{oc} = \cos^{-1}\theta_{oc} = \cos^{-1} 0.128814 = 82.5989°$$
$$Y_e = G_c - jB_m$$
$$G_c = |Y_e|\cos\theta_{oc} = 4.5198 \times 10^{-3}S \times 0.128814 = 5.8221 \times 10^{-4}S$$
$$B_m = |Y_e|\sin\theta_{oc} = 4.5198 \times 10^{-3}S \times \sin 82.5989° = 44.8214 \times 10^{-4}S$$
$$R_c = \frac{1}{G_c} = \frac{1}{5.8221 \times 10^{-4}S} = 1717.59\Omega$$
$$X_m = \frac{1}{B_m} = \frac{1}{44.8214 \times 10^{-4}S} = 223.11\Omega$$
$$L_m = \frac{X_m}{2\pi f_1} = \frac{223.11\Omega}{2\pi \times 50Hz} = 710.1739mH$$

where,
V_{oc}, I_{oc} and P_{oc} are open-circuit voltage, current and power respectively;
PF_{oc} and θ_{oc} are open-circuit power factor and power factor angle respectively;
Y_e, G_c and B_m are admittance, core conductance and magnetising susceptance of excitation branch respectively;
f_1 is the fundamental frequency of supply voltage.

B. Transformer Short-circuit Test

During transformer short-circuit test, the secondary winding of the transformer is shorted and reduced voltage is applied across primary winding to prevent massive current flow through the transformer windings. As reduced voltage is applied across primary winding and the impedance of transformer excitation branch is massive

compare to winding series impedance, the current flow through the excitation branch is negligible. Therefore, short-circuit test can be used to determine the winding impedance (R_1, R_2 and X_{l1}, X_{l2}) of the transformer. Figure E shows the test setup for transformer short-circuit test. The test is carried out by slowly increase the voltage of AC source until the rated current of the transformer is reached, only small amount of voltage is suffice for rated current flow in the transformer winding as the secondary winding is shorted. The short-circuit voltage, current and power are measured by Yokogawa® WT1600 Power Meter. Figure F shows the voltage and current of transformer short-circuit test. Note that the voltage across secondary winding (U2) that supposed to be zero in theory is not equal to zero in practical test as rated current at secondary winding flowing through impedance of the cable connect between transformer and power meter as well as resistive shunt utilised by WT1600 power meter for current measurement. The value of the measurement is shown in Table B.

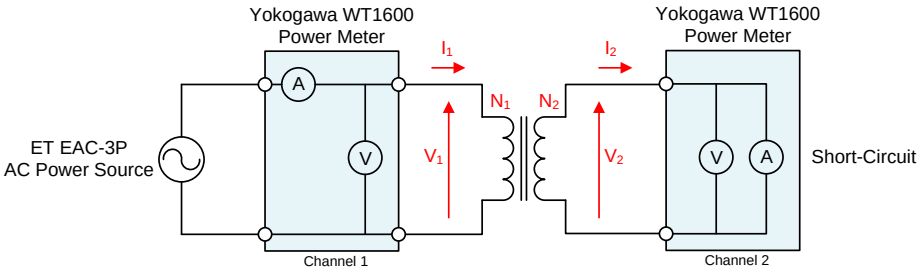

Figure E: Test setup for transformer shirt-circuit test.

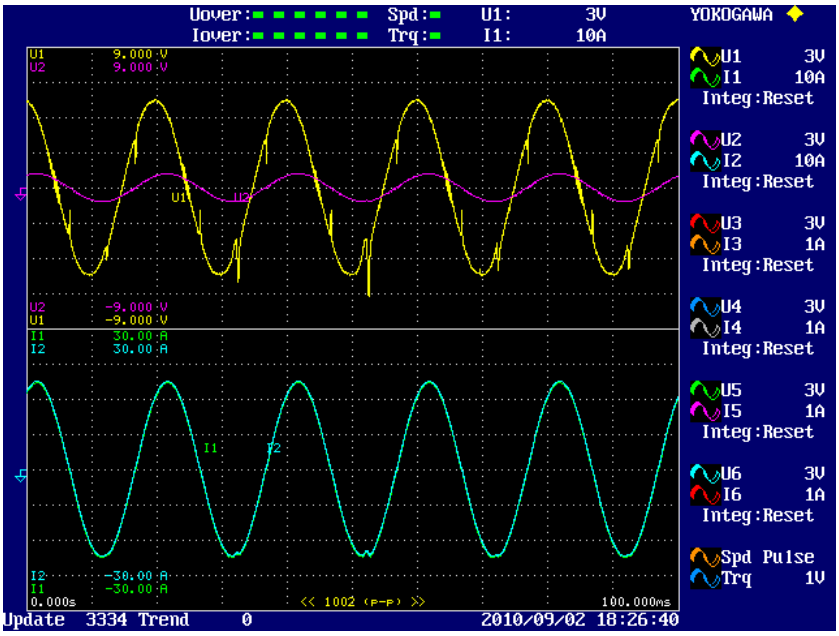

Figure F: Voltage and current waveform of transformer short-circuit test. Trace U1: Terminal voltage of primary winding; Trace I1: Input current of primary winding; Trace U2: Terminal voltage of secondary winding; Trace I2: Output current of secondary winding.

Terminal voltage of primary winding, V_1 (V_{sc})	*3.9683 V (rms)*
Input current at primary winding, I_1 (I_{sc})	*13.192 A (rms)*
Measured power at primary winding, P_1 (P_{sc})	*42.683 W*
Terminal voltage of secondary winding, V_2	*0.62743 V (rms)*
Output current at secondary winding, I_2	*13.194 A (rms)*
Measured power at secondary winding, P_2	*8.2767 W*

Table B: Test value measured by WT1600 for short-circuit test.

As the current flowing through the excitation branch is negligible during short-circuit test, the current flow through the winding dominate the short-circuit current. The excitation branch in the transformer equivalent circuit (Figure A) can then be neglected and the equivalent circuit of short-circuit test can be simplified by winding impedance only, as shown in Figure G.

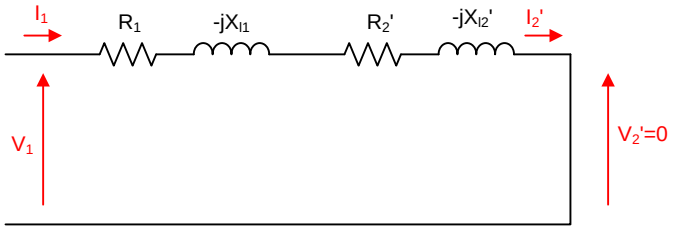

Figure G: Equivalent circuit of transformer short-circuit test.

The winding impedance in Figure G can be lumped into a single quantity notated as equivalent impedance (Z_{eq}). The parameter of winding branch can then be obtained by Ohm's Law and expression below.

$$|Z_{eq}| = \frac{V_{sc}}{I_{sc}} = \frac{3.9683V}{13.192A} = 0.300811\Omega$$

$$P_{sc} = {I_{sc}}^2 R_{sc}$$

$$R_{eq} = \frac{P_{sc}}{{I_{sc}}^2} = \frac{42.683}{13.192^2} = 0.245264\Omega$$

$$Z_{eq} = R_{eq} - jX_{eq}$$

$$|Z_{eq}|^2 = {R_{eq}}^2 + {X_{eq}}^2$$

$$X_{eq} = \sqrt{|Z_{eq}|^2 - {R_{eq}}^2} = \sqrt{0.300811^2 - 0.245264^2} = 0.174163\Omega$$

$$R_{eq} = R_1 + R_2' = R_1 + a^2 R_2$$

$$X_{eq} = X_{l1} + X_{l2}' = X_{l1} + a^2 X_{l2}$$

Since it is 1:1 isolation transformer, hence a=1, R_1=R_2, X_{l1}=X_{l2}.

$$R_1 = R_2 = \frac{R_{eq}}{2} = \frac{0.245264\Omega}{2} = 0.122632\Omega$$

$$X_{l1} = X_{l2} = \frac{X_{eq}}{2} = \frac{0.174163\Omega}{2} = 0.0870815\Omega$$

$$L_{l1} = L_{l2} = \frac{X_{l1}}{2\pi f_1} = \frac{0.0870815\Omega}{2\pi \times 50Hz} = 277.189\mu H$$

where,
V_{sc}, I_{sc} and P_{sc} are short-circuit voltage, current and power respectively;
Z_{eq}, R_{eq} and X_{eq} are equivalent impedance, resistance and reactance;
a is transformer turn ratio;
L_{l1} and L_{l2} are leakage inductance of transformer primary and secondary winding respectively.

C. Determined Isolation Transformer Parameters

The determined parameters of the isolation transformer obtained from open-circuit and short-circuit test is presented in Table C.

Primary winding resistance, R_1	*0.122632 Ω*
Secondary winding resistance, R_2	*0.122632 Ω*
Primary winding leakage inductance, L_{l1}	*277.189 µH*
Secondary winding leakage inductance, L_{l2}	*277.189 µH*
Core resistance, R_c	*1717.59 Ω*
Magnetising inductance, L_m	*710.1739 mH*

Table C: Determined parameter of the isolation transformer.

D. Transformer Resonance

The 1:1 isolation transformer is used as an isolation point in the practical experiment to couple the experimental inverter system to the simulated distribution grid, as shown in Figure H. However, high frequency ripple is observed on the voltage across the primary winding of isolation transformer (V_g in Figure H). This voltage ripple on the primary voltage waveform of the transformer is recorded and shown by Trace 3 of Figure I.

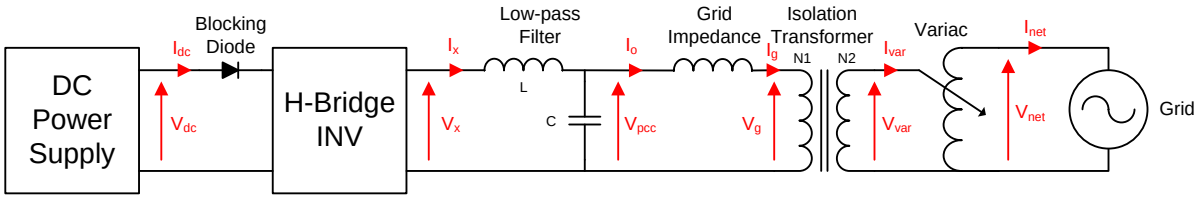

Figure H: Test setup for experimental inverter system interfaced with simulated distribution grid.

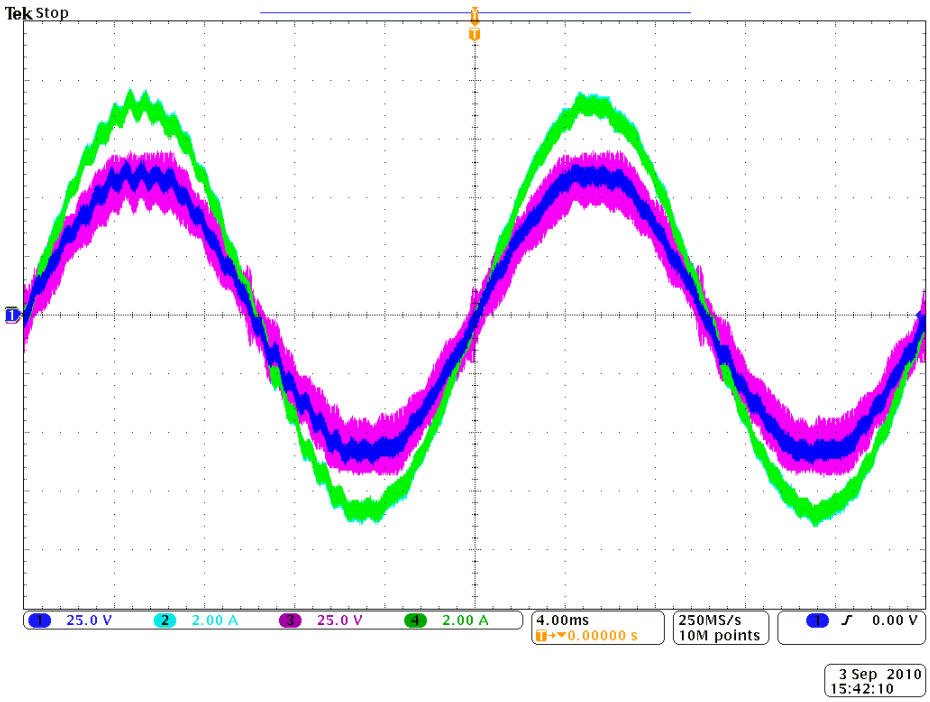

Figure I: Voltage and current waveform of simulated grid experiment with transformer resonance. Trace 1: Voltage at simulated PCC (V_{pcc}); Trace 2: output current of inverter (I_o); Trace 3: background voltage of simulated grid (V_g); Trace 4: current injected into the grid (I_g).

To investigate the cause of the ripple on the transformer voltage, waveform in Figure I is magnified and shown in Figure J via the wave inspector function on Tektronix MSO4034 oscilloscope. As shown in Figure J, the ripple on the voltage of transformer primary winding (Trace 3) is caused by the transients on the simulated point of common coupling (PCC) voltage (V_{pcc} in Figure H and Trace 1 in Figure J). The red arrows and cursors in Figure J show the 4 transients occurred in a cycle of PWM carrier frequency (f_{PWM}=20kHz). These transients on the simulated PCC voltage are due to the switching of IGBTs in H-bridge inverter. As Unipolar PWM is implemented in the experimental system, there are four switching states occurred in a cycle of PWM carrier, as depicted in Figure K. Moreover, this switching transient on PCC voltage is in turn caused the oscillation on background voltage of simulated grid (Vg in Figure J) that trigger by the transients on PCC voltage at the instant the stage of the inverter output voltage (V_x) is being changed, as shown in Figure J.

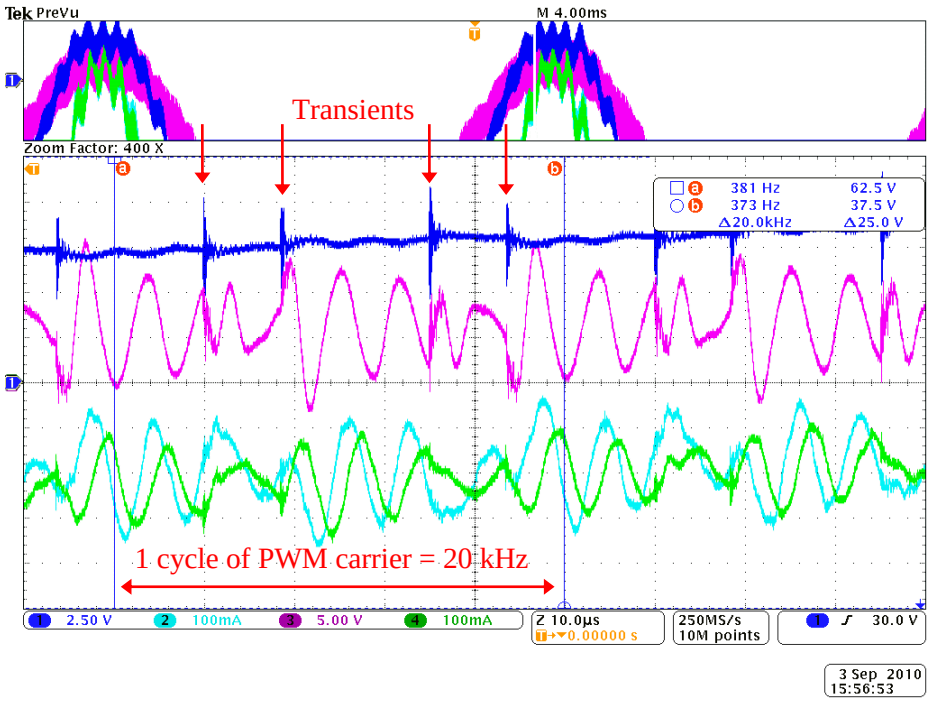

Figure J: Magnification of the waveforms. Trace 1: Voltage at simulated PCC (V_{pcc}); Trace 2: output current of inverter (I_o); Trace 3: background voltage of simulated grid (V_g); Trace 4: current injected into the grid (I_g).

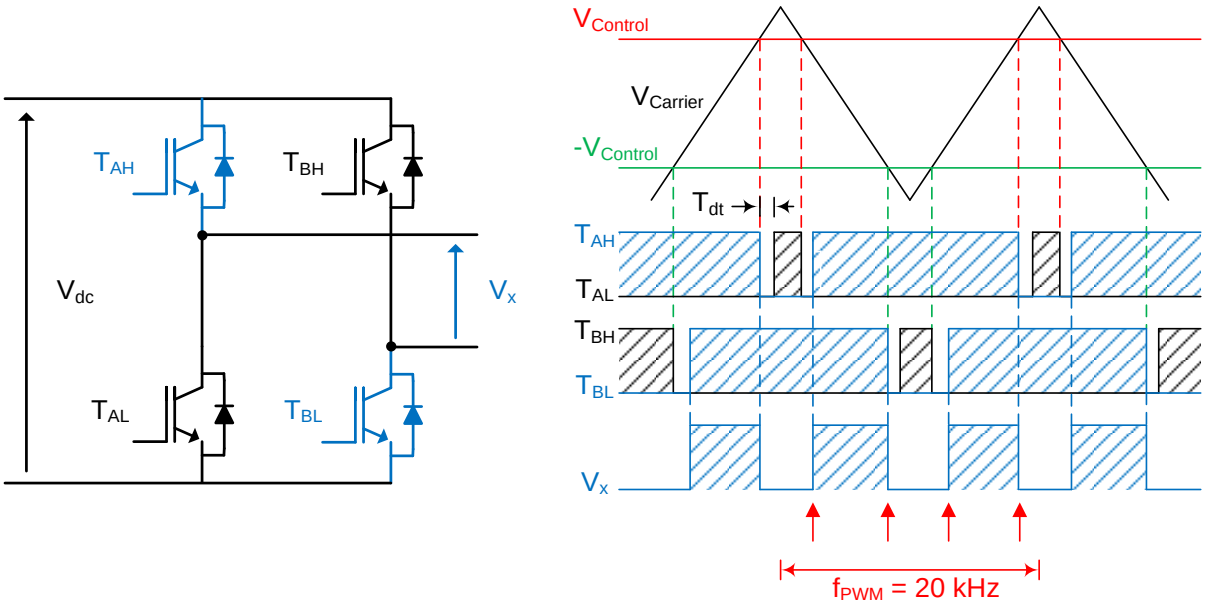

Figure K: Transient at the switching of IGBT in a cycle of Unipolar PWM.

Although the lowpass filter located at the output of H-bridge inverter will attenuate the high frequency transient cause by the switching of IGBTs, it would not be able to completely eliminate this transient. This transient will interact with the impedance in the network, in our case, grid impedance and transformer impedance. If the frequency of the transient sufficient enough to coincide with the resonant frequency of network impedance, resonance phenomenon can then be excited which lead to the oscillation and magnification in either voltage or current waveform, depends on the nature of

resonance. In our case, the transient frequency is coincided with the impedance of the transformer and the grid impedance which led to the excitation of high frequency resonance. This has also caused the high level of high frequency oscillation in simulated grid voltage (V_g in Figure H and Trace 3 in Figure J). As the transformer is typically design to have the resonant frequency higher than 10 kHz, this resonant frequency is sufficiently high for 50Hz or 60Hz of fundamental voltage which occupied in most of the country, but might not high enough for power electronic converter with high switching frequency. However, this high frequency resonance is not low enough to significantly affect the trend and the magnitude of considerable harmonics order which interested in this project (1^{st} to 49^{th} harmonics).

Appendix VI. Schematic of Protection Circuit

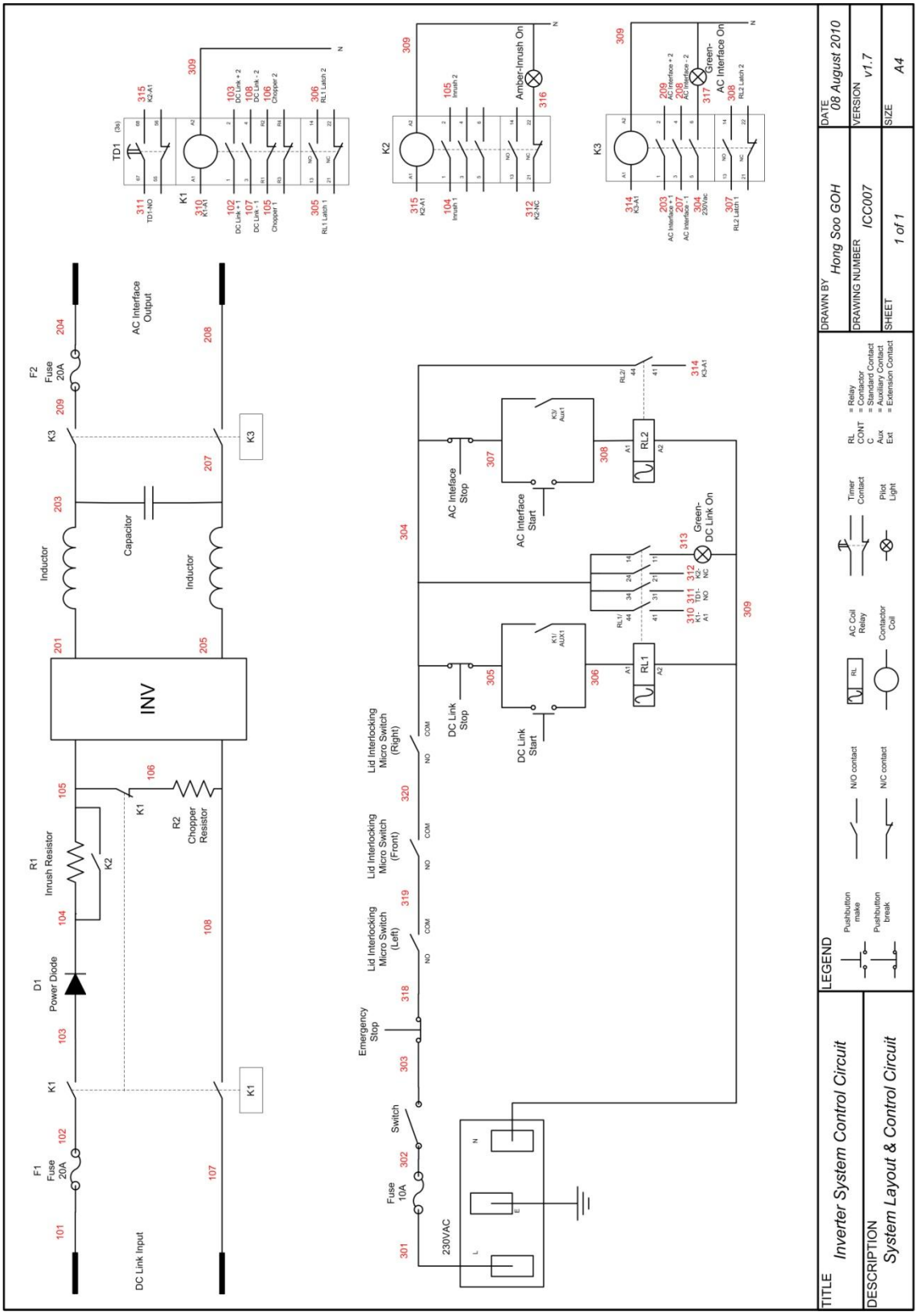

Figure A: Schematics of protection circuit.

Appendix VII. Grid Voltage Distortion and Variation in Harmonic Profile

A. Introduction

This appendix discusses the causes and effects of distortion in the point of common coupling voltage waveform. The first part of this appendix provides an overview on the causes and effects of harmonics in the power network, whilst the second part demonstrates the generation of harmonics and the mechanism leading to distortion of the point of common coupling voltage through simulation in Matlab/Simulink®. This distortion is experimentally validated via practical analysis.

B. Causes and Effects of Harmonics

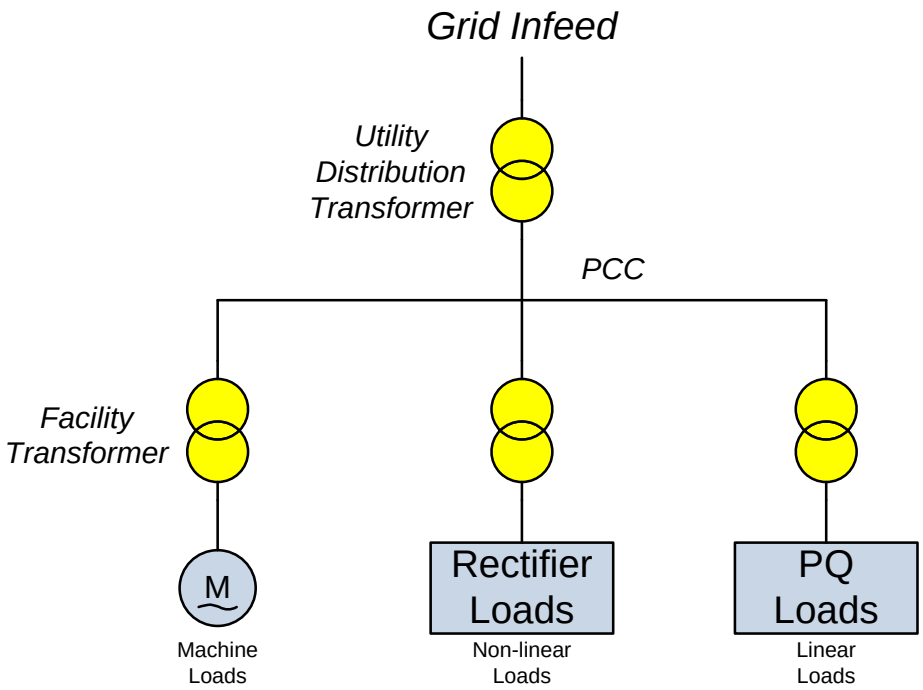

Figure A: Layout of typical distribution grid with various types of loads connected at PCC.

The distribution grid is traditionally fed by the utility source through a utility distribution transformer. It is then dispersed to the various connections at the PCC to provide a grid interface to all network loads. A typical layout is shown in Figure A. The loads that are connected to the PCC could be any type of load (such as rotating machines, non-linear or linear loads). Some loads such as variable speed drives, switch-mode power supplies (SMPS), uninterruptible power supplies (UPS) units and rectifier of electric arc furnaces, often employ power electronic devices for power conversion.

This type of equipment draws non-sinusoidal current from the distribution grid and can inject harmonic currents into the grid. This in turn causes distortion of the grid voltage waveform (Rodriguez and Saldanha [114], Ellis [115], Rockwell Automation Mequon [80], Abbas and Saqib [116]). Moreover, it is suggested by Cobben [81], Chapman [117] and de Castro [118] that the lighting units that employ electronic fluorescent lighting ballasts, such as energy saving bulbs, compact fluorescent lamps (CFL), and high pressure sodium (HPS) lamps for street lighting, are highly non-linear loads that draw extremely distorted current, usually exceeding 100% of the total harmonic distortion (THD).

The presence of harmonics in the power network has operational effects on the connected equipment and has an impact on the reliability of the power network (Subjak and McQuilkin [119], Ortmeyer, Chakravarthi, et al. [11]). It is suggested in previous studies (Chapman [117], Subjak and McQuilkin [119], Hershey Energy Systems [102], Maslowski [120]) that the harmonics in the grid system will cause heating effect on electrical equipment (such as transformers and rotating machines) and lead to significant power losses. Also, high values of harmonics can over-stress power factor correction capacitors. In cable system or overhead lines, the skin effect of the conductor will become significant with the presence of the harmonic above 350Hz and hence cause additional losses and heating effects (Chapman [117], Maslowski [120]). Moreover, as suggested by Hershey Energy System [102] that triple harmonics (multiples of the 3^{rd} harmonic) are the zero sequence harmonics and hence the magnitude of these currents on 3 phases are additive in the neutral. For a three-phase 4-wire system, triple harmonics present in the distribution grid will add up and could lead to vary large currents circulating in the neutral conductor (Chapman [117], Hershey Energy System [102]). If the neutral conductor is not properly sized, it could be overloaded and hence cause the over-heating on the neutral conductor (Hershey Energy System [102]).

With regard to the reliability of the power network, Chapman [117], Subjak and McQuilkin [119] have suggested that presence of harmonics in the power network could cause nuisance tripping of protection devices; such as relays, circuit breaker and fuses. Devices that are sensitive to zero crossings, such as grid synchronisation devices and thyristors, could also malfunction with excessive zero crossing noise created by the harmonics. Furthermore, “flat topping” is often observed on the voltage waveform at the PCC, indicating significant low order harmonic distortion. This is because harmonic

load currents give rise to a harmonic voltage drop across the source impedance (such as impedance of the internal cabling from the PCC and supply transformer) and this leads to distortion of the PCC voltage [117, 119, 121].

C. Source of Non-linear Current in the Network

The grid voltage waveform at the PCC is distorted as a result of volatile operating conditions, such as grid impedance and the connection of multiple non-linear loads throughout the network. These non-linear loads can be categorised as random disturbances (such as motor starting transients) or systematic disturbances (such as long term connected loads) (Simmons and Infield [15]). Random disturbances contribute low level, wide band harmonics, while systematic disturbances can account for a significant level of low frequency harmonics.

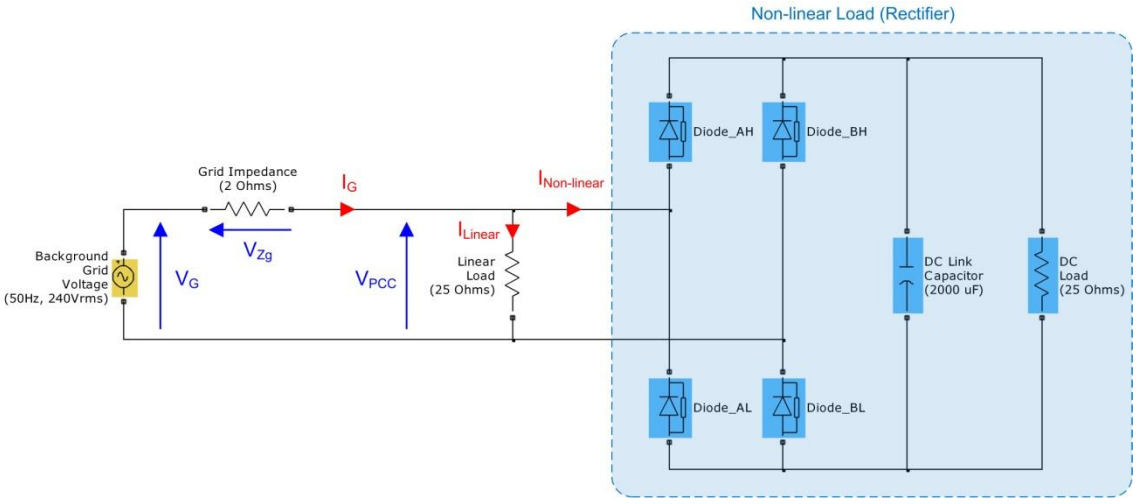

Figure B: Matlab/Simulink® model of single-phase 2.5 kW rectifier connected at PCC.

In practice, the current flowing into non-linear loads does not linearly correspond to the applied voltage. This leads to non-sinusoidal currents circulating in the network. Typical non-linear loads which are commonplace are switched mode power supplies (SMPS), electronic fluorescent lighting ballasts and uninterruptible power supplies (UPS) [114, 117]. Besides this, three-phase loads such as large uninterruptible power supplies and variable speed drives for machines etc, which are commonly used in industry, are also a significant source of non-sinusoidal current (Rockwell Automation Mequon [80], Ellis [115]). To demonstrate the non-sinusoidal current drawn by a non-linear load, a single-phase 2.5 kW rectifier load is modelled in Matlab/Simulink®, as shown in Figure B. In the simulation model, the non-linear load is modelled by a rectifier connected in parallel with the linear load (25Ω resistor) at the PCC. The load

circuit is then supplied by an ideal sinusoidal grid voltage (V_G, 50Hz 240V RMS) through a grid impedance (Z_g). Here, a 2Ω resistor is used instead of inductance to represent the grid impedance and simplify the analysis. In practice, the grid impedance consists of the impedance of the supply transformer at the source substation (such as utility distribution transformer in Figure A), and the impedance of the cabling circuit used to connected the equipment to the supply source (Enslin, Hulshorst, et al. [16]). The phase voltage waveform (V_{PCC}) and non-sinusoidal phase current ($I_{Non\text{-}linear}$) of the rectifier in the simulation are shown in Figure C. As shown, the phase current of the rectifier is highly distorted due to the rectification of the single-phase bridge rectifier, which in turn causes the distortion in the PCC voltage ("flat topping" of V_{PCC} in Figure C).

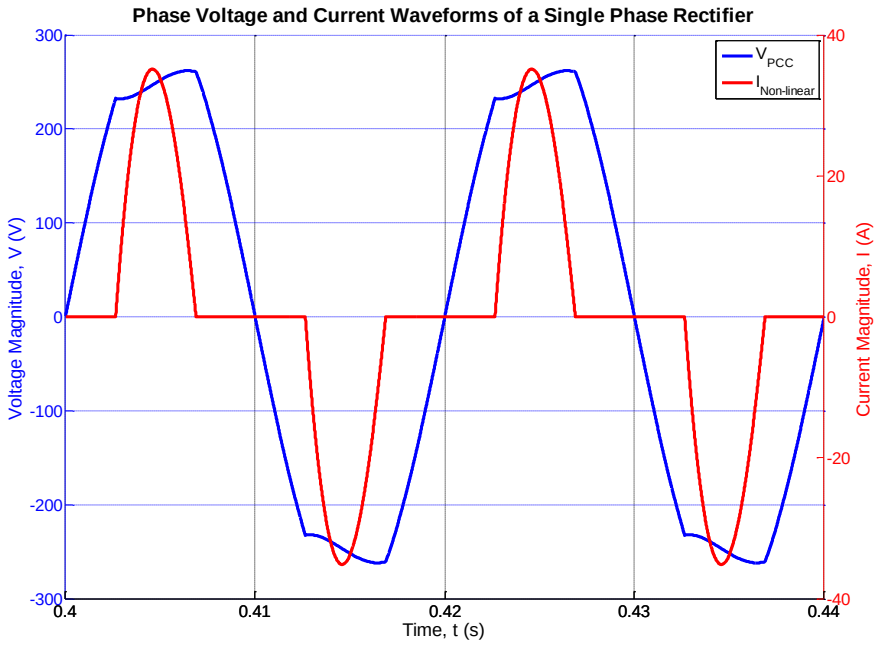

Figure C: Phase voltage and non-sinusoidal phase current of a 2.5 kW single-phase rectifier in the simulation.

D. Cause of Grid Voltage Distortion

In distribution network, the current flowing into the individual loads connected in parallel at the PCC will have an additive effect on the total current supplied by the source substation. As the transformer is normally employed at the source substation to step-down the network voltage to the distribution level (e.g. 400V, 3 phase, line voltage in UK) and the cable or overhead line is used to make the connection between the source substation and PCC, their intrinsic impedance can be summed and represented by a single impedance denominated as grid impedance (Z_g). When current is drawn by the loads at the PCC, a corresponding voltage drop will be observed across the grid

impedance. Hence, the PCC voltage is given by background grid voltage (V_G) subtracted by voltage drop across the grid impedance. If substantial amounts of non-linear loads are connected at the PCC, large amounts of non-linear current will flow from the source substation to the loads at the PCC through the grid impedance. This will lead to highly non-linear voltage drops across the grid impedance and eventually cause high level of distortion in the PCC voltage. The current flowing into the linear load corresponds to the distorted PCC voltage; hence the current flowing through the linear load will be distorted too.

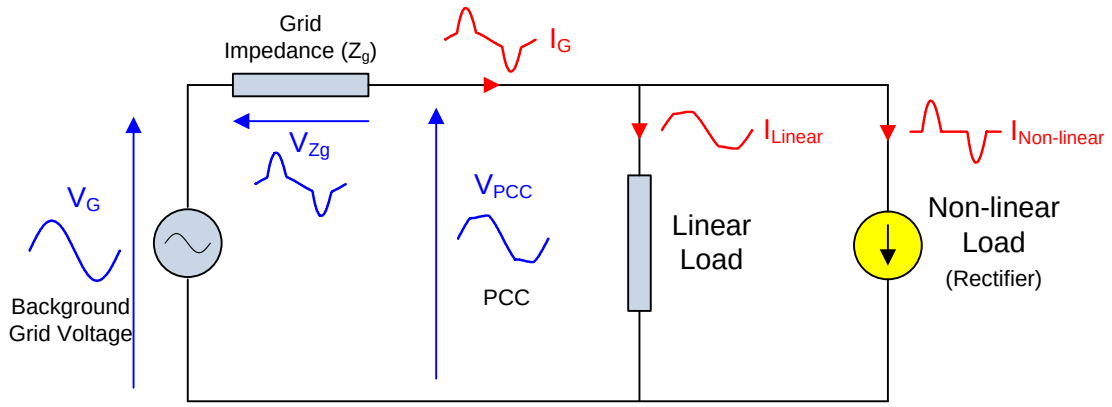

Figure D: Simplified circuit diagram of a 50Hz 240V distribution grid with a 2.5 kW non-linear load connected in parallel with linear load at PCC.
(Blue trace=voltage waveform, red trace=current waveform.)

The effect of non-linear load on the waveforms of PCC voltage and total supply current is explained by Chapman [117] and Hernandez, Castro, et al. [121]. However, the simulation model of the distribution grid, as shown in Figure B, is implemented to further understand the mechanism of the distortion effect in greater depth. To simplify the analysis, the model in Figure B is represented by the simplified circuit diagram as shown in Figure D. In the figure, the non-linear load (rectifier) is represented by a current source, while the background grid voltage is modelled by an ideal sinusoidal voltage source (50Hz 240V RMS). Furthermore, the typical waveforms of the voltage and current at the relevant points of the circuit are presented in the figure by the blue and red traces respectively.

Figure E shows the voltage and current waveforms at the relevant points of the distribution grid model (shown in Figure B and Figure D) when an ideal sinusoidal background grid voltage is applied (shown in Figure E(a)). Figure E(d) shows the current of the rectifier load ($I_{Non\text{-}linear}$) flows only when the PCC voltage (V_{PCC}) is close to the peak of the sinusoidal wave.

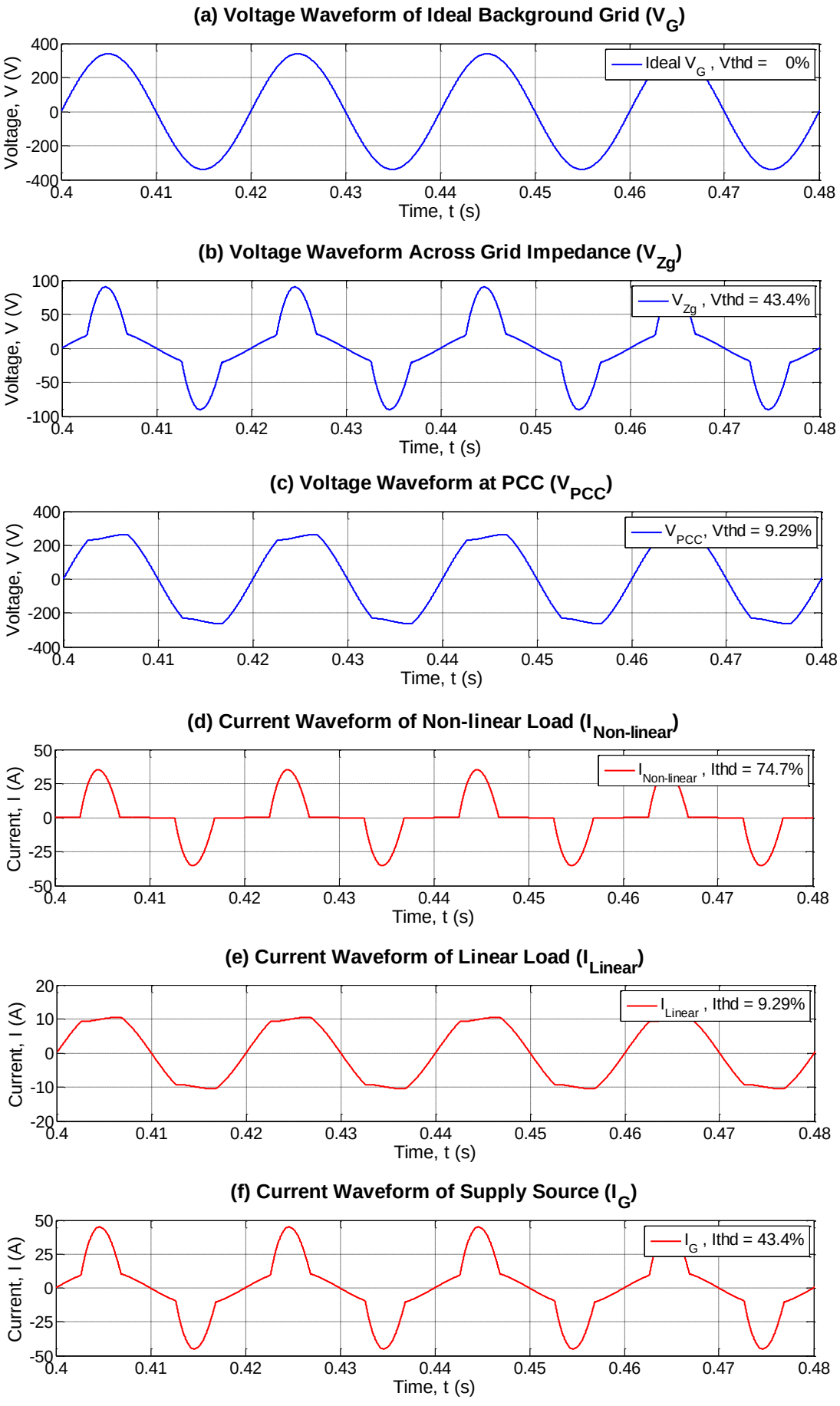

Figure E: Voltage and current waveforms at the relevant points of the distribution grid model in simulation.

At this point, "Diode_AH" and "Diodes_BL" (at positive peak of V_{PCC}), or "Diode_BH" and "Diodes_AL" (at negative peak of V_{PCC}), of the rectifier bridge (as shown in Figure B) are in forward bias as the voltage at PCC (V_{PCC}) exceeds the magnitude of the rectifier DC link capacitor voltage; hence current flows into the rectifier to charge the capacitor. This non-linear current (Figure E(d)) that flow through the non-linear load intermittently is summed with the current of other loads connected in parallel at the PCC (such as the load current of the linear load as shown in Figure E(e)) to form the total supply current (I_G) from the grid; Figure E(f). This distorted total supply current flow through the grid impedance (Z_g) causes the distorted voltage drop across the grid impedance (V_{Zg}), as shown by Figure E(b). The highest magnitude of the voltage drop across the grid impedance is at the peak of the sinusoidal waveform (shown in Figure E(b)), whereby it has the most significant effect at the apex of PCC voltage (V_{PCC}). This leads to the apex of PCC voltage being chopped, as shown by the "flat topping" characteristic of the PCC voltage in Figure E(c). Eventually, the distortion in PCC voltage causes the distortion in the load current of the linear load (I_{Linear}), as shown Figure E(e).

With regard to the harmonic interaction of the loads and distribution grid, the voltage and current waveforms in Figure E are analysed by the FFT function in Matlab/Simulink®. This interaction is shown by the harmonic profile of the voltage and current in Figure F. Figure F(a) shows the harmonic profiles of non-linear load current ($I_{Non\text{-}linear}$), linear load current (I_{Linear}) and total supply current from the grid (I_G) in RMS value. It is shown in the figure that the harmonics of the total supply current from the grid is the harmonic sum of non-linear and linear load current. At fundamental frequency (1^{st} harmonic), the harmonic of linear load current is in-phase with the harmonic of non-linear load current and hence the harmonic of total supply current is the addition of the non-linear and linear load current harmonics. In contrast to the fundamental harmonic, the harmonics of the linear load current are in anti-phase with the corresponding harmonics of non-linear load current at higher frequencies (higher than fundamental) and hence the harmonics of total supply current at these frequencies are the algebraic subtraction of the non-linear and linear load current harmonics.

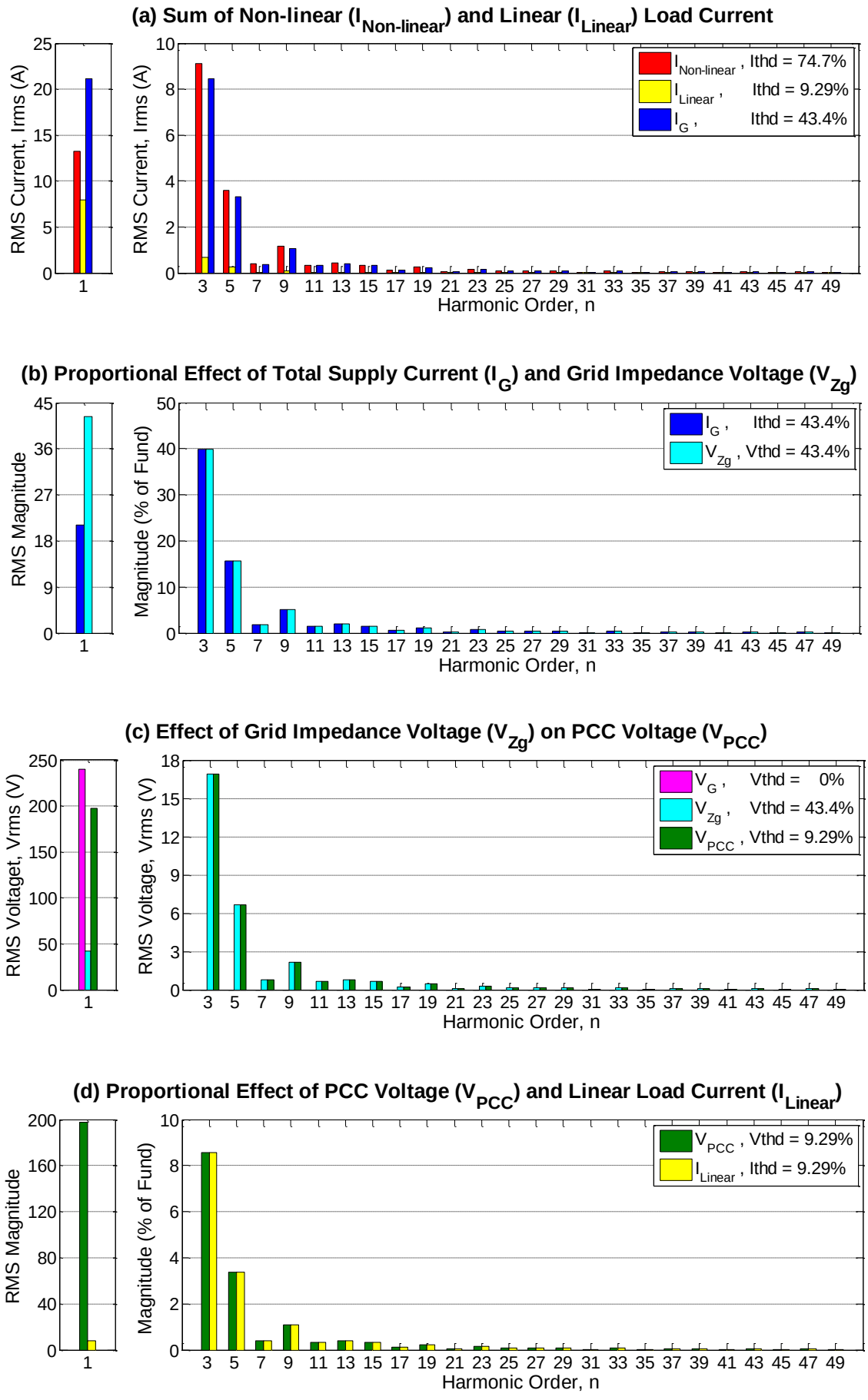

Figure F: Harmonic profiles of current and voltage in the simulation showing the interaction in distribution grid.

Figure F(b) shows that voltage drop across grid impedance (V_{Zg}) is directly proportional to the total supply current (I_G) flowing through it. This can be seen in the figure where the harmonic distortion factor (HDF, harmonic magnitude in % of fundamental harmonic) of the grid impedance voltage harmonics are the same magnitude as the total supply current harmonics, although their fundamental harmonics are different in rms magnitude. This proportional effect adheres to the well-known Ohm's Law which can be expressed by Equation (A), where Z is the impedance, I is the current flowing through the impedance, and V is the voltage drops across the impedance due to current flow (Alexander and Sadiku [75], Hughes [76]).

$$V = IZ \tag{A}$$

In the distribution network as shown in Figure D, the background grid voltage (V_G) is divided by the grid impedance voltage (V_{Zg}) and PCC voltage (V_{PCC}). This can be observed in Figure F(c) where the harmonics of PCC voltage are the remnant of the background grid voltage harmonics subtracted by the grid impedance voltage harmonics. It is noted that as the background grid voltage is a perfect sinusoidal wave it only contains the fundamental harmonic (shown in Figure F(c)), the presence of harmonics in grid impedance voltage have caused the waveform of PCC voltage consists of a fundamental harmonic that in-phase with the fundamental harmonic of background grid voltage, and a range of harmonics (higher than fundamental frequency) that anti-phase but same magnitude with the grid impedance harmonics (shown in Figure F(c)).

With regard to the current of the linear load (I_{Linear}), it is proportional to the PCC voltage (V_{PCC}) applied to its effective impedance, as shown by Ohm's Law in Equation (A). This proportional effect can also be seen on Figure F(d) where the HDF of the linear load current harmonics are the same magnitude as the PCC voltage harmonics, although their fundamental harmonics are different in RMS magnitude. Besides this, as the linear load current is proportional to the PCC voltage, the phase characteristic of the PCC voltage harmonics will in turn cause the fundamental harmonic of the linear load current to be in-phase with the fundamental harmonic of the non-linear load current, while all other harmonics are anti-phase with the corresponding harmonics of non-linear load current, as shown in Figure F(a).

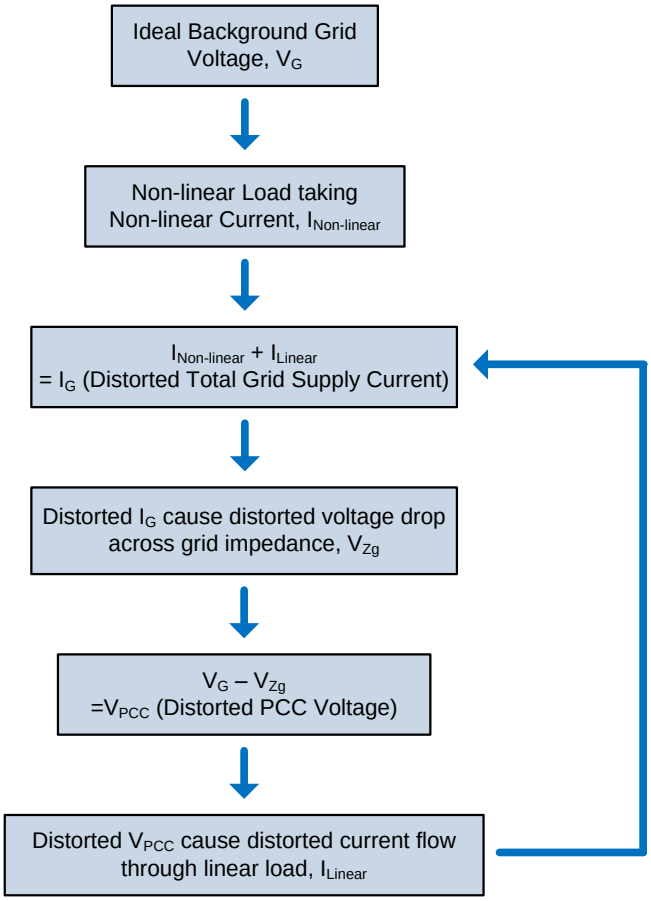

Figure G: Mechanism of the interaction between the PCC loading condition, background grid voltage and grid impedance in distribution grid.

By concluding the analysis in Figure E and Figure F, it can be confirmed that the voltage waveform at PCC and hence the harmonic profile of PCC voltage varies over time due to the change in the loading condition of distribution grid. In other words, the operating conditions of the distribution grid are varied over time due to the interaction between the PCC loading condition, background grid voltage and grid impedance. The mechanism of this interaction phenomenon is summarised and shown by the flowchart in Figure G.

E. Time Variant of PCC Voltage Distortion

The voltage waveform of the PCC varies over time due to the change in the operating conditions of the distribution grid. To verify this, the distribution grid voltage (which represents the PCC voltage) in the Power Electronics, Drives and Machines (PEDM) laboratory at Newcastle University is measured by a Yokogawa® PZ4000 Power Analyser at the output of a variac (used to generate experimental low voltage). Few measurements at different times of the day are taken and presented in Figure H. It compares the PCC voltage measurements at four different times on a given day to an

ideal PCC voltage (V_{PCC} Ideal). It is shown in the figure that the actual PCC voltage waveform changes with time and the distortion level varies (as shown by the voltage THD in Figure H). The apex of the PCC voltage waveforms in Figure H is magnified and illustrated in Figure I.

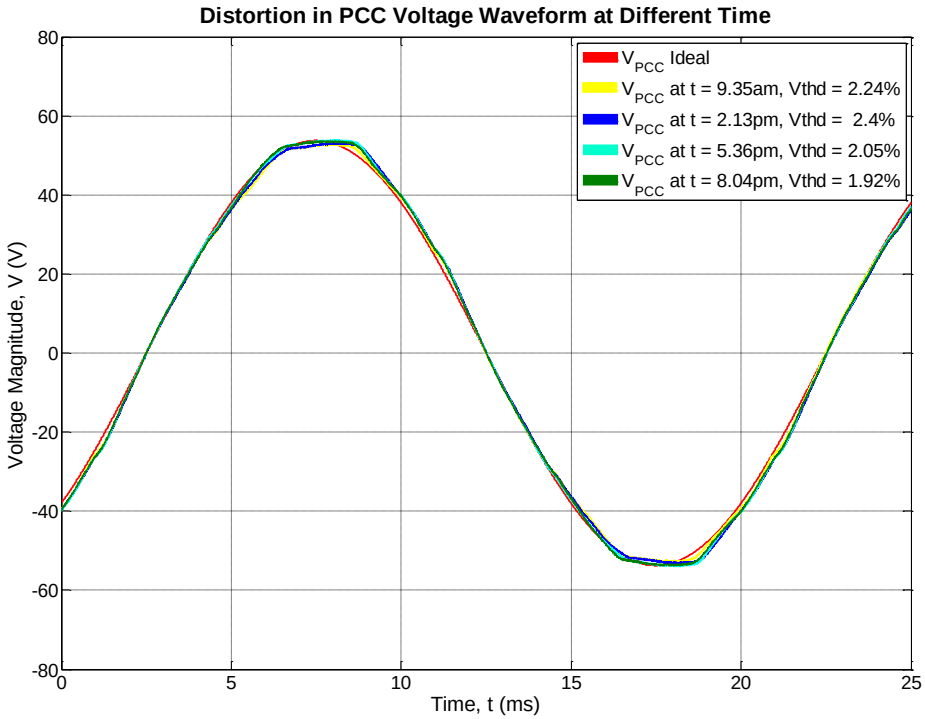

Figure H: Distortion in actual PCC voltage (V_{PCC}) waveform at different time.

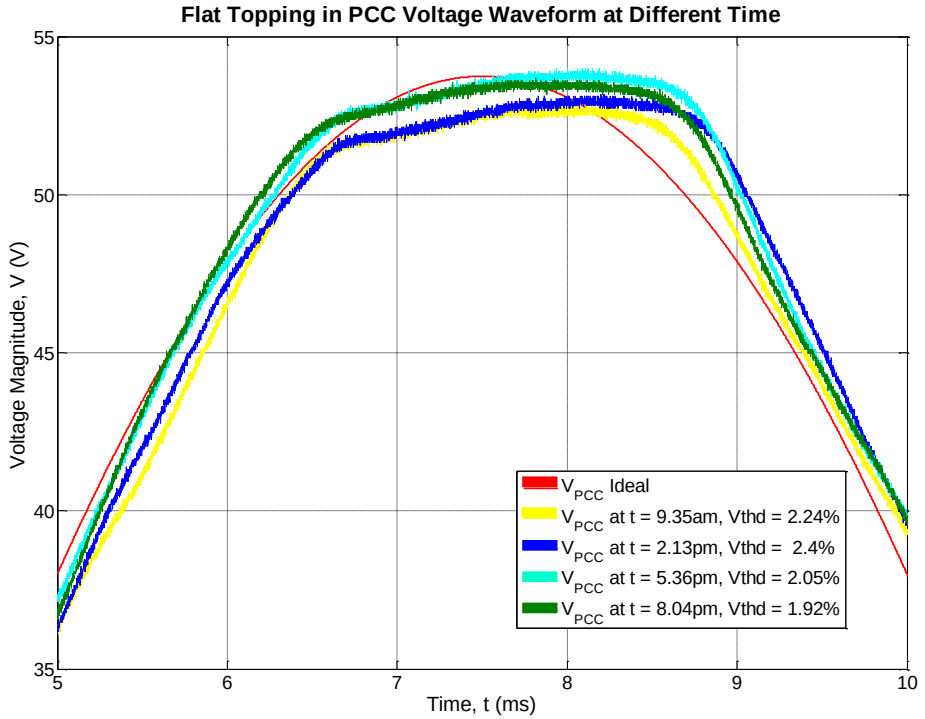

Figure I: Flat topping in PCC voltage (V_{PCC}) waveform at different time.

In Figure H and Figure I, it is apparent that the distortion appears in the waveform of PCC voltage, in particularly there is a "flat topping" at the apex of the PCC voltage waveform. Furthermore, it is apparent that the waveforms vary significantly over time. This in turn is reflected by the variation in harmonic profile of the PCC voltage. Figure J shows the corresponding change in low order harmonics (from the 3rd up to the 21st harmonics) of the PCC voltage.

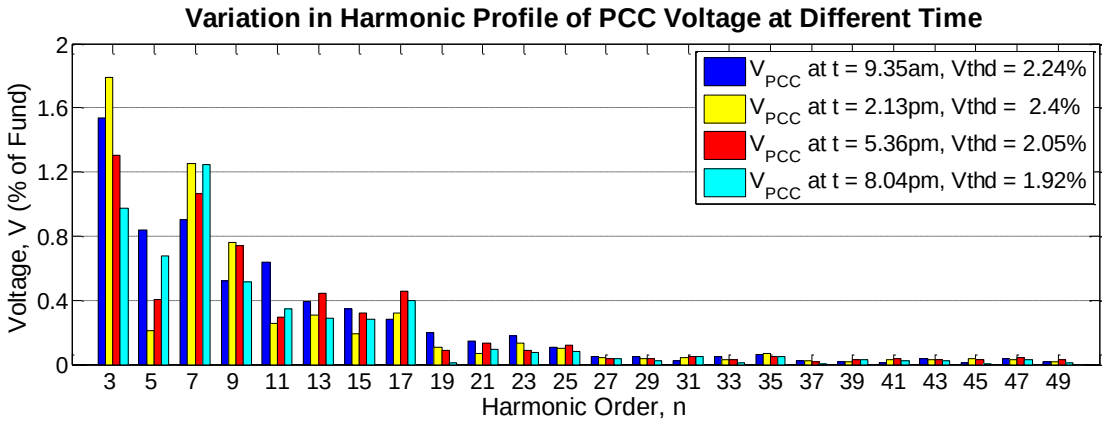

Figure J: Variation in harmonic profile of PCC voltage (V_{PCC}) at different time in practice.

F. Summary

This appendix has presented an overview of the causes and effects of harmonics present in the voltage and current waveforms in the distribution network. Through simulation the mechanism of the interaction between the PCC loading condition, background grid voltage and grid impedance is demonstrated. In particularly, the cause of distortion in the PCC voltage waveform due to the connection of non-linear load at PCC has been analysed and discussed. To verify this, the PCC voltage at different time in practice is measured and compared. The presented result show that the waveform and harmonic profile of the PCC voltage vary over time due to the change in the loading condition of the PCC, and hence the operating condition of the distribution grid. Chapter 4 considers the effect of the variation in this operating condition on the harmonic performance of the grid-connected PV inverter system.

Appendix VIII. Mechanism of Harmonic Interaction

Harmonic model of LCL branch

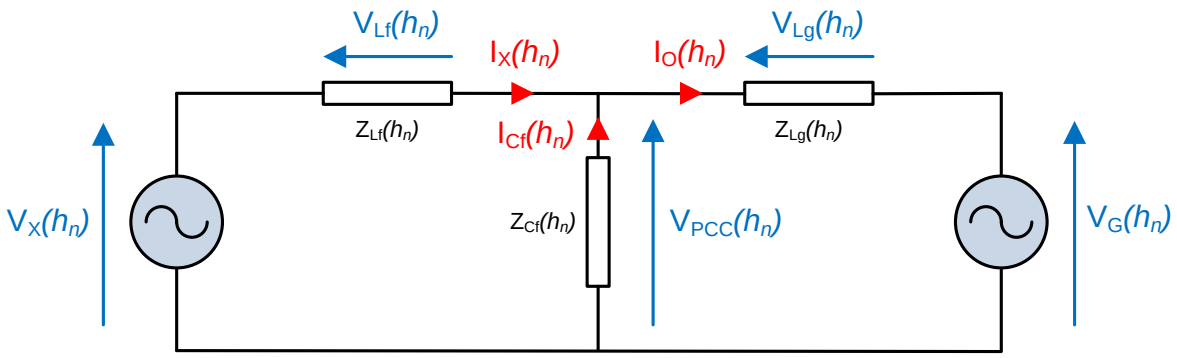

$$X_{Lf}(h_n) = \omega_n L_f = 2\pi f_1 L_f n$$

$$X_{Cf}(h_n) = \frac{1}{\omega_n C_f} = \frac{1}{2\pi f_1 C_f n}$$

$$X_{Lg}(h_n) = \omega_n L_g = 2\pi f_1 L_g n$$

$$\vec{Z}_{Lf}(h_n) = R_{Lf} + jX_{Lf}(h_n)$$

$$\vec{Z}_{Cf}(h_n) = R_{Cf} - jX_{Cf}(h_n)$$

$$\vec{Z}_{Lg}(h_n) = R_g + jX_{Lg}(h_n)$$

Superposition Theorem of V_{PCC}

1) Shorted V_G:

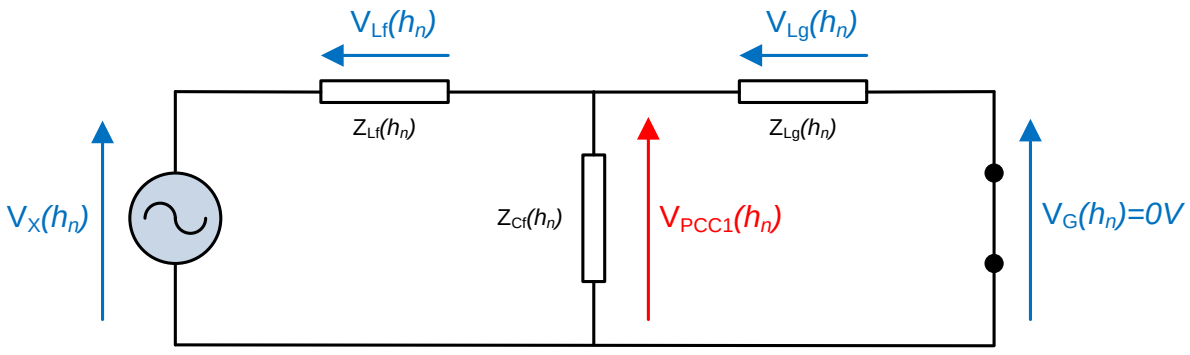

$$\vec{V}_{PCC1} = \vec{V}_X \times \frac{[\vec{Z}_{Cf} \parallel \vec{Z}_{Lg}]}{[\vec{Z}_{Cf} \parallel \vec{Z}_{Lg}] + \vec{Z}_{Lf}}$$

$$\vec{V}_{PCC1} = \vec{V}_X \times \frac{\frac{\vec{Z}_{Cf}\vec{Z}_{Lg}}{\vec{Z}_{Cf}+\vec{Z}_{Lg}}}{\frac{\vec{Z}_{Cf}\vec{Z}_{Lg}}{\vec{Z}_{Cf}+\vec{Z}_{Lg}}+\vec{Z}_{Lf}}$$

$$\vec{V}_{PCC1} = \vec{V}_X \times \frac{\frac{\vec{Z}_{Cf}\vec{Z}_{Lg}}{\vec{Z}_{Cf}+\vec{Z}_{Lg}}}{\frac{\vec{Z}_{Cf}\vec{Z}_{Lg}+\vec{Z}_{Lf}(\vec{Z}_{Cf}+\vec{Z}_{Lg})}{\vec{Z}_{Cf}+\vec{Z}_{Lg}}}$$

$$\vec{V}_{PCC1} = \vec{V}_X \times \frac{\vec{Z}_{Cf}\vec{Z}_{Lg}}{\vec{Z}_{Cf}\vec{Z}_{Lg}+\vec{Z}_{Lf}\vec{Z}_{Cf}+\vec{Z}_{Lf}\vec{Z}_{Lg}}$$

$$\vec{V}_{PCC1} = \frac{\vec{V}_X\vec{Z}_{Cf}\vec{Z}_{Lg}}{\vec{Z}_{Cf}(\vec{Z}_{Lg}+\vec{Z}_{Lf})+\vec{Z}_{Lf}\vec{Z}_{Lg}}$$

2) Shorted V_X:

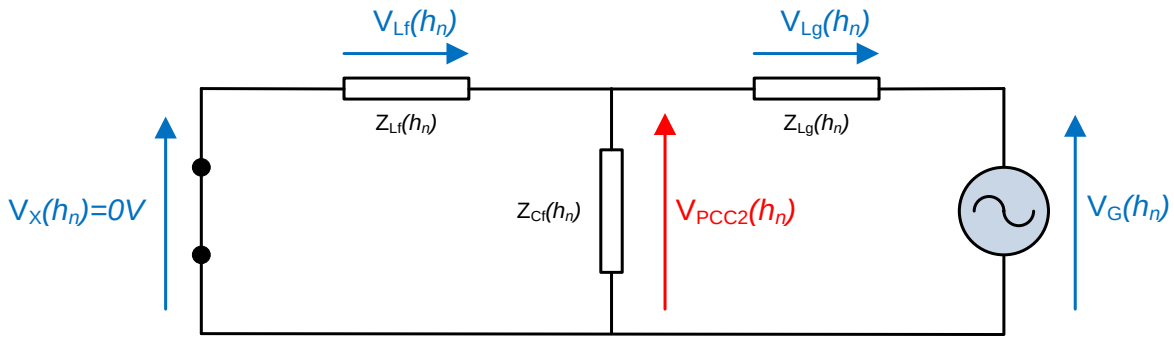

$$\vec{V}_{PCC2} = \vec{V}_G \times \frac{[\vec{Z}_{Cf} \parallel \vec{Z}_{Lf}]}{[\vec{Z}_{Cf} \parallel \vec{Z}_{Lf}]+\vec{Z}_{Lg}}$$

$$\vec{V}_{PCC2} = \vec{V}_G \times \frac{\frac{\vec{Z}_{Cf}\vec{Z}_{Lf}}{\vec{Z}_{Cf}+\vec{Z}_{Lf}}}{\frac{\vec{Z}_{Cf}\vec{Z}_{Lf}}{\vec{Z}_{Cf}+\vec{Z}_{Lf}}+\vec{Z}_{Lg}}$$

$$\vec{V}_{PCC2} = \vec{V}_G \times \frac{\frac{\vec{Z}_{Cf}\vec{Z}_{Lf}}{\vec{Z}_{Cf}+\vec{Z}_{Lf}}}{\frac{\vec{Z}_{Cf}\vec{Z}_{Lf}+\vec{Z}_{Lg}(\vec{Z}_{Cf}+\vec{Z}_{Lf})}{\vec{Z}_{Cf}+\vec{Z}_{Lf}}}$$

$$\vec{V}_{PCC2} = \vec{V}_G \times \frac{\vec{Z}_{Cf}\vec{Z}_{Lf}}{\vec{Z}_{Cf}\vec{Z}_{Lf}+\vec{Z}_{Lg}\vec{Z}_{Cf}+\vec{Z}_{Lg}\vec{Z}_{Lf}}$$

$$\vec{V}_{PCC2} = \frac{\vec{V}_G \vec{Z}_{Cf} \vec{Z}_{Lf}}{\vec{Z}_{Cf}\left(\vec{Z}_{Lf} + \vec{Z}_{Lg}\right) + \vec{Z}_{Lg}\vec{Z}_{Lf}}$$

Combine V_{PCC1} and V_{PCC2}:

$$\vec{V}_{PCC} = \vec{V}_{PCC1} + \vec{V}_{PCC2}$$

$$\vec{V}_{PCC} = \frac{\vec{V}_X \vec{Z}_{Cf} \vec{Z}_{Lg}}{\vec{Z}_{Cf}\left(\vec{Z}_{Lg} + \vec{Z}_{Lf}\right) + \vec{Z}_{Lf}\vec{Z}_{Lg}} + \frac{\vec{V}_G \vec{Z}_{Cf} \vec{Z}_{Lf}}{\vec{Z}_{Cf}\left(\vec{Z}_{Lf} + \vec{Z}_{Lg}\right) + \vec{Z}_{Lg}\vec{Z}_{Lf}}$$

$$\vec{V}_{PCC} = \frac{\vec{V}_X \vec{Z}_{Cf} \vec{Z}_{Lg} + \vec{V}_G \vec{Z}_{Cf} \vec{Z}_{Lf}}{\vec{Z}_{Cf}\left(\vec{Z}_{Lf} + \vec{Z}_{Lg}\right) + \vec{Z}_{Lf}\vec{Z}_{Lg}}$$

$$\vec{V}_{PCC} = \frac{\vec{Z}_{Cf}\left(\vec{V}_X \vec{Z}_{Lg} + \vec{V}_G \vec{Z}_{Lf}\right)}{\vec{Z}_{Cf}\left[\left(\vec{Z}_{Lf} + \vec{Z}_{Lg}\right) + \frac{\vec{Z}_{Lf}\vec{Z}_{Lg}}{\vec{Z}_{Cf}}\right]}$$

$$\vec{V}_{PCC} = \frac{\vec{V}_X \vec{Z}_{Lg} + \vec{V}_G \vec{Z}_{Lf}}{\vec{Z}_{Lf} + \vec{Z}_{Lg} + \frac{\vec{Z}_{Lf}\vec{Z}_{Lg}}{\vec{Z}_{Cf}}}$$

For particular harmonic order of V_{PCC}:

$$\vec{V}_{PCC}(h_n) = \frac{\vec{V}_X(h_n) \vec{Z}_{Lg}(h_n) + \vec{V}_G(h_n) \vec{Z}_{Lf}(h_n)}{\vec{Z}_{Lf}(h_n) + \vec{Z}_{Lg}(h_n) + \frac{\vec{Z}_{Lf}(h_n)\vec{Z}_{Lg}(h_n)}{\vec{Z}_{Cf}(h_n)}}$$

Voltage drop across filter inductance and grid inductance:

$$\vec{V}_{Lf}(h_n) = \vec{V}_X(h_n) - \vec{V}_{PCC}(h_n)$$

$$\vec{V}_{Lg}(h_n) = \vec{V}_{PCC}(h_n) - \vec{V}_G(h_n)$$

Inverter bridge output current:

$$\vec{I}_X(h_n) = \frac{\vec{V}_{Lf}(h_n)}{\vec{Z}_{Lf}(h_n)} = \frac{\vec{V}_X(h_n) - \vec{V}_{PCC}(h_n)}{\vec{Z}_{Lf}(h_n)}$$

By substituting $\vec{V}_{PCC} = \frac{\vec{V}_X \vec{Z}_{Lg} + \vec{V}_G \vec{Z}_{Lf}}{\vec{Z}_{Lf} + \vec{Z}_{Lg} + \frac{\vec{Z}_{Lf}\vec{Z}_{Lg}}{\vec{Z}_{Cf}}}$,

$$\vec{I}_X = \frac{\vec{V}_X - \dfrac{\vec{V}_X\vec{Z}_{Lg} + \vec{V}_G\vec{Z}_{Lf}}{\vec{Z}_{Lf} + \vec{Z}_{Lg} + \dfrac{\vec{Z}_{Lf}\vec{Z}_{Lg}}{\vec{Z}_{Cf}}}}{\vec{Z}_{Lf}}$$

$$\vec{I}_X = \frac{\dfrac{\vec{V}_X\left(\vec{Z}_{Lf} + \vec{Z}_{Lg} + \dfrac{\vec{Z}_{Lf}\vec{Z}_{Lg}}{\vec{Z}_{Cf}}\right) - \vec{V}_X\vec{Z}_{Lg} - \vec{V}_G\vec{Z}_{Lf}}{\vec{Z}_{Lf} + \vec{Z}_{Lg} + \dfrac{\vec{Z}_{Lf}\vec{Z}_{Lg}}{\vec{Z}_{Cf}}}}{\vec{Z}_{Lf}}$$

$$\vec{I}_X = \frac{\vec{V}_X\vec{Z}_{Lf} + \vec{V}_X\vec{Z}_{Lg} + \vec{V}_X\dfrac{\vec{Z}_{Lf}\vec{Z}_{Lg}}{\vec{Z}_{Cf}} - \vec{V}_X\vec{Z}_{Lg} - \vec{V}_G\vec{Z}_{Lf}}{\vec{Z}_{Lf}\left(\vec{Z}_{Lf} + \vec{Z}_{Lg} + \dfrac{\vec{Z}_{Lf}\vec{Z}_{Lg}}{\vec{Z}_{Cf}}\right)}$$

$$\vec{I}_X = \frac{\vec{Z}_{Lf}\left(\vec{V}_X + \vec{V}_X\dfrac{\vec{Z}_{Lg}}{\vec{Z}_{Cf}} - \vec{V}_G\right)}{\vec{Z}_{Lf}\left(\vec{Z}_{Lf} + \vec{Z}_{Lg} + \dfrac{\vec{Z}_{Lf}\vec{Z}_{Lg}}{\vec{Z}_{Cf}}\right)}$$

$$\vec{I}_X = \frac{\vec{V}_X - \vec{V}_G + \vec{V}_X\dfrac{\vec{Z}_{Lg}}{\vec{Z}_{Cf}}}{\vec{Z}_{Lf} + \vec{Z}_{Lg} + \dfrac{\vec{Z}_{Lf}\vec{Z}_{Lg}}{\vec{Z}_{Cf}}}$$

For particular harmonic order of I_X:

$$\vec{I}_X(h_n) = \frac{\vec{V}_X(h_n) - \vec{V}_G(h_n) + \vec{V}_X(h_n)\dfrac{\vec{Z}_{Lg}(h_n)}{\vec{Z}_{Cf}(h_n)}}{\vec{Z}_{Lf}(h_n) + \vec{Z}_{Lg}(h_n) + \dfrac{\vec{Z}_{Lf}(h_n)\vec{Z}_{Lg}(h_n)}{\vec{Z}_{Cf}(h_n)}}$$

Inverter system output current:

$$\vec{I}_O(h_n) = \frac{\vec{V}_{Lg}(h_n)}{\vec{Z}_{Lg}(h_n)} = \frac{\vec{V}_{PCC}(h_n) - \vec{V}_G(h_n)}{\vec{Z}_{Lg}(h_n)}$$

By substituting $\vec{V}_{PCC} = \frac{\vec{V}_X\vec{Z}_{Lg} + \vec{V}_G\vec{Z}_{Lf}}{\vec{Z}_{Lf} + \vec{Z}_{Lg} + \frac{\vec{Z}_{Lf}\vec{Z}_{Lg}}{\vec{Z}_{Cf}}}$,

$$\vec{I}_O = \frac{\frac{\vec{V}_X\vec{Z}_{Lg} + \vec{V}_G\vec{Z}_{Lf}}{\vec{Z}_{Lf} + \vec{Z}_{Lg} + \frac{\vec{Z}_{Lf}\vec{Z}_{Lg}}{\vec{Z}_{Cf}}} - \vec{V}_G}{\vec{Z}_{Lg}}$$

$$\vec{I}_O = \frac{\frac{\vec{V}_X\vec{Z}_{Lg} + \vec{V}_G\vec{Z}_{Lf} - \vec{V}_G\left(\vec{Z}_{Lf} + \vec{Z}_{Lg} + \frac{\vec{Z}_{Lf}\vec{Z}_{Lg}}{\vec{Z}_{Cf}}\right)}{\vec{Z}_{Lf} + \vec{Z}_{Lg} + \frac{\vec{Z}_{Lf}\vec{Z}_{Lg}}{\vec{Z}_{Cf}}}}{\vec{Z}_{Lg}}$$

$$\vec{I}_O = \frac{\vec{V}_X\vec{Z}_{Lg} + \vec{V}_G\vec{Z}_{Lf} - \vec{V}_G\vec{Z}_{Lf} - \vec{V}_G\vec{Z}_{Lg} - \vec{V}_G\frac{\vec{Z}_{Lf}\vec{Z}_{Lg}}{\vec{Z}_{Cf}}}{\vec{Z}_{Lg}\left(\vec{Z}_{Lf} + \vec{Z}_{Lg} + \frac{\vec{Z}_{Lf}\vec{Z}_{Lg}}{\vec{Z}_{Cf}}\right)}$$

$$\vec{I}_O = \frac{\vec{Z}_{Lg}\left(\vec{V}_X - \vec{V}_G - \vec{V}_G\frac{\vec{Z}_{Lf}}{\vec{Z}_{Cf}}\right)}{\vec{Z}_{Lg}\left(\vec{Z}_{Lf} + \vec{Z}_{Lg} + \frac{\vec{Z}_{Lf}\vec{Z}_{Lg}}{\vec{Z}_{Cf}}\right)}$$

$$\vec{I}_O = \frac{\vec{V}_X - \vec{V}_G - \vec{V}_G\frac{\vec{Z}_{Lf}}{\vec{Z}_{Cf}}}{\vec{Z}_{Lf} + \vec{Z}_{Lg} + \frac{\vec{Z}_{Lf}\vec{Z}_{Lg}}{\vec{Z}_{Cf}}}$$

For particular harmonic order of I_O:

$$\vec{I}_O(h_n) = \frac{\vec{V}_X(h_n) - \vec{V}_G(h_n) - \vec{V}_G(h_n)\frac{\vec{Z}_{Lf}(h_n)}{\vec{Z}_{Cf}(h_n)}}{\vec{Z}_{Lf}(h_n) + \vec{Z}_{Lg}(h_n) + \frac{\vec{Z}_{Lf}(h_n)\vec{Z}_{Lg}(h_n)}{\vec{Z}_{Cf}(h_n)}}$$

References

[1] H. J. Moller, *Semiconductors for Solar Cells*. Norwood: Artech House, 1993.

[2] E. T. Livezey. (1980, November 6). Hazardous waste. *The Christian Science Monitor* [Online]. Available: http://www.csmonitor.com/1980/1106/110653.html

[3] *Kyoto Protocol to the United Nations Framework Convention on Climate Change,* United Nations, 1998.

[4] SolarPowerIsTheFuture. (2011, August 25). *How Efficient is Solar Energy? Factors that Affect Efficiency* [Online]. Available: http://www.solarpoweristhefuture.com/how-efficient-is-solar-energy.shtml

[5] K. Bullis. (2008, May 1). *A Price Drop for Solar Panels* [Online]. Available: http://www.technologyreview.com/Biztech/20702/

[6] D. Clark. (2011, August 25). *Price of Solar Panels to drop to $1 by 2013, Report Forecasts* [Online]. Available: http://www.guardian.co.uk/environment/2011/jun/20/solar-panel-price-drop

[7] "Trends in photovoltaic applications: Survey report of selected IEA countries between 1992 and 2009," International Energy Agency (IEA), IEA-PVPS T1-19, 2010.

[8] *Communication from the Commission to the European Council and the European Parliament: An Energy Policy for Europe,* Commission of the European Communities COM(2007) 1, 2007.

[9] "RE-thinking 2050: A 100% renewable energy vision for the European Union," European Renewable Energy Council (EREC),2010.

[10] B. Verhoeven, "Utility aspects of grid connected photovoltaic power systems," International Energy Agency (IEA), Report PVPS T5-01, December 1998.

[11] T. H. Ortmeyer, K. R. Chakravarthi, and A. A. Mahmoud, "The effects of power system harmonics on power system equipment and loads," *IEEE Transactions on Power Apparatus and Systems,* vol. PAS-104, pp. 2555-2563, 1985.

[12] A. F. Povlsen, "Impacts of Power Penetration from Photovoltaic Power Systems in Distribution Networks," IEA PVPS T5-10, 2002.

[13] R. Hacker, J. Thornycroft, D. Munro, and E. Rudkin, "Co-ordinated experimental research into PV power interaction with the supply network-Phase I," ETSU S/P2/00233/REP, 1999.

[14] A. Canova, L. Giaccone, F. Spertino, and M. Tartaglia, "Electrical impact of photovoltaic plant in distributed network," in *Industry Applications Conference*, 2007, pp. 1450-1455.

[15] A. D. Simmons and D. G. Infield, "Current waveform quality from grid-connected Photovoltaic inverters and its dependence on operating conditions," in *Progress in Photovoltaics: Research and Applications*, 2000, pp. 411-420.

[16] J. H. R. Enslin, W. T. J. Hulshorst, A. M. S. Atmadji, P. J. M. Heskes, A. Kotsopoulos, J. F. G. Cobben, and P. Van der Sluijs, "Harmonic interaction between large numbers of photovoltaic inverters and the distribution network," in *IEEE Bologna Power Tech Conference*, 2003, p. 6 pp. Vol.3.

[17] *IEEE Recommended Practice for Utility Interface of Photovoltaic (PV) Systems,* IEEE Std 929, 2000.

[18] *Voltage Characteristics of Electricity Supplied by Public Distribution Networks,* BS EN50160, 2007.

[19] *Electromagnetic Compatibility (EMC). Limits. Limits for Harmonic Current Emissions (Equipment Input Current ≤ 16 A Per Phase),* BS EN61000-3-2, 2006.

[20] R. A. Messenger and J. Ventre, *Photovoltaic Systems Engineering* 2nd ed.: CRC Press, 2004.

[21] M. Armstrong, D. J. Atkinson, C. M. Johnson, and T. D. Abeyasekera, "Auto-calibrating DC link current sensing technique for transformerless, grid connected, H-Bridge inverter systems," *IEEE Transactions on Power Electronics,* vol. 21, pp. 1385-1393, 2006.

[22] *Recommendations for the Connection of Small-scale Embedded Generators (Up to 16A per Phase) in Parallel with Public Low-voltage Distribution Networks,* ENA G83/1-1, 2008.

[23] W. Knaupp, "Evaluation of PV module designs at irregular operation conditions," in *26th IEEE Photovoltaic Specialists Conference*, 1997, pp. 1213-1216.

[24] H. Koizumi and K. Kurokawa, "A novel maximum power point tracking method for PV module integrated converter," in *36th IEEE Power Electronics Specialists Conference*, 2005, pp. 2081-2086.

[25] J. Li and H. Wang, "Maximum power point tracking of photovoltaic generation based on the fuzzy control method," in *International Conference on Sustainable Power Generation and Supply*, 2009, pp. 1-6.

[26] J. J. Bzura, "Performance of grid-connected photovoltaic systems on residences and commercial buildings in New England," *IEEE Transactions on Energy Conversion*, vol. 7, pp. 79-82, 1992.

[27] M. Armstrong, "Power quality improvement of grid connected photovoltaic inverter system," Ph.D. thesis, Newcastle University, Newcastle upon Tyne, 2007.

[28] N. Mohan, T. M. Undeland, and W. P. Robbins, *Power Electronics: Converters, Applications, and Design*, 3rd ed. Hoboken, NJ: John Wiley & Sons, 2003.

[29] E. T. Schonholzer, "Inverters for utility interactive photovoltaic power plants," in *Mediterranean Electrotechnical Conference*, 1989, pp. 16-20.

[30] M. Calais, J. Myrzik, T. Spooner, and V. G. Agelidis, "Inverters for single-phase grid connected photovoltaic systems-an overview," in *33rd IEEE Annual Power Electronics Specialists Conference*, 2002, pp. 1995-2000.

[31] F. Blaabjerg, R. Teodorescu, Z. Chen, and M. Liserre, "Power converters and control of renewable energy systems," in *6th International Conference on Power Electronics*, Busan, Korea, 2004.

[32] B. Lindgren, "Topology for decentralised solar energy inverters with a low voltage AC-bus," in *8th European Conference on Power Electronics and Applications*, Lausanne, Switzerland, 1999.

[33] B. M. T. Ho and H. S. H. Chung, "An integrated inverter with maximum power tracking for grid-connected PV systems," *IEEE Transactions on Power Electronics*, vol. 20, pp. 953-962, 2005.

[34] M. Djarallah, B. O. Zeidane, and B. Azoui, "Energy transfer mechanism for a grid-connected residential PV system within the Matlab/Simulink environment," in *42nd International Universities Power Engineering Conference*, 2007, pp. 763-770.

[35] T. Abeyasekera, "Improvements to grid connected photovoltaic inverters," Ph.D. thesis, Newcastle University, 2005.

[36] S. Ott, I. Roasto, and D. Vinnikov, "Neutral point clamped quasi-impedance-source inverter," in *7th International Conference-Workshop Compatibility and Power Electronics*, 2011, pp. 348-353.

[37] Z. Dongsheng and D. G. Rouaud, "Dead-time effect and compensations of three-level neutral point clamp inverters for high-performance drive applications," *IEEE Transactions on Power Electronics*, vol. 14, pp. 782-788, 1999.

[38] K. H. Ahmed, S. J. Finney, and B. W. Williams, "Passive filter design for three-phase inverter interfacing in distributed generation," in *Compatibility in Power Electronics*, 2007, pp. 1-9.

[39] K. Jalili and S. Bernet, "Design of LCL filters of active-front-end two-level voltage-source converters," *IEEE Transactions on Industrial Electronics*, vol. 56, pp. 1674-1689, 2009.

[40] H. R. Karshenas and H. Saghafi, "Basic criteria in designing LCL filters for grid connected converters," in *IEEE International Symposium on Industrial Electronics*, 2006, pp. 1996-2000.

[41] A. Kitamura, F. Yamamoto, H. Matsuda, K. Akhmad, and Y. Hamakawa, "Test results on DC injection phenomenon of grid connected PV system at Rokko test center," in *25th IEEE Photovoltaic Specialists Conference*, 1996, pp. 1377-1379.

[42] L. Bowtell and A. Ahfock, "Direct current offset controller for transformerless single-phase photovoltaic grid-connected inverters," *IET Renewable Power Generation*, vol. 4, pp. 428-437, 2010.

[43] V. Salas, E. Olias, M. Alonso, F. Chenlo, and A. Barrado, "DC current injection into the network from PV grid inverters," in *4th IEEE World Conference on Photovoltaic Energy Conversion*, 2006, pp. 2371-2374.

[44] R. Gonzalez, J. Lopez, P. Sanchis, and L. Marroyo, "Transformerless inverter for single-phase photovoltaic systems," *IEEE Transactions on Power Electronics*, vol. 22, pp. 693-697, 2007.

[45] O. Lopez, R. Teodorescu, and J. Doval-Gandoy, "Multilevel transformerless topologies for single-phase grid-connected converters," in *32nd IEEE Annual Conference on Industrial Electronics*, 2006, pp. 5191-5196.

[46] B. Wang, X. Guo, H. Gu, Q. Mei, and W. Wu, "Real-time DC injection measurement technique for transformerless PV systems," in *2nd IEEE International Symposium on Power Electronics for Distributed Generation Systems*, 2010, pp. 980-983.

[47] F. Blaabjerg, R. Teodorescu, M. Liserre, and A. V. Timbus, "Overview of control and grid synchronization for distributed power generation systems," *IEEE Transactions on Industrial Electronics*, vol. 53, pp. 1398-1409, 2006.

[48] A. Kitamura, H. Matsuda, F. Yamamoto, and T. Matsuoka, "Islanding phenomenon of grid connected PV systems," in *28th IEEE Photovoltaic Specialists Conference*, 2000, pp. 1591-1594.

[49] G. H. Kim, H. R. Seo, S. J. Jang, S. S. Park, S. Y. Kim, N. W. Kim, M. Park, and I. k. Yu, "Performance analysis of the anti-islanding function of a PV-AF system under multiple PV system connections," in *International Conference on Electrical Machines and Systems*, 2009, pp. 1-5.

[50] M. Valentini, S. Munk-Nielsen, F. Valderrey Sanchez, and U. Martinez De Estibariz, "A new passive islanding detection method for grid-connected PV inverters," in *International Symposium on Power Electronics, Electrical Drives, Automation and Motion*, 2008, pp. 223-228.

[51] B.-G. Yu, M. Matsui, and G.-J. Yu, "A correlation-based islanding-detection method using current-magnitude disturbance for PV system," *IEEE Transactions on Industrial Electronics*, vol. 58, pp. 2935-2943, 2011.

[52] X. D. Sun, M. Matsui, and B. G. Yu, "A novel islanding detection method based on minute asymmetrical current injection for three-phase grid-connected PV inverters," in *7th Internatonal Conference on Power Electronics*, 2007, pp. 841-846.

[53] M. D. Lutovac, D. V. Tosic, and B. L. Evans, *Filter Design for Signal Processing: Using MATLAB and Mathematica* Prentice Hall, 2001.

[54] R. D. Strum and D. E. Kirk, *Contemporary Linear Systems: Using MATLAB 4.0*: PWS Publishing Company, 1996.

[55] C.-T. Chen, *Digital Signal Processing: Spectral Computational and Filter Design*: Oxford University Press, 2001.

[56] *Consideration of Reference Impedances and Public Supply Network Impedances for Use In Determining Disturbance Characteristics of Electrical Equipment Having a Rated Current ⩽75A Per Phase,* IEC 60725, 2005.

[57] P. J. M. Heskes, P. M. Rooij, J. F. G. Cobben, and H. E. Oldenkamp, "Estimation of the potential to pollute the electricity network with harmonics due to the use of small micro generators with inverters," ENC-C--04-087, August 2004.

[58] T. Abeyasekera, C. M. Johnson, D. J. Atkinson, and M. Armstrong, "Suppression of line voltage related distortion in current controlled grid connected inverters," *IEEE Transactions on Power Electronics,* vol. 20, pp. 1393-1401, 2005.

[59] E. Twining and D. G. Holmes, "Grid current regulation of a three-phase voltage source inverter with an LCL input filter," *IEEE Transactions on Power Electronics,* vol. 18, pp. 888-895, 2003.

[60] G. Ellis, *Control System Design Guide - A Practical Guide*: Elsevier, 2004.

[61] S. Buso and P. Mattavelli, *Digital Control in Power Electronics*: Morgan & Claypool, 2006.

[62] "TMS320F2810, TMS320F2811, TMS320F2812, TMS320C2810, TMS320C2811, TMS320C2812 Digital signal processors data manual," Texas Instrument, Data Manual SPRS174O, 2007.

[63] The MathWorks, "MATLAB", R2010a ed, 2010.

[64] M. Bartoli, A. Reatti, and M. K. Kazimierczuk, "High-frequency models of ferrite core inductors," in *20th International Conference on Industrial Electronics, Control and Instrumentation*, 1994, pp. 1670-1675.

[65] "Environment design rules of MOSFETs in medium power applications," SGS-Thomson Microelectronics, Application Note.

[66] G. H. Tomlinson, *Electrical Networks and Filters: Theory and Design*. Hertfordshire: Prentice Hall International (UK) Ltd, 1991.

[67] M. Armstrong, D. J. Atkinson, C. M. Johnson, and T. D. Abeyasekera, "Low order harmonic cancellation in a grid connected multiple inverter system via current control parameter randomization," *IEEE Transactions on Power Electronics,* vol. 20, pp. 885-892, 2005.

[68] M. Shahidehpour and F. Schwarts, "Don't let the sun go down on PV," *IEEE Power and Energy Magazine* vol. 2, pp. 40-48, 2004.

[69] S. Dasgupta, S. N. Mohan, S. K. Sahoo, and S. K. Panda, "A Lyapunov function based current controller to control active and reactive power flow in a three phase grid connected PV inverter under generalized grid voltage conditions," in *8th IEEE International Conference on Power Electronics and ECCE Asia,* 2011, pp. 1110-1117.

[70] S. Dasgupta, S. N. Mohan, S. K. Sahoo, and S. K. Panda, "Derivation of instantaneous current references for three phase PV inverter connected to grid with active and reactive power flow control," in *8th IEEE International Conference on Power Electronics and ECCE Asia*, 2011, pp. 1228-1235.

[71] S. Dasgupta, S. K. Sahoo, and S. K. Panda, "A novel current control scheme using Lyapunov function to control the active and reactive power flow in a single phase hybrid PV inverter system connected to the grid," in *International Power Electronics Conference*, 2010, pp. 1701-1708.

[72] S. Kim, G. Yoo, and J. Song, "A bifunctional utility connected photovoltaic system with power factor correction and UPS facility," in *25th IEEE Photovoltaic Specialists Conference*, 1996, pp. 1363-1368.

[73] K. Turitsyn, P. Sulc, S. Backhaus, and M. Chertkov, "Local control of reactive power by distributed photovoltaic generators," in *1st IEEE International Conference on Smart Grid Communications*, 2010, pp. 79-84.

[74] A. Cagnano, E. De Tuglie, M. Liserre, and R. Mastromauro, "On-line optimal reactive power control strategy of PV-inverters," *IEEE Transactions on Industrial Electronics*, vol. PP, pp. 1-1, 2011.

[75] C. K. Alexander and M. N. O. Sadiku, *Fundamentals of Electric Circuits*, 4th ed. New York: McGraw-Hill Companies, 2009.

[76] E. Hughes, *Hughes Electrical and Electronic Technology*, 9th ed. Essex: Pearson Education Limited, 2005.

[77] Nellis Air Force Base. Nellis Air Force Base Solar Power System. [Online]. Available: http://www.nellis.af.mil/shared/media/document/AFD-080117-043.pdf

[78] B. Mulliken, "Next to go mainstream: Mass energy storage," *Green Energy News*, vol. 16, March 20, 2011.

[79] K. J. Lee, N. J. Park, R. Y. Kim, D. H. Ha, and D. S. Hyun, "Design of an LCL filter employing a symmetric geometry and its control in grid-connected inverter applications," in *IEEE Power Electronics Specialists Conference*, 2008, pp. 963-966.

[80] "Straight talk about PWM AC drive harmonic problems and solutions," Rockwell Automation Mequon, WI, Technical Paper.

[81] J. F. G. Cobben, "Power quality: Implications at the point of connection," Ph.D. thesis, Technische Universiteit Eindhoven, Eindhoven, 2007.

[82] A. J. A. Bosman, J. F. G. Cobben, J. M. A. Myrzik, and W. L. Kling, "Harmonic modelling of solar inverters and their interaction with the distribution grid," in *41st International Universities Power Engineering Conference*, 2006, pp. 991-995.

[83] P. J. M. Heskes and J. H. R. Enslin, "Power quality behaviour of different photovoltaic inverter topologies," August 2003.

[84] W. Enders, C. Halter, and P. Wurm, "Investigation of typical problems of PV-inverters," in *17th European Photovoltaic Solar Energy Conference and Exhibition*, Munich, Germany, 2001.

[85] E. Caamano, J. Thornycroft, H. D. Moor, S. Cobben, M. Jantsch, T. Erge, H. Laukamp, D. Suna, and B. Gaiddon, "State-of-the-art on dispersed PV power generation: Publications review on the impacts of PV distributed generation and electricity networks," EIE/05/171/SI2.420208, 23rd June 2007.

[86] D. G. Infield, P. Onions, A. D. Simmons, and G. A. Smith, "Power quality from multiple grid-connected single-phase inverters," *IEEE Transactions on Power Delivery*, vol. 19, pp. 1983-1989, 2004.

[87] M. C. Benhabib, J. M. A. Myrzik, and J. L. Duarte, "Harmonic effects caused by large scale PV installations in LV network," in *9th International Conference on Electrical Power Quality and Utilisation*, 2007, pp. 1-6.

[88] T. R. Kuphaldt. (2011, June 14). *Lessons In Electric Circuits (6 ed.)* [Online]. *Volume II - AC*.

[89] E. Twining and D. G. Holmes, "Grid current regulation of a three-phase voltage source inverter with an LCL input filter," *Power Electronics, IEEE Transactions on*, vol. 18, pp. 888-895, 2003.

[90] *Photovoltaic (PV) systems. Characteristics of the Utility Interface*, BS EN 61727, 1996.

[91] M. Liserre, R. Teodorescu, and F. Blaabjerg, "Stability of grid-connected PV inverters with large grid impedance variation," in *35th IEEE Annual Power Electronics Specialists Conference*, 2004, pp. 4773-4779 Vol.6.

[92] A. Kotsopoulos, P. J. M. Heskes, and M. J. Jansen, "Zero-crossing distortion in grid-connected PV inverters," *IEEE Transactions on Industrial Electronics*, vol. 52, pp. 558-565, 2005.

[93] M. J. Ryan, W. E. Brumsickle, and R. D. Lorenz, "Control topology options for single-phase UPS inverters," *IEEE Transactions on Industry Applications*, vol. 33, pp. 493-501, 1997.

[94] E. Twining and D. G. Holmes, "Modelling grid-connected voltage source inverter operation," in *The Australasian Universities Power Engineering Conference*, Perth, Australia, 2001.

[95] E. M. Lightner and S. E. Widergren, "An orderly transition to a transformed electricity system," *IEEE Transactions on Smart Grid*, vol. 1, pp. 3-10, 2010.

[96] C. Wessels, J. Dannehl, and F. W. Fuchs, "Active damping of LCL-filter resonance based on virtual resistor for PWM rectifiers - Stability analysis with different filter parameters," in *IEEE Power Electronics Specialists Conference*, 2008, pp. 3532-3538.

[97] W. Gullvik, L. Norum, and R. Nilsen, "Active damping of resonance oscillations in LCL-filters based on virtual flux and virtual resistor," in *European Conference on Power Electronics and Applications*, 2007, pp. 1-10.

[98] V. Blasko and V. Kaura, "A novel control to actively damp resonance in input LC filter of a three-phase voltage source converter," *IEEE Transactions on Industry Applications*, vol. 33, pp. 542-550, 1997.

[99] S. Engel, K. Rigbers, and R. W. De Doncker, "Digital repetitive control of a three-phase flat-top-modulated grid tie solar inverter," in *13th European Conference on Power Electronics and Applications*, 2009, pp. 1-10.

[100] C. P. Dick, S. Richter, M. Rosekeit, J. Rolink, and R. W. De Doncker, "Active damping of LCL resonance with minimum sensor effort by means of a digital infinite impulse response filter," in *European Conference on Power Electronics and Applications*, 2007, pp. 1-8.

[101] E. Zaneta, B. Anton, and M. Mucha, "Harmonic distortion produced by synchronous generator in thermal power plant," in *6th WSEAS International Conference on Power Systems*, Lisbon, Portugal, 2006, pp. 424-428.

[102] "Power quality and the Hershey System," Hershey Energy Systems, Application Guide.

[103] K. Visscher and P. J. M. Heskes, "A method for operational grid and load impedance measurements," in *International Conference on Future Power Systems*, 2005, p. 4.

[104] M. Ciobotaru, R. Teodorescu, and F. Blaabjerg, "On-line grid impedance estimation based on harmonic injection for grid-connected PV inverter," in *IEEE International Symposium on Industrial Electronics*, 2007, pp. 2437-2442.

[105] L. Asiminoaei, R. Teodorescu, F. Blaabjerg, and U. Borup, "A digital controlled PV-inverter with grid impedance estimation for ENS detection," *IEEE Transactions on Power Electronics*, vol. 20, pp. 1480-1490, 2005.

[106] M. Liserre, F. Blaabjerg, and R. Teodorescu, "Grid impedance estimation via excitation of LCL-filter resonance," *IEEE Transactions on Industry Applications*, vol. 43, pp. 1401-1407, 2007.
[107] "A basic introduction to filters-Active, passive, and switched-capacitor," National Semiconductor Application Note AN779, 2010.
[108] D. I. Crecraft and S. Gergely, *Analog Electronics: Circuits, Systems and Signal Processing*. Oxford: Butterworth-Heinemann (Newnes), 2002.
[109] T. Kugelstadt, "Chapter 16 - Active filter design technique," Texas Instruments, Application Report SLOA088.
[110] J. Karki, "Analysis of the Sallen-Key architecture," Texas Instruments Application Report SLOA024B, 2002.
[111] M. M. M. Zin, M. A. Zaw, and M. N. Zaw, "Design and implementation of active band-pass filter for low frequency RFID (Radio Frequency Indentification) System," in *International MultiConference of Engineers and Computer Scientists*, Hong Kong, 2009.
[112] B. C. Baker, "Anti-aliasing, analog filters for data acquisition systems," Microchip Application Note AN699, 1999.
[113] S. Ayasun and C. O. Nwankpa, "Transformer tests using MATLAB/Simulink and their intergration into undergraduate electric machinery courses," *Computer Applications in Engineering Education*, vol. 14, pp. 142-150, 2006.
[114] J. Rodriguez and G. Saldanha, "No harmony in harmonics," Eaton, White Paper WP10-nn, 2010.
[115] R. G. Ellis, "Power system harmonics: A reference guide to causes, effects and corrective measures," Rockwell Automations, Reference Guide MVB-WP011B-EN-P, 2001.
[116] W. Abbas and M. A. Saqib, "Effect of nonlinear load distributions on total harmonic distortion in a power system," in *International Conference on Electrical Engineering*, 2007, pp. 1-6.
[117] D. Chapman, "Power quality application guide: Harmonics causes and effects," Copper Development Association, Application Guide, 2001.
[118] A. G. de Castro, A. M. Munoz, V. P. Lopez, and A. A. Perez, "Harmonic effect in street lighting," in *7th International Conference-Workshop Compatibility and Power Electronics*, 2011, pp. 16-21.
[119] J. S. Subjak, Jr. and J. S. McQuilkin, "Harmonics-causes, effects, measurements, and analysis: an update," *IEEE Transactions on Industry Applications*, vol. 26, pp. 1034-1042, 1990.
[120] W. A. Maslowski, "Harmonics in power systems," in *IEEE Annual Textile, Fiber and Film Industry Technical Conference*, 1993, pp. 11/1-1110.
[121] J. L. Hernandez, M. A. Castro, J. Carpio, and A. Colmenar, "Harmonics in Power Systems," in *International Conference on Renewable Energies and Power Quality*, Valencia, Spain, 2009.